



**HAL**  
open science

# Study of the variability of surface salinity in the Bay of Bengal from C/X band radiometric satellite data and an ocean model

Marie Montero

► **To cite this version:**

Marie Montero. Study of the variability of surface salinity in the Bay of Bengal from C/X band radiometric satellite data and an ocean model. Oceanography. Université de Bretagne occidentale - Brest, 2023. English. NNT : 2023BRES0019 . tel-04368931

**HAL Id: tel-04368931**

**<https://theses.hal.science/tel-04368931>**

Submitted on 2 Jan 2024

**HAL** is a multi-disciplinary open access archive for the deposit and dissemination of scientific research documents, whether they are published or not. The documents may come from teaching and research institutions in France or abroad, or from public or private research centers.

L'archive ouverte pluridisciplinaire **HAL**, est destinée au dépôt et à la diffusion de documents scientifiques de niveau recherche, publiés ou non, émanant des établissements d'enseignement et de recherche français ou étrangers, des laboratoires publics ou privés.

# THÈSE DE DOCTORAT DE

L'UNIVERSITÉ  
DE BRETAGNE OCCIDENTALE

ÉCOLE DOCTORALE N° 598  
*Sciences de la Mer et du Littoral*  
Spécialité : *Océanographie physique et Environnement*

Par

**Marie MONTERO**

**Étude de la variabilité de la salinité de surface dans le Golfe du Bengale à partir de données satellitaires radiométriques en bande C/X et d'un modèle d'océan**

Thèse présentée et soutenue à Plouzané, le 18 Avril 2023  
Unité de recherche : Laboratoire d'océanographie physique et spatiale (LOPS)

## Rapporteurs avant soutenance :

Antonio TURIEL  
Chercheur Senior ICM, Barcelona (Spain)  
Gaël ALORY  
Enseignant-Chercheur CNAP, Toulouse

## Composition du Jury :

Président : Xavier CARTON  
Professeur UBO, Brest  
Examineurs : Antonio TURIEL  
Chercheur Senior ICM, Barcelona (Spain)  
Gaël ALORY  
Enseignant-Chercheur CNAP, Toulouse  
Jacqueline BOUTIN  
Directrice de Recherche, CNRS, Paris  
Gilles REVERDIN  
Directeur de Recherche, CNRS, Paris  
Dir. de thèse : Jean TOURNADRE  
Directeur de Recherche, IFREMER, Brest

## Invité(s) :

Co-dir. de thèse : Clément DE BOYER MONTÉGUT  
Chargé de Recherche, IFREMER, Brest  
Co-dir. de thèse : Nicolas REUL  
Directeur de Recherche, IFREMER, Toulon  
Co-dir. de thèse : Jérôme VIALARD  
Directeur de Recherche, IRD, Paris



# ACKNOWLEDGEMENT

---

Le travail de recherche présenté dans ce mémoire de thèse a été rendu possible grâce au soutien financier de la région Bretagne et du CNES, que je remercie chaleureusement pour leur soutien. Outre ces aspects financiers, cette thèse est le fruit de plusieurs années de travail acharné, de remises en question, de doutes et de découvertes, et je n'aurais pas pu y arriver sans le soutien et l'encouragement de nombreuses personnes auxquelles je tiens à exprimer ma profonde gratitude.

Je commence par remercier chaleureusement mon directeur de thèse, Dr Jean Tournadre pour toutes les discussions inspirantes sur le rugby, le Japon et même l'océanographie. Je suis ravie d'avoir travaillé en sa compagnie, car outre son appui scientifique, il a toujours été là pour me soutenir et me conseiller au cours de l'élaboration de cette thèse.

Je voudrais aussi remercier grandement mes encadrants de thèse, le Dr Clément de Boyer Montégut, Dr Jérôme Vialard et Dr Nicolas Reul pour m'avoir guidée tout au long de ce projet et pour avoir partagé leur savoir, leur expertise et leur temps avec moi.

J'aimerais également remercier les rapporteurs, le Dr Antonio Turiel et le Dr Gaël Alory, pour leur contribution précieuse à l'évaluation de ma thèse. Je suis également reconnaissante envers les membres de mon jury de thèse, qui ont accepté de consacrer leur temps et leur expertise pour évaluer mes travaux.

Le Dr Jacqueline Boutin et le Dr Fabien Durand m'ont fait l'honneur d'être membres de mon comité de suivi individuel, ils ont pris le temps de m'écouter et de discuter avec moi. Leurs remarques m'ont permis d'envisager mon travail sous un autre angle et leurs soutiens m'ont permis de m'améliorer chaque année. Pour tout cela je les en remercie.

Je suis reconnaissante envers le CNES et la région de Bretagne pour leur généreuse contribution financière à cette recherche. Leur soutien a rendu possible la réalisation de ce projet.

Je remercie les personnes du laboratoire LOPS pour leur accueil bienveillant et de leur aide que ce soit des problèmes informatiques ou des nombreuses discussions scientifiques. En particulier Jean-Marc et Tina, qui m'ont beaucoup soutenu et m'ont apporté beaucoup de conseils tout au long de ma thèse.

---

Un grand merci à mes collègues et amis de bureau, Marine, Sophia, Luc. Vous m'avez apporté énormément de soutien, bonne humeur et aide précieuse, surtout dans des moments plus critiques. Merci aussi aux autres thésards/postdocs du labo : Edouard, Léo, Roy, Arthur, Théo, j'en oublie sûrement, mais sachez que votre présence au labo, votre bonne humeur et vos encouragements m'ont beaucoup aidé et motivé.

Merci à Marion, qui depuis le tout début de cette thèse est présente. C'était un énorme plaisir de découvrir la Bretagne avec toi. Merci pour ton aide tout en long de ces trois ans et demi. Merci aussi à Diane. Grâce à toi la pandémie du Covid et le confinement ont été moins durs et soutenable. Ces amitiés trouvées sont la cerise sur le gâteau, permettant de finir cette aventure de manière parfaite.

Merci aussi à toi Camille, qui, de loin, m'a toujours encouragé et soutenu. Tu as été mon alliée la plus loyale, toujours prête à me donner un coup de main pour marquer des essais et à me rappeler de garder la tête haute, même lorsque la partie était difficile.

Également un merci à mes amies en Allemagne, particulièrement Svenja. Nos conversations m'ont souvent permis de déconnecter, faire une petite pause pour ensuite continuer avec des idées plus claires et de nouvelles motivations.

Jasmin, danke dass du du bist. Egal wie mein Zustand war, ein Telefonat mit dir, etwas ay ay ay und uie uie uie und schon ging es mir besser. Deine Verrücktheit hat es doch immer wieder geschafft mich aus jedem Tief in dieser verrückten Achterbahnfahrt mit der Kraft von 3G zu befreien, und um zum nächsten Hoch zu rasen.

Danke auch euch, Ines und Gerd, für die Unterstützung, und eure Energie. Selbst 1300 km konnten euch nicht abhalten damit ich etwas von zu Hause fühlen kann. Ines, danke, das du Familie bist, und kein Weg dir zu weit war es zu beweisen.

Enfin, je voudrais remercier ma famille pour leur amour, leur encouragement et leur soutien inconditionnel tout au long de mes études. Spécialement mon père, qui n'a jamais hésité à consacrer son temps pour m'aider, conseiller, et de discuter et qui m'a permis de poursuivre mes études dans toute la France.

# TABLE OF CONTENTS

---

<b>Abstract</b>	<b>13</b>
<b>French summary</b>	<b>15</b>
<b>Preamble</b>	<b>25</b>
<b>1 General Introduction</b>	<b>29</b>
1.1 From Sea Surface Salinity (SSS)...	29
1.1.1 What is Salinity?	29
1.1.2 Sea Surface Salinity (SSS) Global Distribution	32
1.1.3 Fundamental Role and Impacts of the Salinity on Ocean and Climate	35
1.2 ... to Space-Born Microwave Remote Sensing	43
1.2.1 Physical Principles of Salinity Remote Sensing	43
1.2.2 SSS Retrieval From Radiometers Operated From L-Band	48
1.2.2.1 History of L-Band radiometers	51
1.2.3 Attempts to retrieve SSS with C- and X-band radiometer data	55
1.3 Bay of Bengal (BoB): A Singular Tropical Ocean Basin	64
1.3.1 Impacts of salinity	65
1.3.2 Seasonal Cycle	66
1.3.3 Interannual Variability	70
1.3.4 Review of SSS remote sensing (L-band radiometer) in the BoB	73
1.4 Objectives and Plan	75
<b>2 Data</b>	<b>77</b>
2.1 Satellite observations	77
2.1.1 AMSR-E	77
2.1.2 Climate Change Initiative (CCI)	80
2.2 In situ observations	81
2.2.1 ARGO profiler floats	81
2.2.2 Ships of opportunity: bucket and XCTD's	81

TABLE OF CONTENTS

---

2.3	Merged Satellite and in situ observations	
	- GlobeCurrent . . . . .	82
2.4	Ocean General Circulation Model - Project IMHOTEP . . . . .	83
2.5	Ocean Reanalysis . . . . .	86
	2.5.1 GLORYS2V4 . . . . .	87
	2.5.2 GLORYS12V1 . . . . .	87
<b>3</b>	<b>Retrieving SSS from C-/X-band radiometers</b>	<b>89</b>
3.1	Article Summary . . . . .	89
3.2	SSS estimates from AMSR-E radiometer in the BoB . . . . .	91
	3.2.1 Abstract . . . . .	91
	3.2.2 Introduction . . . . .	92
	3.2.3 Data . . . . .	95
	3.2.3.1 AMSR-E data . . . . .	95
	3.2.3.2 Sea Surface Salinity European Space Agency (ESA) Cli- mate Change Initiative (CCI) Product . . . . .	97
	3.2.3.3 In Situ Sea Surface Salinity data . . . . .	97
	3.2.3.4 Ocean re-analyses . . . . .	98
	3.2.4 AMSR-E SSS Retrieval Algorithm . . . . .	98
	3.2.4.1 Algorithm Principles . . . . .	98
	3.2.4.2 Algorithm Refinements for the BoB Case . . . . .	105
	3.2.4.2.1 Choice for an SST product: diurnal cycle impact . . . . .	105
	3.2.4.3 Brightness temperature contamination by land . . . . .	105
	3.2.4.4 Algorithm empirical adjustments . . . . .	107
	3.2.4.4.1 Empirical surface roughness correction . . . . .	108
	3.2.4.4.2 Empirical SST-dependent correction . . . . .	111
	3.2.4.4.3 Empirical water vapor and liquid water dependent correction	112
	3.2.4.5 Additional spatial and temporal filtering . . . . .	114
	3.2.4.6 Specific SSS inversion algorithm for the BoB . . . . .	115
	3.2.5 AMSR-E SSS retrieval and validation . . . . .	116
	3.2.5.1 Consistency check: comparison with CCI data . . . . .	116
	3.2.5.2 Validation with in-situ data . . . . .	119
	3.2.5.3 Comparing AMSR-E and ocean re-analyses SSS interan- nual variability . . . . .	119

3.2.6	Summary and Discussion . . . . .	122
3.2.6.1	Summary . . . . .	122
3.2.6.2	Discussion . . . . .	123
3.3	Corrective Measures for Developing Accurate Algorithms . . . . .	126
3.3.1	The Impact of the Empirical GMF . . . . .	126
3.3.2	The Impact of the Learning Period . . . . .	127
3.3.3	The Impact of the AMSR-E Swath Directionality . . . . .	128
3.3.4	The Impact of Additional Filtering . . . . .	130
3.3.5	The Impact of the Diurnal Cycle . . . . .	131
3.3.6	Influences of IOD . . . . .	131
3.4	Additional results since submission . . . . .	135
<b>4</b>	<b>SSS variability in the BoB</b>	<b>137</b>
4.1	Influences ... . . . .	137
4.1.1	... of the IOD . . . . .	137
4.1.2	... of Eddies . . . . .	140
4.2	Methodology of the variability determination . . . . .	142
4.3	Validation of the IMHOTEP dataset . . . . .	145
4.3.1	Removal of a spurious SSS signal in the IMHOTEP dataset . . . . .	145
4.3.2	Seasonal Cycle Validation . . . . .	148
4.3.3	Validation of non-seasonal signals . . . . .	148
4.4	Intrinsic Variability: qualitative analysis . . . . .	159
4.5	Intrinsic Variability: quantitative analysis . . . . .	162
<b>5</b>	<b>Conclusion and Perspectives</b>	<b>169</b>
<b>A</b>	<b>Appendix from Article</b>	<b>176</b>
A.I	. . . . .	176
A.II	. . . . .	177
A.III	. . . . .	177
A.IV	. . . . .	178
<b>B</b>	<b>Complementary figures</b>	<b>179</b>
B.I	Temporal differences of SSS in the BoB . . . . .	179
B.II	Temporal differences of detrended SSS in the BoB . . . . .	180
B.III	Seasonal Comparison between SLA from IMHOTEP and Glorys . . . . .	181

TABLE OF CONTENTS

---

B.IV Seasonal Comparison between SSS from IMHOTEP and CCI . . . . .	184
B.V Regression with the IOD for different datasets . . . . .	187
<b>Bibliography</b>	<b>191</b>

# ACRONYMS

---

AMSR-E	Advanced Microwave Scanning Radiometer for Earth observing system.
ARGO	Array for Real-time Geostrophic Oceanography.
BoB	Bay of Bengal.
CCI	Climate Change Initiative.
CTD	Conductivity-Temperature-Depth.
DJF	December-January-February.
DMI	Dipole Mode Index.
ECI	East Coast of India.
ECV	Essential Climate Variable.
EICC	East Indian Coastal Current.
ENSO	El Niño-Southern Oscillation.
EOF	Empirical Orthogonal Function.
ESA	European Space Agency.
FOV	Field Of View.
GB	Ganga-Brahmaputra.
Glorys	Glorys $\frac{1}{12}^\circ$ .
GMF	Geophysical Model Function.
IAPSO	International Association for the Physical Sciences of the Oceans.

IMHOTEP	Impacts of freshwater discharge interannual variability on Ocean heat-salt contents and regional sea level change over the altimetry Period.
IOD	Indian Ocean Dipole.
JJA	June-July-August.
MAD	Median Absolute Deviation.
MAM	March-April-May.
MIRAS	Microwave Imaging Radiometer with Aperture Synthesis.
NASA	National Aeronautics and Space Administration.
NEDT	Noise Equivalent Temperature Difference.
NEMO	Nucleus for European Modelling of the Ocean.
PC	Principal Components.
REMSS	REMOte Sensing System.
RFI	Radio Frequency Interference.
RTM	Radiative Transfer Model.
SAR	Synthetic Aperture Radar.
SDI	Sea level Dipole Index.
SLA	Sea Level Anomaly.
SMAP	Soil Moisture Active-Passive.
SMOS	Soil Moisture and Ocean Salinity.
SON	September-October-November.
SSS	Sea Surface Salinity.
SST	Sea Surface Temperature.
Ssurf	shallowest measurement of salinity.
TC	Tropical Cyclone.
TEOS-10	Thermodynamic Equation Of Seawater 2010.

TOA	Top Of Atmosphere.
TSG	Thermo-SalinoGraph.
XCTD	eXpandable Conductivity-Temperature-Depth.

# LIST OF SYMBOLS

---

Symbol	Description	Unit
$L$	atmospheric columnar cloud liquid Water	mm
$R$	reflection coefficient	None
$T_A$	brightness temperature measured at antenna level	K
$T_B$	oceans brightness temperature	K
$U_{10}$	10 m height near-surface wind speed	$\text{m s}^{-1}$
$V$	atmospheric columnar water vapor	mm
$\Delta e$	perfectly flat sea surface emissivity contrast	None
$a$	absorptivity	None
$e$	emissivity	None
$f$	frequency	$\text{s}^{-1}$
$\varepsilon_r$	dielectric constant	None
$\varepsilon_s$	dielectric constant of seawater	None
$SSS'$	Sea Surface Salinity Anomaly	pss

# ABSTRACT

---

## English

This thesis focuses on understanding the Bay of Bengal (BoB) Sea Surface Salinity (SSS) variability, because of its impact on regional rainfall, tropical cyclones, and biogeochemical productivity. L-band radiometry has been used to estimate BoB SSS since 2010, but BoB SSS was not well constrained by in situ data before. In the first part, I reconstruct BoB SSS using AMSR-E satellite data, yielding eight additional years of data. I demonstrate the necessity of carefully screening land contamination and applying empirical corrections on ascending and descending passes separately. The resulting dataset has some issues but captures non-seasonal variations along the east coast of India during several multi-year periods. The second part aims to resolve inconsistent results about BoB interannual SSS variability obtained from observational satellite datasets and modelling analyses over longer periods. Using Ocean General Circulation Model experiments, I test the hypothesis that internal oceanic variability associated with stirring by oceanic eddies blurs and modulates wind-forced signals associated with the Indian Ocean Dipole climatic mode. The focus is on the “river in the sea,” a post-monsoon low salinity band along the east coast of India. Eddies strongly modulate the “river in the sea” offshore extension, but not its length, and forced variability dominates near the coast. The “river in the sea” length modulation during IOD-neutral years needs to be explained by another phenomenon, and I hypothesize that intraseasonal wind variations may be responsible. Overall, the thesis provides insight into BoB SSS variability and the associated processes, using satellite data and modelling analyses.

## **Français**

L'objet de cette thèse est d'approfondir notre compréhension de la variation de la salinité en surface de la Baie du Bengale (BoB) en raison de son impact sur les précipitations régionales, les cyclones tropicaux et la productivité biogéochimique. Avant 2010, l'estimation de la SSS de la BoB était basée sur un nombre limité de données in situ, ce qui créait une estimation spatialement restreinte. Depuis l'introduction de la radiométrie de bande L en 2010, il est désormais possible d'estimer la SSS de la BoB de manière plus étendue spatialement.

La radiométrie L-band a été utilisée pour estimer la SSS de la BoB depuis 2010, mais la SSS de la BoB n'était pas bien contrainte par des données in situ auparavant. Dans la première partie, je reconstitue la SSS de la BoB en utilisant des données satellitaires d'AMSR-E, ce qui permet d'obtenir huit années supplémentaires de données. Je démontre la nécessité de bien filtrer les contaminations terrestres et d'appliquer des corrections empiriques aux orbites ascendants et descendants séparément. Le jeu de données obtenu présente quelques problèmes mais permet de capturer les variations non saisonnières le long de la côte Est de l'Inde pendant plusieurs périodes pluriannuelles.

La deuxième partie vise à résoudre les résultats incohérents obtenus à propos de la variabilité de la SSS interannuelle de la baie du Bengale à partir de données satellites d'observation et d'analyses de modélisation sur de plus longues périodes. En utilisant des expériences de modélisation de la circulation générale océanique, je teste l'hypothèse selon laquelle la variabilité océanique interne associée à l'agitation par les tourbillons océaniques brouille et module les signaux forcés par le vent associés au mode climatique de Dipôle de l'Océan Indien (IOD). L'accent est mis sur la "rivière dans la mer", une bande de basse salinité post-mousson le long de la côte Est de l'Inde. Les tourbillons modulent fortement l'extension au large de la "rivière dans la mer", c'est-à-dire jusqu'à où cette longue d'eau douce peut s'étaler le long de la côte Est Indienne, mais pas sa longueur, et la variabilité forcée domine près de la côte. La modulation de la longueur de la "rivière dans la mer" pendant les années neutres du IOD-neutres doit être expliquée par un autre phénomène, et j'emets l'hypothèse que les variations éoliennes intrasaisonnières pourraient en être responsables. De manière générale, la thèse fournit des informations sur la variabilité de la SSS de la baie du Bengale et les processus associés, en utilisant des données satellites et des analyses de modélisation.

# RESUMÉ FRANÇAIS

---

L'étude de la salinité de surface océanique (SSS) est un domaine de recherche critique dans le domaine de l'océanographie et de la science du climat. La SSS joue un rôle crucial dans de nombreux processus océanographiques (par exemple, la circulation océanique, la densité et la thermodynamique de l'eau de mer, la chimie), les écosystèmes marins et le cycle de l'eau mondial. Elle contribue également à la surveillance des changements à long terme du cycle hydrologique, tels que ceux attendus en raison de l'augmentation de l'humidité spécifique de l'atmosphère en réponse au réchauffement climatique. Par conséquent, il s'agit d'un paramètre essentiel pour comprendre les interactions complexes entre l'océan et le système climatique de la Terre.

La Baie du Bengale (BoB) est une zone d'étude particulièrement importante pour la SSS. C'est un bassin dans lequel la SSS est supposée influencer les interactions air-mer associées aux moussons ou aux cyclones tropicaux, la productivité océanique et où la SSS est à la fois contrastée et variable. La BoB est un bassin semi-fermé situé dans la partie nord-est de l'océan Indien, bordé par l'Inde, le Bangladesh, le Myanmar et la Thaïlande. Il reçoit d'importants apports d'eau douce de plusieurs grands fleuves, dont le Gange, le Brahmapoutre et l'Irrawaddy, ainsi que des précipitations de la mousson. Cette particularité en fait un "bassin de dilution" où la SSS est, en moyenne, plus basse que dans les autres océans tropicaux. De multiples études ont montré que la SSS dans la BoB varie considérablement à des échelles de temps saisonnières et interannuelles, l'influence de plusieurs facteurs tels que la circulation océanique, les apports fluviaux, les précipitations et l'évaporation. Par exemple, pendant la saison des moussons d'été, la BoB reçoit de grandes quantités d'eau douce des fleuves Gange et Brahmapoutre, ce qui entraîne une baisse de la SSS dans la partie nord du golfe. En revanche, pendant la saison des moussons d'hiver, la SSS augmente en raison de la réduction des apports d'eau douce et de l'augmentation de l'évaporation.

Les variations de la salinité dans la Bob peuvent avoir des conséquences importantes sur la circulation océanique et la variabilité de la mousson. En effet, les changements de salinité peuvent impacter la densité de l'eau, ce qui peut à son tour affecter les modèles de circulation océanique, la répartition de la chaleur et des nutriments dans l'océan, en

influençant les gradients de pression horizontaux et le mélange vertical. La SSS joue également un rôle dans le système de mousson, car des variations dans cette dernière peuvent influencer l'intensité et la période de précipitations de mousson. De plus, l'introduction d'eau douce, qui est très flottante et se situe donc près de la surface, peut renforcer la stabilité de la couche superficielle en augmentant sa résistance au mélange vertical, entraînant ainsi une diminution de sa profondeur. Une faible profondeur de la couche mélangée et une éventuelle présence de couche barrière peuvent contribuer à maintenir les cyclones tropicaux les plus forts à travers le monde.

Ainsi, une étude minutieuse de la variabilité de la SSS dans la BoB est nécessaire. Bien que la SSS ait été mesurée pendant de nombreuses années, les méthodes et technologies utilisées ont évolué avec le temps. À l'origine, la salinité était mesurée en collectant des échantillons d'eau et en analysant leur teneur en sel en laboratoire. Au fil des décennies, de nouvelles technologies ont émergé permettant des mesures plus exhaustives et continues de la SSS. Parmi ces technologies, les flotteurs ARGO sont en mesure de mesurer avec grande précision et exactitude la salinité à diverses profondeurs de l'océan.

Cependant, la distribution spatiale des mesures in situ dans la BoB, en particulier près des côtes, n'est pas suffisamment complète pour contraindre les anomalies de salinité non saisonnières sur l'ensemble de la baie. Ce problème a été résolu avec le lancement de radiomètres L-band à partir de 2010 (SMOS, Aquarius et SMAP), qui ont grandement amélioré notre compréhension de la distribution mondiale de la SSS et de sa variabilité. Toutefois, la période de seulement 13 ans reste insuffisante pour étudier la variabilité interannuelle de la SSS. De plus, les mécanismes sous-jacents qui entraînent la variabilité non saisonnière/interannuelle de la SSS dans la partie ouest de la BoB restent mal compris. Ces défis scientifiques seront l'objet de ma thèse de doctorat.

Le développement d'un algorithme innovant par Nicolas Reul en 2009 permet de récupérer les données de SSS au-dessus du panache de l'Amazone à partir de mesures provenant de radiomètres à bande C et X (AMSR-E), mis en orbite en 2002. Cependant, le lancement de SMOS (2010) peu après cette étude innovante a fourni des mesures dix fois plus sensibles que celles des bandes C/X, mettant ainsi le projet quelque peu en attente.

Mon premier objectif de cette thèse consistera à obtenir une série temporelle plus étendue de la SSS afin d'établir des liens plus solides avec d'autres facteurs. Pour ce faire, je vais utiliser l'approche proposée par Reul et al. (2009) pour estimer la SSS à partir des données satellitaires AMSR-E et ainsi prolonger la série temporelle jusqu'en 2002. Les questions scientifiques qui se poseront dans cette partie de ma thèse en télédétection

seront les suivantes:

- L'approche de Reul et al. (2009) peut-elle être appliquée avec succès dans la région de la BoB ?
- Quelles adaptations, le cas échéant, sont nécessaires pour que l'approche soit efficace dans la région de la BoB ?
- À quel niveau de précision peut-on parvenir en utilisant l'approche de Reul et al. (2009) dans la région de la BoB ?
- Les données de SSS obtenues sont-elles suffisantes et utiles pour les études interannuelles dans la région de la BoB?
- Les liens interannuels entre la SSS et d'autres facteurs changent-ils lorsqu'on utilise une série temporelle plus longue ?

Après une analyse minutieuse des données, il a été constaté une forte différence de la température de brillance entre les passages ascendants et descendants, en particulier près de la côte, révélant ainsi une contamination résiduelle des terres. Afin d'éliminer cette contamination des points océaniques en aval des passages sur les terres, des masques terre-mer distincts sont appliqués aux passages ascendants et descendants. Les passages sont ensuite traités indépendamment, avec des corrections empiriques distinctes. Les corrections empiriques pour le vent en surface, la température de surface océanique (SST) et la teneur en eau atmosphérique sont effectuées dans cet ordre en utilisant les données de la Climate Change Initiative (CCI) de la SSS et les données de vent, de la SST et de l'eau atmosphérique colocalisées de AMSR-E sur la période commune SMOS/Aquarius-AMSR-E. En outre, un filtrage supplémentaire des données pour éliminer les valeurs aberrantes et un lissage médian de  $0,75^\circ \times 0,75^\circ$  ont également été trouvés pour influencer considérablement les performances finales de la récupération des données.

Malgré la présence de quelques biais de fraîcheur près des côtes, notre produit final est en mesure de se comparer favorablement à la climatologie observée du CCI. En effet, il présente une corrélation de 0,66 et une différence de racine carrée moyenne de pss de 1,09 lorsqu'il est comparé à la salinité de surface in situ colocalisée des flotteurs ARGO. Bien que notre produit ne soit peut-être pas aussi précis que les radiomètres en bande L, il semble tout de même posséder un certain niveau de capacité.

Nous avons également évalué la capacité de notre produit à reconstruire les variations interannuelles de la SSS avant 2010 en comparant les variations interannuelles de la SSS avec celles des réanalyses océaniques dans deux points chauds pour la variabilité inter-

annuelle de la SSS: le nord de la BoB et la côte est de l'Inde. Les résultats suggèrent que notre produit présente peu de compétences sur le nord de la baie du Bengale, mais est plus favorable le long de la côte est de l'Inde. Bien que notre produit soit parfois capable de reproduire les variations interannuelles générales du CCI dans les réanalyses sur de longues périodes (3-5 ans), une amélioration du traitement des données peut être nécessaire.

Des études antérieures, telles que Akhil et al. (2014), ont identifié des variations de la SSS à l'échelle du bassin associées à l'oscillation interdécennale de l'océan Indien (IOD) dans la BoB, ainsi que des variations localisées près de l'estuaire du Gange-Brahmapoutre associées aux débits fluviaux. Cependant, les analyses récentes du jeu de données SMOS par Akhil et al. (2020) (et des analyses similaires utilisant CCI et incluant une année supplémentaire de données dans cette thèse) suggèrent que l'influence de l'IOD sur la SSS dans la BoB, en particulier sur le "fleuve dans la mer" le long de la côte est de l'Inde, n'est pas systématique. De plus, il est difficile d'identifier clairement l'impact des débits fluviaux à partir des ensembles de données existants. Étant donné le rôle important des tourbillons dans l'influence de la distribution de la SSS dans la BoB (Fournier et al., 2017), cette étude visait à estimer la variabilité intrinsèque (tourbillons) par rapport à la variabilité forcée (par exemple, IOD et débits fluviaux) de la SSS dans la BoB afin d'investiguer si la modulation par les tourbillons pouvait expliquer la relation pas tellement systématique entre l'IOD et le fleuve dans la mer.

En conclusion, bien que AMSR-E contienne des informations utiles sur la variabilité interannuelle de la SSS de la BoB, une amélioration supplémentaire du traitement des données est encore nécessaire pour exploiter pleinement cette information.

La deuxième partie de ma thèse doctorale se concentre sur l'océanographie physique de la BoB, plus précisément sur les processus qui régissent les variations non saisonnières de la SSS. Des études antérieures ont suggéré que la relation entre le Indian Ocean Dipole (IOD) et la variabilité de la SSS dans la BoB n'est pas systématique. Mon objectif est d'examiner la possibilité que la variabilité des tourbillons puisse contribuer à l'apparition de signaux de SSS qui altèrent ou obscurcissent la variabilité induite par l'IOD.

- Quelles sont les contributions relatives de la variabilité de la SSS non saisonnière, forcée (vent, eau douce) et intrinsèque (tourbillons mésoéchelle) dans la région de la BoB?
- Comment la distribution de ces contributions varie-t-elle dans le temps (saisons) et dans l'espace dans la région de la BoB?

- Quels sont les origines et les mécanismes possibles des contributions identifiées à la variabilité de la SSS dans la région de la BoB?

Afin de répondre à la question scientifique sur la variabilité intrinsèque du SSS dans la baie du Bengale, j'utilise les sorties de simulation en ensemble (décrites dans la Section 2.4).

L'approche en ensemble est couramment utilisée depuis les années 1990 pour l'atmosphère (e.g., Rowell, 1998). Cette technique permet de traiter les instabilités de turbulence qui créent des anticyclones et des dépressions d'environ 1000/2000 km de taille, qui peuvent être résolus par la capacité numérique des modèles atmosphériques ayant des résolutions typiques d'environ 200 km. En sciences océaniques, cependant, les simulations en ensemble sont une approche assez récente et innovante, car les tourbillons de mésoéchelle ont des tailles typiques de 100/200 km.

Avec l'augmentation de la variabilité synoptique dans les modèles atmosphériques à haute résolution, ces modes de variabilité supplémentaires dans l'océan rendent les simulations en ensemble nécessaires pour étudier les relations de cause à effet dans le climat de la Terre."

Le projet IMHOTEP adopte une telle approche en ensemble, ce qui donne un bon cadre pour quantifier la contribution de la variabilité intrinsèque de l'océan (c'est-à-dire les tourbillons) à la variabilité non saisonnière totale du SSS dans le BOB.

Comme IMHOTEP n'a jamais été validé pour la région BoB, il était inévitable de procéder d'abord à la validation. Cela a permis de constater la nécessité de supprimer une dérive parasite à long terme dans l'ensemble de données. Cette suppression de la dérive semble fonctionner relativement bien en comparaison avec d'autres ensembles de données (CCI, réanalyse Glorys). Néanmoins, IMHOTEP sous-estime la variabilité des tourbillons de la région BoB (probablement en raison de sa résolution horizontale permettant les tourbillons), sous-estime légèrement la réponse de la circulation à l'IOD et ne reproduit la réponse de la SSS à l'IOD que le long de la côte est de l'Inde (bien qu'elle soit sous-estimée).

D'après l'analyse, la variabilité interne liée aux tourbillons de mésoéchelle est prédominante pour la variabilité de l'anomalie du niveau de la mer (SLA) et de la SSS au large de la côte est de l'Inde. Toutefois, les signaux forcés sont plus importants près de la côte et dans la moitié est de la BoB, en raison de l'influence du guide d'ondes côtières et de la radiation vers l'ouest des ondes de Rossby depuis la bordure orientale de la BoB. La seule région où la variabilité totale et la variabilité interne sont fortes (la variabilité interne

représentant plus de 50% de la variabilité totale) se trouve à la bordure maritime de la zone de la "rivière dans la mer", où les tourbillons modulent l'extension de l'eau de faible salinité vers le large, et non pas sur sa longueur, comme le démontrent des études de cas menées sur plusieurs années.

## Perspectives

En entamant ma recherche de thèse de doctorat, j'ai pris conscience des difficultés liées à la faible sensibilité de la bande C à la salinité de la surface de la mer (SSS) ainsi qu'aux risques de contamination terrestre et d'interférences radiofréquences dans la Baie du Bengale. Malgré ces obstacles, les données que j'ai recueillies constituent la première tentative de récupération de la SSS à partir des données d'AMSR-E dans la Baie du Bengale et semblent prometteuses dans la capture de signaux de SSS non saisonniers, comme en témoigne la reproduction réussie de certains signaux interannuels observés le long de la côte ouest de l'Inde. Cependant, des améliorations supplémentaires sont nécessaires pour améliorer la précision et la fiabilité de l'algorithme. Il convient de noter que la récupération de la SSS à partir de SMOS, lorsqu'elle a été analysée pour la première fois, était presque inutilisable pour la Baie du Bengale et ses performances étaient inférieures à celles de  $SSS_{AMSR-E}$  (Akhil et al., 2016b). Des améliorations substantielles des méthodes de prétraitement, notamment une correction de biais meilleure, saisonnière et dépendante de la latitude, ainsi qu'un contrôle plus strict des données près des terres pour éliminer les interférences radiofréquences restantes, ont été nécessaires pour réduire considérablement les erreurs et transformer l'ensemble de données de SMOS en la ressource précieuse qu'elle est aujourd'hui pour la Baie du Bengale.

En poursuivant mes recherches, je constate que les produits de SSS d'AMSR-E pour la baie du Bengale pourraient être améliorés. Bien que j'utilise actuellement deux masques stationnaires pour exclure les données en aval des terres sur les passes ascendantes et descendantes, il existe des techniques de masquage plus avancées et des méthodes de filtrage dynamique qui pourraient augmenter la précision des mesures de  $SSS_{AMSR-E}$ . Par exemple, l'utilisation d'un masque dynamique permettrait de comparer les pixels voisins pour éliminer les valeurs aberrantes locales et temporelles qui affectent le filtrage spatial, réduisant ainsi les signaux erronés dans la série chronologique.

Ainsi, j'ai l'intention d'explorer ces méthodes pour améliorer la fiabilité et l'exactitude de la récupération de  $SSS_{AMSR-E}$ . En appliquant ces approches plus rigoureuses, nous

pourrons avancer considérablement dans notre compréhension de cet élément océanographique essentiel et contribuer à une analyse plus détaillée et précise de l'océanographie de la baie du Bengale.

En outre, l'exploration d'approches alternatives aux corrections empiriques actuellement utilisées dans mon étude pourrait être bénéfique pour améliorer la précision des récupérations de SSS. Bien que j'aie appliqué des corrections pour le vent, la SST et la vapeur d'eau en trois étapes séquentielles, l'utilisation de réseaux de neurones pourrait nous permettre d'effectuer toutes les corrections en une seule étape et de prendre en compte de manière plus efficace le couplage non linéaire entre les variables. Cette approche permettrait également l'inclusion de paramètres supplémentaires tels que la distance à la côte ou la direction du vent, qui pourraient être pondérés en conséquence pour améliorer la récupération finale de SSS. En explorant ces approches alternatives, nous pourrions être en mesure d'améliorer encore la précision et la fiabilité des récupérations de SSS à partir des données d'AMSR-E dans la baie du Bengale.

Enfin, étant donné que le but de cette étude utilise principalement les anomalies de la SSS, une procédure possible pourrait être la création d'un algorithme de récupération de l'anomalie de la SSS. Cette approche impliquerait d'analyser les différences entre les valeurs observées de la SSS et les valeurs climatologiques, puis de déduire l'anomalie de la SSS à partir de ces différences. Cette technique pourrait réduire l'impact des erreurs et des biais dans les valeurs absolues de la SSS et permettre de se concentrer plus précisément sur la variabilité océanique. Par conséquent, la mise en œuvre d'un algorithme de récupération de l'anomalie de la SSS pourrait être une voie prometteuse pour améliorer davantage ma recherche et augmenter la compréhension de la variabilité de la SSS dans la BoB.

En regardant plus loin dans le futur, le lancement prévu du satellite Copernicus Imaging Microwave Radiometer (CIMR) devrait apporter une contribution significative à l'étude de la SSS. CIMR est une mission satellite de haute priorité dans le programme d'expansion Copernicus de la Commission européenne et comportera un imageur radiomètre fonctionnant sur cinq bandes spectrales, correspondant à des fréquences de 1.4, 6.9, 10.65, 18.7 et 36.5 GHz. Par conséquent, l'analyse des données radiométriques obtenues à partir du même instrument dans les canaux L-, C- et X pourrait aider à affiner davantage l'algorithme actuel à l'avenir.

IMHOTEP semble présenter plusieurs limitations pour capturer avec précision les caractéristiques clés de la variabilité de la SSS dans la région. Il sous-estime les tourbillons, qui sont une force motrice importante de la variabilité interne de la SSS, de manière

significative (50%). De plus, il ne reproduit pas correctement les signaux de SSS induits par l'IOD qui ont été observés dans d'autres études (Akhil et al., 2016a; Akhil et al., 2020) utilisant différentes sources de données, telles que SMOS et CCI. En outre, IMHOTEP présente des gradients de SSS excessivement forts près des côtes, ce qui peut affecter sa capacité à capturer avec précision la variabilité de la SSS dans ces régions.

Compte tenu de ces limitations, il est difficile de déterminer si l'estimation de la contribution intrinsèque à la variabilité totale de la Sea Surface Salinity (SSS) est trop faible ou trop élevée. Cependant, la découverte d'une forte contribution des tourbillons à l'extension offshore du fleuve de la mer confirme des études précédentes qui ont souligné l'importance de l'agitation des tourbillons ou du transport offshore dans cette région (Benshila et al., 2014; Chaitanya et al., 2021; Fournier & Lee, 2021; Hareesh Kumar et al., 2013).

Bien qu'une simulation d'ensemble à résolution plus élevée dans la BoB serait idéale, elle n'est actuellement pas disponible. Par conséquent, un processus de correction et de validation de dérive plus approfondi est nécessaire pour assurer la robustesse de nos résultats. À l'heure actuelle, j'utilise une technique rudimentaire pour corriger les étapes en calculant une tendance temporelle de base et en la soustrayant de chaque point de données. Néanmoins, une correction plus sophistiquée qui prend en compte à la fois les étapes et les biais résiduels pourrait être explorée et utilisée pour améliorer la précision des résultats. En outre, une quantification plus approfondie de l'impact de l'amplitude du champ de tourbillons et des gradients de SSS climatologiques sur la variabilité interne est nécessaire. Cela peut être réalisé en estimant des valeurs dérivées de l'observation pour la variabilité de SSS induite par les tourbillons, qui peuvent ensuite être comparées avec les valeurs du modèle. De telles analyses nous permettraient de mieux comprendre et modéliser la dynamique complexe de la Baie du Bengal, ce qui conduirait finalement à des prévisions améliorées des changements futurs dans la région.

L'analyse des simulations avec un écoulement de la rivière climatologique dans la BoB (IMHOTEP expérience ES) en plus des simulations existantes pourrait être bénéfique. Ces simulations pourraient fournir de nouvelles informations sur les sources potentielles de biais et le rôle de l'écoulement de la rivière dans la variabilité de la BoB. En comparant ces simulations avec celles utilisées dans cette étude (IMHOTEP expérience EGAI), une meilleure compréhension de la contribution de l'écoulement de la rivière à la variabilité forcée de BoB peut être obtenue.

Finalement, mon étude suggère que bien que les années positives de l'IOD tendent à

être associées à une courte "rivière dans la mer" et que les années négatives de l'IOD soient associées à une longue rivière, il y a des années d'IOD neutres qui semblent également avoir une rivière anormalement courte ou longue. Les résultats de cette étude indiquent que les tourbillons n'expliquent pas entièrement cette modulation de la longueur de la "rivière dans la mer". En fait, ils suggèrent même que les signaux de circulation forcée dominent près de la côte est de l'Inde. Bien que l'IOD induise une réponse océanique (Akhil et al., 2016a; Suresh et al., 2018), ce n'est pas le seul phénomène qui peut induire une réponse de la circulation dans le guide d'onde côtier de la BoB. Plusieurs études indiquent que les variations de vent équatorial intrasaisonniers associées à l'oscillation de Madden Julian en hiver boréal (Zhang, 2005) et aux phases actives de la mousson en été boréal (Goswami & Xavier, 2005) peuvent induire de fortes réponses de la circulation dans le guide d'onde côtier de l'océan Indien nord (Suresh et al., 2013; Vialard et al., 2009). Les variations de niveau de la mer résultantes ont généralement une période d'environ 90 jours, ce qui est suffisant pour générer des variations significatives dans le courant côtier équatorial est indien (EICC), et par conséquent, dans le débit de la rivière dans la mer, à condition que la phase soit appropriée. À l'avenir, je prévois d'étudier si ces variations entraînées par le vent pourraient jouer un rôle dans la variabilité non saisonnière de la salinité de surface de la mer (SSS) le long de la côte est de l'Inde, en conjonction avec l'IOD.



# PREAMBLE

---

The study of the Sea Surface Salinity (SSS) is a critical area of research in the field of oceanography and climate science. SSS plays a crucial role in many oceanographic processes (e.g., ocean circulation, seawater density and thermodynamic, chemistry), in marine ecosystems, and the global water cycle. It also contributes to monitoring long-term changes of that hydrological cycle, such as those expected due to the increase in atmospheric specific humidity in response to global warming. As a result, it is an essential parameter for understanding the complex interactions between the ocean and the Earth's climate system.

The Bay of Bengal (BoB) is a particularly important area of study when it comes to SSS. It is a basin where SSS is thought to influence air-sea interactions associated with the monsoons or Tropical Cyclones, oceanic productivity, and where SSS is both contrasted and variable. The Bay of Bengal is a semi-enclosed basin located in the northeastern part of the Indian Ocean, bordered by India, Bangladesh, Myanmar, and Thailand. It receives significant freshwater inputs from several large rivers, including the Ganges, Brahmaputra, and Irrawaddy, as well as from monsoon rainfall. That makes the BoB what we call a "dilution basin", receiving a great excess of fresh water over a year, and exhibiting an average low SSS compared to other tropical oceans. Multiple studies have shown that SSS in the Bay of Bengal varies significantly on seasonal and interannual timescales due to a number of factors, including ocean circulation, river runoff, and precipitation, evaporation. For example, during the summer monsoon season, the Bay of Bengal receives large amounts of freshwater from the Ganges and Brahmaputra rivers, leading to a decrease in SSS in the northern part of the bay. In contrast, during the winter monsoon season, SSS increases due to reduced freshwater inputs and increased evaporation.

These Bay of Bengal variations can have significant impacts on ocean circulation and monsoon variability. Indeed, changes in SSS can affect the density of seawater, which can in turn impact ocean circulation patterns and the distribution of heat and nutrients in the ocean, through its influence on horizontal pressure gradients and vertical mixing. SSS also plays a role in the monsoon system, as changes in SSS can affect the strength and timing of monsoon rainfall. Moreover, the shallowness of the mixed layer and the

presence of a barrier layer participate in sustaining some of the strongest tropical cyclones earth-wide. Given that a significant portion of the population resides in coastal areas, the potential casualties resulting from such events, including both human lives and material losses, are always a concern.

Thus a close study of the SSS variability in the BoB is necessary. SSS has been measured for many years, but the methods and technologies used to measure it have evolved over time. Historically, measurements of the sea surface salinity were done by collecting water samples and analyzing their salt content in a laboratory. In recent decades, new technologies have emerged that allow for more comprehensive and continuous measurements of the sea surface salinity. One such technology is the use of ARGO floats profilers, which can measure salinity at various depths in the ocean with high precision and accuracy. However, the spatial distribution of in situ measurements in the BoB, especially near the coasts, is not sufficient for constraining non-seasonal SSS anomalies over the entire bay. This issue was remedied with the launch of L-band radiometers starting in 2010 (SMOS, Aquarius, and SMAP) which have greatly improved our understanding of the global distribution of sea surface salinity and its variability. Unfortunately, the period of only 13 years remains very short to study SSS interannual variability.

An innovative algorithm, created by Nicolas Reul in 2009, now allows the retrieval of SSS over the Amazon Plume by using measurements coming from C- and X band radiometers, starting as early as year 2002. However, SMOS was launched shortly after this innovative study, providing measurements ten times more sensitive than the SSS from C/X bands, hence putting this project somehow on standby. With the idea of resurrecting the project and applying the algorithm to the BoB by taking advantage of the additional 8 years to study the variability within it, I started my PhD thesis in 2019 at the *Laboratoire d'Océanographie Physique et Spatiale (LOPS)* in Brest, France. Since an innovative modelling approach (ocean ensemble simulations from the IMHOTEP project) was meant to emerge during my PhD, the idea of comparing the results of the variability study between the remotely sensed data and the model output was put forward.

Under the supervision of Jean Tournadre and Nicolas Reul, I created an algorithm based on the aforementioned amazon case study for the BoB. With the additional supervision of Jérôme Vialard and Clément de Boyer Montégut I was able to carry out my study by validating the reconstructed SSS and analyzing the limits of the approach. Under their guidance I was then able to take my study a step further by analyzing the variability of the SSS in the BoB using simulation outputs from IMHOTEP project.

To provide a better understanding, the dissertation starts with a detailed introduction to ocean salinity, radiometric remote sensing, the Bay of Bengal, and presents its plan and objectives. The different steps of the algorithm's creation, validation, and limitations are then presented along with the characteristics of the produced SSS dataset. The thesis then deals with the first results of the IMHOTEP project in the BoB and its applications for studying the variability of SSS.



# GENERAL INTRODUCTION

---

"The Blue Planet" - this nickname has been attributed to our planet because of the impressive extent of the oceans on it. Indeed, over 70% of our planet's surface is covered with water, connecting each part of the planet. This one big ocean is estimated to possess 97% of the water on Earth, creating an important impact on the atmosphere and thus, on the climate.

While the influence of the temperature on the dynamics of the ocean and on its interactions with the atmosphere is a generally well-known fact, the importance of salinity is not as well known. However, salinity is a critical parameter in oceanography, providing crucial information on the water's density and circulation, or for freshwater budget and overall health of the oceans.

In this introductory chapter I first start with an examination of salinity, including its global distribution and general impacts on the ocean physics, ecosystems, and eventually on the Earth's climate system. The use of remote sensing technology to measure salinity is then thoroughly analyzed in a second time, including a discussion of the various methods currently in use. Then I focus on my study area, the Bay of Bengal (BoB), by highlighting its unique oceanic and climatic conditions and the challenges associated with salinity in this area. Finally, the chapter outlines the objectives and key scientific questions addressed in my PhD research.

## 1.1 From Sea Surface Salinity (SSS)...

### 1.1.1 What is Salinity?

Ocean salinity refers to the total mass of dissolved materials present in one kilogram of seawater, typically expressed in grams per kilogram of seawater (g/kg) or parts per thousand (ppt). These dissolved materials primarily consist of salts, which are ionic com-

pounds made up of an assembly of cations and anions with no net electric charge. Unlike molecular compounds, salts are highly soluble in water, forming a solution composed of their anionic and cationic components. The two most abundant dissolved ions in seawater are sodium ( $\text{Na}^+$ ) and chloride ( $\text{Cl}^-$ ), which combine to form table salt ( $\text{NaCl}$ ), a familiar compound in our everyday lives (Figure 1.1). These elements are not very reactive with marine particles and minerals and are mainly brought into the ocean through fresh water runoff and groundwater from the land, typically containing about 1g/kg or less of dissolved matter. However, many of the ions also originate from the internal chemistry of the ocean, the dissolving of biological matter, or sediments from the ocean floor. This dissolved matter contributes to the ocean's salinity, which averages around 34.7 g/kg (or roughly 35g/kg, Figure 1.1). This value remains relatively stable over time as the inputs and departures (e.g., sedimentation and marine evaporates in various arid coastal regions and underwater weathering) of salts are balanced.

A remarkable and important property of seawater is that the ionic ratios of the major elements of marine salinity ( $\text{Cl}^-$ ,  $\text{Na}^+$ ,  $\text{SO}_4^{2-}$ ,  $\text{Mg}^{2+}$ ,  $\text{Ca}^{2+}$ ,  $\text{K}^+$ ) remain constant in time and space if away enough from large river estuaries, and even if locally, evaporation, precipitation or runoffs can concentrate or dilute the water from the sea. This is the evidence that a constant highly effective mixing takes place on geological times scales in the world's oceans (Beer, 2017). Those major elements, being less reactive in the marine environment, have indeed a very long residence time in the ocean, typically from one to a hundred million years, compared to the mixing time of the ocean by deep currents (1,500 years,  $^{14}\text{C}$  dating) and the time of renewal of sea water by rivers (about 40,000 years). As discussed hereunder, this property of seawater is used by oceanographers to measure salinity by recognizing the equivalence of chlorinity (chlorine content) and salinity (total salt content).

Salinity in rivers, lakes, and the ocean is conceptually simple and a basic property of those waters, but it is technically challenging to define and measure precisely. Measurement and definition difficulties arise because natural waters contain a complex mixture of many different elements from different sources (not all from dissolved salts) in different molecular forms.

Hence, several definitions and measurements of salinity were used over time so as to approximate the absolute salinity of seawater. Salinities were largely measured using titration-based techniques before the 1980s, giving chlorinity. The latter was then multiplied by a factor to account for all other constituents. The resulting "Knudsen salinities"

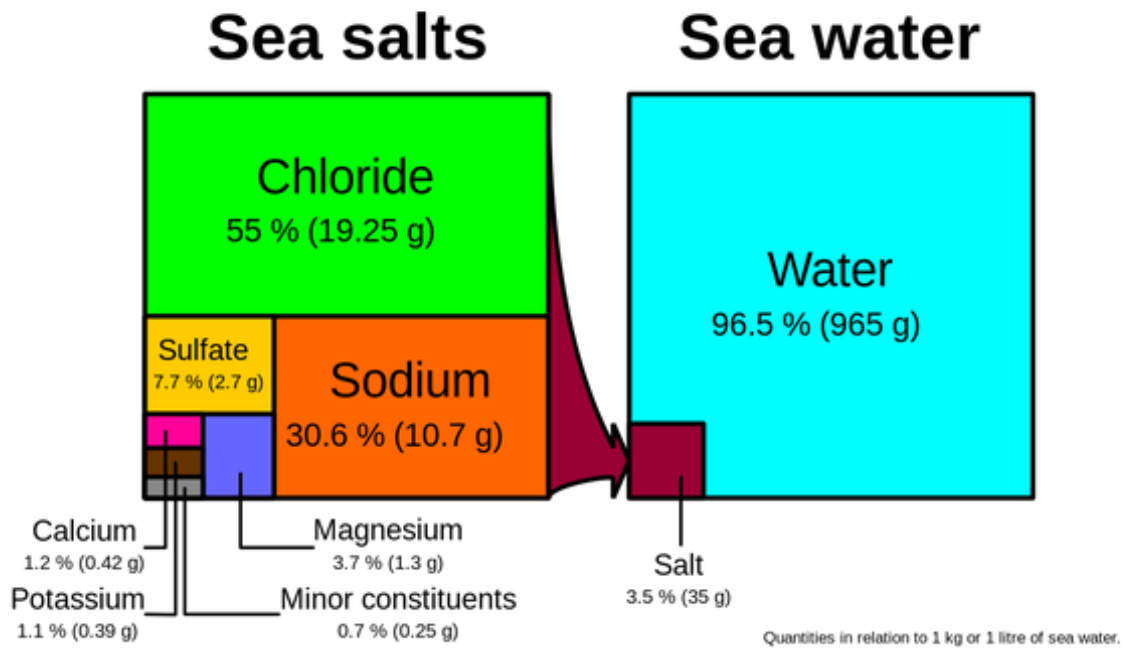


Figure 1.1 – Major constituents of seawater. Light blue represents the mass of pure water ( $H_2O$ ) in 1 kilogram of seawater. The brown square – 35 grams – represents the salt (i.e., ions, mostly sodium and chloride, but there are other dissolved matters, as well). Note that the proportions of each ion in seawater to the total salt component is also given as those are mostly constant over the global ocean. (from Hannes Grobe, Alfred Wegener Institute for Polar and Marine Research, Bremerhaven, Germany, via Wikipedia)

are expressed in units of parts per thousand (ppt or ‰). A bottled seawater product known as International Association for the Physical Sciences of the Oceans (IAPSO) Standard Seawater, especially certified in chlorinity, is used by oceanographers to standardize their measurements with enough precision. In the past thirty to forty years, however, the chlorinity titration has been replaced by the measurement of electrical conductivity for salinity determination and this has led to the development of the scale called the "practical salinity scale 1978" (pss-1978 or pss, Unesco, 1981b), including revisions of the definition of salinity (Lewis, 1980; Unesco, 1981a). The latest revision in Unesco (1985) defines the pss as the ratio of the electrical conductivity of the sea water at the temperature of 15°C and the pressure of the standard atmosphere, to that of a potassium chloride (KCL) solution (with mass fraction of KCl being  $32.4359 \times 10^{-3}$ ) at the same temperature and pressure. If that ratio equals to 1 then salinity is 35 pss.

In 2010 a new standard for the properties of seawater called the Thermodynamic Equation Of Seawater 2010 (TEOS-10) was introduced. It advocates absolute salinity as a replacement for practical salinity, hence officially allowing mass fraction units for salinity (g/kg of solution) and making oceanographic papers more readable for the wider scientific community (IOC et al., 2010; McDougall et al., 2012; Wright et al., 2011). This standard includes a new scale called the reference composition salinity scale. Salinities on this scale are determined by combining electrical conductivity measurements with other information that can account for regional changes in the composition of seawater.

In the main parts of this PhD thesis, I focus on the salinity at the surface of the ocean, also called SSS for Sea Surface Salinity. To express SSS values, I use the pss, as quite all in situ salinity measurements are made through conductivity and given in pss (e.g., Argo floats data, see Chapter 2). Note that, thanks to the TEOS10 packages, exact conversion of salinity from pss to mass fraction (g/kg) and reverse can be done easily when needed, and that the pss and the g/kg unit are practically nearly equivalent (e.g.  $35 \text{ pss} \approx 35\text{g/kg}$ ).

### 1.1.2 Sea Surface Salinity (SSS) Global Distribution

SSS has been identified by the World Meteorological Organization as an Essential Climate Variable (ECV). An ECV is a physical, chemical or biological variable that can be observed reliably and that critically contributes to the characterization of the Earth's climate system.

At the surface, the averaged SSS value over the global ocean is about 35 pss, varying mostly between 32 and 38 pss (Figure 1.2b), depending on freshwater fluxes. Lowest values of SSS (brackish waters below 30 pss) can be reached locally in closed seas (e.g., 8 pss in Baltic Sea) and at the mouth of the rivers (about 15 pss), while highest values are encountered in the Mediterranean Sea ( $\sim 38$  pss) and in the Red Sea ( $\sim 40$  pss). The SSS global distribution is largely controlled by addition (precipitation and ice melting) and removal (evaporation and sea-ice formation) of freshwater (Beer, 2017; Knauss, 1997; Lee et al., 2006).

As we can see on Figure 1.2b, SSS is highest in tropical and subtropical regions. Subsiding air of the subtropical high-pressure centers feeds the trade winds that induce strong evaporation which exceeds precipitation and river runoff (see Figure 1.2a), leading to an increase in salt concentration (Yu et al., 2020).

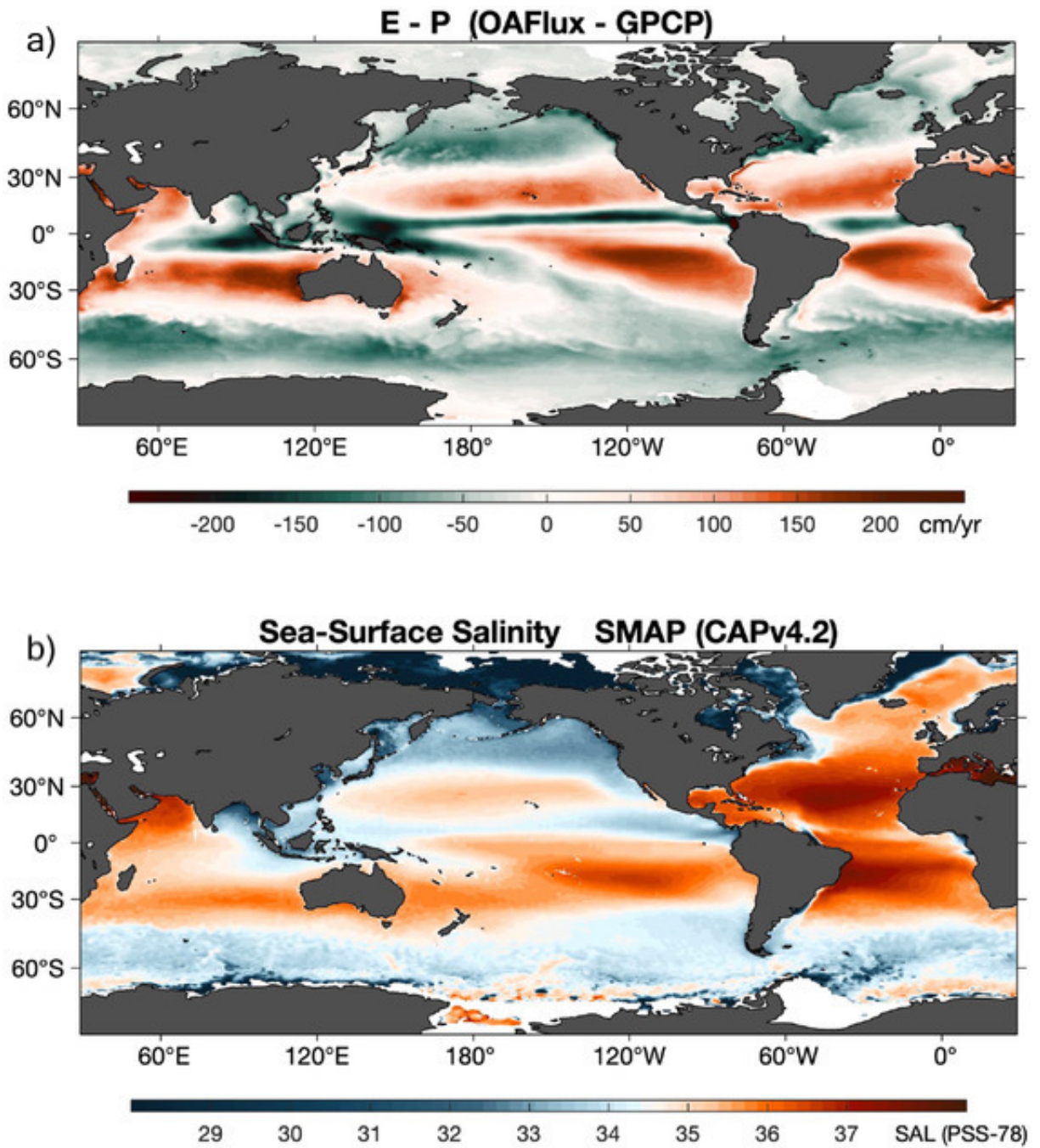


Figure 1.2 – a) The mean evaporation-minus-precipitation (E-P) flux from OAFlux2 and GPCP. b) Mean sea surface salinity observed from SMAP. The period of 2016–2018 was used in constructing both mean fields. (After Yu et al., 2020)

In contrast, SSS is lower in temperate and polar regions due to high precipitation and river runoff that dilute the salt content. The same goes for the deep tropics, which belong to the wettest regions on the planet with trade-wind convergence which forces the water-laden air to rise in altitude. This leads to a formation of clouds and an intense rain fall in the Intertropical Convergence Zone (ITCZ) near the equator in all the ocean basins, and the South Pacific Convergence Zone (SPCZ) in the western South Pacific (Figure 1.2a; Dessier & Donguy, 1994; Yu et al., 2020).

Another, much smaller but nevertheless important, controller of the SSS distribution is the creation and melting of ice. As we can also see in Figure 1.2b, the Pacific Ocean possesses, between 40°N and 60°N, low SSS which is caused by freshening induced by icebergs in North Pacific. The same goes for the coast of Greenland in the Atlantic Ocean, which is due to glacier melting in the case of Greenland and due to inflow from the Arctic (Garcia-Eidell et al., 2017; Supply et al., 2022). In the other hand, the seasonal creation of sea ice will influence the SSS distribution along the perimeter of Antarctica. During the growth of sea ice, the salt contained in the sea water will be locked in the ice, creating a highly concentrated solution of salt in water known as brine. When brine is exposed to lower temperatures or lower pressures, or when additional water is added to the solution, the excess salt cannot remain dissolved and begins to precipitate out of the solution, forming crystals or solid deposits, which are injected in the underlying waters. This is known as salt release or salt precipitation (Broecker, 1997).

There is also a significant variation in sea surface salinity between different ocean basins, with the Pacific Ocean having generally lower salinity levels compared to the Atlantic and Indian Oceans. Especially in the Pacific and Atlantic Ocean the SSS distribution could not be more different, with differences in the SSS going up to 2 pss (Craig et al., 2017). According to Broecker (1997) and Schmitt (2008) this is mostly due to the narrowness of the Atlantic: the evaporation induced by a dry, continental air outweighs the freshwater input. Furthermore, only little moisture transports arrive at the Atlantic Ocean from the Indian Ocean whereas it is easily transported to the Pacific across the Central American isthmus (Schmitt, 2008).

Additionally, salinity levels can vary greatly within a single ocean basin, as observed in the Indian Ocean with the Arabian Sea in the west and the Bay of Bengal in the east. These semi-closed basins exhibit distinct salinity patterns, with the Arabian Sea dominated by evaporation and the Bay of Bengal influenced by freshwater input from river discharges and monsoon rains (Akhil et al., 2014; de Boyer Montégut, 2005; Nyadjro &

Subrahmanyam, 2016). The impact of river runoff on ocean salinity can also be observed in Figure 1.2b, where low salinity patterns are evident around the mouths of major world rivers such as the Amazon and the Congo.

### 1.1.3 Fundamental Role and Impacts of the Salinity on Ocean and Climate

Salinity is a thermodynamic state variable that, along with temperature and pressure governs the physical characteristics of the water, like its density and heat capacity. It is also an important factor for determining many aspects of the chemistry of natural waters, or of the biological processes within it. The global sea surface salinity distribution plays a crucial role in the Earth's climate system. In the following section, I further delve into some of these impacts which influence the climate system.

#### Impact on Water Masses

This concept of "water masses" borrows from the concept of "air masses" in meteorology and refers to distinct water bodies with different characteristics in terms of temperature and salinity. These characteristics are acquired at the ocean surface in a formation region (Dinnat, 2003; Emery, 2001). This concept is particularly valuable for studying deep ocean circulation since the properties of water masses change slowly along their Lagrangian paths below the highly turbulent surface mixing zone.

Water masses can originate from various source regions and possess different properties, such as temperature, salinity, nutrients, and sediments, which can influence the watercolor (S Chen & Hu, 2017). When two water masses with highly contrasting properties (e.g., temperature and salinity) meet, they can form a boundary layer without directly mixing together, as shown in Figure 1.3 where each water mass possess a different color. Similarly, the influence of riverine inputs can be observed as low salinity patterns around river mouths, in a similar way as shown in Figure 1.4, where the riverine inputs can be seen with the bare eye thanks to the different watercolor.

As salinity is one of the characteristics of the water mass, it is also possible to use it to track the water masses (e.g., frontal features and eddies), their origins, and analyze their transformations when exchanging with the surrounding water masses (Chaitanya et al., 2014b; Shen et al., 2005; Supply et al., 2022, to mention some).



Figure 1.3 – Boundary zone where two ocean water masses are colliding (Oregon Marine Reserves)

### **Impact on the Density-Driven Global Ocean Circulation and Deep Convection**

The circulation between the oceans is an important component of the Earth’s climate system. By transporting heat, carbon, nutrients, and freshwater around the world, the circulation has strong impacts on climate, weather, and marine ecosystems. There are essentially two main components: the fast and energetic wind-driven circulation, and the slow (migrates in decades or centuries) and large density-driven circulation which dominates the deep sea. The latter is thus affected by salinity, temperature and the depth of the water (Dinnat, 2003; Wunsch, 2002).

One of these deep-ocean circulation is the thermohaline circulation: circulation caused by the joint effect of thermohaline forcing and turbulent mixing. Positive net heat flux causes the surface of the ocean to change the density, becoming lighter and more buoyant, creating a stable layer. The cooling of water and the accumulation of salt in salt formation regions lead to an increase in water density, which in turn decreases its stability. Aiming to establish equilibrium with other water masses it sinks into the ocean’s interior, generating circulation (e.g., deep-water currents like the North Atlantic Deep Water (NADW),



Figure 1.4 – The Mackenzie River in Canada seen from space. (NASA)

or the Antarctic Bottom Water (AABW)) beneath the wind-driven ones (Dijkstra, 2008; Rahmstorf, 2003, 2006). As water sinks, it transports heat and nutrients to the deep ocean, impacting global climate and oceanic ecosystems (Emery, 2001). The sinking of dense water also drives the global thermohaline circulation, which connects different ocean basins and regulates heat transport on a global scale (see Figure 1.5, AL Gordon, 1986; Rahmstorf, 2006). This downward movement is closely associated with convection and induces mostly diffusion, advection, and double diffusion (Beer, 2017).

The SSS is therefore a key factor because freshwater creates a shallow thermohaline structure. The presence of buoyant freshwater near the ocean's surface will increase the stability of the surface layer, rendering it less prone to mixing downwards and isolates the deeper ocean from communicating with the atmosphere (Weller et al., 2016). This makes the formation of deep waters impossible e.g., in the North-Pacific where sea ice

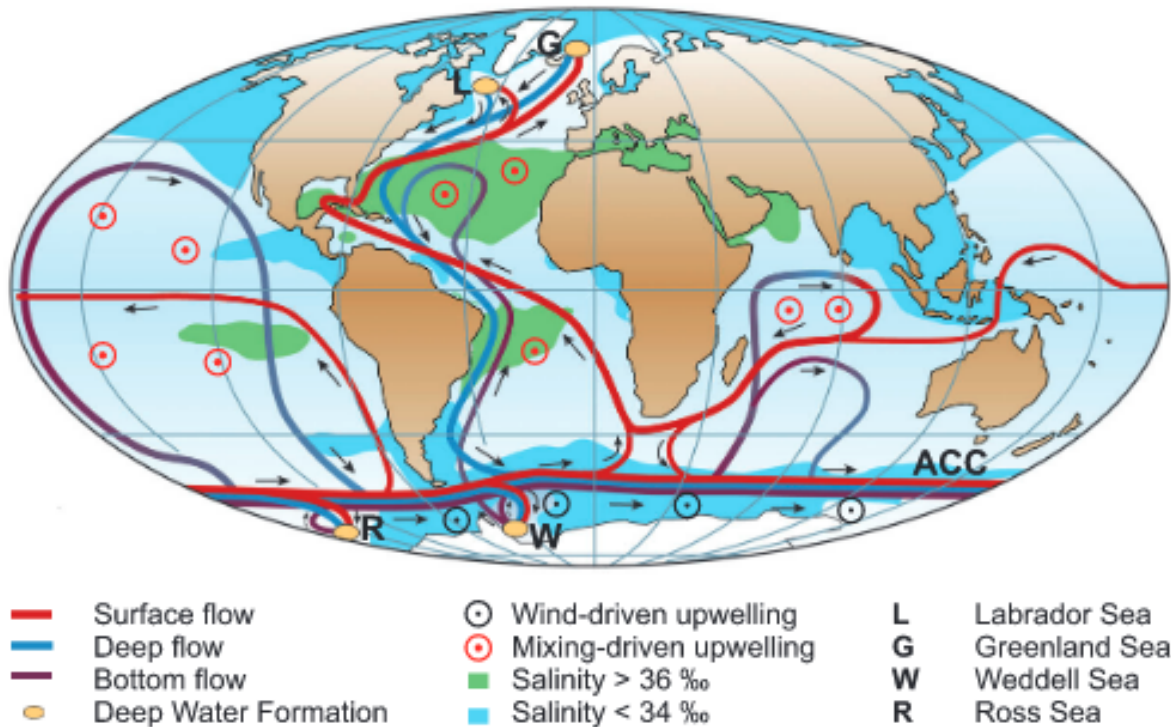


Figure 1.5 – Schematic representation of the global thermohaline circulation. Surface currents are shown in red, deep waters in light blue and bottom waters in dark blue. The main deep-water formation sites are shown in orange. (After Rahmstorf, 2006)

melting injects huge quantities of freshwater (Dijkstra, 2008). Thus, the deep-water formation only takes place in a few localized areas (see Figure 1.5 yellow points): in the Greenland-Norwegian Sea, the Labrador Sea, the Mediterranean Sea, the Weddell Sea, and in the Ross Sea (Lascaratos et al., 1999; Rahmstorf, 2006; Weaver et al., 1999).

### Impact on the Stratification of the Ocean Surface Layer

As mentioned in the section above, in the deep Ocean heat and freshwater are sequestered and released on longer time and global scales, creating a quiescent and deep layer. Opposed to it is the surface layer, which undergoes constantly forcing from winds, heat, and freshwater. The classic surface layer is divided in (see Figure 1.6): (i) an upper mixed layer, vertically homogeneous in temperature and salinity, which is directly affected by the atmosphere, (ii) an eventual barrier layer, confined between the top of the halocline and of the thermocline, (iii) the pycnocline, a highly density stratified zone below where

vertical property gradients are maximum (e.g., de Boyer Montégut et al., 2007).

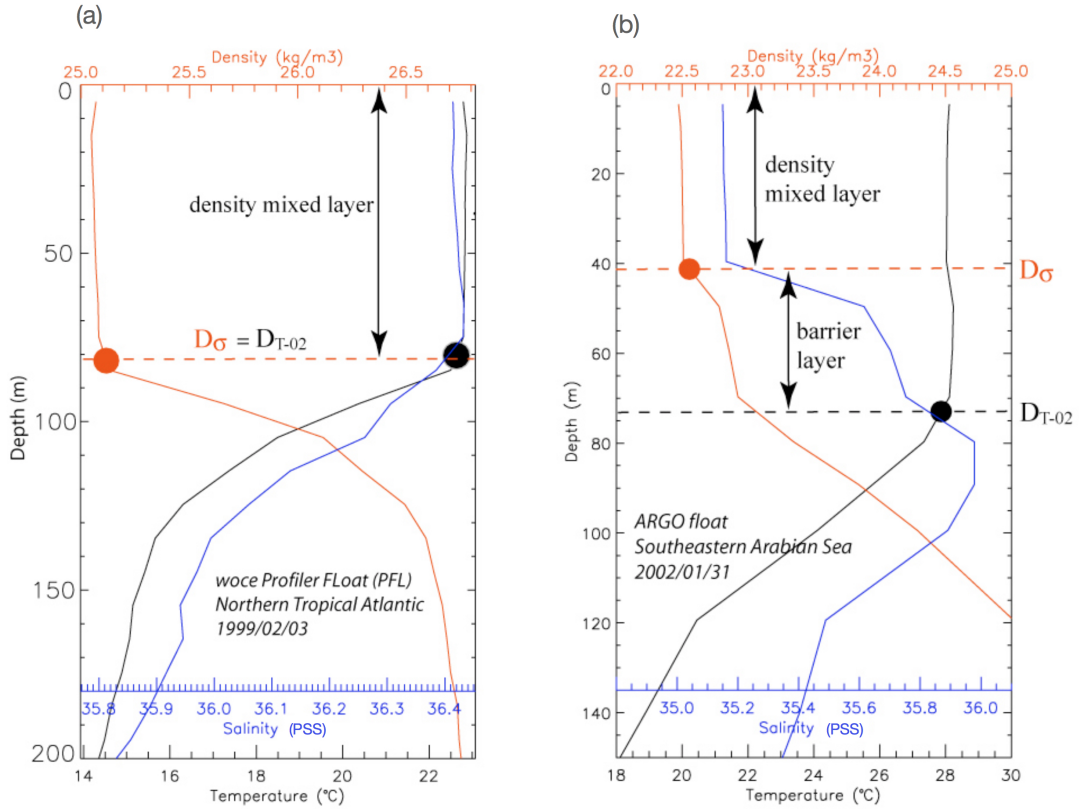


Figure 1.6 – Examples of vertical profiles of temperature (black), salinity (blue), and density (red, actually =  $\sigma_T$  = seawater density - 1000 kg/m<sup>3</sup>) in the first 100 to 200 m depth of the ocean. (a) the case of the rather usual configuration for profiles in the surface layer, with the warm mixed layer in contact with the cold deeper ocean (halocline and thermocline at the same depth). (b) the so-called "Barrier Layer" (BL) case, where the mixed layer is "isolated" from the colder deep ocean by an intermediate layer (BL) with the same (or possibly slightly higher) temperature (fresher waters on top with the first shallowest halocline being above the thermocline). (Adapted from de Boyer Montégut et al. (2007))

Shown in Figure 1.6a, the mixing generally occurs within the first tens of meters. By creating a layer within which salinity, temperature, and density are almost uniform, this layer directly interacts with the atmosphere and has fast variations (de Boyer Montégut et al., 2004; Kantha & Clayson, 2003; Sprintall & Cronin, 2001).

The pycnocline is in some sort an envelope of maximum depths reached by the active vertical mixing. During a daily cycle, the mixed layer usually alternates between a well-mixed state during night-time convection, and a weakly stratified state during the day

(Brainerd & Gregg, 1995). Apart from this recurrent daily cycle, the mixed layer also displays lower-frequency variability, such as at intraseasonal, seasonal and interannual timescales (de Boyer Montégut et al., 2004).

Buoyant low salinity (or even fresh) water near the surface can increase the stability of the surface layer by increasing the resistance to the vertical mixing leading to a reduction of the surface layer depth (Weller et al., 2016). The depth of the mixed layer in its turn controls the input of nutrients from different depths into the upper layers. When the depth of the mixed layer is too shallow, fewer nutrients will be admitted in the surface layer, inducing a decline in the biological productivity (e.g., chlorophyll; Prasanna Kumar et al., 2002).

Studies have investigated how changes in oceanic stratification, specifically modifications to thermocline depth, can influence the expansion of Tropical Cyclones (TCs), which derive energy from the heat of the oceans. As TCs move, they generate strong winds that cause evaporation and vertical mixing. If the thermocline is shallow, the TC rapidly deepens it and introduces colder water at the ocean surface, which reduces the energy supply to the TC and creates negative feedback on its intensity. However, if the thermocline is deep, the TC may not expand its depth, and cooling may not be induced, allowing the TC to continue to intensify (Reul et al., 2020; Sengupta et al., 2008; Vincent et al., 2014).

When there is a substantial inflow of freshwater (through precipitation, river runoff, or advection like the southward subduction of high-salinity water from the subtropical North Atlantic) into the ocean's surface layer, a shallow salinity stratification can arise within a deeper isothermal layer. As a result, the top of the halocline becomes shallower than that of the thermocline, resulting in the creation of a barrier layer (see Figure 1.6b). Although quasi-permanent in most of the equatorial and deep tropical basins (within roughly  $10^\circ$  of the equator), such features are typically seasonal in the northern subpolar regions, the Labrador Sea, and parts of the Arctic and Southern Ocean (Mignot et al., 2007). This layer has important consequences on the air-sea interactions and important potential climatic impact. When they occur, the energy transferred from the atmosphere via wind and buoyancy forcing will be trapped in the upper mixed layer. Moreover, a thick barrier layer has an isolating characteristic obstructing the heat exchanges between the surface layer and the thermocline and thus obstructing the surface cooling (de Boyer Montégut

et al., 2007; Foltz & McPhaden, 2009; Mignot et al., 2007).

Various studies (Balaguru et al., 2012; Balaguru et al., 2020; Sengupta et al., 2008) stipulates that the presence of a thick ( $> 10$  m) barrier layer can strongly influence TC. Not only does the increased stability and stratification of the ocean reduce TC-induced vertical mixing (thus hinder the decrease of the cyclone) but in case of a temperature inversion it may even increase its intensity. When a temperature inversion (the temperature of the surface layer is less than in the barrier layer, e.g., on Figure 1.6b) occurs in the same time as a cyclone, the resulting mixing can actually increase the surface temperature, thus increasing the energy the cyclone has at disposal.

### **Influence on the Hydrological Cycle and Climate Change**

The oceans are known for their role in the stocking and the transfer of thermal energy (with a heat capacity 1,100 times greater than the atmosphere) which the sun adds to the atmosphere-ocean system. Being in a constant interaction, the atmosphere and the ocean constantly exchange momentum, heat, water, and radiation (Dinnat, 2003; Reul et al., 2014; Weller et al., 2016).

The total amount of available water on Earth is about some  $1.4 \times 10^9$  km<sup>3</sup>, distributed as shown in Figure 1.7a in oceans, land ice and glaciers, groundwater, and in the atmosphere in the form of water vapor. The continuous exchange of water between those various reservoirs is called the hydrological cycle and is shown in Figure 1.7b (Bengtsson, 2010; Chahine, 1992; Dorigo et al., 2021).

The hydrological cycle has a significant impact on the climate, as it involves the exchange of moisture and heat between the Earth's surface and the atmosphere. This exchange plays a fundamental role in the dynamics and thermodynamics of the climate system. During phase transitions water has opposing effects on the environment by either heating or cooling, e.g., the evaporation is approximately responsible for 50% of the surface cooling. Moreover, water vapor in the atmosphere is a potent greenhouse gas that amplifies the effects of greenhouse warming caused by carbon dioxide, methane, and other similar gases, almost doubling their impact (Myhre et al., 2013). Last but not least, clouds play a crucial role in controlling the climate by affecting the Earth's radiation budget. The release of latent heat during cloud condensation contributes to approximately 30% of the thermal energy that drives the atmospheric circulation of the Earth (Chahine, 1992).

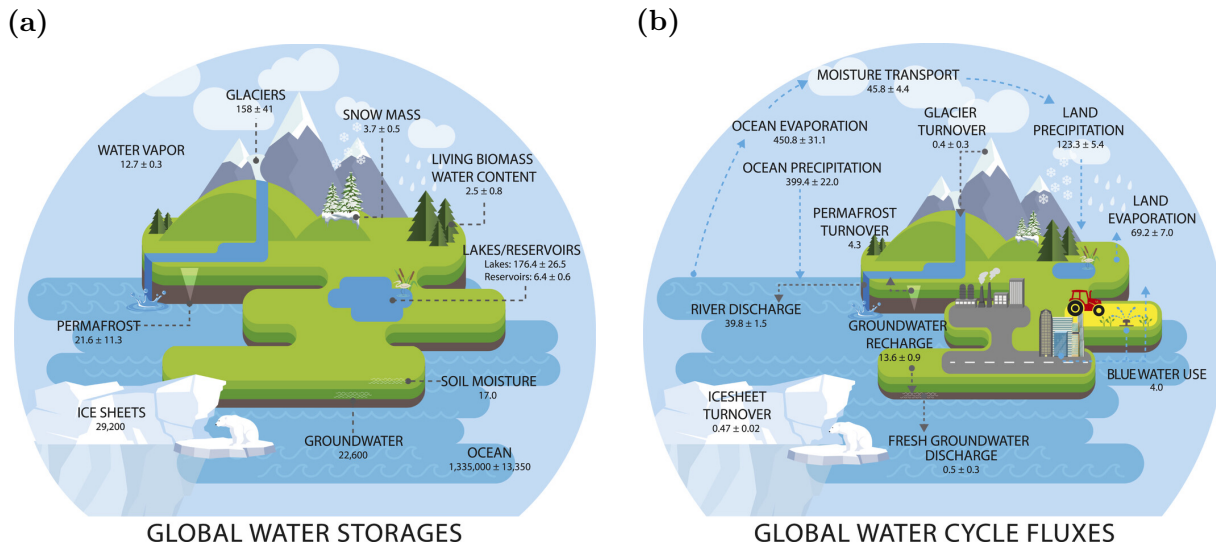


Figure 1.7 – a) Observed estimates of global water cycle storage (in  $10^3 \text{ km}^3$ ) and their uncertainties. b) Observed estimates of annual global water cycle fluxes (in  $10^3 \text{ km}^3$ ) and their trends. Both figures after Dorigo et al. (2021)

There are five main components which drives the hydrological cycle: clouds and radiation, atmospheric moisture, precipitation, ocean fluxes and land surface processes. Even if salinity does not have a direct impact on the hydrological cycle, it influences strongly the ocean fluxes. The cycling of freshwater between evaporation  $E$  and precipitation  $P$  ( $E - P$  can be seen in Figure 1.2a) acts in concert with the runoff  $R$  impacting ocean circulation and mixing, which are closely linked to the salinity distribution (see Figure 1.2b). Salinity can thus be seen as a proxy of the cycle (Chahine, 1992; Dorigo et al., 2021; Reul et al., 2014; Schmitt, 2008; Yu et al., 2020).

As the climate warms, the atmosphere's water holding capacity increases due to the Clausius-Clapeyron relationship, resulting in an ocean-atmosphere imbalance that leads to a roughly 7% increase in atmospheric water vapor per Kelvin of warming. Even in the absence of circulation changes, the lower-tropospheric moisture convergence leads to changes in precipitation minus evaporation ( $P-E$ ) patterns, a phenomenon commonly referred to as the "dry-gets-drier and wet-gets-wetter" concept (Held & Soden, 2006). Observations spanning several decades indicate that mean salinity patterns have intensified, causing the subtropical ocean to become more saline and the tropical and high-latitude regions to become fresher (Durack & Wijffels, 2010; Durack et al., 2012), in line with the "dry-gets-drier and wet-gets-wetter" concept. This underscores the oceans' critical role in

understanding long-term changes in the water cycle and the impacts of climate change (Dorigo et al., 2021; Yu et al., 2020).

However, ocean warming increases near-surface stratification, which can prolong existing salinity differences and further amplify surface salinity patterns. Changes in atmospheric circulation patterns can also alter the locations of wet and dry areas, potentially reducing the signal of water cycle changes passed on to the ocean. Therefore, salinity should be used with caution as a climate change indicator, as other processes may also contribute to changes in ocean salinity (Allan et al., 2020).

## 1.2 ... to Space-Born Microwave Remote Sensing

Remote sensing is a powerful tool for monitoring and understanding the physical properties of the ocean. In recent years, passive microwave radiometry has emerged as a promising technique for measuring Sea Surface Salinity (SSS) from space. In particular, L-band radiometry promises high accuracy and spatial resolutions. This technique takes advantage of the natural emission of microwave radiation by seawater, which is directly related to its salinity.

In this section, I first provide an overview of passive microwave remote sensing for SSS retrieval, describing the principles of the Radiative Transfer Model (RTM). Then, I review the history and development of L-band radiometers, discussing the strengths and limitations of the different missions. I provide a review of the different remote sensing researches on SSS carried out in the BoB using L-band radiometers. Finally, I close this section by presenting two studies where SSS was retrieved from combined C- and X-band radiometers.

### 1.2.1 Physical Principles of Salinity Remote Sensing

The realization of the importance to measure globally and follow SSS is dated, but measuring techniques have been only found recently. In situ measurements, i.e., direct measurements at given locations, have been collected via different ways (Reul et al., 2020, Figure 11):

- Argo float profilers which can normally measure SSS between 1 m and 10 m depth,
- Thermo-SalinoGraph (TSG) sensors installed onboard ships of opportunity (Alory et al., 2015), research vessels (Gaillard et al., 2015), or sailing ships (Reynaud et al.,

2022),

- upper-level data from salinity equipped moorings (McPhaden et al., 2010),
- surface drifters measuring the upper 50 cm (Morisset et al., 2012), and
- marine mammals (Treasure et al., 2017) equipped with Conductivity-Temperature-Depth (CTD) sensors (principally in polar regions).

However, the temporal distribution of in situ measurements in the BoB is sparse (see Figure 1.8a). As can be seen in Figure 1.8b in the early 2000s in situ measurements are not covering the BoB and are not located near the estuaries. In 2008, the number of in situ deployments per month starts reaching an asymptotic behavior in the BoB (around  $\sim 400$  Argo profiles per month). However, even at its maximum the SSS coverage of the BoB remains patchy. By using in situ measurements, it is thus possible to identify variations associated with the seasonal cycle (Sengupta et al., 2016). However, it is not possible to detect interannual variations or the impact of river runoffs on SSS (Akhil et al., 2020) and short temporal scale ( $< 1$  month) variability.

Using remote sensing techniques, it is possible to retrieve a synoptic monthly SSS map over the complete BoB (see for example Figure 1.25). This allows a detailed investigation of the spatial distribution of SSS over this region. The usual revisit time of polar-satellite sensors is around three days (see Section 1.2.2.1), permitting an in-depth study of the interannual SSS variability. With a spatial resolution around 50 km (see Section 1.2.2.1) satellite sensors allows even a follow-up of the impacts of mesoscale eddies (radius larger than 50 km and lifespan longer than 30 days, Dandapat and Chakraborty (2016)).

Receiving radiation from the Sun and sky, the ocean will in turn emit electromagnetic waves which are typical for its energy, with power frequently described as oceans brightness temperature ( $T_B$ ). It is defined as the temperature of a theoretical black body that would emit the same amount of thermal radiation as the observed surface at a given frequency ( $f$ ). It depends on the emissivity ( $e$ ) and the absolute temperature of the sea surface ( $T$ ) (Lagerloef et al., 2008):

$$T_B = e(f) * SST[K] \tag{1.1}$$

Salinity remote sensing is only possible because the emissivity at a given frequency depends on the dielectric constant, which itself depends on temperature and salinity of sea water (Klein & Swift, 1977; Meissner & Wentz, 2012).

For a perfectly flat (or specular) ocean surface, the emissivity depends on salinity and

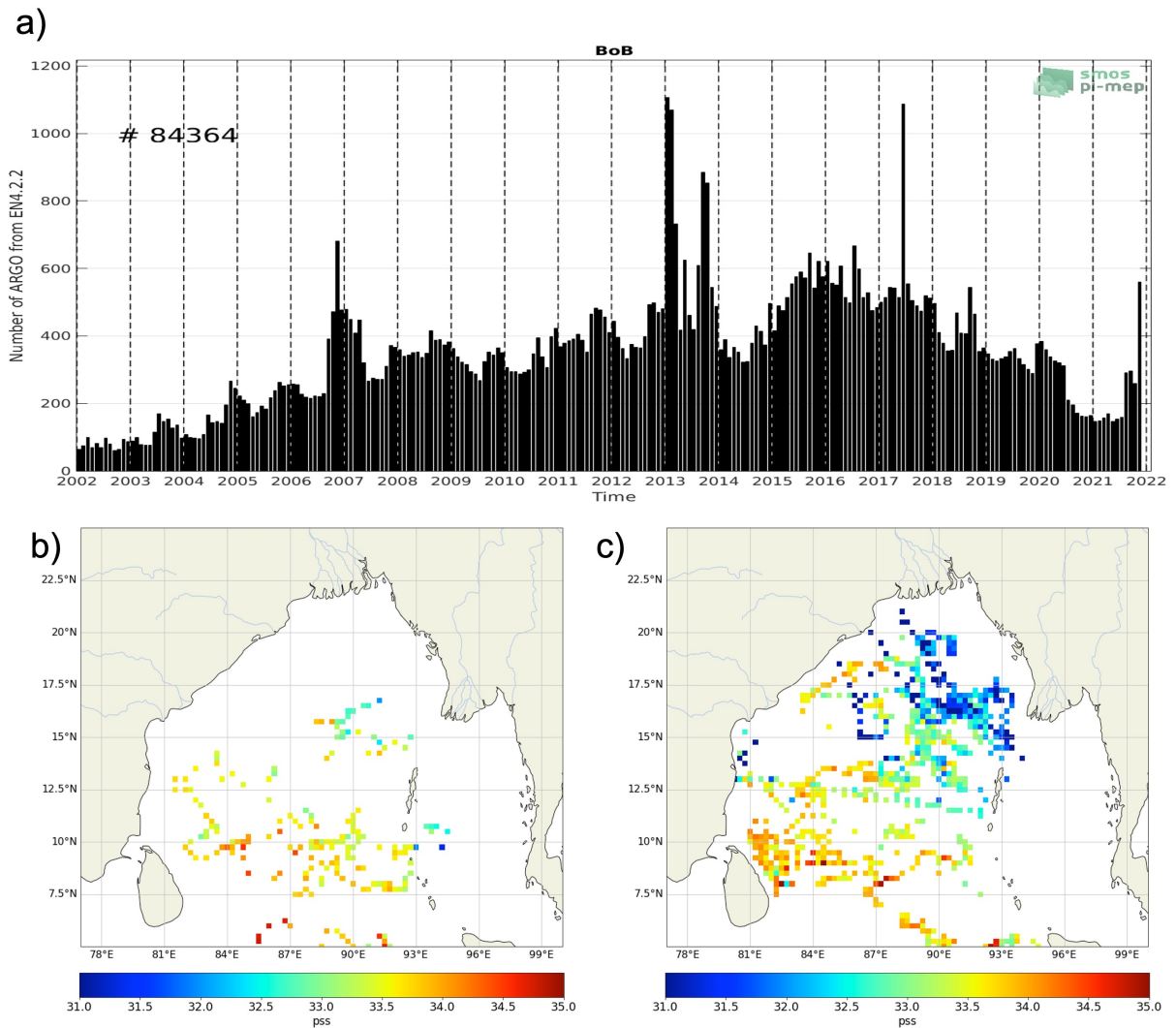


Figure 1.8 – a) monthly number of ARGO in situ measurements between 2002 and 2022 in the BoB, extracted from the SMOS-Pimep site; Snapshot of mean SSS In situ measurements in the BoB, extracted from the World Ocean Data (WOD), for b) the year 2003 and c) the year 2008.

temperature, as well as the look direction (incidence angle) and polarization. But this is hardly the case, the sea surface often becoming rough under constant drills received locally by winds or from distance by swell waves and thus modify the surface emissivity and absorption. Moreover, strong winds can tear off droplets from the ocean surface and create foam that increases the emissivity. Once emitted by the ocean surface, the electromagnetic radiation has to cross the atmosphere in which different components such

as oxygen or water in different states are present and modify the radiation. Finally, the antenna and the sky will also emit a radiometric radiation, that alter the received signal (Dinnat, 2003; Supply, 2020).

At a state of thermodynamic equilibrium, the emissivity is equivalent to the absorptivity ( $a$ ), which reflects the proportion of power received by the sea surface that is absorbed, giving:

$$\begin{aligned} e &= a \\ &= (1 - R) \end{aligned} \tag{1.2}$$

where  $R$  is the reflectivity of the sea surface.

A challenge when estimating SSS from radiometer data is to estimate oceans brightness temperature ( $T_B$ ) from the brightness temperature measured at antenna level ( $T_A$ ). After obtaining an estimate of the  $T_B$ , the next step involves converting it into SSS. To achieve this in calm sea conditions, a simple model is employed, which assumes that the sea surface is flat and has an infinite extent as compared to the instrument's wavelength  $\lambda_0$ . Under this assumption, the reflection at the surface is specular, and the reflection coefficient is referred to as the Fresnel reflection coefficient ( $R_{Fr}$ ). The  $R_{Fr}$  is dependent on the angle of incidence  $\theta$  (with no azimuthal dependence as the sea surface is isotropic in this simplified model) and the permittivity  $\varepsilon_r$  of seawater. Thus, we have:

$$T_{B_{sea}}(\theta, SST, SSS) \simeq T_{B_{spec}} = SST \cdot (1 - R_{Fr}(\theta, \varepsilon_r(SST, SSS))) \tag{1.3}$$

where  $T_{B_{spec}}$  is the brightness temperature of a specular sea surface. The Fresnel coefficients provide the reflection coefficients for vertical ( $R_v$ ) and horizontal ( $R_h$ ) polarization (Peake, 1959):

$$\begin{aligned} R_v &= R_{Fr,v} \\ &= \left| \frac{\varepsilon_r \cos \theta - \sqrt{\varepsilon_r - \sin^2 \theta}}{\varepsilon_r \cos \theta + \sqrt{\varepsilon_r - \sin^2 \theta}} \right|^2 \end{aligned} \tag{1.4}$$

and

$$\begin{aligned}
 R_h &= R_{Fr,h} \\
 &= \left| \frac{\cos \theta - \sqrt{\varepsilon_r - \sin^2 \theta}}{\cos \theta + \sqrt{\varepsilon_r - \sin^2 \theta}} \right|^2
 \end{aligned} \tag{1.5}$$

The seawater's relative permittivity, also known as the dielectric constant ( $\varepsilon_r$ ), is a complex function that depends on temperature and salinity. Dielectric constant can be estimated by Debye (1929)'s function of the electromagnetic frequency  $f = \frac{2\pi}{\omega}$ , which has been determined empirically through laboratory experiments:

$$\varepsilon = \varepsilon_\infty + \frac{(\varepsilon_s - \varepsilon_{\text{inf}})}{1 - i\omega\tau} - i \frac{\sigma}{\omega\varepsilon_0} \tag{1.6}$$

in which  $i$  is the imaginary unit,  $\varepsilon_\infty$  is the electrical permittivity at very high frequencies.  $\varepsilon_s$ ,  $\tau$ , and  $\sigma$  are functions of temperature and salinity and represent respectively the static dielectric constant, the relaxation time and the ionic conductivity. Finally,  $\varepsilon_0$  is the permittivity of free space.

The transmission of electromagnetic waves in seawater will vary as a function of its frequency (Somaraju & Trumpf, 2006).

Historically, the functions related to salinity had been evaluated by Ellison et al. (1998), Klein and Swift (1977), A Stogryn (1971), and AP Stogryn et al. (1995) before the development of the first salinity mission.

Following prelaunch comparisons and analyses of the Soil Moisture and Ocean Salinity (SMOS) mission (Blanch & Aguiasca, 2004; Camps et al., 2004; Wilson et al., 2004), the Klein and Swift (KS) model was selected in the Level 2 Ocean Salinity (OS) processor for the SMOS mission in the first phases of post-launch (Argans, 2016). An alternative model function, denoted MW and developed by Meissner and Wentz (2004), fits the seawater dielectric data to a double Debye relaxation polynomial that performs best at higher frequencies. The MW model is used in the Aquarius and SMAP SSS retrieval algorithms (Meissner et al., 2018).

The MW model function was recently updated by providing small adjustments to the Debye parameters based on including results for the C-band and X-band channels of WindSat and AMSR (Meissner & Wentz, 2012; Meissner et al., 2014).

Direct laboratory measurements of the  $\varepsilon_r$  at 1.413 GHz and SSS=30, 33, 35, and 38 (Lang et al., 2016) were used to develop a new model (Zhou et al., 2017) by fitting the

measurements with a third-order polynomial. This new L-band model has been compared with KS and MW. The authors claimed that this new model function gives more accurate SSS at high (25°C to 30°C) and low (0.5°C to 7°C) Sea Surface Temperature (SST) than other existing model functions. However, the model showed inconsistent behavior between partitioned salinities.

To overcome these problems, two new parameterizations were recently developed. One is based on SMOS satellite multi-angular brightness temperature measurements by Boutin et al. (2021b), hereafter BV, and the other is based on new George Washington laboratory measurements by Zhou et al. (2021) (hereafter denoted GW2020). These two approaches are fully independent. The brightness temperatures  $T_B$  simulated through the BV and GW2020 parameterizations agree particularly well for most SSS and SST conditions commonly observed over the open ocean, and better than with earlier parameterizations previously used in the SMOS, SMAP and Aquarius SSS retrievals. Nevertheless, uncertainty remains below 10°C where a  $\sim 0.1$  K relative difference between the two models is observed.

### 1.2.2 SSS Retrieval From Radiometers Operated From L-Band

The  $T_B$  of the ocean surface depends on the measured electromagnetic frequency. The  $T_B$ 's at different frequencies have differing sensitivities to geophysical parameters such as SST, SSS, and wind speed, as well as other contributions such as atmospheric and galactic emissions. The sensitivity of  $T_B$  to these parameters thus varies with frequency (Figure 1.9). For  $f > 1$  GHz, the sensitivity of  $T_B$  to SSS is highest at a frequency of  $\sim 1$  GHz (L-band, see Table 1.1).

The frequency of 1.4 GHz is commonly used for SSS remote sensing as it provides a good balance between sensitivity to sea surface salinity and because it is a protected frequency for Radio-Astronomy. The brightness temperature measured by satellite sensors is significantly influenced by others geophysical factors such as SST, roughness, atmospheric and galactic emissions (see Figure 1.10). With respect to SSS impacts, these factors need to be corrected. Therefore, it is important to incorporate these contributions into the correction process to ensure the accurate retrieval of SSS from L-band radiometer measurements (Reul et al., 2020). The fact that the frequency is protected for Radio-Astronomy reduces human-caused Radio Frequency Interferences (RFI).

As mentioned by Reul et al. (2020), the sensitivity to SSS of the oceans brightness temperature from the sea surface at 1.4 GHz and in vertical (VV) polarization (see Fig-

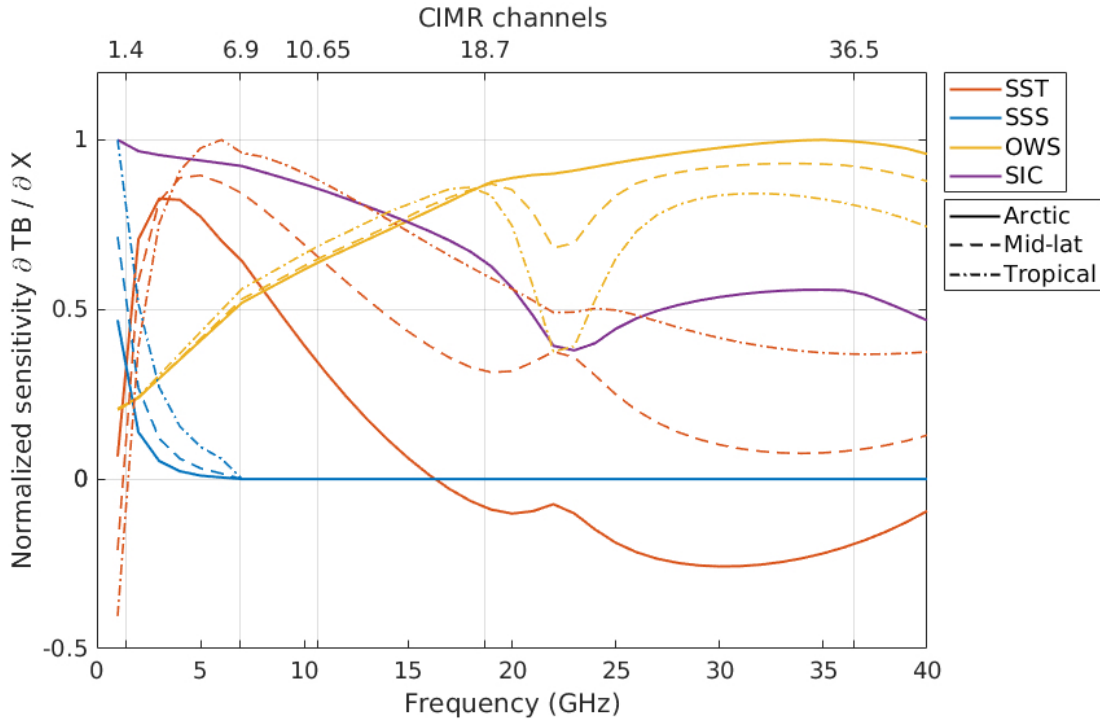


Figure 1.9 – Illustration of the sensitivities of the low passive microwave brightness temperature at the top-of-the-atmosphere, in terms of Sea Surface Temperature (SST), Sea Surface Salinity (SSS), Ocean Wind Speed (OWS) and Sea Ice Concentration (SIC) as a function of frequency from 1 GHz to 40 GHz. The Copernicus Imaging Microwave Radiometer (CIMR) channels are indicated at the top of the figure. Three different geophysical conditions are considered: arctic, midlatitude and tropical. For each parameter the sensitivity is normalized by the maximum of sensitivity between the three considered environments, for the full-frequency range from 1 to 40 GHz (after Kilic et al., 2020).

ure 1.11), varies only between  $\partial T_B / \partial SSS \sim -0.5$  to  $-1$  K/pss for incidence angles from  $0^\circ$  to  $60^\circ$  at characteristic ocean conditions ( $SSS = 35$  pss and  $SST = 15^\circ\text{C}$ ). Compared to the noise characteristics of currently operating radiometers ( $\sim 0.3$  to  $2$  K) and the restricted range of the natural SSS variability in the open ocean (32 to 38 pss), this  $T_B$  sensitivity is relatively small. Additionally, as illustrated in Figure 1.11, the  $\partial T_B / \partial SSS$  is strongly varying with the SST and decreases with a decreasing SST (from  $\sim -0.7$  K/pss at  $30^\circ\text{C}$  to  $\sim -0.2$  K/pss at  $0^\circ\text{C}$ ). This strongly complicates the estimation of SSS at the high latitudes.

As mentioned in the previous section, the dielectric model function varies depending

Band designator	Frequency $f$ (GHz)	Wavelength in free space $\lambda$ (cm)
L	1-2	30-15
S	2-4	15-7.5
C	4-8	7.5-3.8
X	8-12	3.8-2.5
Ku	12-18	2.5-1.7
K	18-27	1.7-1.1
Ka	27-40	1.1-0.75
V	40-75	0.75-0.40
W	72-110	0.40-0.27

Table 1.1 – Standard microwave frequencies and nomenclature

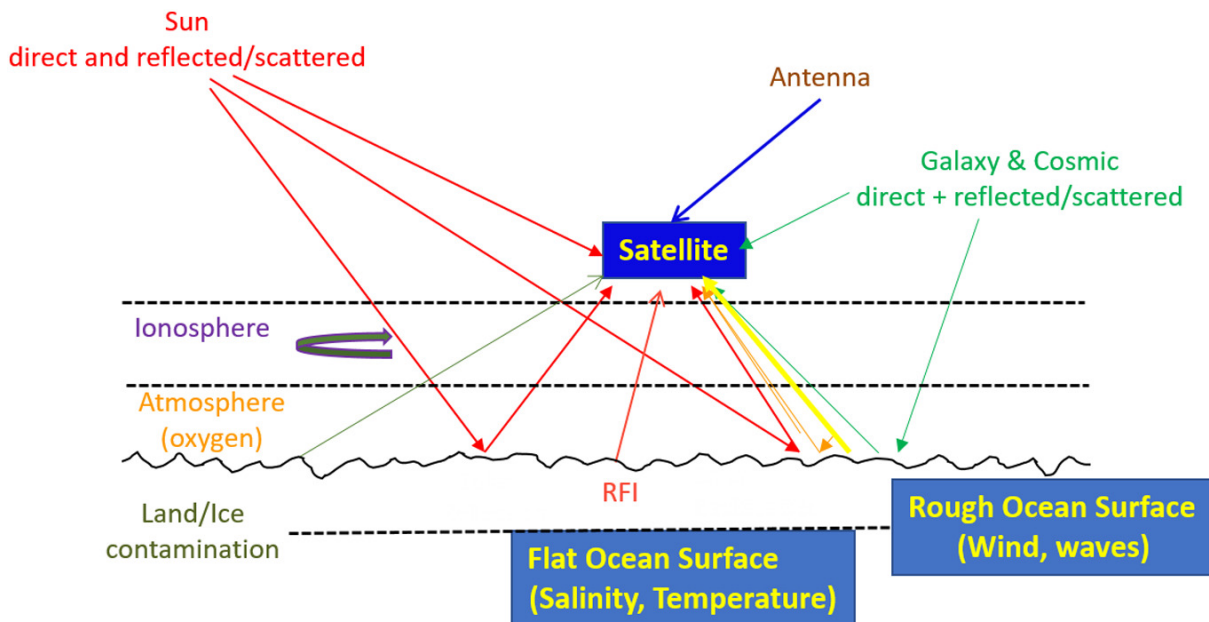


Figure 1.10 – schematic representation of the various signals received by an L-band radiometer (after Reul et al., 2020)

on the frequency used to measure the oceans brightness temperature. Especially the accurate retrieval of SSS from L-band oceans brightness temperature is highly reliant on having a good understanding of  $\epsilon_r$  variations with respect to temperature and salinity (Lang et al., 2016).

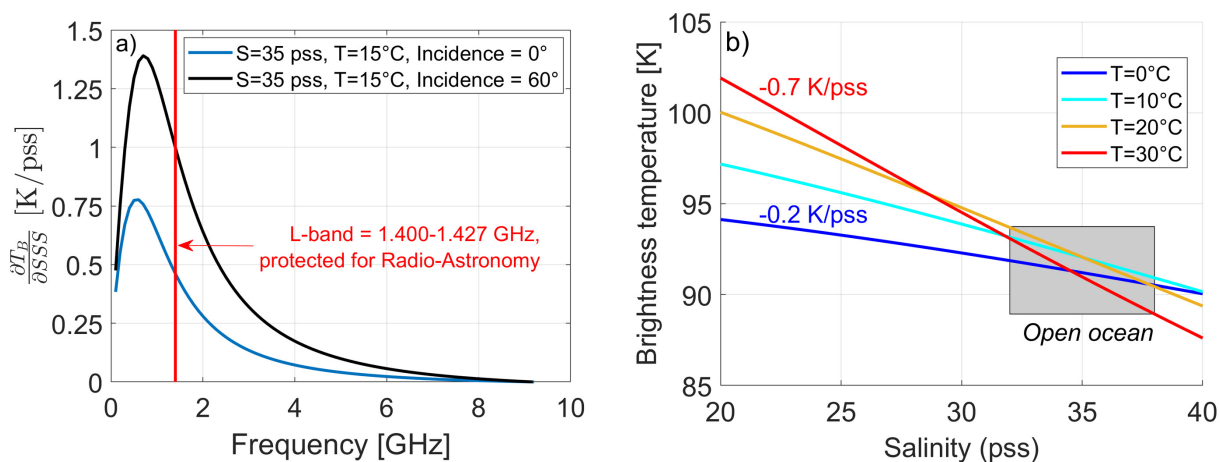


Figure 1.11 – (a) sensitivity of the ocean surface microwave brightness temperature to salinity (First Stokes parameter) in VV-polarization as a function of electromagnetic frequency and incidence angle (blue curve =  $0^\circ$ , black curve =  $60^\circ$ ) and for a water body with salinity of 35 pss and temperature of  $15^\circ\text{C}$ . (b) Brightness temperature changes at 1.4 GHz and nadir as a function of salinity (x-axis) and temperature (colors). The gray domain indicates the range of SSS values mostly encountered in the open ocean. (After Reul et al., 2020)

### 1.2.2.1 History of L-Band radiometers

To be able to measure SSS at 1.4 GHz, the antenna size required by the radiometer sensors must be quite large (according to Dinnat (2003) between 3 and 8 m in diameter) to meet a useful spatial resolution on the ground. As Reul et al. (2020) points out, this antenna technology was just not available before the late 1990s.

In Figure 1.12 is shown the timeline of satellites carrying L-band radiometers (SMOS, Aquarius, and SMAP), which is further detailed in the section below. The timeline of Advanced Microwave Scanning Radiometer for Earth observing system (AMSR-E) which Reul et al. (2009) used for SSS retrieval and which is the subject of this thesis is also shown.

**SMOS** The spaceborne L-band microwave radiometer era started with the SMOS mission, launched at the end of 2009 by the European Space Agency (ESA). It carries a single payload, L-Band 2-D interferometric radiometer (Microwave Imaging Radiometer with Aperture Synthesis (MIRAS)) operating in the 1400-1427-MHz protected band. The SMOS mission follows a helio-synchronous orbit and crosses the equator at 6 A.M./6 P.M.

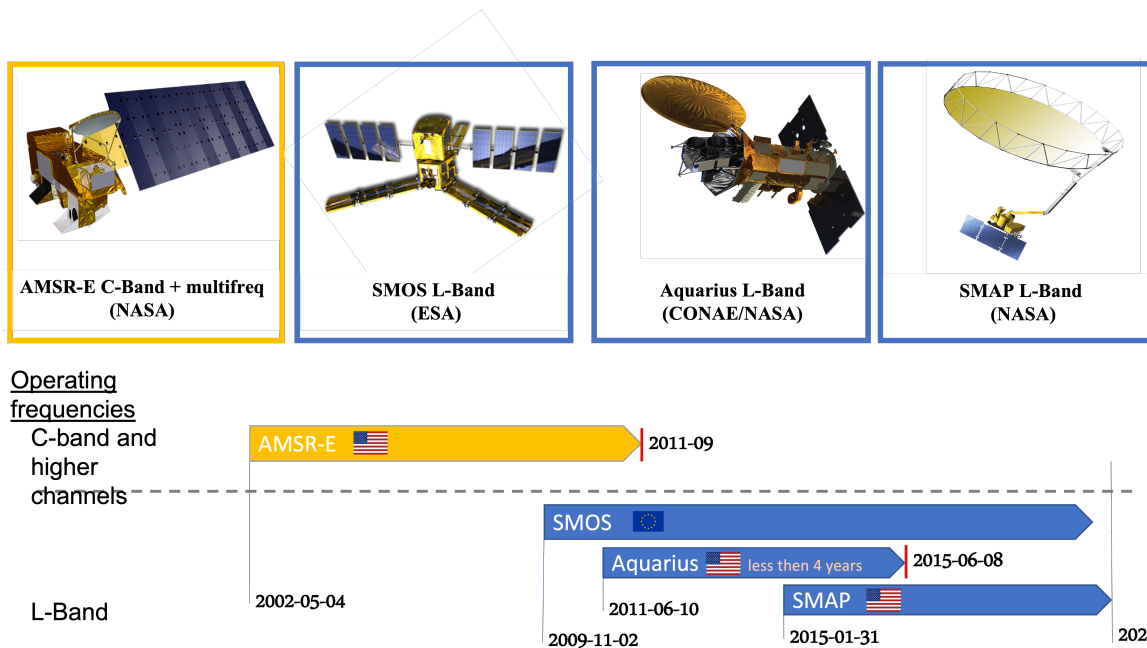


Figure 1.12 – Schematic representation of the timeline of L-band satellites and C-/X-band satellite AMSR-E. The flag represents the county/union owning the satellite.

in ascending/descending direction with a mean altitude of 758 km and an inclination of  $98.44^\circ$ . It is described in detail in Kerr et al. (2010) and Mecklenburg et al. (2012), and Reul et al. (2020). MIRAS determines "visibilities" that are complex cross-correlations of signals collected by pairs of antennas within a 69-receiver array on a deployable Y-shaped structure (see Figure 1.13 left) (Kerr et al., 2010; Supply, 2020). The approximate revisit time is in the order of 18 days and a spatial resolution varying from thirty-five to sixty kilometers, which is further detailed in Lagerloef and Font (2010) and Reul et al. (2020) (Figure 1.13 right).

In 2023, SMOS is still in good shape and operating, although it was supposed to be a five-year only mission and it gives thus access to the longest (13 years) time series of satellite SSS.

**Aquarius** In 2011, the Argentinean Comision Nacional de Actividades Espaciales (CONAE) launched the Satelite de Aplicaciones Cientificas-D (SAC-D) with onboard National Aeronautics and Space Administration's (NASA) instrument Aquarius (see Figure 1.14 left). It is a combined L-band radiometer (1.413 GHz) and scatterometer (1.26 GHz) (Bindlish

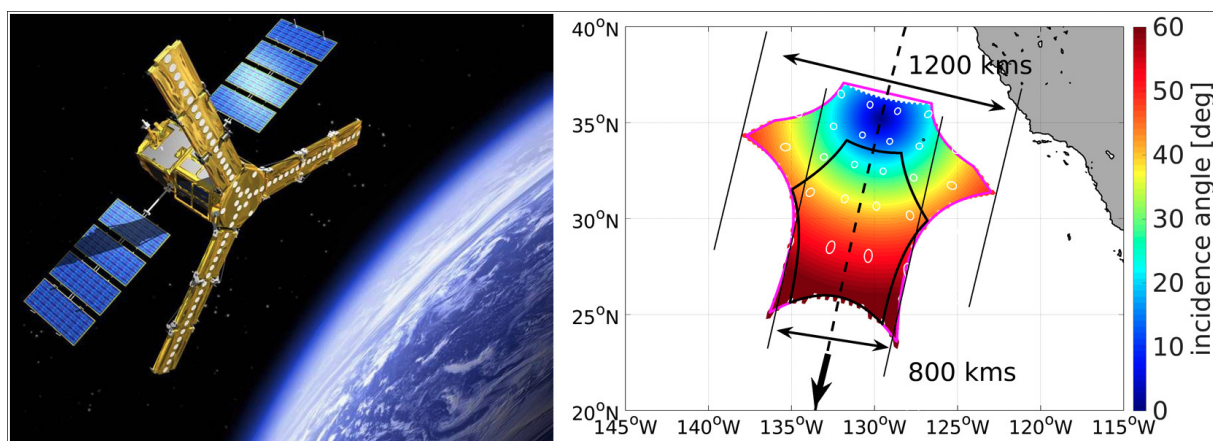


Figure 1.13 – (Left) Artistic view of SMOS sensors (Right) shape of a snapshot brightness temperature image as reconstructed from SMOS observations, the color indicates the varying Earth incidence angle, the thick-dash line and large arrow indicate the sub-satellite track and satellite propagation direction, respectively. The widths of the extended Field Of View (FOV) and alias free FOV are indicated by the pink and black hexagonal shapes, respectively. White ellipses give an indication of the varying footprint sizes from about 35 km at boresight to  $\sim 60$  km at the FOV borders. (After Reul et al., 2020)

et al., 2015). The mission ended in 2015 when an essential part of the power and altitude control system for the spacecraft stopped operating. As can be seen on the right of Figure 1.14, the antenna is an offset parabolic reflector. It possesses a diameter of 2.5 m and is equipped with three feed horns. Combined, the three beams measured by the feed horns form a swath of about 390 km in width. The maximal spatial resolution of Aquarius was only 150 km (see Figure 1.14 right), the SSS accuracy was 0.2 psu, and the revisit was every 7 days (Lagerloef et al., 2008; Le Vine et al., 2010; Reul et al., 2020).

**SMAP** Just before Aquarius ceased to function, the NASA launched Soil Moisture Active-Passive (SMAP) in early 2015, which has on board a combined active-passive microwave instrument. It possesses a unique 6 m long, rotating reflector (see Figure 1.15 top left), shared between a radiometer and a Synthetic Aperture Radar (SAR) which ceased transmissions in July 2015 but is still in a receive-only configuration (Peng et al., 2017; Piepmeier et al., 2017), both in L-band frequency. Due to the rotation of the antenna (see Figure 1.15 top right), measurements in aft- and for-views of the earth stargate are provided during the azimuthal scan of the satellite. This permits a decrease of the impact coming from RFI's but adds complexity to the calibration as the self-emissivity of the

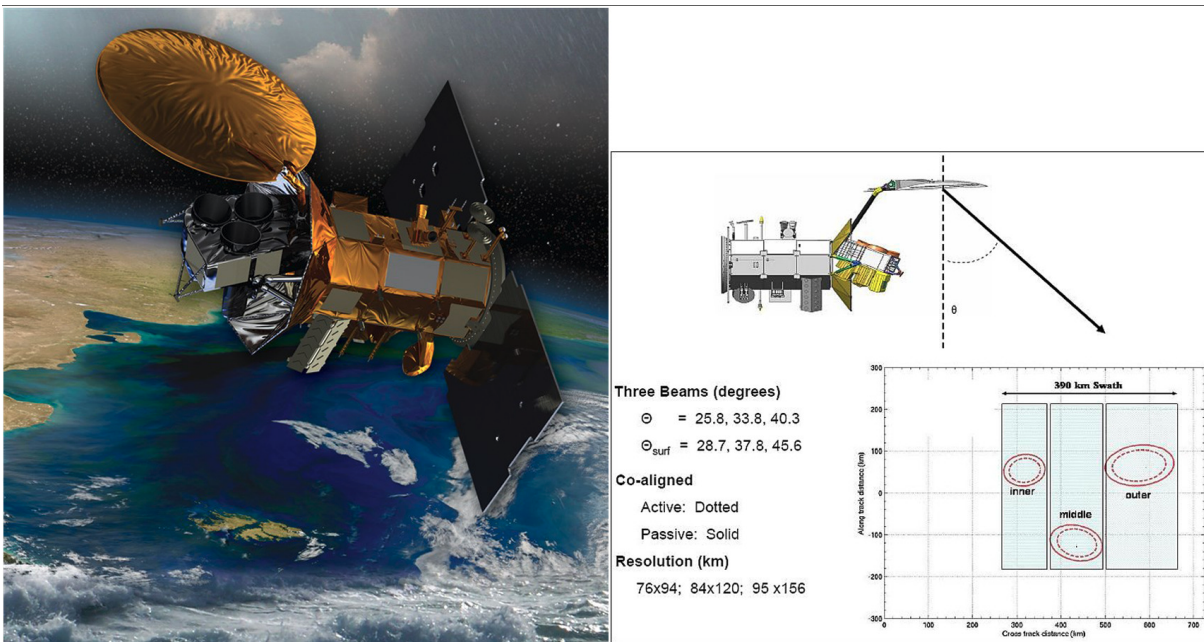


Figure 1.14 – (Left) Artistic view of Aquarius mission, (Right) schematic indicating the 390 km wide swath formed by the three radiometer and scatterometer beams of Aquarius. (After Reul et al., 2020)

antenna has to be corrected (Supply, 2020). SMAP is on a sun-synchronous orbit and crosses the equator at 6 A.M./6 P.M. in descending/ascending direction (which is the inverse to SMOS). A quasi-global spatial coverage is performed in three days, with a maximal spatial resolution of 40 km (see Figure 1.15 bottom, Piepmeier et al., 2017).

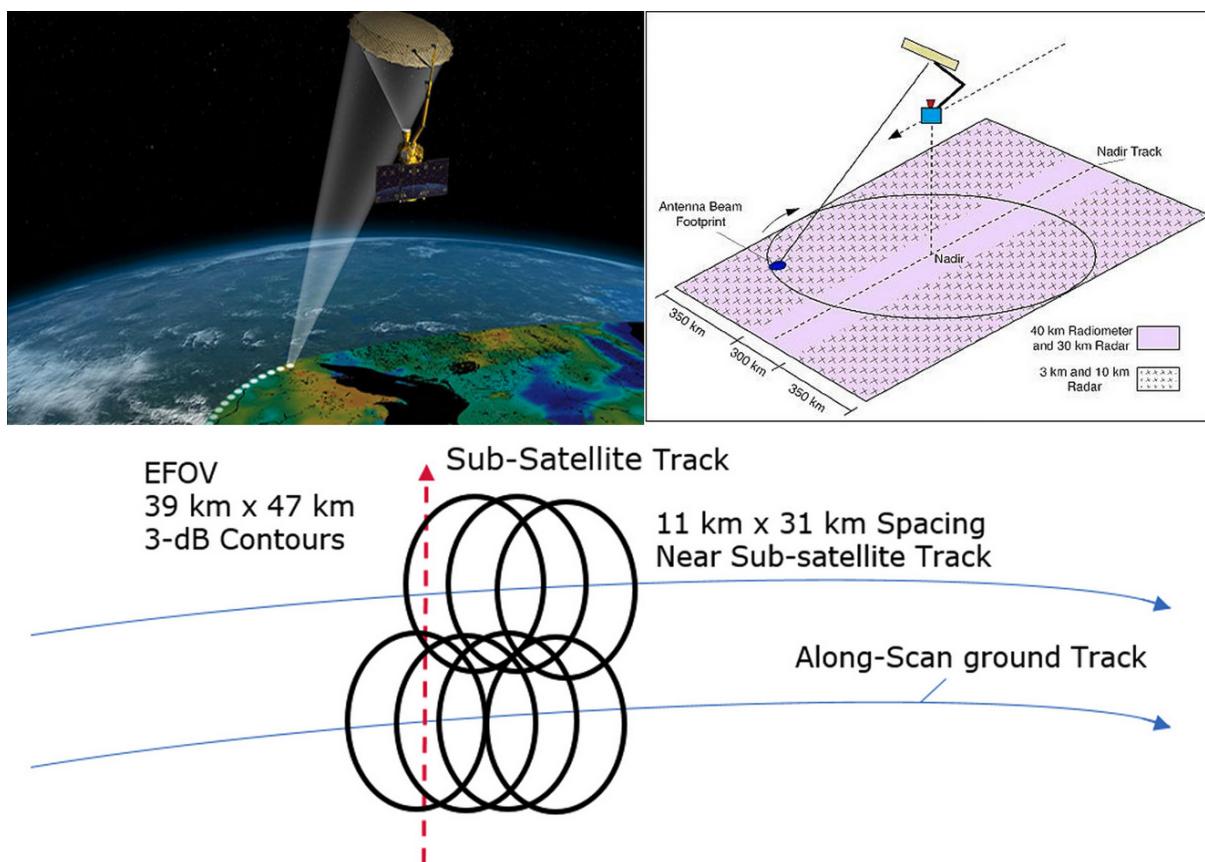


Figure 1.15 – (Top Left) Artistic view of NASA/SMAP mission, (Top Right) schematic indicating the  $\sim 1000$  km wide swath formed by the scanning radiometer and radar beams of SMAP. (Bottom) Radiometer Extended FOV spacing. The sub-satellite point is moving in the direction of the red dashed arrow. The blue curves indicate the azimuthal scanning directions and the black ellipses illustrate the successive 3-dB footprint of the radiometer in that direction. (After Reul et al., 2020)

### 1.2.3 Attempts to retrieve SSS with C- and X-band radiometer data

Before the launch of the first L-band satellite (see Section 1.2.2.1), Reul et al. (2009) developed an algorithm to retrieve SSS from the AMSR-E C- and X-band (6.9 GHz and 10.7 GHz) radiometer channel data.

As can be seen in Figure 1.16, for an SST of  $15^\circ\text{C}$  and SSS of 35 psu, the sensitivity of oceans brightness temperature to SSS is significantly lower for the C-band than that at the L-band (by a factor of 10), whereas for the X-band, it is nearly zero.

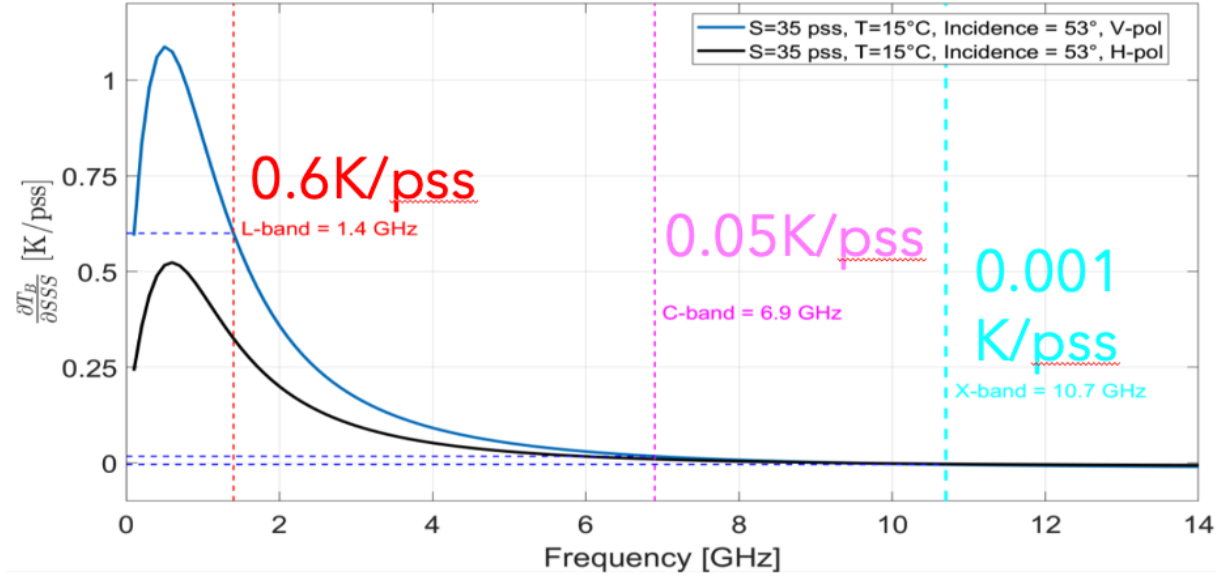


Figure 1.16 – Sensitivity of oceanic brightness temperature to SSS,  $\partial T_B/\partial SSS$  in function of the electromagnetic frequency, calculated from Klein and Swift, 1977 for a given salinity ( $S = 35$  pss) and temperature ( $T = 15$  °C) and an incidence angle of  $53^\circ$  (similar to AMSR-E), in vertical and horizontal polarization

Furthermore, a warmer SST will increase the  $T_B$  sensitivity to SSS: In  $v$ -polarization, for the C-band (respectively X-band) from  $\partial T_B/\partial SSS \approx -0.024$  K/pss (resp.  $0.003$  K/pss) at an SST =  $20$  °C to  $\partial T_B/\partial SSS \approx -0.053$  K/pss (resp.  $-0.0069$  K/pss) at SST =  $30$  °C (see Figure 1.17a, b).

For the same polarization, the sensitivity of oceans brightness temperature to the SST,  $\partial T_B/\partial SST$ , is at these frequencies significantly higher than  $\partial T_B/\partial SSS$ , with  $\partial T_B/\partial SST \approx 0.65$  K/°C ( $0.69$  K/°C) for C-band and  $\approx 0.61$  K/°C ( $0.63$  K/°C) for the X-band at SSS =  $35$  pss (respectively SSS =  $20$  pss) (see Figure 1.18). The signal is more sensitive to SST than to SSS by a factor of more than 10. The  $h$  polarization (respectively c and d on Figure 1.17 and Figure 1.18) shows a loss of sensibility for the two channels by a factor of  $\approx 2$ .

Additionally, Reul et al. (2009) pointed out that surface waves roughness can cause significant changes in the observed brightness temperature that may mask the weak salinity signatures (see Figure 1.19). Meissner and Wentz (2012) showed that the wind-induced emissivity in H-polarization (Figure 1.19b) for wind speeds at  $1$  m/s already contributes

1 K, which increases strongly after for increasing speed. For wind-speeds smaller than 10 m/s the emissivity induced by the wind is up to 6 K. Contrarily, the wind induces emissivity in  $v$ -polarization (Figure 1.19a) is close to zero for wind speed  $< 2$  m/s, and do not exceed  $\pm 1$  K until the wind speed exceeds 10 m/s. In addition,  $T_B$  sensitivity to SSS ( $\partial T_B / \partial SSS$ ) is higher in vertical polarization (V-pol) than in horizontal polarization (H-pol) (see Figure 1.17, Figure 1.18). Therefore, for the present work, only  $v$ -polarization data is considered.

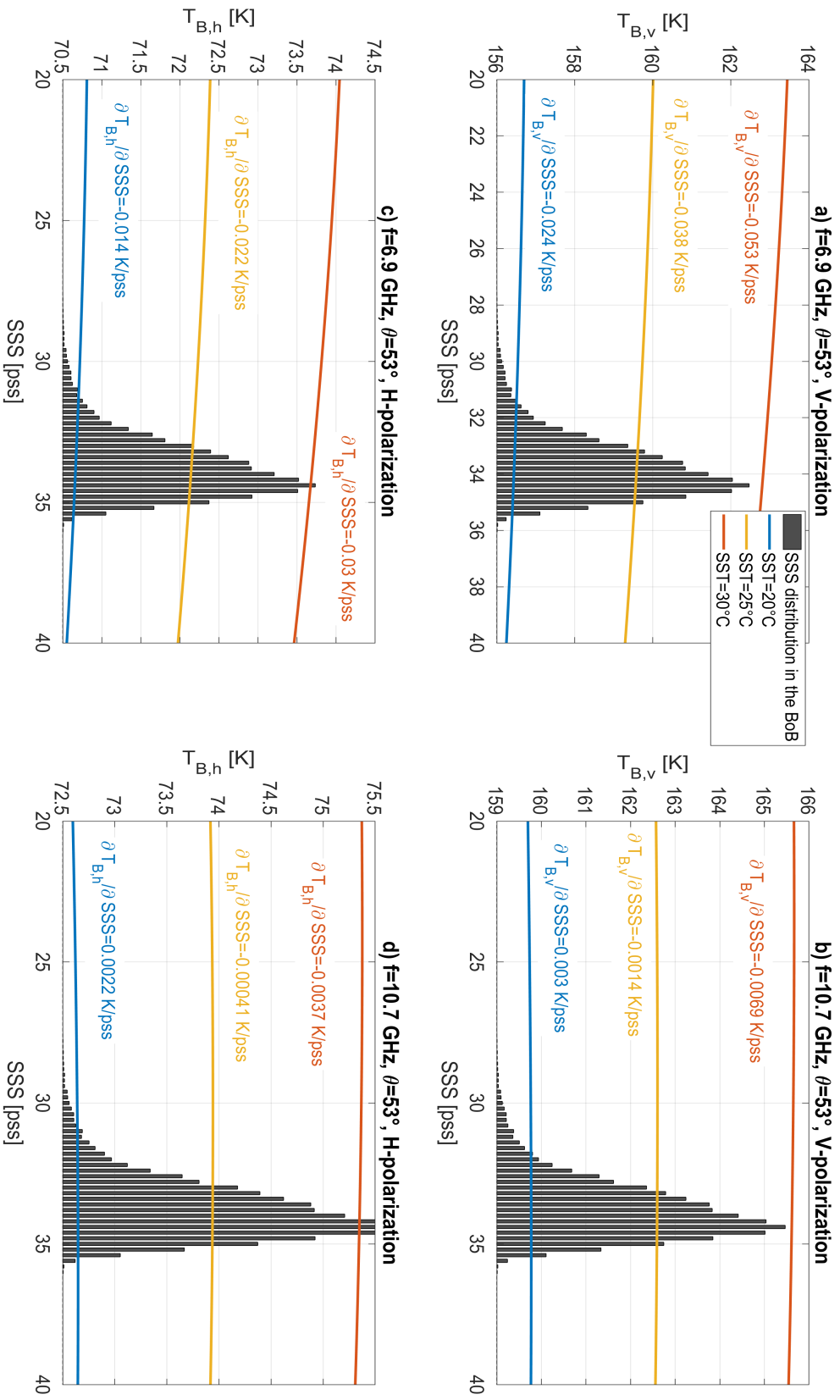


Figure 1.17 – Relationship between oceanic brightness temperature ( $T_B$ ) and sea surface salinity (SSS) for SSTs of 20°C, 25°C, and 30°C in the Bay of Bengal (BoB), with SSS distribution in the background. Panels a) and c) illustrate the sensitivity of C-band, while panels b) and d) demonstrate the sensitivity of X-channel for vertical and horizontal polarization, respectively.

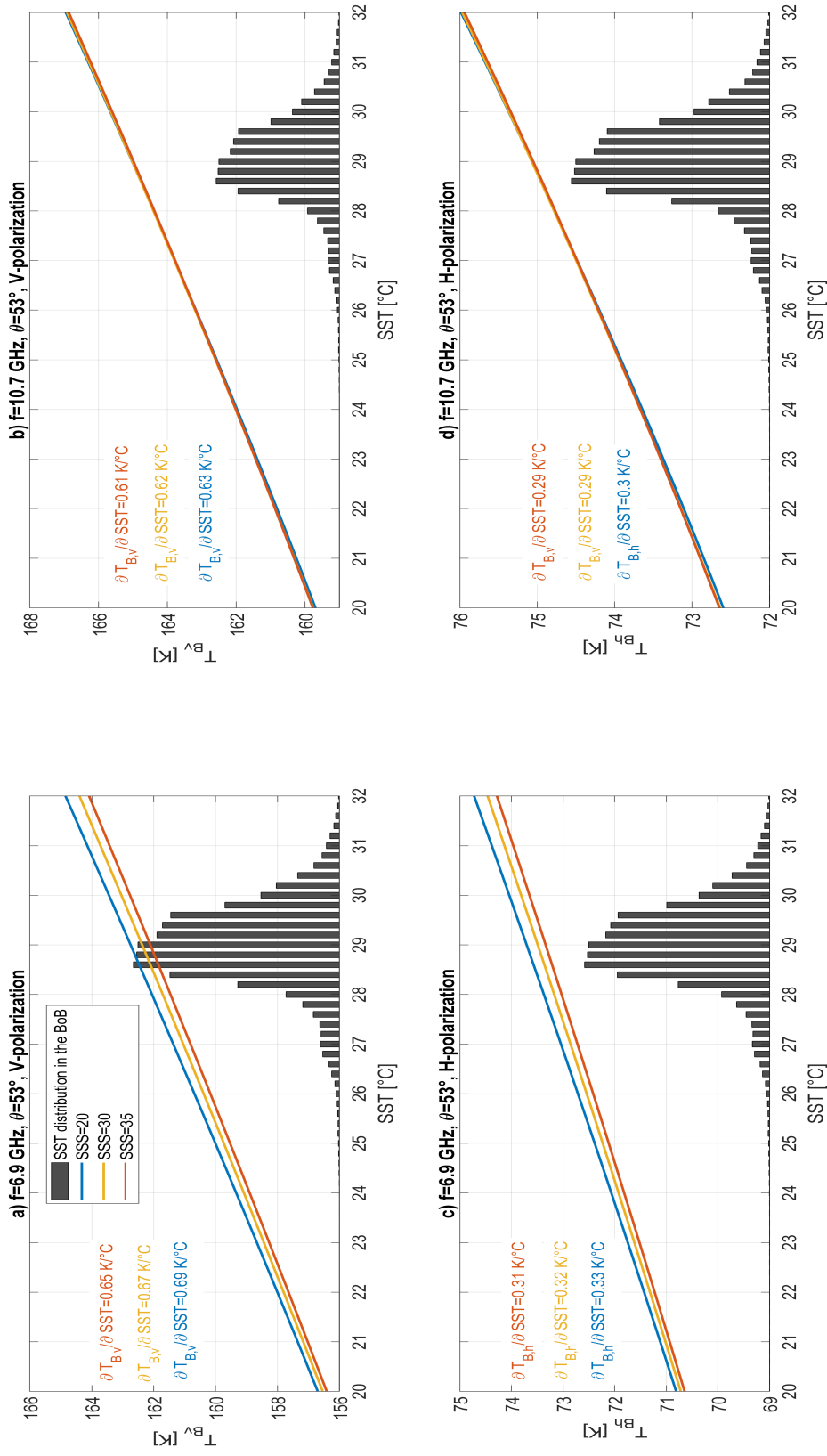


Figure 1.18 – Relationship between oceanic brightness temperature ( $T_B$ ) and sea surface temperature (SST) for SSSs of 20 pss, 30 pss, and 35 pss in the Bay of Bengal (BoB), with SST distribution in the background. Panels a) and c) illustrate the sensitivity of C-band, while panels b) and d) demonstrate the sensitivity of X-channel for vertical and horizontal polarization, respectively.

Reul et al. (2009) proposed to minimize these SST and surface wind impacts by using the oceans brightness temperature difference quantity:

$$\Delta T_B^\nu = T_v^{6.9} - T_v^{10.7} \quad (1.7)$$

where  $T_v^{6.9}$  and  $T_v^{10.7}$  are the oceans brightness temperature at the ocean surface in V-pol retrieved from C- and X-channels, respectively.

As illustrated in Figure 1.20 and Figure 1.21, taking the difference between X- and C-band allows to:

- (i) strongly minimize the SST impact on the oceans brightness temperature while only weakly impacting its sensitivity to SSS ( $\partial\Delta T_B/\partial SSS \cong 0.0046$  K/pss (SST = 30°C) and  $\partial\Delta T_B/\partial SST \cong -0.04$  K/°C, see Figure 1.21a and b, and
- (ii) reduce in average the dependence to the sea surface roughness:  $T_v^{6.9}$  and  $T_v^{10.7}$  reacts similarly to the changes in the surface wind speed from about 0 to 10  $\text{m s}^{-1}$  (see Figure 1.19a).

Reul et al. (2009) used this method over the Amazon plume region in the Northwestern Tropical Atlantic. The authors showed that monthly and bimonthly surface salinity could be retrieved with a relative accuracy ( $\sim 0.5$  pss). AMSR-E SSS clearly helps monitoring the large-scale spatial structures of the freshwater Amazon plume that extends about 600 km offshore.

After this study, Song and Wang (2017) created a similar algorithm based on Reul et al. (2009), in order to retrieve SSS from satellite HY-2A radiometer. Both algorithmn are based on the following Radiative Transfert Model (RTM):

$$T_B = T_{BU} + \tau[eT_S + T_{B\Omega}] \quad (1.8)$$

where  $T_B$  is the brightness temperature of the radiometer,  $T_{BU}$  is the upwelling atmospheric brightness temperature,  $T_{B\Omega}$  is the sky radiation scattered upward by the Earth surface,  $T_S$  is the SST,  $\tau$  is the atmospheric transitivity.  $T_{B\Omega}$  can generally be expressed as  $T_{B\Omega} = R \cdot M$ , with M a function of the downwelling atmospheric radiation, atmospheric transmissivity, corrections to the sea surface scattering, and cosmological background radiation, and R the sea surface reflectance. By using the Kirchhoff thermal law the

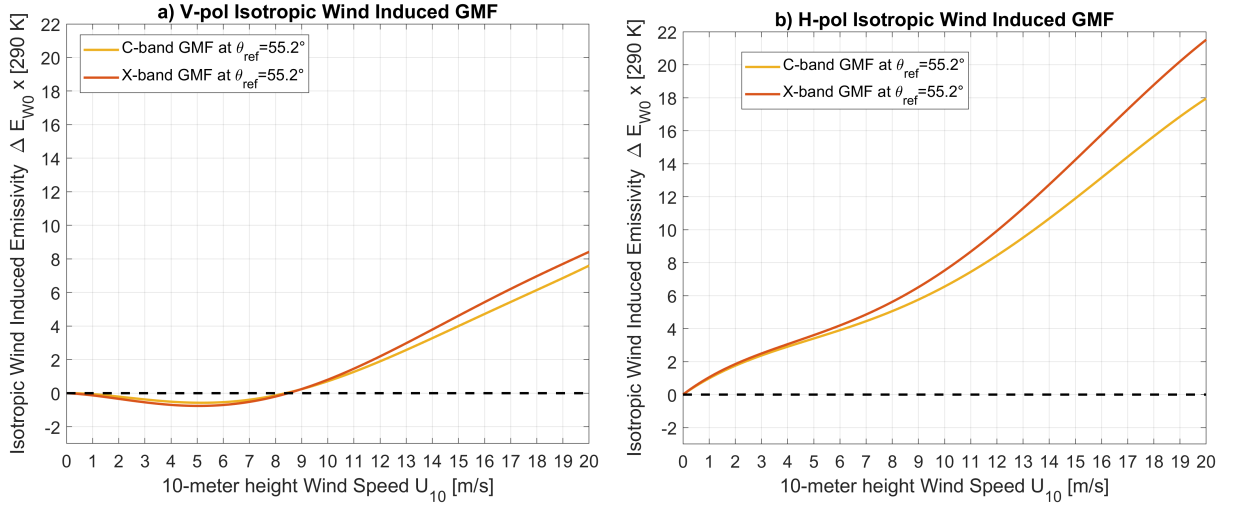


Figure 1.19 – Isotropic wind induced emissivity at C- and X-band for (a) V-polarization and (b) H-polarization. The GMF from Meissner and Wentz (2012) are given a nominal incidence angle of  $55.2^\circ$

following equation for the sea surface reflectance is given:

$$R = \frac{(T_B - T_{BU})/\tau - T_S}{M - T_S}. \quad (1.9)$$

By combining the RTM model and a sea water dielectric constant model, the SSS can thus be retrieved ( $R_{HY-2A}$ ). Song and Wang (2017) then uses the SST products from the radiometer and SSS from the World Ocean Atlas 09 (WOA09) to train the reflectance model  $R_{KS}$  with the Klein and Swift dielectric constant model, at both channels. Finally,  $R_{HY-2A}$  issued from the HY-2A satellite is then calibrated with the modeled  $R_{KS}$  before retrieving the SSS.

The retrieved SSS presents reasonable features of the freshwater runoff near the Yangtze Delta compared to WOA09 climatology. Also, for the Northwest Pacific it is possible to see mesoscale features in the SSS in the South China Sea. Song and Wang (2017) specifies that the root-mean square error for the one-year data is about 0.56 on a monthly time scale. It significantly reduces to 0.35 after the data has been bilinear interpolated to the grid spacing ( $0.5^\circ \times 0.5^\circ$ ).

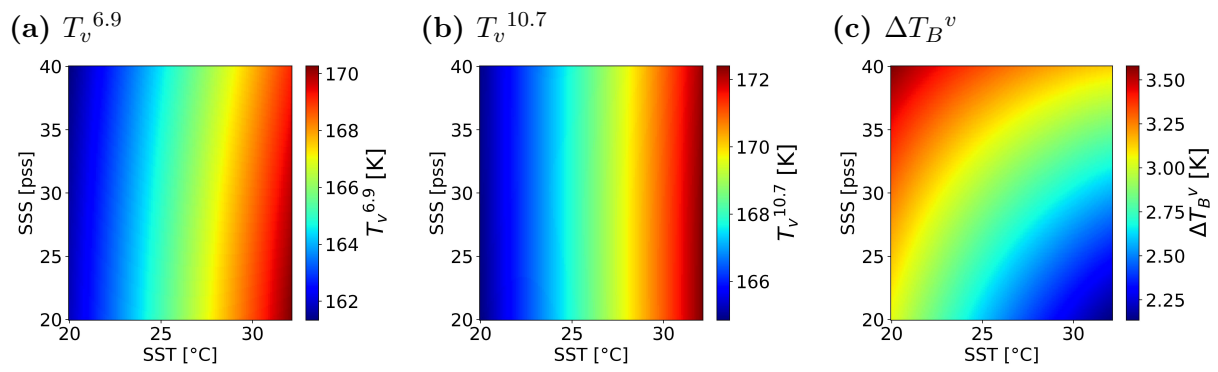


Figure 1.20 – V-polarized oceans brightness temperature as a function of SSS and SST at an incidence angle of  $55^\circ$  for a) C-band ( $T_v^{6.9}$ ), b) X-band  $T_v^{10.7}$  and c) the oceans brightness temperature difference between X- and C-band ( $\Delta T_B^v$ ).

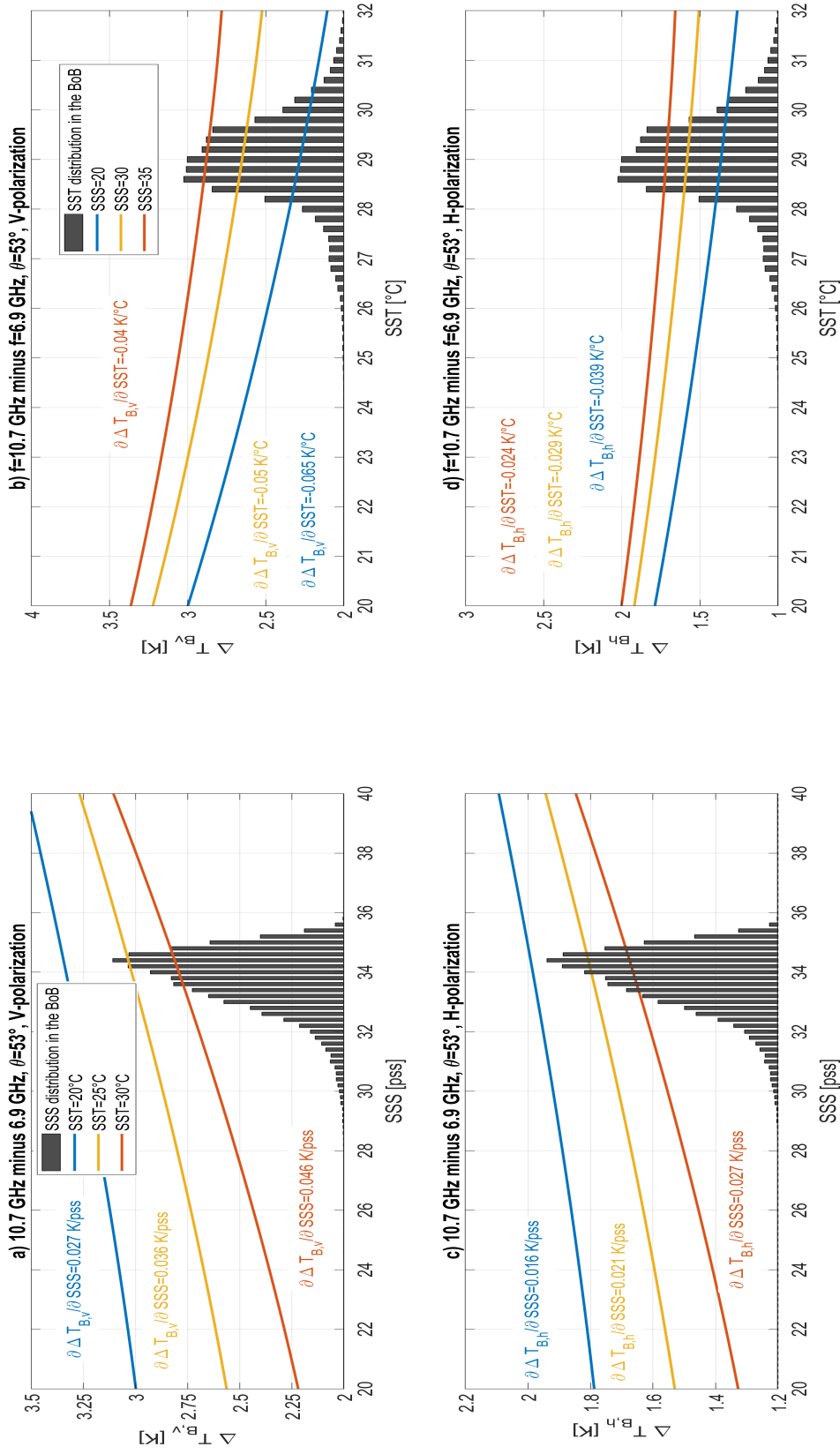


Figure 1.21 – Oceanic brightness temperature difference ( $\Delta T_{B}$  oceans brightness temperature) plotted against sea surface salinity (SSS) and sea surface temperature (SST) in the Bay of Bengal (BoB), with corresponding background distributions, in vertical polarization (top) and horizontal polarization (bottom). The different colors represent study cases with SSTs of 20°C, 25°C, and 30°C, and 30 psu, 30 psu, and 35 psu.

### 1.3 Bay of Bengal (BoB): A Singular Tropical Ocean Basin

The BoB is situated in the northeast of the Indian Ocean and is a peculiar zone because of its unique geography and climate characteristics. Bounded by India to the west, Bangladesh to the north, and Myanmar to the east, it forms a semi-closed basin (see Figure 1.22). During boreal summer large differential heating is thus created between the Asian subcontinent and the ocean. This drives the most dramatic monsoonal wind system in the world (Schott & McCreary, 2001).

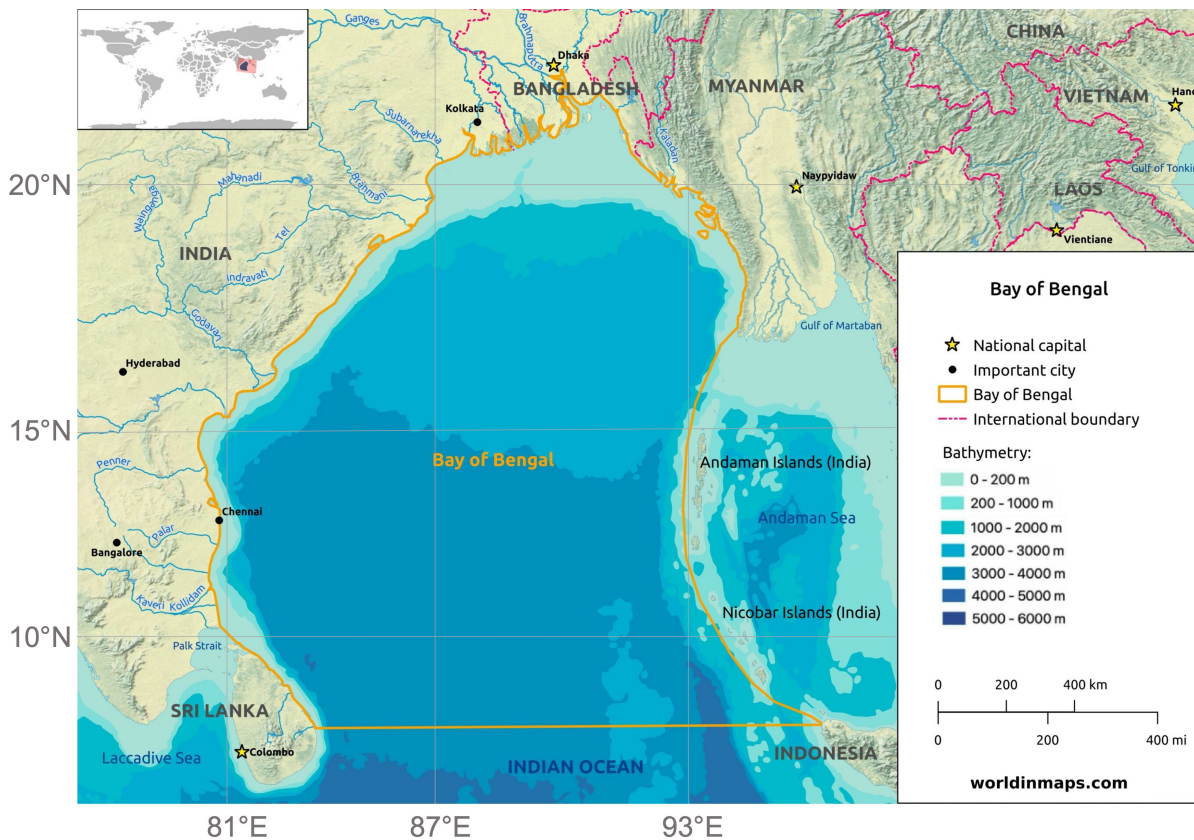


Figure 1.22 – Map of the Bay of Bengal (contour in yellow). The different blue tones represent the bathymetry. Image taken from <https://worldinmaps.com>

The BoB covers an area of approximately 2.2 million square kilometers and has an average depth of 2,600 meters (Figure 1.22).

Five of the world’s 50 largest rivers, including the Brahmaputra, the Ganga, the

Irrawaddy, the Godavari, and the Mahanadi, empty into the Bay of Bengal north of  $15^{\circ}\text{N}$ , contributing a total annual continental runoff (R) of approximately  $2950 \text{ km}^3$ . When combined with annual rainfall (P) of  $4500 \text{ km}^3$ , the total freshwater input exceeds annual evaporation (E) of  $3500 \text{ km}^3$ , resulting in a net annual freshwater supply of about 1.6 m to the Bay of Bengal. As a result, the Bay of Bengal acts as a dilution basin ( $E - P - R < 0$ ), and its circulation must export the excess freshwater it receives from rainfall and rivers (Schott & McCreary, 2001; Sengupta et al., 2006).

### 1.3.1 Impacts of salinity

The intense freshwater flux in a small and semi-closed basin as the BoB results in an intense dilution of the salt contained in seawater, letting the BoB stand out with a mean SSS below 33 pss in the Tropics (Chaitanya et al., 2014b). The surface freshwater flux induces a contrast between the surface- (top 40 m) and the deep-layer, creating a sharp near-surface haline stratification (Chaitanya et al., 2014b). This stratification has important impacts on the near-surface ocean stability and is believed to be a part of a positive feedback loop that maintains high SST and rainfall over the BoB (Shenoi et al., 2002). As explained in the section above, the haline stratification creates a barrier layer and prevent the mixing of the surface layer with the deeper layer (de Boyer Montégut et al., 2007). This contributes in maintaining the SST above the  $\sim 28.5^{\circ}\text{C}$  threshold for deep atmospheric convection causing intense rainfall above the BoB (Gadgil et al., 1984). However, Krishnamohan et al. (2019), using a coupled model simulation, did not find any evidence of salinity influencing the climatological SST and rainfall in the BoB.

The Bay of Bengal (BoB) has one of the highest numbers of casualties due to tropical cyclones (TCs) globally. According to Alam et al. (2003), between 1974 and 1999, TCs accounted for approximately 5% of the global TC casualties. The TCs that develop in the BoB are among the most lethal globally, with 14 out of 20 of the deadliest TCs, mainly due to the densely populated and vulnerable coastal areas and inadequate disaster management strategies (Neetu et al., 2012). These TCs usually occur before or after the Indian summer monsoon, between April to May for the pre-monsoon and October to December for the post-monsoon (Neetu et al., 2019). Sengupta et al. (2008) proposed that the stratification of the sea surface salinity was responsible for hindering mixing below the TCs in the Bay of Bengal, resulting in stronger cyclones than in the Arabian Sea. Neetu et al. (2012) confirmed that the salinity stratification played a significant role in the cooling below cyclones. However, Neetu et al. (2019) questioned the potential

role of the salinity distribution on the strongest TCs in the BoB, and found that air-sea interactions below tropical cyclones influenced the characteristics of strong TCs.

Another important role salinity can have in the BoB is its ability to trace water masses. The strong seasonal reversals of wind-stress forcing in the Bay of Bengal give rise to an intense oceanic dynamic, which is influenced not only by local forcing but also by remote forcing such as Kelvin and Rossby waves. The East Indian Coastal Current (EICC) is one important example of this dynamic. It undergoes a reversal twice a year, carrying freshwater generated by river runoff and summer rains from the north to the south during winter and creating a freshwater tongue. This tongue has a width of approximately 200 km and will expand itself for 2.000 km, all along the Eastern Indian coast, as far as Sri Lanka, creating a "River in the Sea" shortly after the winter monsoon (Akhil et al., 2014; Chaitanya et al., 2014b; Fournier et al., 2017).

### 1.3.2 Seasonal Cycle

During four months (June-September, Figure 1.23b), south-westerly winds flush over the surface of the ocean (see e.g., Fig. 1 from Schott and McCreary, 2001), collecting water vapor, before releasing it over India and the BoB. The rain over India feeds large rivers that flow into the BoB as can be seen in Figure 1.23a. Together with the monsoon rains (in summer and autumn), they create shallow freshwater pools in the northeast BoB. As a result, SSS mirrors the seasonal evolution of the Ganga-Brahmaputra (or Irrawaddy) and rainfall, as can be seen on Figure 1.25c (Chaitanya et al., 2014b; Fournier & Lee, 2021).

The SST in the BoB displays a seasonal behavior along the year: the freshwater coming from the rivers contributes to a lower SST in the northeastern BoB (see Figure 1.24b), especially During December to February. During April and May, the averaged SST reaches its peak. Soon after the onset of the monsoon in June, the winds strengthen, and SST decreases. In contrast, the neighboring Arabian Sea cools rapidly during the monsoon season, whereas SST in the BoB remains higher than 28 °C (see Figure 1.24a) (the threshold for deep convection in the atmosphere over tropical oceans mentioned in the section above). Shenoi et al. (2002) supposes that the increase in stratification creates a shallow mixed layer, leading to SST higher than 28 °C, as the heat influx from the atmosphere is trapped in a smaller mixed layer depth.

The SSS in the BoB displays a distinct seasonal cycle, resulting in a strong SSS gradient across the entire bay. During summer monsoon, the SSS in the BoB decreases due to

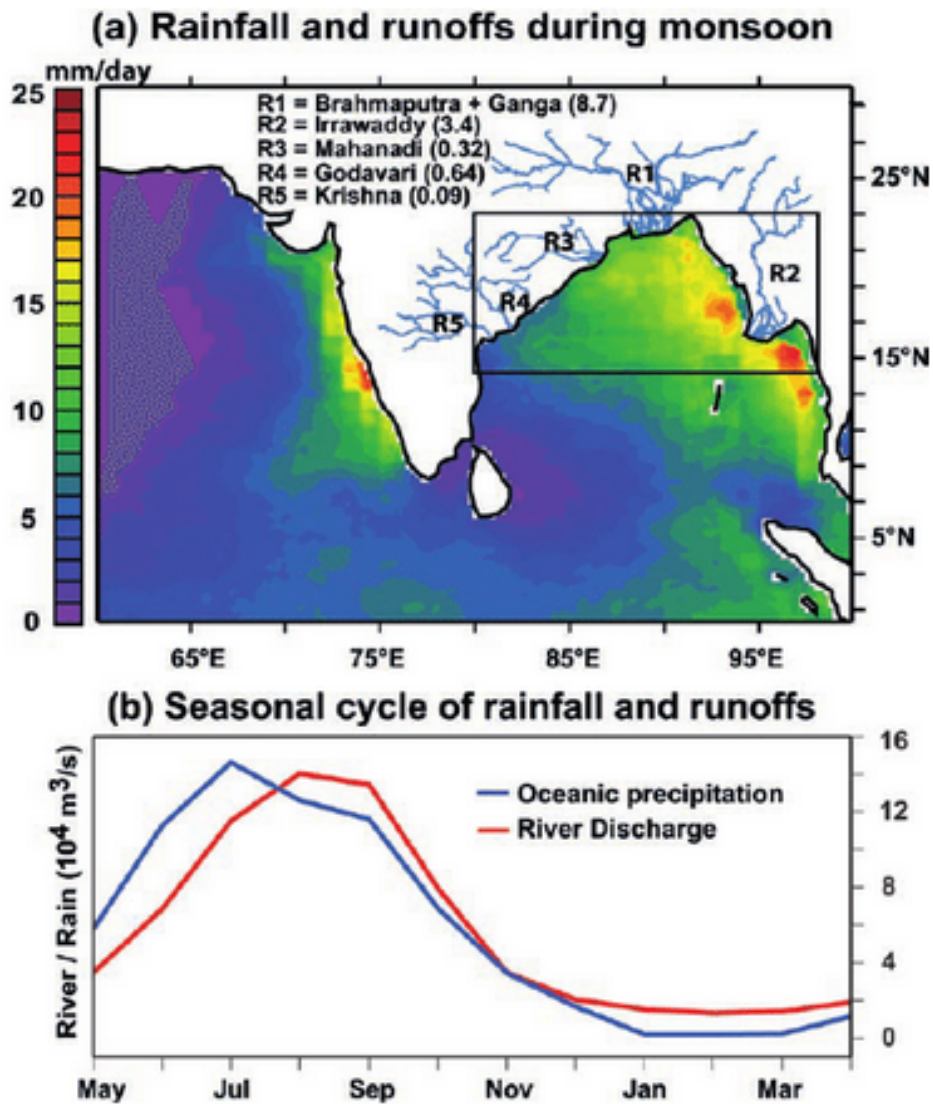


Figure 1.23 – (a) Average climatological rainfall from Jul to Sep (mm day<sup>-1</sup>) from Tropical Rainfall Measuring Mission (TRMM) 3B42 data. The major rivers in the northern BoB are drawn on the map and their average river discharge during Jul–Sep ( $10^4 \text{ m}^3 \text{ s}^{-1}$ ) is indicated. (b) Average fresh water flux into the BoB ( $10^4 \text{ m}^3 \text{ s}^{-1}$ ) north of 14°N from rainfall over the ocean (blue curve) and the major rivers (red curve) indicated in (a) (Chaitanya et al., 2014b).

monsoon rainfall and runoff. This deposit of fresh water at the surface forms a barrier layer (see details hereafter) and the vertical mixing with higher salinity waters partly counteracts this decrease in salinity at the surface during end of summer and autumn

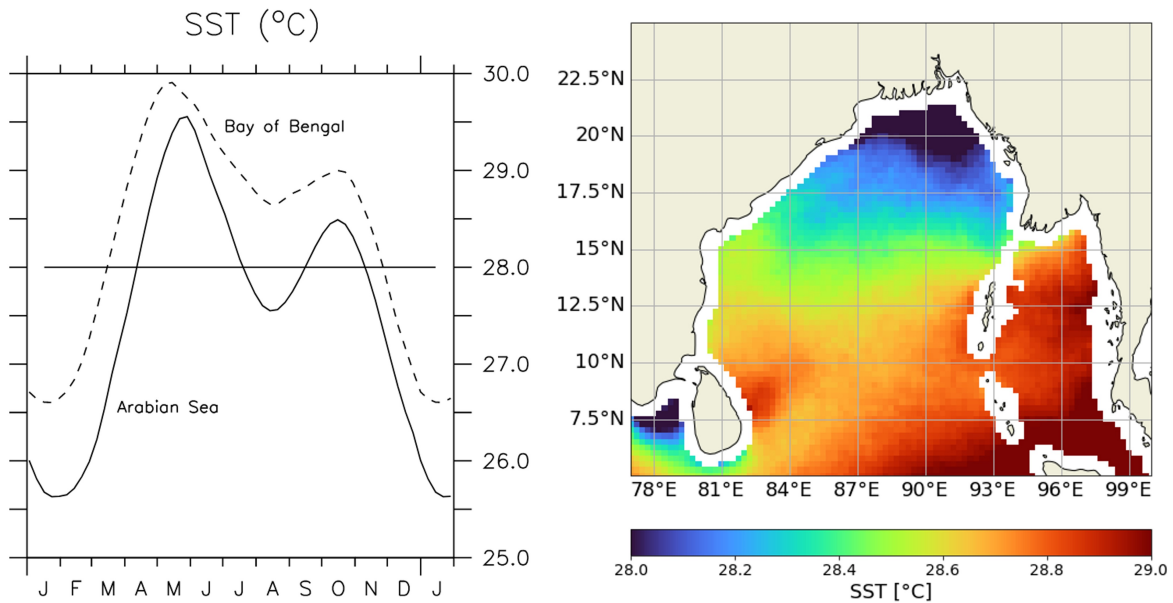


Figure 1.24 – a) SST in the Arabian Sea (solid) and Bay of Bengal (dashed). The temperatures were averaged over the region between  $6^{\circ}$  and  $25^{\circ}$ N in both basins (after Shenoi et al. (2002)). b) annual SST in the BoB using the CCI dataset.

(Benshila et al., 2014; de Boyer Montégut, 2005). From winter, SSS increases again as precipitations are weak and evaporation dominates due to northeasterly monsoonal winds from the land. It is important to note that the contribution of horizontal advection can be locally strong, as for example along the coasts of eastern India (see details hereafter).

The thickness of the barrier layer in the BoB shows a seasonal cycle induced by fresh-water inputs and surface circulation patterns (Mignot et al., 2007). In June to September, the barrier layer thickness increases along the eastern boundary, while a band of low thickness is recorded between the Indo-Sri Lanka region and the eastern boundary south of  $12^{\circ}$ N. This is due to high salinity water transport from the Arabian Sea causing stratification and greater mixing. In November to December, increased river discharges lead to a pattern of thick barrier layer extending all along the boundary of the BoB and farther northeast (Kumari et al., 2018; Mignot et al., 2007).

Another seasonal cycle which occurs in the BoB is the EICC, a major current along the western boundary of the BoB. It is responsible for most of the surface and thermocline water transport in this basin and connects the BoB with the equatorial Indian Ocean and the Arabian Sea (Akhil et al., 2014; Schott & McCreary, 2001). Before and during

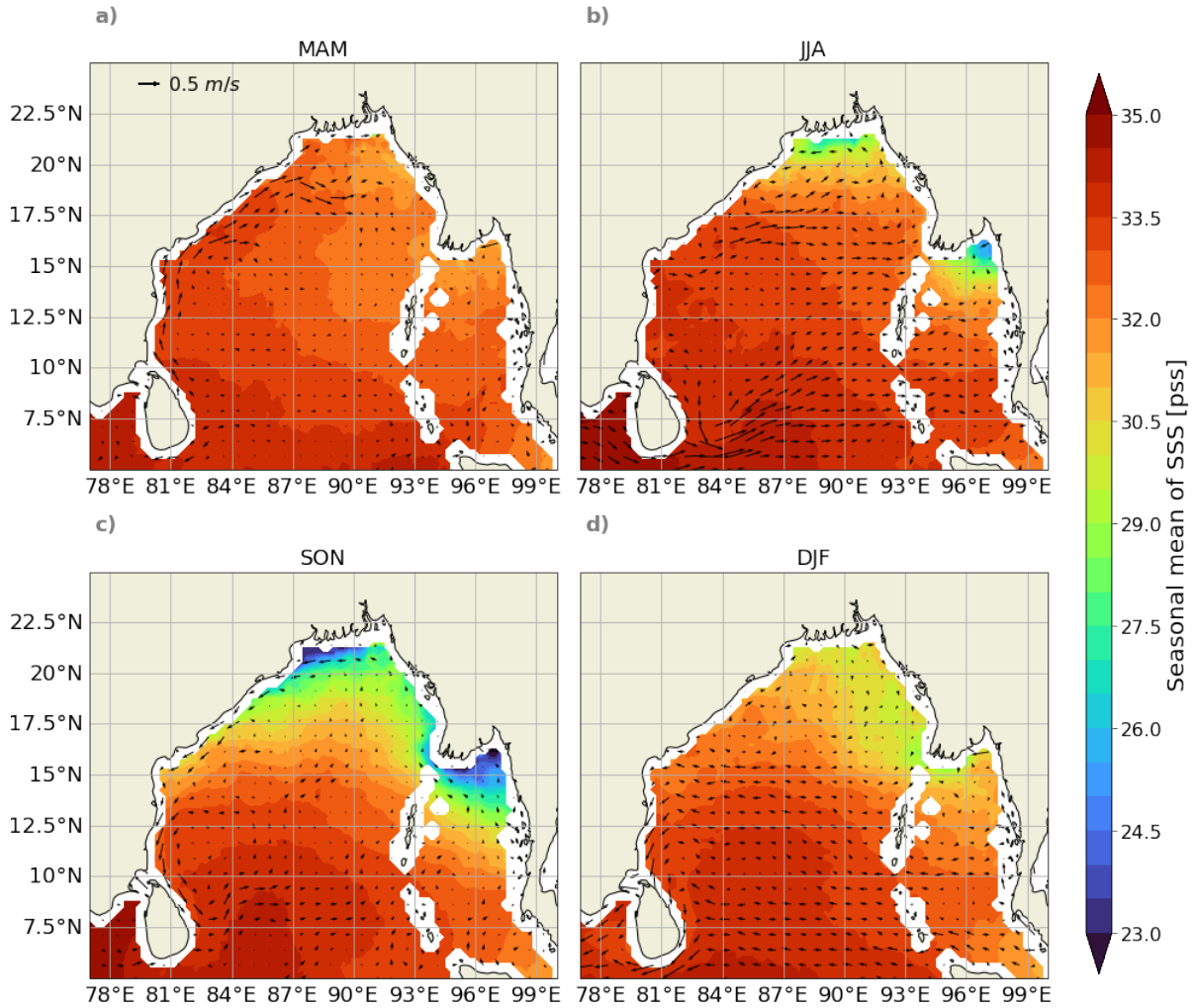


Figure 1.25 – In the background is the seasonal mean climatology of SSS and in the foreground the surface currents between June 2010 and December 2016 in the BoB using Climate Change Initiative (CCI) (Boutin et al., 2021a) and Globe Current datasets (Reyes et al., 2022). a) represents the mean of March-April-May, b) the mean of June-July-August, c) the mean of September-October-November and d) the mean of December-January-February.

summer monsoon (February until September) the EICC flows northeastward, forced by southwesterly winds (Figure 1.25a). After the monsoon (October to January) it reverses itself, flowing southwestward forced by northeasterly winds (see Figure 1.25c). Only during November–December and March–April when the EICC reaches a peak, a continuous flow between the northern BoB and the southeastern coast of Sri Lanka is reached (Akhil

et al., 2014; Schott & McCreary, 2001).

The reversal occurs about one month before the wind reversal in the Bay of Bengal. This is because of the remote wind forcing from the equatorial Indian Ocean and eastern rim of the Bay of Bengal, which travels to the east coast of India in the form of coastal Kelvin waves (coastally trapped waves that travel counterclockwise around the BoB at a speed of approximately  $2.5 - 3 \text{ m s}^{-1}$ ). In addition to coastal Kelvin waves, Rossby waves forced by wind stress curl in the BoB interior also propagate westward towards the east coast of India. Together with the remote equatorial wind variations, these waves play an important role in the current reversal. It is worth noting that local alongshore forcing only becomes dominant at a later stage of the process. (Akhil et al., 2014; Chaitanya et al., 2014b; Durand et al., 2009; McCreary et al., 1996).

### 1.3.3 Interannual Variability

The interannual variability of SSS refers to anomalies relative to the seasonal cycle that last more than a season. In the BoB, this variability is primarily associated with climate variability from either the El Niño-Southern Oscillation (ENSO) in the Pacific or the Indian Ocean Dipole (IOD) in the Indian Ocean (see Figure 1.26 (Schott et al., 2009).

At interannual timescales, ENSO is the leading mode of climate variability. It develops through air-sea interaction in the Pacific but influences the Indian Ocean through changes in the Walker Circulation. While the Indian Ocean experiences warming during an ENSO event primarily due to subsidence over the basin, circulation changes in the Northern Indian Ocean appear to be more strongly linked with another local mode: the IOD (Currie et al., 2013; Rao & Behera, 2005).

The IOD is associated with air-sea interactions over the Indian Ocean equatorial sector (Saji et al., 1999; Webster et al., 1999). A positive IOD is characterized by warming in the western Indian Ocean and cooling in the eastern equatorial Indian Ocean, and a negative IOD by the opposite polarity. It develops in June, with a peak in October, suggesting an influence of ocean dynamics (Reverdin et al., 1986; Saji et al., 1999; Schott et al., 2009; Webster et al., 1999).

Recent studies have highlighted the possible influence of the IOD on the extension of the "river in the sea" mentioned before. A positive IOD event can lead to the formation of easterly wind anomalies in the equatorial region. These conditions drive equatorial

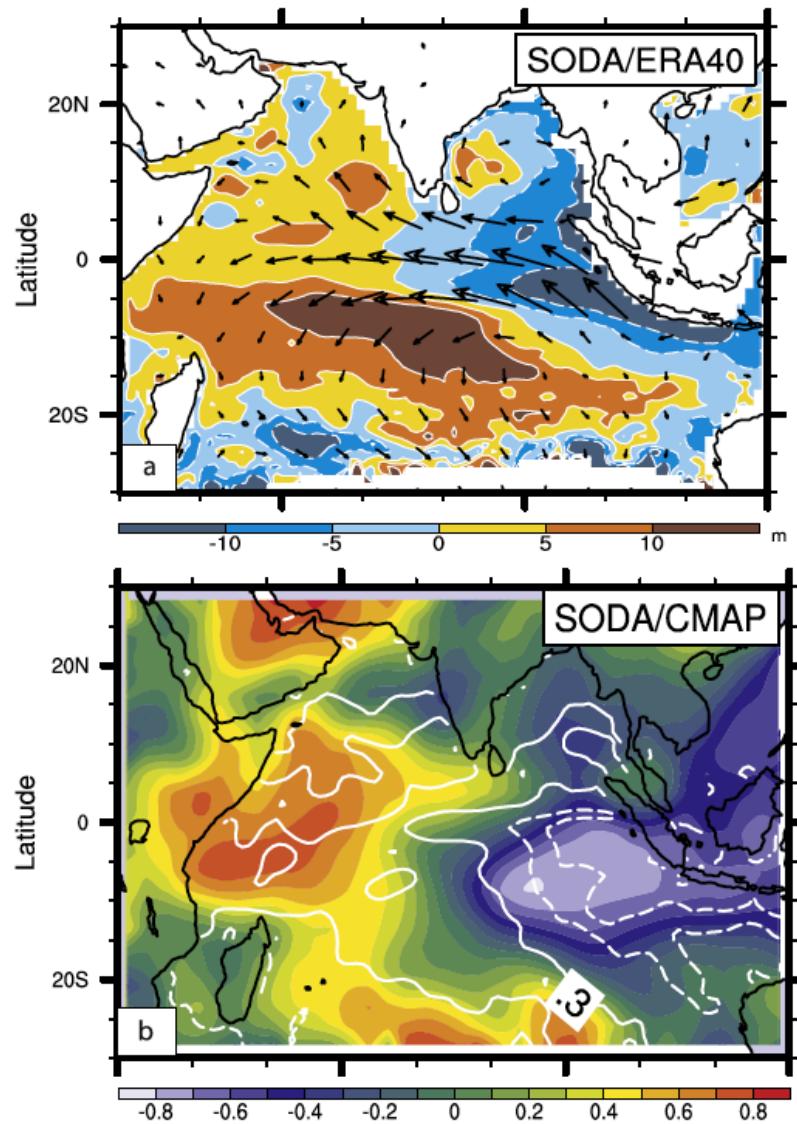


Figure 1.26 – IOD pattern during September–November. (a) Regression of 20°C isotherm depth (Z20; shades in m) and surface wind velocity (m/s) upon the first principal component of Z20 and (b) correlation of precipitation (shades) and SST (contoured at 0.3, 0.6, and 0.9 with zero omitted and negative dashed) with the first principal component of Z20 (After Saji et al., 2006)

upwelling Kelvin waves, which travel into the BoB as coastal upwelling Kelvin waves, moving anticlockwise around the rim of the Bay of Bengal. As a result, negative sea-level anomalies develop along the east coast of India, which weakens the East India Coastal Current (EICC) and reduces the southward flow of freshwater from the northern part of

the Bay of Bengal during the season (Akhil et al., 2016a). Furthermore, Kumari et al. (2018) demonstrated that these Kelvin waves generate upwelling and downwelling phases of Rossby waves, impacting the barrier layer thickness. The thickness of the barrier layer, like the EICC, is stronger during negative IOD years compared to positive ones.

In their study, Akhil et al. (2016a) investigated the possible processes controlling the BoB SSS interannual variability using Empirical Orthogonal Function (EOF)s. The first EOF mode, which accounted for 37% of the total variance, was strongly linked with the IOD with a correlation of 0.88. The second EOF mode, which accounted for 16% of the total variance, was associated with local SSS anomalies in the northern BoB in response to variations in Ganga-Brahmaputra River discharge, with a correlation of 0.76. Confirming these findings, Chaitanya et al. (2021) showed that oceanic rainfall and Ganga-Brahmaputra freshwater equally contribute to the post-monsoon freshening of the west coast of India. Furthermore, they found that Irrawady-Salween waters remain trapped in the northern half of the Andaman basin due to the more sluggish circulation in this region.

However, Akhil et al. (2020) demonstrated that although satellite data seems to confirm the influence of the IOD, albeit less pronounced than using the model, the impact of runoff is not detected. Higher-order EOFs of the SMOS data or a regression to Ganges Brahmaputra runoff data do not reveal any consistent signal with those discussed by Akhil et al. (2016a). The authors suspect that this is caused by the relatively short SMOS satellite record, which prevents the extraction of weaker-amplitude variability. Additional studies (Benshila et al., 2014; Chaitanya et al., 2021; Fournier et al., 2017; Hareesh Kumar et al., 2013) suggest a stronger role of eddies induced "erasing" of the runoff influence.

To summarize, the individual contributions of different forcing factors such as wind, runoff, and eddies on the SSS variability in the BoB remain unclear. Specifically, the less robust correlation between the IOD and SSS in satellite observations compared to models raises the question of whether eddies play a role in the weaker relationship in observations and/or if the short duration of the satellite data is responsible for the discrepancy.

### 1.3.4 Review of SSS remote sensing (L-band radiometer) in the BoB

Since the launch of SMOS, numerous studies have been done in the BoB with L-band radiometric data. The following section summarizes these studies.

**Seasonal Variability** In Sharma et al. (2010), a 15-year simulation of SSS in the tropical Indian Ocean was conducted using an ocean general circulation model (OGCM) forced by the NCEP-NCAR daily reanalysis product. The study aimed to evaluate the model's ability to provide realistic SSS simulations and characterize SSS variability to prepare for upcoming satellite salinity missions. Model fields were evaluated in terms of mean, standard deviation, and characteristic temporal scales of SSS variability. The standard deviations ranged from 0.2 to 1.5 psu, with larger values in regions with strong seasonal transitions of surface currents and along the coast in the BoB. In Nyadjro et al. (2011), the seasonal variability of salinity transport in the Indian Ocean was investigated using the high-resolution global HYbrid Coordinate Ocean Model (HYCOM). The study identified freshwater forcing and zonal advection as the dominant mechanisms of SSS variability, with zonal SSS transport being higher than meridional SSS transport. D'Addezio et al. (2015) analyzed the seasonal variability of salinity in the northern Indian Ocean using observational datasets (Aquarius and Argo) and model simulations. The study revealed different salinity processes in the northern Indian Ocean that are dominantly related to the semiannual monsoons. In Pant et al. (2015), an in situ gridded data of salinity comprising Argo and CTD profiles were used to study the interannual variability of near-surface salinity in the Bay of Bengal during the years 2005-2013. The study found that the Level-3 SSS data derived from Aquarius satellite showed good agreement with the in situ data. Akhil et al. (2016a) used an ocean general circulation model to study BoB interannual SSS variability, which is largest in boreal fall in three regions. In the northern BoB, summer-fall Ganga-Brahmaputra runoff interannual variations drive the largest variations, while wind-driven interannual current anomalies are responsible for a large fraction of SSS interannual variability in most of the basin.

**Data Validation** The BoB has varying SSS, making it challenging to apply satellite-derived SSS measurements due to potential RFI and land-induced contamination. Akhil et al. (2016a) validated SMOS and Aquarius level-3 monthly gridded SSS products to in situ SSS data for the BoB. SMOS SSS retrievals do not perform better than existing

climatologies, while Aquarius outperforms both SMOS and available SSS climatologies everywhere in the BoB, accurately capturing the seasonal signal in the entire basin and non-seasonal anomalies. However, Akhil et al. (2020) show that due to enhanced correction of systematic errors and an improved quality control procedure, SMOS data now offers data quality comparable to that of SMAP. Aquarius can be used to monitor large-scale year-to-year SSS variations in the BoB.

**IOD** Mishra et al. (2015) used a high-resolution ocean general circulation model to investigate salinity in the Northern Indian Ocean and found that the model is able to capture the contrasting distributions of SSS in the Arabian Sea and the BoB, and the strong seasonality of the SSS in the changing climate. The interannual SSS variability is 2-4 times smaller than seasonal variability in the region of study, and the regions of great interannual variability are located near river mouths in the Bay of Bengal. The relative role of wind and solar radiation on the sea surface salinity was also investigated.

**Estimations of Subsurface Properties** The strong salinity stratification in the BoB affects the ocean's response to surface heat fluxes. Mahadevan et al. (2016) found that freshwater adds stability, trapping heat within subsurface layers, causing delayed surface temperature rises and heat loss. Scientists use Aquarius along-track surface salinity and satellite-derived surface velocities to trace freshwater's evolution with the mesoscale circulation. This provides an interpolation of monthly salinity fields and estimates the salinification rate of water leaving the northern bay, likely related to submesoscale mixing processes observed during field campaigns.

**Mesoscale features** A Gordon et al. (2016) reported that the BoB and the Arabian Sea differ in their salinity stratification due to the Asian monsoon injecting freshwater into the BoB and removing it via evaporation from the Arabian Sea. Mesoscale features and an intrathermocline eddie were observed within the BoB during the R/V Revelle November and December 2013 Air-Sea Interactions Regional Initiative cruises, which obscure the regional surface water and thermohaline stratification patterns. Sengupta et al. (2016) showed that a thin layer of fresh water from summer monsoon rain and river runoff in the north BoB persists due to large-scale flow and eddies, as well as O(1-10) km submesoscale salinity fronts. Fournier et al. (2017) demonstrated that the EICC transports these freshwaters southward after the monsoon as an approximately 200 km

wide, 2,000 km long "river in the sea" along the East Indian coast. SSS from the SMAP satellite provides unprecedented views of this feature, with a very favorable signal-to-noise ratio in coastal areas, and is consistent with previous modeling results that suggested a modulation of the EICC/GB plume southward extent by the IOD.

**Primary Production** A study by Singh et al. (2015) suggests that cyclonic eddies play a role in enhancing primary production in the northern BoB potentially contributing to nutrient cycling and transfer of production to deeper waters. Meanwhile, seasonal reversals in boundary currents in the Indian Ocean can have significant impacts on productivity and trophic interactions, as observed in various regions such as the West Indian coast, East Indian shelf, and coast of Java (Hood et al., 2017).

## 1.4 Objectives and Plan

Despite multiple studies using in situ and remote measurements of Sea Surface Salinity in the BoB, investigating interannual variability in this region remains a challenge due to the short period of remote SSS measurements and the limited deployment of in situ instruments. Furthermore, the underlying mechanisms driving non-seasonal/interannual variability of SSS in the western part of the BoB remain poorly understood. These scientific challenges will be the focus of my PhD thesis work.

In an attempt to estimate more robust links between SSS and other factors, my first objective will be to have a longer time-series of SSS. For this I will use the Reul et al. (2009) approach so as to be able to estimate SSS from AMSR-E satellite and expand the time-series back to 2002. Scientific questions raised in this remote sensing part of this PhD will be:

- Can the Reul et al. (2009) approach be successfully applied in the BoB region?
- What adaptations, if any, are required for the approach to be effective in the BoB region?
- What level of precision can be achieved using the Reul et al. (2009) approach in the BoB region?
- Is the resulting SSS data sufficient and useful for interannual studies in the BoB region?
- Do the interannual links between SSS and other factors change when using a longer time series?

The second part of my PhD is articulated around the BoB physical oceanography, and more specifically the processes that control SSS non-seasonal variations. Previous studies suggest that the relation between the IOD and SSS variability in the BoB is not systematic. My goal is to investigate the possibility that the variability of eddies could contribute to the appearance of SSS signals that obscure or alter the IOD-induced variability.

- What are the relative contributions of non-seasonal, forced (wind, freshwater), and intrinsic (mesoscale eddies) SSS variability in the BoB region?
- How does the distribution of these contributions vary over time (seasons) and spatially in the BoB region?
- What are the possible origins and mechanisms of the identified contributions to SSS variability in the BoB region?

The following dissertation is composed of five chapters. While the current chapter serves as the general introduction, Chapter 2 will provide a detailed description of all the data utilized in this PhD thesis. Chapter 3 and Chapter 4 represent the core of this work and can be structured into two parts: a radiometric part and a physical oceanography part.

The radiometric part, presented in Chapter 3, focuses on the creation of an algorithm and methodology for retrieving SSS from AMSR-E data in the BoB. This chapter takes the form of a submitted paper<sup>1</sup>, including the validation of the newly created SSS dataset and an assessment of the impact of corrections applied throughout the study on accurate reconstruction.

The physical oceanography part, which constitutes Chapter 4, investigates the impact of internal ocean SSS variability. This chapter will present an innovative approach that uses Ocean General Circulation Model (OGCM) ensemble simulations to quantify intrinsic and forced variability.

Finally, the last Chapter 5 concludes this dissertation by summarizing the findings and offering suggestions and perspectives for future studies in this field.

---

1. As I have chosen to base this chapter on my submitted article, Section 3.2.3 about data repeats some of the content mentioned in the sections before. This is a deliberate choice, as I wanted to go further into detail and group all data I used during this PhD thesis in the same Chapter.

Throughout this study, various Sea Surface Salinity (SSS) measurements are used, obtained from different instruments and retrieval methods. In this chapter, an in-depth analysis of each measurement is provided, starting with remote measurements, followed by in-situ measurements, forced model-generated SSS and ocean reanalysis models.

## 2.1 Satellite observations

### 2.1.1 AMSR-E

The radiometer Advanced Microwave Scanning Radiometer for Earth observing system (AMSR-E) was launched into a 705 km orbit on NASA's Aqua satellite and operated from May 2002 to October 2011. Aqua follows a near-polar orbit with a sun-synchronous early afternoon crossing (1.30 A.M./1.30 P.M. for descending/ascending). The following section presents the characteristics of AMSR-E as given in Kawanishi et al. (2003), Martin (2014), Oreopoulos et al. (2023), and Wentz and Meissner (2000), and Robinson (2004).

The AMSR-E is a twelve-channel, six-frequency, total power passive-microwave radiometer system. It measures antenna brightness temperatures  $T_{BA}$  at the following frequencies: 6.925 (C-band), 10.65 (X-band), 18.7 (K-band), 23.8 (K-band), 36.5 (Ka-band), and 89.0 GHz (W-band), at both vertical and horizontal polarization in all channels. The Earth's microwave radiation is captured by a 1.6-meter diameter parabolic reflector that scans the Earth in a conical pattern at a rate of 40 r/min. This reflector maintains a constant Earth incidence angle of  $55^\circ \pm 0.3^\circ$ , the slight variation due to the slight eccentricity of the orbit and the oblateness of the earth. This is resulting in a swath width of 1445 kilometers, and the observation angle over a range of  $\pm 61^\circ$  (see Figure 2.1a). The mean spatial resolution of the individual measurements varies from 5.4 km at 89.0 GHz to 56 km at 6.9 GHz with an accuracy going from 0.3K for C-band to 1.1K for W-band measurements (for more details see Table 2.1).

Band	Frequency (GHz)	Polarization	3-dB Footprintsize (km x km)	Spatial resolution (km)	Sensitivity (K)
C	6.925	V, H	75 x 43	56	0.3
X	10.65	V, H	51 x 29	38	0.6
K	18.7	V, H	28 x 16	21	0.6
K	23.8	V, H	32 x 18	24	0.6
Ka	36.5	V, H	14 x 8	12	0.6
W	89.0	V, H	6 x 4	5.4	1.1

Table 2.1 – Polarization and spatial resolution for the 3-dB footprintsize for each frequency. The 3-dB footprintsize represents the domain where 50% of the energy is emitted.

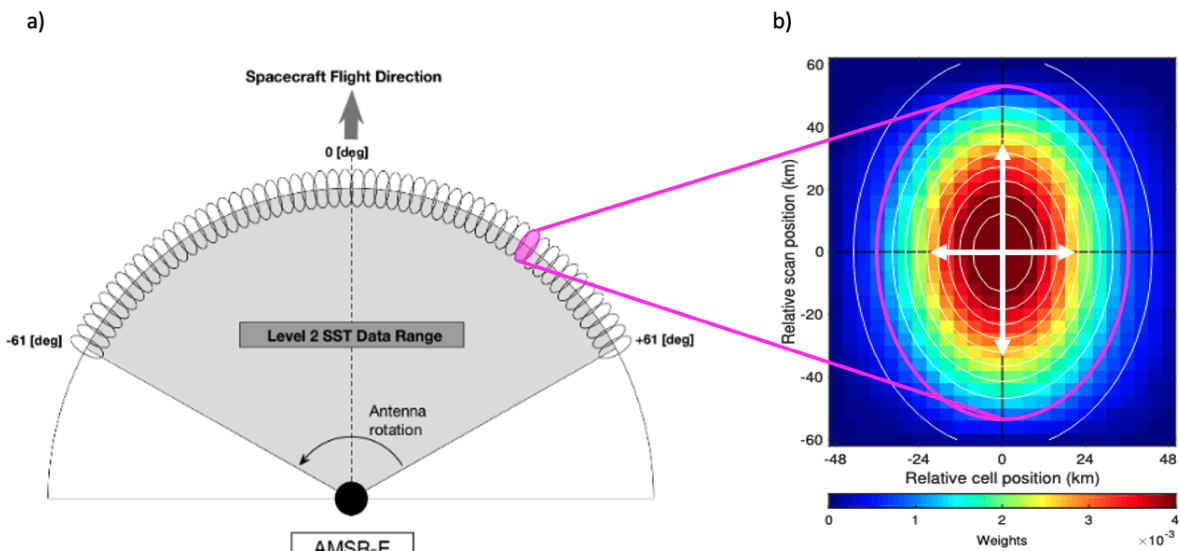


Figure 2.1 – a) The scan geometry of the AMSR-E. The ellipses schematically illustrate the AMSR-E footprint. In b) is the representation of the one of the footprints obtained by averaging the across-track footprints. Both pictures are taken from Boussidi et al., 2019. The white cross represents the size of the 3-dB Footprint which are detailed in 2.1

In this study, two different AMSR-E datasets were used and are further described below.

## **L2A Global Swath Spatially-Resampled Brightness Temperatures, Version 4 (AE\_L2A)**

This product contains daily 50-minute half-orbit swath brightness temperatures for all channels ranging from 6.9 GHz to 89 GHz. The characteristics are given in Ashcroft and Wentz (2018) and are distributed by the National Snow and Ice Data Center (NSIDC). In this version the data are resampled at varying spatial resolutions ranging from 5.4 km at 86 GHz to 56 km at the lowest frequency. By using the low resolution ( $\sim 56$  km) data associated with the 6.9 GHz (C-band) and 10.7 GHz (X-band) channel data is used, as it contains most of the SSS signal.

The radiometer noise value for a 6.9 GHz observation is 0.3 K. However, during the conical scanning of the instrument, 6.9 GHz observations are greatly over-sampled: during the scan period of 1.5 seconds, the spacecraft sub-satellite point travels only 10 km (see Figure 2.1a), signifying that Earth observations are recorded at equal intervals of 10 km along the scan, even if the footprint is 56 km. During the Level-2A processing, these adjacent observations are averaged together along scans in such a way as to reduce the Noise Equivalent Temperature Difference (NEDT) to 0.1 K (Boussidi et al., 2019). In doing this averaging, the spatial resolution is smoothed (see Figure 2.1b) and will be slightly degraded by a maximum of 2%. The resampling method is given in Wentz and Meissner (2000).

## **L2B Global Swath Ocean Products derived from Wentz Algorithm, Version 2**

During this study the Aqua L2B Global Swath Ocean Products, Version 2 distributed by the National Snow and Ice Data Center (NSIDC) is also used. This daily data set includes the Sea Surface Temperature (SST), 10 m height near-surface wind speed ( $U_{10}$ ), atmospheric columnar water vapor ( $V$ ) and atmospheric columnar cloud liquid Water ( $L$ ) retrieved from the L2A brightness temperatures based on the method given in Wentz and Meissner (2004). It uses the RTM as described in Wentz and Meissner (2000) that incorporates an atmospheric absorption model for water vapor, oxygen, liquid cloud water, and a sea surface emissivity model. The atmospheric columnar water vapor and cloud liquid water algorithms only use the 19, 23, and 37 GHz channels, the SST algorithm all channels, and the wind algorithm all but the 6.9 GHz channel.

This emissivity model is a function of the SST, salinity, wind speed, and direction. Some parts of the RTM have been updated in recent versions of the algorithm, such as the

dielectric constant of sea and cloud water Meissner and Wentz (2004), the isotropic wind induced sea surface emissivity Meissner and Wentz (2006), and the wind directional signal of the sea surface emissivity (Meissner & Wentz, 2002; Meissner & Wentz, 2006).

Note that the range of valid values for the AMSR-E L2B atmospheric columnar cloud liquid Water ( $L$ ) is -0.05 to 2.45 mm. The small unrealistic negative values are used by REMote Sensing System (REMSS) to consider the random noise in the data. Note that a SSS monthly climatology (World Ocean Atlas, Boyer et al. (2018)) is used to correct for the average SSS impact on the AMSR-E oceans brightness temperature used in the SST retrieval.

### 2.1.2 Climate Change Initiative (CCI)

SSS measurements from the first three dedicated L-band satellite sensors SMOS, Aquarius/SAC-D, and SMAP (see Figure 1.12), have been merged by the ESA’s Climate Change Initiative (CCI) project (CCI + SSS, Boutin et al., 2021a). The goal is to produce the CCI L4 SSS time series over the global ocean from January 2010 to present. This study uses the daily data from the last product release (version 3.21, <https://catalogue.ceda.ac.uk/uuid/4ce685bff631459fb2a30faa699f3fc5>), available at a spatial resolution of  $1/4^\circ \times 1/4^\circ$  ( $\sim 50\text{km} \times 50 \text{ km}$ ). These daily products are derived using a 7-day running mean temporal window. The common period between AMSR-E operation and CCI SSS product spans from January 2010 – to September 2011.

Note that during the first 18 months of this period, the CCI SSS products were generated from SMOS data alone, while the last 1.2 months are based on both SMOS and Aquarius data. The first 5 months also correspond to the SMOS mission commissioning phase during which the data quality was degraded (Kerr et al., 2010). To develop the AMSR-E SSS retrieval algorithm, therefore only the 16 month-long period from June 2010 to September 2011 were used. Akhil et al., 2020 have specifically assessed this product for the BoB, and have underlined its very good performance, even during the period where only SMOS data is used, with a  $\sim 0.85$  correlation, -0.02 pss bias and 0.55 pss rms-difference to co-located in situ data (their Fig. 16).

## 2.2 In situ observations

To have an independent validation of the AMSR-E SSS estimates in the BoB, in situ observations of salinity are used. They are composed out of a fusion from two different datasets: the ARGO floats measurements and ship-born measurements.

### 2.2.1 ARGO profiler floats

The Array for Real-time Geostrophic Oceanography (ARGO) profilers data used in this study were collected from the Ifremer Argo GDAC in November 2021 (Argo, 2022). They are autonomous drifters that provide every 5 to 10 days temperature and salinity profiles from 2000 m depth to the surface. Only the data that passed delayed mode quality controls, a quality control flag value of 1 or 2 (good or probably good data), have been selected. As a proxy of the observed SSS, the shallowest measurement of salinity (Ssurf) made on each profile between 1 and 6 m depth is taken. The majority of those measurements are between 4 and 5 meters. Akhil et al. (2016a) examined the differences between salinity at 10 m depth (S10) and salinity at 1m depth, based on mooring daily data in the BoB and found a tendency for saltier S10 at low SSS, as expected, but this effect is small (rms-difference of 0.2 pss) and should minor compared to the Ssurf estimates being shallower than 10 m depth. Finally, a binning of the Ssurf values on the same grid as AMSR-E data ( $1/4^\circ \times 1/4^\circ$ ) and on a monthly basis is applied, by taking the median of all values if two or more observations are present in the grid cells.

### 2.2.2 Ships of opportunity: bucket and XCTD's

This dataset is used in Chaitanya et al. (2014a, 2014b) and Chaitanya et al. (2015) and belongs to the Indian Ships of Opportunity Program. The Council of Scientific and Industrial Research's National Institute of Oceanography (CSIR-NIO, Goa, India) deploys expendable bathythermographs (XBTs) or eXpendable Conductivity-Temperature-Depth's (XCTD) along several shipping lanes in the seas around India. Especially two merchant ship tracks are repeatedly used: the track between Chennai and Port Blair and the track between Kolkata and Port-Blair.

During each cruise, a scientific observer onboard collects surface seawater samples with bucket samples and XCTD's profiles every 50 km - 100 km. The spatial and temporal

resolution of the bucket samples and XCTD casts along both routes varies, but stays near  $1^\circ$  and 2 months. The samples are subsequently brought back to CSIR-NIO headquarters in Goa, where the salinity will be measured using an 8400 Autosal salinometer from Guild Line, with the accuracy of  $\pm 0.002$  pss. The measurement accuracy is high, but an automatic quality control is still performed in order to remove possible human induced outliers (e.g., labeling the samples) or geophysical noise (e.g., extreme rainfall event). In order to increase the XCTD accuracy, only the 5 m record was used as SSS. The upper 4 m XCTD salinity records were discarded to account for the delay in the conductivity sensor response.

Note that an error in the SSS estimation can be introduced because the data originates at different depths in the upper 10 m of the water column. Thus, the spatial patterns of SSS variability does not alter between measurements derived from 8 m depth and 5 m depth. As this is not the case, it is therefore unlikely that the varying depth of data collection induces a significant error when creating a dataset which spans from September 2006 to January 2013 at a typically monthly frequency.

## **2.3 Merged Satellite and in situ observations**

### **- GlobeCurrent**

The GlobCurrent data repository incorporates a diverse range of currents, including the surface geostrophic current, the Ekman current at the surface and 15 meters depth, as well as the combined geostrophic and Ekman currents. These datasets are interpolated and collocated onto a standardized grid with a spatial resolution of 25 kilometers. The geostrophic current data has a temporal resolution of 1 day, while the Ekman currents and combined currents have a temporal resolution of three hours. Spanning a significant period of 23 years, from January 1993 to May 2016, this data provides valuable insights into ocean currents. Additionally, a specialized regional product for the Mediterranean Sea is available, which has been interpolated to a finer spatial resolution of  $1/8^\circ$  and a temporal resolution of three hours. Further information can be found at <http://globcurrent.ifremer.fr/products-data/data-catalogue>.

Ocean Surface Currents (OSC) encompass the coherent movement of surface ocean water, exhibiting both horizontal and vertical components within a specific depth range. These currents possess a consistent velocity and are confined by the upper boundary where the ocean interacts with the atmosphere. They persist over defined geographical

regions and time periods. The measurement and estimation of OSC, including related quantities like frontal boundaries, involve the utilization of various satellite sensors and complementary in-situ measurements.

Satellite sensors, such as altimetry (both Low Resolution Mode and Synthetic Aperture Radar Mode), gravimetry, Synthetic Aperture Radar (SAR), scatterometry, optical sensors (visible and thermal infrared), and passive microwave sensors, offer both direct and indirect estimates of OSC and derived quantities. Despite limitations like resolution, coverage, accuracy, depth integration, cloud interference, and reliance on empirical retrieval methods, these sensors enable the observation of OSC characteristics.

Moreover, in situ observations from drifting and moored buoys, coastal High-Frequency (HF) radar installations, Argo floats, gliders, and ship-based observations provide valuable sparse measurements of ocean currents, supplementing the satellite data. These in situ measurements contribute additional insights into OSC dynamics. Each measurement technique, whether satellite-based or in situ, possesses specific strengths and limitations.

To optimize the utilization of available data, systematic data merging, and sensor synergy techniques are employed, along with advanced processing tools and simulation models. By integrating the strengths of different sensing techniques, it becomes possible to alleviate deficiencies associated with individual methods, such as resolution constraints, limited coverage, and empirical retrieval methods. This approach facilitates the generation of more consistent, regular, and reliable estimates of OSC and higher-level derived products, including frontal boundaries. Consequently, the improved accuracy and consistency of satellite-based OSC products enhance their utilization and adoption in relevant applications and research fields.

## **2.4 Ocean General Circulation Model - Project IMHOTEP**

IMHOTEP is an Ocean Surface Topography Science Team (OST/ST) joined research EUMETSAT/CNES-NASA project led by Thierry Penduff (IGE, Grenoble) and William Llovel (Ifremer, LOPS, Brest), in which I was involved as a collaborator. This project spans a 4-year period between 2021 and 2024. IMHOTEP stands for IMpacts of fresh-water discHarge interannual variability on Ocean heaT-salt contents and rEgional sea level change over the altimetry Period. This initiative is aimed at exploring the effect of varying freshwater discharges on regional sea level, ocean heat, freshwater content, water

mass properties, and regional/basin-scale circulation, with a specific focus on the inter-annual to long-term trend signals in the north/tropical Atlantic ocean and Indian oceans, which receive significant amounts of continental freshwater. For this IMHOTEP will take advantage of synergies between satellite/in situ observations and simulations from the Nucleus for European Modelling of the Ocean (NEMO) ocean model.

NEMO is an Ocean General Circulation Model (OGCM, see Madec et al., 2022) adapted to regional and global ocean circulation problems. The intention of this code is to be a flexible tool for studying the ocean and its interactions with the other components of the earth climate system over a wide range of space and time scales. For the IMpacts of freshwater discHarge interannual variability on Ocean heaT-salt contents and rEgional sea level change over the altimetry Period (IMHOTEP) project, NEMO is used in its 4.0.6 version. The model solves the primitive equations on a curvilinear orthogonal grid (Arakawa C-type grid), with a second-order finite difference scheme. It assumes the Boussinesq and hydrostatic approximations, the incompressibility hypothesis, and uses a free-surface formulation. The density is computed from conservative temperature, absolute salinity, and pressure using the TEOS10 equation of state (IOC et al., 2010). IMHOTEP uses the global configuration from NEMO at a  $1/4^\circ$  eddy-permitting horizontal resolution (27 km at the equator, decreasing poleward), with 75 vertical levels. This configuration is extended to the south (eORCA025) in order to better represent the continental freshwater flows from Antarctica.

NEMO allows to take into account the Cumulative surface FreshWater Forcing (CFWF) of various origins (river discharges, melting of ice shelves, iceberg calving and drift) and the CFWF from the Greenland that considers the previous sources by including the influences of fjords (shape of the fjords, communication between the fjords and the open ocean downstream of a topographic sill that prevents deep fjord water and large icebergs from passing, and melting of icebergs in the inside of the fjord). The river discharge is distributed over a 10m thickness along the coastline (NEMO RNF modulus). The daily runoff (1979-2018) comes from outputs of the ISBA-CTRIP global land surface modeling system (Decharme et al., 2019).

The simulations are all surface-forced with JRA-55 (Kobayashi et al., 2015) and differ in the interannual or climatic character of the runoffs on its land boundaries. Three runoff areas are highlighted:

- (i) the subtropical Atlantic (Amazon, Orinoco, Niger, Congo)

- (ii) the North Indian (Ganges, Brahmaputra, Irrawaddy)
- (iii) Greenland liquid and solid runoffs

A spin-up run (used for spinning up the model to some equilibrium state) and the five simulations with a specific set of freshwater discharge forcing were carried out, creating the first set of experiments (WP1) :

- **IMHOTEP02**: period 1958-2019, Spinup run with all freshwater sources set as climatological (and SSS restoring)
- **S**: 60-year simulation with climatological runoffs, and SSS restoring to derive freshwater air-sea flux corrections for the next runs. The next runs will be initialized from this run on January 1st, 1980;
- **GAI**: 39-year (1980-2018) reference run with interannual runoffs (all rivers + Greenland),
- **AI**: same as **GAI** with climatological runoffs for Greenland melt,
- **GI**: same as **GAI** with climatological runoffs for equatorial Atlantic rivers,
- **GA**: same as **GAI** with climatological runoffs for North Indian rivers.

These simulations permits to identify the zones where the freshwater variability is the highest. However, Penduff et al. (2011) show that in a NEMO-based  $\frac{1}{4}^\circ$  global ocean/sea-ice model a strong low-frequency chaotic intrinsic variability spontaneously emerges from the ocean. Mesoscale eddies are resulting from it, which can in turn induce chaotic fluctuations at longer time and space scales, leaving random imprints on decadal regional sea level trends. After Llovel et al. (2018) these chaotic trends remains substantial in an ocean driven by the full range of atmospheric timescales but they can partially mask the regional sea level trends due to the atmospheric forcing and constitute a source of uncertainty.

In order to identify and separate this chaotic part, the IMHOTEP project performs, for each experiment, a 10-member ensemble simulation: the WP2 experiments ES, EGAI, and EAI. To create the members, a simulation will start the 1974/12/31 from a single restart file of **IMHOTEP02**. As can be seen on Figure 2.2, for one year (1975), a stochastic parameterization derived from the Oceanic Chaos: ImPacts, strUcture, predicTability (OCCIPUT) project (Bessières et al., 2017; Carret et al., 2021; Penduff et al., 2019; Penduff et al., 2018) for the Equation of state (EOS) is used, thus creating the different members, before being switched off. After five years (1979/12/31) a restart file for each member will be used for each simulation (see blue boxes on Figure 2.2). Until today, only

**ES**, and **EGAI** are available, the other simulations will follow soon. During my PhD work, the daily and monthly outputs from the **EGAI** simulations are used.

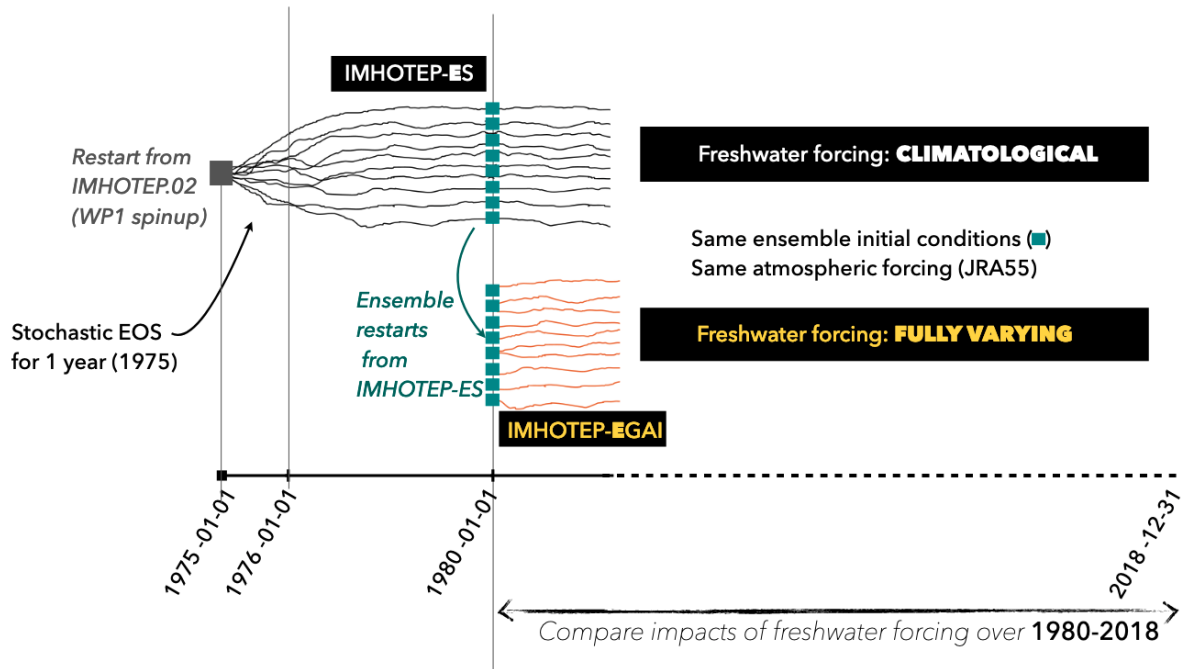


Figure 2.2 – Schematic representation and timeline of the member creation. Only represented is the creation of ES and EGAI (yellow writing and lines) simulations. The EGAI simulations restart from the 1980 Es simulations (blue boxed). The right description in the black boxes recalls the specific freshwater discharge forcing used for the specific simulation. Figure issued from a personal communication with Stephanie Leroux, Datlas, Grenoble, France.

## 2.5 Ocean Reanalysis

Global ocean reanalysis is an homogeneous 3D gridded description of the physical state of the ocean covering several decades, produced with a numerical ocean model constrained with data assimilation of satellite and in situ observations. The goal is to produce a comprehensive record of how ocean properties are changing over time, which is as close as possible to the observations (i.e., realistic) and in agreement with the model physics. The multi-model ensemble approach allows uncertainties or error bars in the ocean state to be estimated. Usually, plots are made with the average of all these products  $\pm 1$  std of the

inter-model spread as an indication of the level of agreement (or disagreement) between the following 5 reanalyses.

### **2.5.1 GLORYS2V4**

GLORYS2V4 from Mercator Ocean (Fr), ORAS5 from ECMWeF, GloSea5 from Met Office (UK), and C-GLORSv7 from CMCC (It) are four reanalyses that are used to create the ensemble Service (2019) that covers the post January 1st 1993 “altimetric era”. Each provides an independent time series of global ocean simulations 3D monthly estimates. This ensemble is the CMEMS Global Ocean Ensemble Reanalysis product performed with NEMOv3.1 ocean model in configuration ORCA025\_LIMat  $1/4^\circ$  degree resolution. No satellite retrievals of SSS were assimilated in those reanalyses, so they provide an independent estimate of SSS with respect to either the CCI or the AMSR-E derived products. For this study the monthly SSS from the CMEMS Global Ocean Ensemble Reanalysis product is used.

### **2.5.2 GLORYS12V1**

The fifth reanalysis is the monthly SSS from the higher resolution ( $1/12^\circ$ ) GLORYS12V1 reanalysis.



# RETRIEVING SEA SURFACE SALINITY FROM C-/X-BAND RADIOMETERS

---

The BoB has a very strong spatial and temporal variability in its SSS, which can reach up to 10 pss range.

Before 2010, the in situ data coverage in the BoB was insufficient to describe the basin-scale SSS variations. With the advent of L-band satellite SSS remote sensing, the interannual SSS variations in the basin have been measured since 2010. AMSR-E comprises channels in the C- and X-band, which are much less sensitive to SSS than the L-band. However, previous studies by Reul et al. (2009) and Song and Wang (2017) have shown that with a careful data processing, SSS signals can still be captured in regions with strong SSS contrasts and high SST such as the BoB. This chapter outlines the methodology used in the study in the form of an article, along with additional results obtained since the initial article submission. It also discusses the different versions of the algorithm, leading up to the final published version and their impact. In the final section of this chapter, the newly created dataset is used to conduct a case study on the influence of IOD.

## 3.1 Article Summary

In the present study, we aim at reconstructing the pre-2010 BoB SSS based on AMSR-E data. The X- and C- bands have similar sensitivities to wind and SST signals, allowing us to reduce the impact of these parameters by considering X- minus C- brightness temperature contrasts. As the X- minus C- brightness temperature sensitivity to SSS is low,  $\sim 0.05$  K/pss, a careful elimination of other residual signals is imperative.

A thorough analysis of the data showed strong  $T_B$  difference between ascending and descending passes - especially near the coast - revealing a residual land contamination. To eliminate this contamination (of ocean points) downstream of passages over land, sep-

arate land-sea masks are applied to ascending and descending passes. The ascending and descending passes are then processed independently, with distinct empirical corrections. Empirical corrections for surface wind, SST, and atmospheric water content are performed in that order based on CCI SSS and AMSR-E collocated wind, SST, and atmospheric water data over the SMOS/Aquarius-AMSR-E common period. An additional screening of the data to eliminate outliers and a  $0.75^\circ \times 0.75^\circ$  median smoothing are also found to strongly influence the final data retrieval performance.

Although our final product exhibits some fresh biases near the coasts, it is still able to compare favorably with the observed CCI climatology, displaying a correlation of 0.66 and a pss root mean square difference of 1.09 when compared to the co-located in situ surface salinity from ARGO floats. While our product may not be as accurate as L-band radiometers, the comparison still suggests that it possesses some level of capability. To evaluate the ability of our product to reconstruct interannual SSS variations prior to 2010, we compared the SSS interannual variations with those from ocean re-analyses in two hotspots for SSS interannual variability: the northern BoB and the east coast of India. The comparison with oceanic re-analyses suggests that our product has little skill over the Northern Bay of Bengal but is more favorable along the east coast of India. Our product is sometimes able to reproduce the broad CCI interannual variations in re-analyses over long periods (3-5 years), but an improved data processing may be required.

In conclusion, our findings suggest that AMSR-E contains useful information about BoB SSS interannual variability, but further improvement in data processing is still needed to fully utilize this information.

The article has been submitted at the IEEE Transactions on Geoscience and Remote Sensing Journal on the 21st of December 2022, and accepted with minor reviews on the 10th of June 2023.

## 3.2 Article: SSS estimates from AMSR-E radiometer in the Bay of Bengal: algorithm principles and limits

*Transactions on Geoscience and Remote Sensing, Manuscript ID: TGRS-2022-04859*

Marie Montero<sup>1</sup>, Nicolas Reul<sup>1</sup>, Clément de Boyer Montégut<sup>1</sup>, Jérôme Vialard<sup>2</sup>, Sidonie Brachet<sup>3</sup>, Sébastien Guimbard<sup>4</sup>, Doug Vandemark<sup>5</sup>, and Jean. Tournadre<sup>1</sup>

<sup>1</sup> Laboratoire d'Océanographie physique et spatiale, Univ Brest, Ifremer, CNRS, IRD, LOPS, F-29280 Plouzané, France

<sup>2</sup> Laboratoire d'Océanographie et du Climat: Expérimentations et Approches Numériques-Institut Pierre Simon Laplace (LOCEAN/IPSL), Sorbonne Université, CNRS, IRD, MNHN, Paris, France

<sup>3</sup> Oceanium, F-29200 Brest, France

<sup>4</sup> OceanScope: F-29280 Plouzané, France

<sup>5</sup> University of New Hampshire, OPAL, Durham, NH, 03824, USA

### 3.2.1 Abstract

The monsoon freshwater and wind forcing drive high Sea Surface Salinity (SSS) contrasts and variability (up to 10 pss range) in the Bay of Bengal (BoB), with important consequences for upper ocean mixing and air-sea interactions. Synoptic SSS maps did only become available with the advent of L-band radiometers in 2010, due to insufficient prior in situ data coverage. Here, we build tools aiming at reconstructing the monthly BoB SSS at  $\frac{1}{4}^\circ$  resolution since 2002 from Advanced Microwave Scanning Radiometer for Earth observing system (AMSR-E) radiometer data. The C-band low sensitivity to SSS requires a very careful processing. Taking the X- minus C- bands signals reduce the impact of Sea Surface Temperature (SST) and wind on brightness temperatures. It was however further necessary to train the algorithm with SSS data from L-Band radiometers to remove residual surface winds, SST, and atmospheric water contents signals. We also found that a separate treatment of the ascending and descending passes was necessary, as well as a proper data screening to minimize contamination by land signals. The resulting SSS product reproduces the broad BoB climatological SSS, and has a 0.66 correlation,

1.08 pss rms-difference to co-located in situ surface salinity from Argo floats. Comparisons with ocean re-analyses in two SSS interannual variability hotspots indicate poor performance in the Northern BoB, but some skill along the East Coast of India. Our results provide a proof of concept for reconstructing the BoB SSS from AMSR-E data, and we discuss possible future improvements of the data processing to further reduce the impact of spurious signals.

**Index terms** - AMSR-E, Bay of Bengal, ESA Climate Change Initiative program, Reconstruction, Sea Surface Salinity, Radiometers

### 3.2.2 Introduction

Salinity influences seawater density and hence the ocean vertical stability, horizontal pressure gradients and ocean currents. Sea Surface Salinity (SSS), in particular, is considered a key ocean and climate variable due to its influence on the global thermohaline circulation and climate variability, and its usefulness to monitor changes in the hydrological cycle (Boutin et al., 2021a). The Bay of Bengal (BoB) is one of the tropical hotspots where SSS is both highly variable spatially and temporally (seasonal cycle of up to 6 pss amplitude in the Northern BoB, e.g. Chaitanya et al., 2014b). The monsoon indeed results in a strong river runoff (most notably the Ganga and Brahmaputra (Papa et al., 2012), Irrawaddy in the Northern BoB) and a strong rainfall seasonal cycle, as well as a complete annual reversal of the Northern Indian Ocean circulation (Schott & McCreary, 2001). These two effects combine in creating strong salinity contrasts after southwest monsoon, with Northern BoB SSS up to 10 pss fresher than that in the southern BoB Akhil et al. (2020). The East Indian Coastal Current (EICC) carries northern BoB freshwater southward, creating a low-salinity tongue along the coast of India in Boreal Fall and Winter (Akhil et al., 2014; Chaitanya et al., 2014b; Chaitanya et al., 2021). The Indian Ocean Dipole (IOD), an ocean-atmosphere climate mode similar to El Niño that develops in the Indian Ocean, further generates a large SSS interannual variability in the equatorial Indian Ocean (Durand et al., 2013) and Bay of Bengal (Akhil et al., 2016b; Akhil et al., 2020; Fournier et al., 2017), in particular along the East coast of India. Finally, energetic eddies (Chelton et al., 2011) also modulate the BoB SSS at shorter timescales (Fournier et al., 2017). There are thus large SSS contrasts and variability in the BoB at sub-seasonal, seasonal, and interannual timescales.

This SSS variability is thought to have strong consequences, because low SSS is associated with a strong density stratification (de Boyer Montégut et al., 2007), which limits the wind-induced vertical mixing in the upper ocean. For instance, low SSS reduces vertical mixing of heat below BoB Tropical Cyclone (TC), therefore reducing the oceanic cooling they induce (Neetu et al., 2012) and hence the negative feedback of this cooling on the cyclones (Neetu et al., 2019). TCs can hence reach larger intensities when they develop over low SSS; this is particularly important when knowing that BoB TCs (only 5% of global TC count) represent 80% of the worldwide TC-induced fatalities. The effect of SSS on vertical heat exchanges is also thought to influence the BoB climatological rainfall through its effect on climatological Sea Surface Temperature (SST) de Boyer Montégut et al. (2007) and Shenoi et al. (2002, e.g.), although coupled model experiments suggest this effect is weak (Krishnamohan et al., 2019; Seo et al., 2009). Finally, low SSS in the BoB are also believed to limit biological productivity by reducing the upward vertical flux of nutrients to the mixed layer (Prasanna Kumar et al., 2002). BoB SSS is thus not only very contrasted and variable, but it is thought to have significant impacts on climate and productivity, making the observability of basin-scale SSS a must in this basin.

Before 2010, in situ measurements were the only source of SSS estimates in the BoB. Argo profiler floats data (Riser et al., 2016) is now the main source of basin-scale salinity data, and Argo data were extremely sparse in the BoB before 2002 Beal et al. (2020). The accumulation of Argo and previous hydrological data over time allows depicting the seasonal variations of SSS in the BoB quite well. On the other hand, the Argo network coverage was insufficient to produce basin-scale seasonal SSS maps for the 2009 and 2010 years (Fig. 5 of Akhil et al., 2016b), and hence unable to describe the SSS interannual variations before the advent of SSS remote sensing. Satellite SSS observation only started with ESA's SMOS (2010-now), followed by NASA's Aquarius (2011-2015) and SMAP (2015-now) missions. These three satellites are all equipped with microwave radiometers operated at L-band (central frequency  $\sim 1.4$  GHz), a frequency for which the sensitivity of the sea surface emissivity to SSS is highest Song and Wang (2017). The SMOS SSS retrievals in the BoB were initially highly contaminated by radio-frequency interferences from illegal transmitters and biased because of land contamination (Akhil et al., 2016b). Improved quality control and bias corrections later allowed similar performances to Aquarius and SMAP, with correlations and rms-differences to co-located in situ data of 0.8 and 0.6 pss, respectively (Akhil et al., 2020). Data from the SMOS, Aquarius, and SMAP radiometers then allowed to describe the interannual SSS signals associated with

the remote influence of the IOD in the BoB, including clear SSS variations along the east coast of India (Akhil et al., 2020; Fournier et al., 2017; Priyanka et al., 2022), as well as sub-seasonal SSS signals associated with meso-scale eddies (Fournier et al., 2017). Yet, the SSS satellite record (13 years, 2010-2022) is too short to confidently describe interannual SSS signals (Akhil et al., 2020), or SSS variability at longer timescales, such as the expected long-term BoB freshening in response to the hydrological cycle intensification due to anthropogenic forcing (e.g. Durack et al. (2012)). This is mainly because of the sparsity of in situ observations prior the full deployment of the Argo float network and the relatively recent L-band satellite radiometer era.

Advanced Microwave Scanning Radiometer for Earth observing system (AMSR-E) onboard Aqua satellite (Kawanishi et al., 2003) has microwave channels spanning the 6.9 - 89.0 GHz range (including the 6.9 (C- band) and 10.7 GHz (X-band) frequencies). AMSR-E was initially designed for monitoring atmospheric water, SST, and surface winds over the ocean. However, the C- and X-band channels also display some sensitivity to SSS at high SST, although much weaker than that for the L-band. At the AMSR-E incidence angle of  $55^\circ$  and an SST of  $30^\circ\text{C}$ , the perfectly flat sea surface brightness temperature sensitivity to SSS in vertical polarization is  $\sim 0.05$  K/pss for the C-band and less than 0.01 K/pss for the X- band, against 0.9 K/pss for the L-Band (Reul et al., 2009). Reul et al. (2009) noted that C- and X- bands have a roughly similar sensitivity to SST and surface roughness. As a result, the X- minus C-band emissivity contrast is much less affected by SST and surface roughness, while conserving the C-band sensitivity to SSS ( $\sim 0.05$  K/pss). They used that approach to estimate SSS in the Amazon River plume region. This is possible in areas with high SST (which maximize the sensitivity to SSS) and strong salinity contrasts (because the low sensitivity results in a poor accuracy). Such a principle has recently been applied to retrieve SSS from HY-2A data for the freshwater runoff near the Yangtze Delta (Song & Wang, 2017). The BoB also displays high SST (with an average SST over  $26.5^\circ\text{C}$  all year long Shenoi et al. (2002)) and very strong salinity contrasts. In this paper, we investigate whether the concept of Reul et al. (2009) can be applied to AMSR-E C/X bands data to reconstruct BoB SSS over the 2002-2011 period. Combined with the SSS time series from L-band radiometers, this would yield an almost 20-year-long satellite SSS record in the BoB. The WindSat radiometer performed C- and X-band brightness temperature measurements since 2003 Gaiser et al. (2004) but they are not publicly available. HY-2A was only launched in 2011, a period for which more accurate L-band retrievals are available. These two datasets were hence not considered

in the present study.

Herein we discuss the development of a new algorithm based on Reul et al. (2009) to retrieve SSS from AMSR-E data over the BoB. This is to our knowledge the first attempt to apply such a strategy over this region. Our goal is to explore the applicability of this algorithm to the BoB and potential limitations induced by land contamination in the large land-enclosed BoB basin. In section II, we describe the datasets used in this study, especially the input data used by the algorithm, and the L-band-derived SSS data used for its training. The algorithm based on the Radiative Transfer Model (RTM) of Meissner and Wentz (2012) (hereafter MW12) is described in detail in section III. This section also describes the necessary empirical adjustments to the RTM and the empirical inversion model linking the X- minus C-band emissivity contrast to SSS. Those were specifically determined for the BoB conditions using co-located oceans brightness temperature ( $T_B$ ), surface wind, SST, water vapor and cloud liquid water data from AMSR-E, as well as SSS data from SMOS and Aquarius/SAC-D, all collected during the common period of operation of these satellites (June 2010-September 2011). This algorithm is then used to produce monthly-averaged SSS fields for the BoB, at a spatial resolution of  $1/4^\circ \times 1/4^\circ$  from May 2002 to Sep 2011. Key features of the retrieved SSS fields, along with a validation against in situ co-located observations and ocean re-analyses are presented in section IV. A synthesis of the AMSR-E SSS data quality in the BoB, and a discussion of future algorithm improvements are provided in a section V.

### 3.2.3 Data

#### 3.2.3.1 AMSR-E data

The Aqua satellite operated from May 2002 to October 2011 and carried AMSR-E, a twelve-channel, six-frequency, total power passive-microwave radiometer system. AMSR-E measures brightness temperature measured at antenna level ( $T_A$ ) at the following frequencies: 6.925 (C-band), 10.65 (X-band), 18.7 (K-band), 23.8 (K-band), 36.5 (Ka-band), and 89.0 GHz (W-band). Vertically- and horizontally polarized measurements are collected for all channels. The Earth-emitted microwave radiation is collected by an offset 1.6 m diameter parabolic reflector that scans across the Earth along an imaginary conical surface, maintaining a constant Earth incidence angle of  $55^\circ$ . The spatial resolution of the individual measurements varies from 5.4 km at 89.0 GHz to 56 km at 6.9 GHz. Below, we describe the AMSR-E datasets used in our algorithm.

- (i) We use the AMSR-E Version 4 Level-2A Global Swath Spatially Resampled Brightness Temperatures product (AE\_L2A) (Ashcroft & Wentz, 2018) distributed by the National Snow and Ice Data Center (NSIDC) ([https://nsidc.org/data/AE\\_L2A](https://nsidc.org/data/AE_L2A)). It contains daily 50-minute half-orbit swath brightness temperatures for all channels ranging from 6.9 GHz through 89 GHz. Data are re-sampled at varying spatial resolutions ranging from 5.4 km at 86 GHz to 56 km at the lowest frequency. We use the low resolution ( 56 km) data associated with the 6.9 GHz (C-band) and 10.7 GHz (X-band) channel data, which contain most of the SSS signal. The radiometer noise value for one 6.9 GHz observation is 0.3 K. However, during the conical scanning of the instrument, 6.9 GHz observations are greatly over-sampled: during the scan period of 1.5 seconds, the spacecraft sub-satellite point travels only 10 km, signifying that Earth observations are recorded at equal intervals of 10 km along the scan, even if the footprint is 56 km. During the Level-2A processing, these adjacent observations are averaged together along scans in such a way as to reduce the Noise Equivalent Temperature Difference (NEDT) to 0.1 K. In doing this averaging, the spatial resolution is smoothed and will be slightly degraded by a maximum of 2%. The re-sampling method is given in Wentz and Meissner (2000).
- (ii) The study also uses the AMSR-E/Aqua L2B Global Swath Ocean Products, Version 2 distributed by the National Snow and Ice Data Center (NSIDC) at [https://nsidc.org/data/ae\\_ocean/versions/2](https://nsidc.org/data/ae_ocean/versions/2) (**wentz\_\_\_\_frank\_amsr-eaqua\_2004**). This daily data set includes the Sea Surface Temperature (SST), 10 m height 10 m height near-surface wind speed ( $U_{10}$ ), atmospheric columnar water vapor ( $V$ ) and atmospheric columnar cloud liquid Water ( $L$ ) retrieved from the L2A brightness temperatures based on the method given in **wentz\_\_\_\_frank\_amsr-eaqua\_2004empty citation**. The atmospheric columnar water vapor and cloud liquid water algorithms only use the 19, 23, and 37 GHz channels, the SST algorithm all channels, and the wind algorithm all but the 6.9 GHz channel. Note that the range of valid values for the AMSR-E L2B atmospheric columnar cloud liquid Water  $L$  is -0.05 to 2.45 mm. The small negative value is used by REMote Sensing System (REMSS) to consider the random noise in the data. Note that an SSS monthly climatology (World Ocean Atlas, Boyer et al. (2018)) is used to correct for the average SSS impact on the AMSR-E brightness temperature used in the SST retrieval.

### 3.2.3.2 Sea Surface Salinity European Space Agency (ESA) Climate Change Initiative (CCI) Product

SSS measurements from the first three dedicated L-band satellite sensors SMOS, Aquarius SAC/D, and SMAP, have been merged by the Climate Change Initiative Salinity project (CCI + SSS, Boutin et al., 2021a) to produce the Climate Change Initiative (CCI) L4 SSS time series over the global ocean from January 2010 to end of 2020. We used the daily data from the last product release (version 3.21, <https://catalogue.ceda.ac.uk/uuid/7da8723b16e94771be1a2717d8a6e2fe>), available at a spatial resolution of  $1/4^\circ \times 1/4^\circ$ . These daily products are derived using a 7-day running mean temporal window. The common period between AMSR-E operation and CCI SSS product spans from January 2010 – to September 2011. Note that during the first 18 months of this period, the CCI SSS products are generated from SMOS data alone, while the last 3 months are based on both SMOS and Aquarius data. The first 5 months also correspond to the SMOS mission commissioning phase during which the data quality was degraded (Kerr et al., 2010). To develop the AMSR-E SSSretrieval algorithm, we therefore only used the 16 month-long period from June 2010 to September 2011. Akhil et al. (2020) have specifically assessed this product for the BoB, and have underlined its very good performance, even during the period where only SMOS data is used, with a  $\sim 0.85$  correlation,  $-0.02$  pss bias and  $0.55$  pss rms-difference to co-located in situ data (their Fig. 16).

### 3.2.3.3 In Situ Sea Surface Salinity data

To have an independent validation of our AMSR-E SSS estimates in the BoB, we use in situ observations of salinity based on ARGO profiling floats measurements. The ARGO data used in this study were collected from the Ifremer Argo GDAC in November 2021 (Argo, 2022). We selected only the data that have passed the delayed mode quality controls, with quality control flag value of 1 or 2 (good or probably good data). As a proxy of the observed SSS, we took the shallowest measurement of salinity (Ssurf) made on each profile between 1m and 6m depth. The majority of those measurements are between 4 and 5 meters. Akhil et al. (2016a) examined the differences between salinity at 10m depth (S10) and salinity at 1m depth, based on mooring daily data in the BoB and found a tendency for saltier S10 at low SSS, as expected, but this effect is small (rms difference of  $0.2$  pss) and should be minored by our Ssurf estimates being shallower than 10 m depth. Finally, a binning of the Ssurf values on the same grid as AMSR-E data

( $1/4^\circ \times 1/4^\circ$ ) and on a monthly basis is applied, by taking the median of all values if two or more observations are present in the grid cells.

### 3.2.3.4 Ocean re-analyses

Global ocean reanalysis are homogeneous 3D gridded descriptions of the physical state of the ocean covering several decades, produced with a numerical ocean model constrained with data assimilation of satellite and in situ observations. These reanalysis are built to be as close as possible to the observations (i.e. realistic) and in agreement with the model physics. The multi-model ensemble approach allows uncertainties or error bars in the ocean state to be estimated.

i) GLORYS2V4 from Mercator Ocean (Fr), ORAS5 from ECMWF, GloSea5 from Met Office (UK), and C-GLORSv7 from CMCC (It) are four reanalysis that are used to create the ensemble Service (2019) that covers the post January 1st 1993 “altimetric era”. Each provides an independent time series of global ocean simulations 3D monthly estimates. This ensemble is the CMEMS Global Ocean Ensemble Reanalysis product at  $1/4$  degree resolution. No satellite retrievals of SSS were assimilated in those re-analyses, so they provide an independent estimate of SSS with respect to either the CCI or our AMSR-E derived products. We use monthly SSS from the CMEMS Global Ocean Ensemble Reanalysis product.

ii) We also use monthly SSS from the higher-resolution ( $1/12^\circ$ ) GLORYS12V1 reanalysis.

We will usually plot the average of all these products  $\pm 1$  std of the inter-model spread as an indication of the level of agreement (or disagreement) between those 5 re-analyses.

## 3.2.4 AMSR-E SSS Retrieval Algorithm

### 3.2.4.1 Algorithm Principles

As described in Reul et al. (2009), the SSS retrieval algorithm consists in first estimating the V-polarized surface emissivity at both C- and X-band frequency from the Top Of Atmosphere (TOA) AMSR-E Level-2A oceans brightness temperature product (AE\_L2A) and from the retrieved AMSR-E Level-2B Sea Surface Temperature (SST), 10 m height near-surface wind speed ( $U_{10}$ ), atmospheric columnar water vapor ( $V$ ), and

atmospheric columnar cloud liquid Water ( $L$ ) data. As described further, we use the MW12's RTM model for that purpose. Then, we estimate the perfectly flat sea surface emissivity contrast ( $\Delta e$ ) between both frequencies. Given a Geophysical Model Function that relates SSS, SST and perfectly flat sea surface emissivity contrast, one can finally retrieve SSS using

$$SSS = GMF(\Delta e, SST). \quad (3.1)$$

As shown in Reul et al. (2009), one can express the total sea surface emissivity as observed by AMSR-E in vertical polarization and frequency  $f$  as:

$$\begin{aligned} E_{V,f}^{AMSR-E} &= e_{surf,v}^{flat}(\theta, SSS, SST, f) + e_{surf,v}^{rough}(\theta, \varphi, U_{10}, f) \\ &= 1 - \frac{T_{B,v,f} - T_{BU,f} - \tau_f SST}{\tau_f (1 + \Omega_V(\tau, U_{10}, f)) (1 - \tau_f) (T_{BD,f} - T_{cold}) + T_{cold} - SST} \end{aligned} \quad (3.2)$$

where:

- $e_{surf,v}^{flat}$  is the perfectly flat sea surface emissivity,
- $e_{surf,v}^{rough}$  is the roughness-induced emissivity,
- $\theta$  is the radiometer earth incidence angle,
- SSS is the sea surface salinity,
- SST is the sea surface temperature,
- $\varphi$  is the relative azimuth between the radiometer look direction and the wind direction,
- $U_{10}$  is the 10-meter height surface wind speed,
- $T_{B,v,f}$  is the Top Of Atmosphere (TOA) AMSR-E Level-2A oceans brightness temperature ( $T_B$ ) product (AE\_L2A),
- $T_{BU,f}$  is the upwelling brightness temperature,
- $\tau_f$  is the atmospheric opacity,
- $\Omega_V(\tau, U_{10}, f)$  is a term to evaluate the atmospheric and cosmic radiation scattered by the sea surface,
- $\tau$  is the atmospheric transmittance,
- $T_{BD,f}$  is the downwelling brightness temperature,

- $T_{cold} = 2.7$  K is the cosmic microwave background temperature.

The terms  $T_{BU,f}$ ,  $T_{BD,f}$ ,  $\tau_f$ , and  $\Omega_V$ , can all be estimated using the RTM of MW12 applied to AMSR-E Level-2B Sea Surface Temperature, 10 m height near-surface wind speed ( $U_{10}$ ), atmospheric columnar water vapor ( $V$ ), and atmospheric columnar cloud liquid Water ( $L$ ) data. Given a model for the roughness-induced emissivity ( $e_{surf,v}^{rough}(\theta, \varphi, U_{10}, f)$ ), one can further estimate the emissivity of the perfectly flat sea surface, which in theory shall only depends on SSS and SST for a given frequency and incidence angle:

$$e_{surf,p}^{flat}(\theta, f, SSS, SST) = 1 - \frac{T_{B,V,f} - T_{BU,f} - \tau_f SST}{\tau_f (1 + \Omega_V(\tau, U_{10}, f)) (1 - \tau_f) (T_{BD,f} - T_{cold}) + T_{cold} - SST} - e_{surf,v}^{rough}(\theta, \varphi, U_{10}, f) \quad (3.3)$$

At an incidence angle  $\theta$ , polarization p (horizontal or vertical), and electromagnetic frequency ( $f$ ), it is also given by Peake (1959):

$$e_{surf,p}^{flat}(\theta, f, SSS, SST) = \left[ 1 - \left| r_{surf,p}^{flat}(\theta, f, SSS, SST) \right|^2 \right] \quad (3.4)$$

where  $e_{surf,p}^{flat}$  and  $r_{surf,p}^{flat}$  are the flat sea surface emissivity and Fresnel reflection coefficient at polarization p, respectively. The flat sea surface emissivity depends on SSS and SST through the dielectric constant of seawater ( $\epsilon_s$ ). While MW12's model for dielectric constant of seawater has been developed for frequencies between 6 and 90 GHz, it is also applicable and widely used to evaluate dielectric constant of seawater for a frequency of 1.4 GHz (L-band, Meissner et al., 2018). According to MW12's model for dielectric constant of seawater, and for  $\overline{SST} \approx 29$  °C and  $\overline{SSS} \approx 34$  pss (the average conditions encountered at the surface of the BoB, see Figure 3.1), the sensitivity of  $T_v = SST \cdot e_{surf,p}^{flat}(\theta, f, SSS, SST)$  to SSS in vertical polarization and at  $\theta=55^\circ$  drops from  $\partial T_v / \partial SSS \sim 0.9$  K/pss at 1.4 GHz (L-band) to  $\sim 0.056$  K/pss at 6.9 GHz (C-band).  $T_v$  at 10.7 GHz (X-band) is almost insensitive to salinity SSS, with maximum sensitivity  $\partial T_v / \partial SSS \sim 0.01$  K/pss.

The sensitivity of the sea surface brightness temperature to SSS ( $\partial T_h^\theta / \partial SSS$ ) in horizontal polarization and at  $\theta=55^\circ$  is about twice smaller than that at vertical polarization for the two lowest AMSR-E frequencies: we therefore only consider the v-polarized AMSR-E

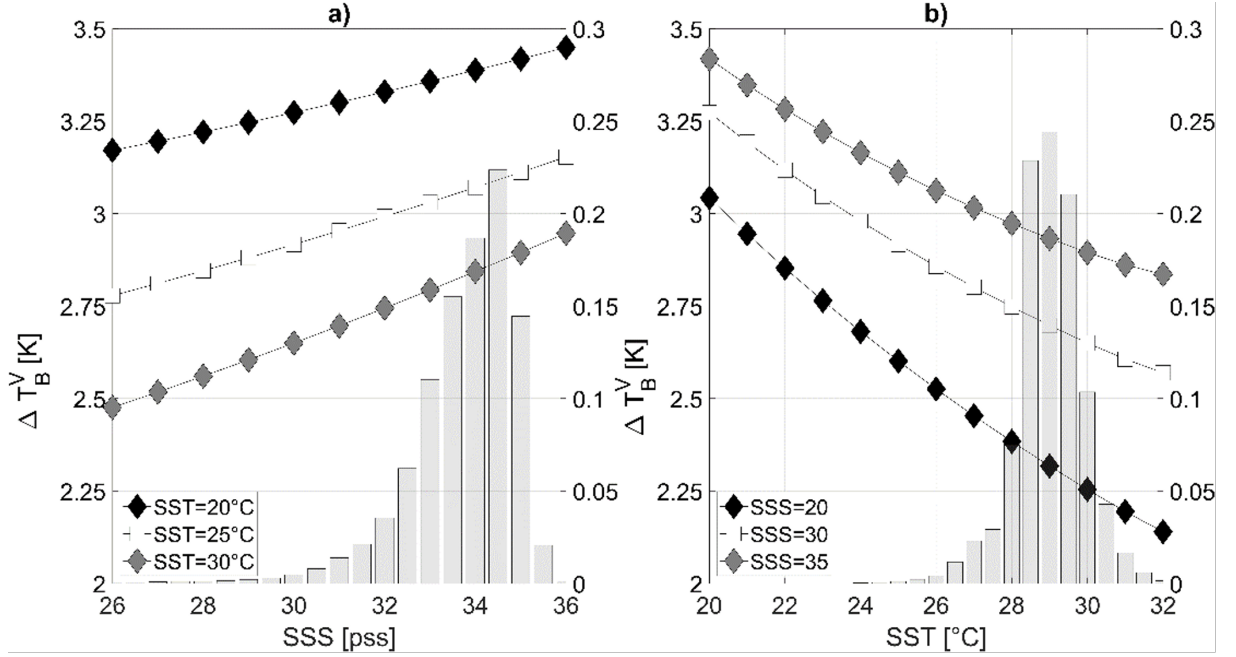


Figure 3.1 – Perfectly Flat Ocean surface vertically polarized brightness temperature contrast  $\Delta T_B = T_{10.7} - T_{6.9}$  between frequencies of 10.7 (X-band) GHz and 6.9 (C-band) GHz, as predicted by MW12’s seawater dielectric constant model and at an incidence angle  $\theta=55^\circ$  (left y-axes).  $\Delta T_B$  is shown as a function of SSS for three selected SST values (a), and as a function of SST for three typical SSS values (b). The probability distribution function (right y-axes) of SSS (a) and SST (b) within the BoB from CCI products are shown as gray-filled histograms in both panels.

brightness temperature data as inputs to the SSS retrieval algorithm. In addition, the sensitivity of  $T_v$  to SST changes ( $\partial\Delta T_v/\partial SST$ ) increases from 0.1 K/°C at 1.4 GHz to  $\sim 0.7$  K/°C, and 0.6 K/°C, at both 6.9 GHz and 10.7 GHz, respectively. Retrieving SSS from C-band radiometer data is therefore very challenging and demands (i) extremely accurate corrections for the different contributions to the signal measured by the radiometer at the top of the atmosphere, and (ii) precise and representative estimation of SST within the AMSR-E low spatial resolution ( $\sim 56$  km) footprint.

Capitalizing on the fact that C- and X-band have very similar sensitivity to SST (as demonstrated in Reul et al. (2009) and illustrated in Figure 3.1), the effect of SST can be strongly reduced by considering the surface  $T_v$  contrast between the X- and C-band channels, namely:  $\Delta T_v = T_{10.7} - T_{6.9}$ . For average conditions within the BoB, the sensitivity of  $\Delta T_v$  to SST (linear approximation) drops to  $\partial\Delta T_v/\partial SSS \cong -0.04$  K/°C

(Figure 3.1b), while the sensitivity to SSS remains  $\partial\Delta T_v/\partial SSS \cong +0.05$  K/pss (Figure 3.1a). Using  $\Delta T_v$  hence strongly minimizes the impact of SST variation on the signal down to a level comparable with SSS impacts.

Given these considerations, the main steps of the present AMSR-E SSS retrieval algorithm is summarized as follows (Figure 3.2):

- (i) AMSR-E Level-2A swath data are extracted within the Bay of Bengal domain [77°E-100°E; 5°N-25°N]. The TOA brightness temperature can reach much higher value than normally expected over the ocean in some specific environmental conditions. These environmental factors include brightness temperature contamination near the land-sea transition, as well as impacts of rain, high wind speeds, sun glint, and Radio Frequency Interference (RFI). Some of these factors are quasi-stable (land), or at least somewhat consistent (rain, winds). Sun glint effects can vary with solar activity, especially solar flare events, and with sea surface roughness. RFI is a continuously evolving source of errors. These specific conditions can be best filtered by applying an advanced quality check according to the AMSR-E L2A and L2B quality flags. We filter out the L2A data if the angle between the spacecraft-viewing vector and the sun specular reflection vector is smaller than 20° to remove data that can be contaminated by sunglint. We only keep data for which the fraction of land in the Field Of View (FOV) is less than 0.2%. In addition, we only select the best quality data using Level-2A and Level-2B summary quality flags: (i.e. Channel\_Quality\_Flag\_6\_to\_52\_bit0=0, rain\_flag==0),
- (ii) each AMSR-E Level-2A Top Of Atmosphere brightness temperature data is then corrected for atmospheric and extraterrestrial contributions. These corrections are estimated using MW12's RTM as described in Wentz and Meissner (2000) and the AMSR-E Level-2B atmospheric columnar water vapor  $V$ , atmospheric columnar cloud liquid Water  $L$ , 10 m height near-surface wind speed  $U_{10}$  and SST to find the atmospheric and extraterrestrial parameters of the RTM terms.
- (iii) After applying these corrections, we estimate the v-polarized total sea surface emissivity  $e_{surf, v}^{total, AMSR-E}$  for the C- and X-band frequencies using (Eq. 3.2),
- (iv) the swath  $\Delta e_v^{AMSR-E}$  data are separated into ascending and descending passes and gridded daily on a  $1/4^\circ \times 1/4^\circ$  regular grid. The data were then filtered for remaining outliers using a temporal median absolute deviation filter (Leys et al., 2013) determined for each node of the grid within the BoB (see section 3.2.4.3),

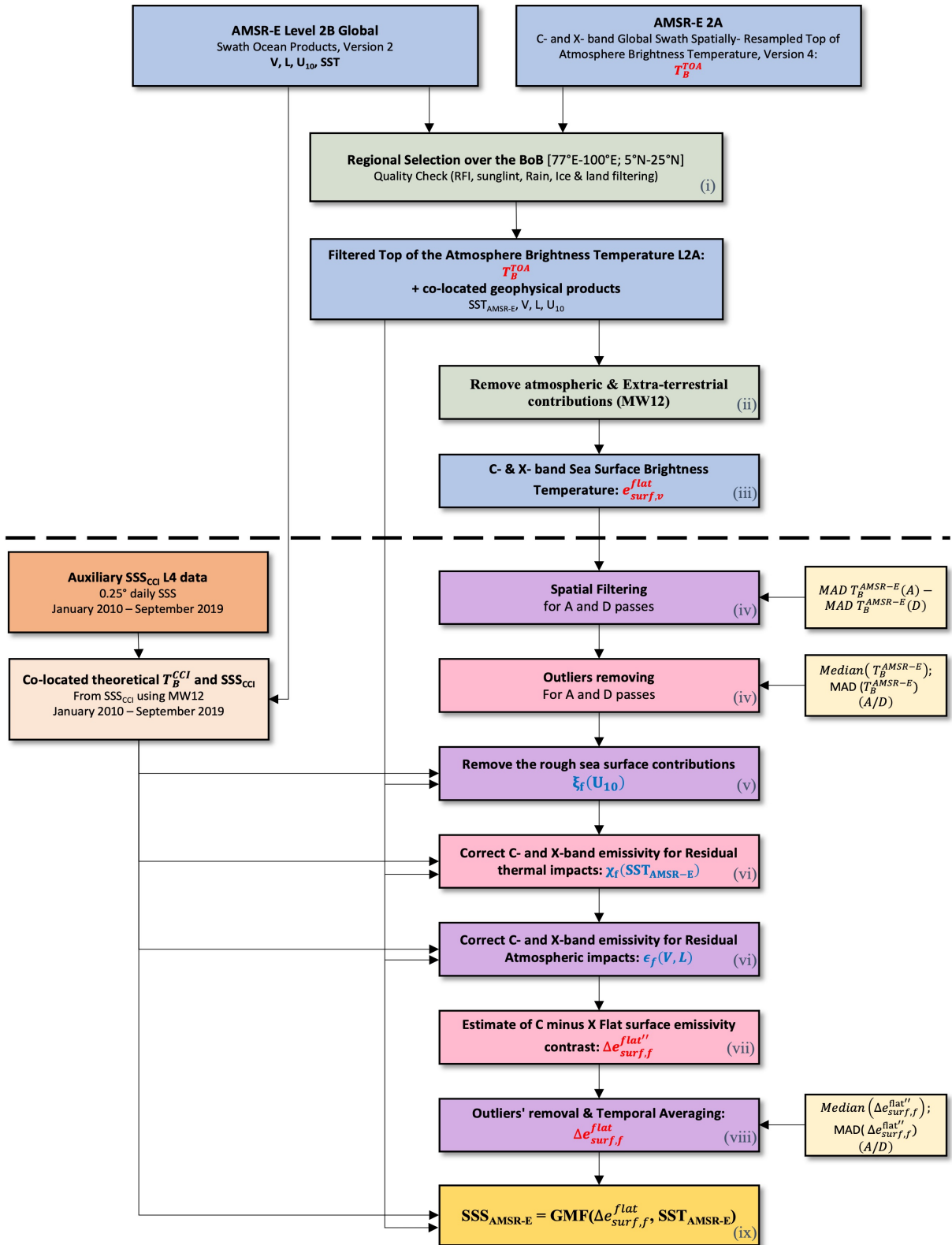


Figure 3.2 – Caption on the next page

- (v) the isotropic roughness impacts are then subtracted to estimate the flat surface emission at each frequency,  $e_{surf,v}^{flat}$  using (Eq. 3.3). This roughness correction is based on an empirical model specifically derived for the BoB (see section 3.2.4.4.1) as a function of AMSR-E Level-2B  $U_{10}$  data.
- (vi) Additional empirical corrections to the MW12 RTM model were determined specifically for the BoB based on the AMSR-E and CCI SSS data common period (see section 3.2.4.4.2 and 3.2.4.4.3). These additional corrections are applied to the  $e_{surf,v}^{flat}$  first as a function of SST, and then as a function of AMSR-E L2B atmospheric columnar cloud liquid Water  $L$ , and atmospheric columnar water vapor  $V$ .
- (vii) After applying these additional empirical data corrections, we compute the difference between the X- and C- band perfectly flat sea surface emissivity:

$$\Delta e_v^{AMSR-E}(SSS, SST) = e_{surf,v,X}^{flat}(SSS, SST) - e_{surf,v,C}^{flat}(SSS, SST) \quad (3.5)$$

- (viii) Additional temporal and spatial filtering of  $\Delta e_v^{AMSR-E}(SSS, SST)$  based on the full AMSR-E archive time series (see section 3.2.4.5).
- (ix) AMSR-E Level-2A brightness temperature data NEDT is 0.1 K and the sensitivity of  $T_V^{AMSR-E}$  to SSS is only reaching 0.05 K/pss: large uncertainties (order of several pss) are therefore expected in the instantaneous SSS retrievals from AMSR-E swath data. Thanks to the quasi-linear dependencies of  $\Delta e_v^{AMSR-E}$  to both SSS and SST in the BoB conditions (Figure 3.1a), the noise level prior SSS retrieval can significantly reduce by monthly averaging  $\Delta e_v^{AMSR-E}$  and the SST swath data. The monthly averaged SSS are then retrieved on a  $1/4^\circ \times 1/4^\circ$  resolution regular lat/lon grid from the monthly averaged SST and  $\Delta e_v^{AMSR-E}$  quantities merged for ascending and descending passes. An empirical Geophysical Model Function (GMF)  $SSS = GMF(SST_{CCI}, \Delta e_v^{AMSR-E})$  is used for the retrieval (see Section 3.2.4.6).

---

Figure 3.2 Schematic flow diagram of the AMSR-E Sea Surface Salinity retrieval algorithm developed for the Bay of Bengal. The (i, ii, iii. . .) labels on each box make reference to the corresponding subsection headings in section 3.2.4. The dashed line split the algorithm into MW12 processing (upper part) and the present paper developments (lower part). The ancillary Median Absolute Deviation inputs (pale yellow panels) are evaluated over 2002-2011 for the variables at each processing level.

### 3.2.4.2 Algorithm Refinements for the BoB Case

The basis of MW12’s wind-induced emissivity model is brightness temperature measurements from the spaceborne microwave radiometer WindSat, and SSM/I, which were collocated with independent measurements of surface wind speeds and directions at global scale (Meissner & Wentz, 2012). To refine the previously described AMSR-E SSS retrieval algorithm for the specific BoB conditions, we used a 16 month-long common period (June 2010 to September 2011) between AMSR-E and the CCI (L-band based) SSS data to estimate empirical adjustments to the MW12’s RTM. Note that these additional adjustments are specific to the BoB region, the period chosen (2010-2011) but also to the auxiliary data we used to characterize the thermohaline conditions at the sea surface within AMSR-E footprint (here the CCI-SSS and AMSR-E SST products). These additional adjustments includes: land contamination filtering, empirical roughness correction, SST bias correction and atmospheric columnar water vapor/cloud liquid water correction adjustments.

#### 3.2.4.2.1 Choice for an SST product: diurnal cycle impact

An SSS monthly climatology (World Ocean Atlas, Boyer et al., 2018) is used to correct for the average SSS impact on the AMSR-E brightness temperature used in the SST retrieval. We hence initially wanted to use a SST product that does not use SSS as an input, and turn to the CCI Infrared based daily composite SST products (Merchant et al., 2014). This however yield degraded SSS products. AMSR-E ascending ( $\sim 01:30$  pm local time) and descending (at  $\sim 01:30$  am) tracks are indeed 12 hours apart, implying that there can be significant differences in the SST due to the diurnal cycle. Neglecting the diurnal SST cycle in the BoB induced large errors on the retrieved SSS (not shown) and we therefore use here the collocated AMSR-E SST data for our algorithm.

#### 3.2.4.3 Brightness temperature contamination by land

The BoB is a semi-enclosed basin, and we can expect strong contamination by land signals: we thus designed a specific approach to eliminate heavily contaminated data with respect the amplitude of the signal we aim to detect. As shown in Figure 3.3, the temporal Median Absolute Deviation (MAD) of the differences between  $\Delta e_v^{AMSR-E}$  for A and D passes over the full AMSR-E archive (2002-2011) are high up to  $\sim 140$  km away from the nearest coasts, before converging to similar values further offshore. The differences larger than 0.1 K between A and D tracks near the coast would correspond to signals  $>$

2 pss, which are way larger than those induced by a potential diurnal SSS cycle in this region (Drushka et al., 2014) and thus very likely linked to land contamination. MAD maps for A and D passes (Figure 3.4 a and b, respectively) database reveal that A and D brightness temperatures display extreme situated downstream of the coast when following the satellite track. These outliers in brightness temperature are thus most likely associated with contamination by land signals. This is attributed to a differing geometry of observation by the sensor of the land-sea transition in between both type of passes. To filter this land-sea contamination, we apply a mask based on the temporal MAD of the ascending data minus that of the descending data (Figure 3.4c). Ascending data are excluded where this field  $+0.06$  K (equivalent of 1.2 pss) and descending data where it is less than  $-0.06$  K. After applying such filter, the variations of the MAD decreases consistently (Figure 3.3 orange curve), indicating a clear attenuation of the land impact on the brightness temperature.

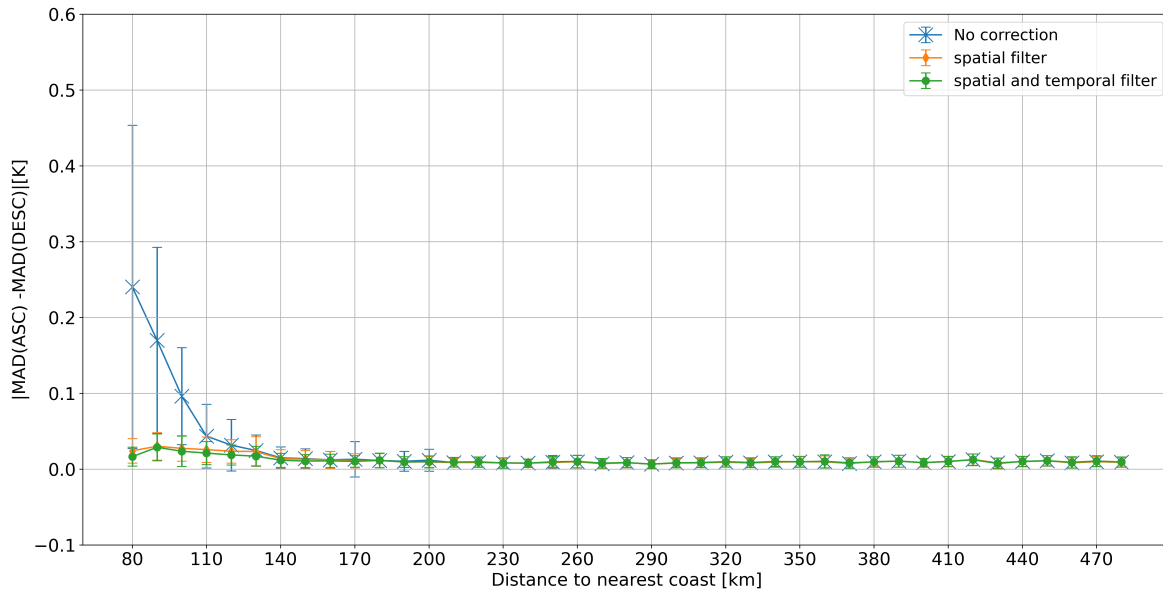


Figure 3.3 – Absolute value of the Median Absolute Difference (MAD) between successive ascending (A) and descending (D) brightness temperature as a function of the distance to the coast in km (K). Raw data in blue. Data once a separate masking of the A and D passes has been performed based on Figure 3.4c (see text for details in orange). Finally, the green curve shows the same statistics once outliers (further than 3 MAD from the median) have been removed at each point.

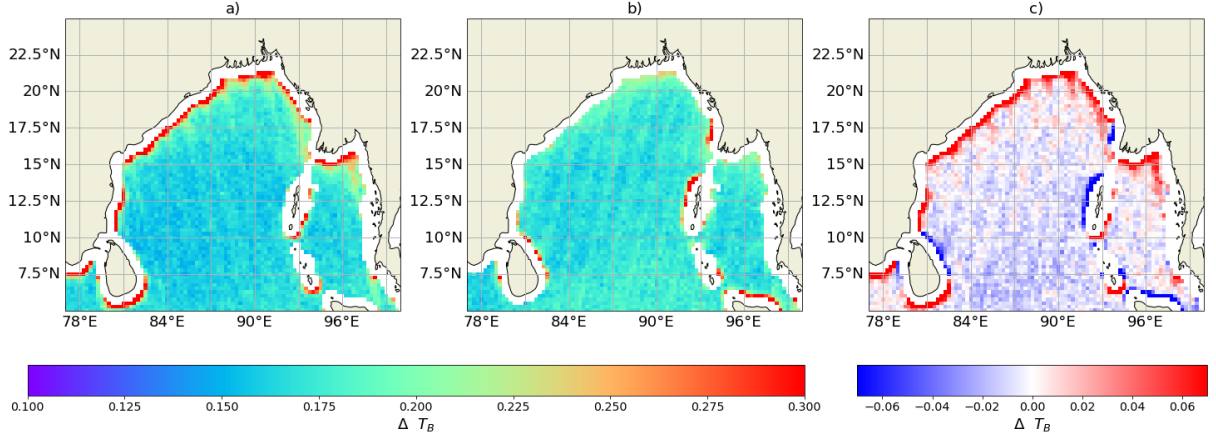


Figure 3.4 – Median absolute deviation of the brightness temperature difference between X- and C-band (K) from all AMSR-E data for a) ascending (A) and b) descending (D) satellite passes and c) their difference.

Once the land contamination masks have been applied, we scan the remaining  $\Delta T_v^{AMSR-E}$  corrected time series at each location to exclude potential outliers, such as those related to Radio Frequency Interference. The temporal MAD of  $\Delta T_v^{AMSR-E}$  is estimated in  $1/4^\circ \times 1/4^\circ$  cell grids, separately for the A and D passes. Outliers (more than 3 MAD away from the median) are then excluded from the dataset. After these two filtering steps, the MAD difference between the A and D passes decreases to less than to 0.02 K ( $\approx 0.4$  pss) (Figure 3.3, green curve).

#### 3.2.4.4 Algorithm empirical adjustments

The local wind and surface roughness conditions in the BoB might induce different roughness contribution  $e_{surf, v}^{rough}(\theta, \varphi, U_{10}, f)$  than the MW12 model derived from global observations. In addition, the specific atmospheric columnar water vapor and atmospheric columnar cloud liquid water conditions of the BoB also differ from the global mean conditions, which were analyzed to produce MW12’s RTM model. To refine the previously described AMSR-E SSS retrieval algorithm for the specific BoB conditions, we used the 16 month-long common period (June 2010 to September 2011) between the AMSR-E and CCI (L-band based) SSS and SST data.

First, the L2A AMSR-E top of the atmosphere C- and X-band swath brightness temperature data were corrected using the MW12 RTM algorithm for all contributions except

the surface roughness one to estimate the total sea surface emission  $E_{v,f}^{AMSR-E}$  (Eq. 3.2) at each frequency. This step of the algorithm uses the L2B AMSR-E  $U_{10}$ ,  $SST_{AMSR-E}$ ,  $V$ , and  $L$  as input data.

For each data point within the AMSR-E swath, the local SSS was estimated from the daily (7-day running mean average) CCI-SSS products using the nearest neighbor interpolation in space and time (denoted  $SSS_{CCI}$  hereafter). The expected perfectly flat surface emission at v-polarization, namely  $e_{v,f}^{flat, CCI}(SSS_{CCI}, SST_{AMSR-E})$  was then estimated at both  $f=6.8$  GHz and  $f=10.7$  GHz, for the AMSR-E local incidence angle, and using the dielectric constant model of MW12 (Meissner & Wentz, 2004).

#### 3.2.4.4.1 Empirical surface roughness correction

The residual wind-induced emissivity contrasts  $\xi_f(U_{10})$  at each frequency were then estimated from the difference between the estimated AMSR-E total sea surface emissivity and the expected perfectly flat surface emission, following:

$$\xi_f(U_{10}) = E_{v,f}^{AMSR-E} - e_{v,f}^{flat, CCI}(SSS_{CCI}, SST_{AMSR-E}) \quad (3.6)$$

The bin-averaged residual wind-induced emissivity  $\xi_f(U_{10})$  was estimated at each frequency for ascending and descending passes as function of  $U_{10}$  (bin width  $\sim 1$  m/s) and from all AMSR-E swath data collected in the BoB from June 2010 to October 2011. Assuming that there is no wind-direction dependency in the brightness temperature frequency contrast, the roughness-induced emission of the emissivity contrast between the X- and C-band frequency was then estimated following  $\Delta e_{rough}(U_{10}) = \xi_X(U_{10}) - \xi_C(U_{10})$  and bin averaged as a function of the co-located AMSR-E surface wind speed  $U_{10}$ .

As shown in Figure 3.5a) and b), the resulting empirical correction  $\Delta e_{rough}(U_{10})$  differs from MW12's model (particularly at high wind speed) and is not similar for Ascending and Descending passes. For the ascending satellite passes (Figure 3.5a) and for low-to moderate wind speeds, the empirical residual curve is similar to MW12 but is significantly different for  $U_{10} > 10$  m/s. The small number of high wind speed samples (histogram in red) is likely to explain this high wind difference. For descending data, the roughness induced residual found in the BoB is near 0 as long as  $U_{10} < 9$  m/s (Figure 3.5b) and slightly increases for the higher speeds.

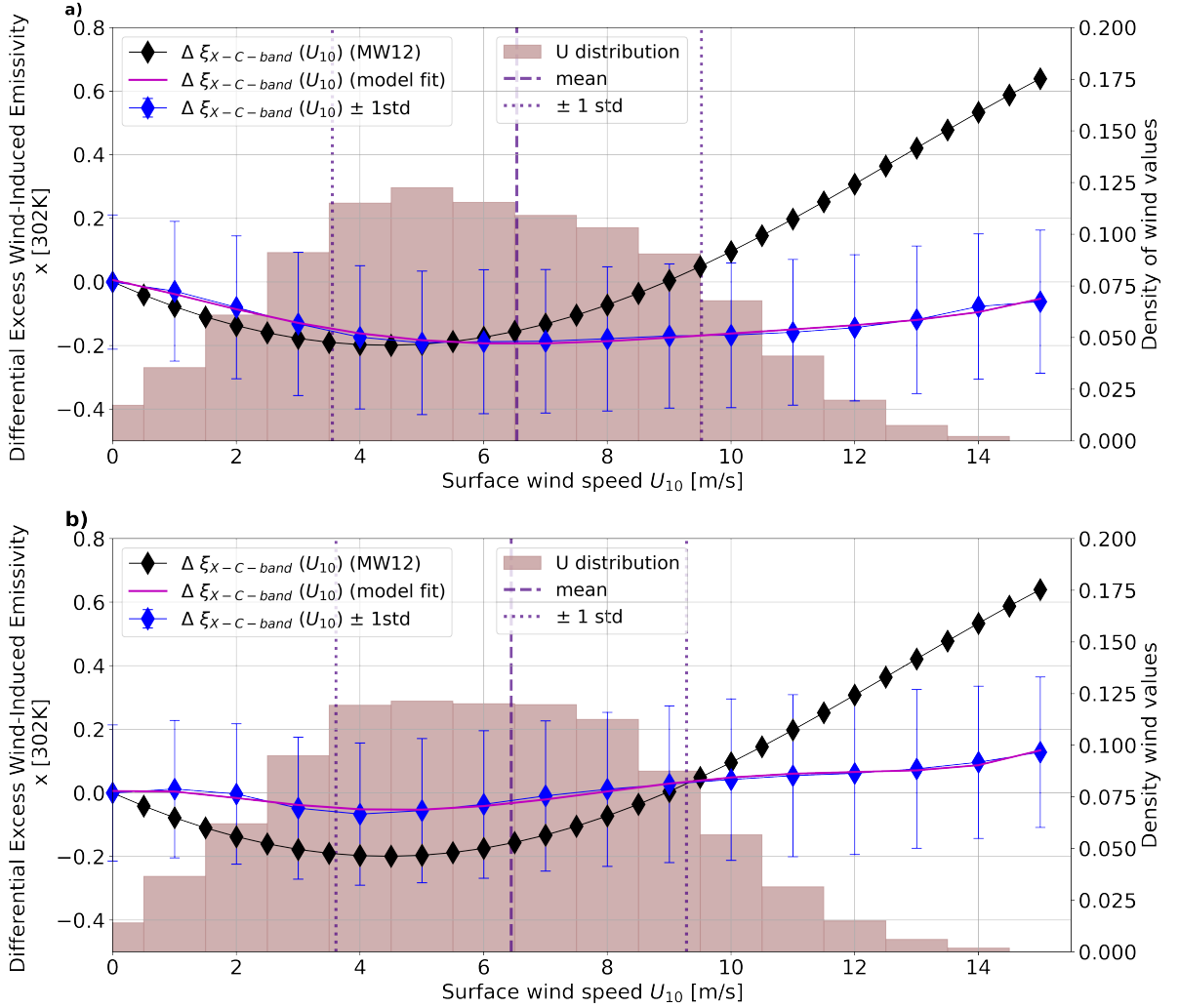


Figure 3.5 – Differences in wind-induced empirical residuals  $\xi_f(U_{10})$  between X- and C- bands from MW12’s model (black filled diamonds) and from AMSR-E and CCI data (blue filled diamonds) for a) ascending and b) descending satellite passes multiplied by the averaged BoB SST. The pink curve represents the empirical residual curve approximation: the difference between C- and X-band polynomial fits. The wind speed distribution is in red in the background, with the dashed line represents the median and the dotted line  $\pm 1$  standard deviation

The exact reasons for the wind-induced emissivity contrast differences between ascending and descending passes are not fully determined yet. Potential sources for the differences are (i) diurnal wind and/or SST impacts (ii) remaining land and RFI contamination. To best account for these A/D differences, the total sea surface emissivity

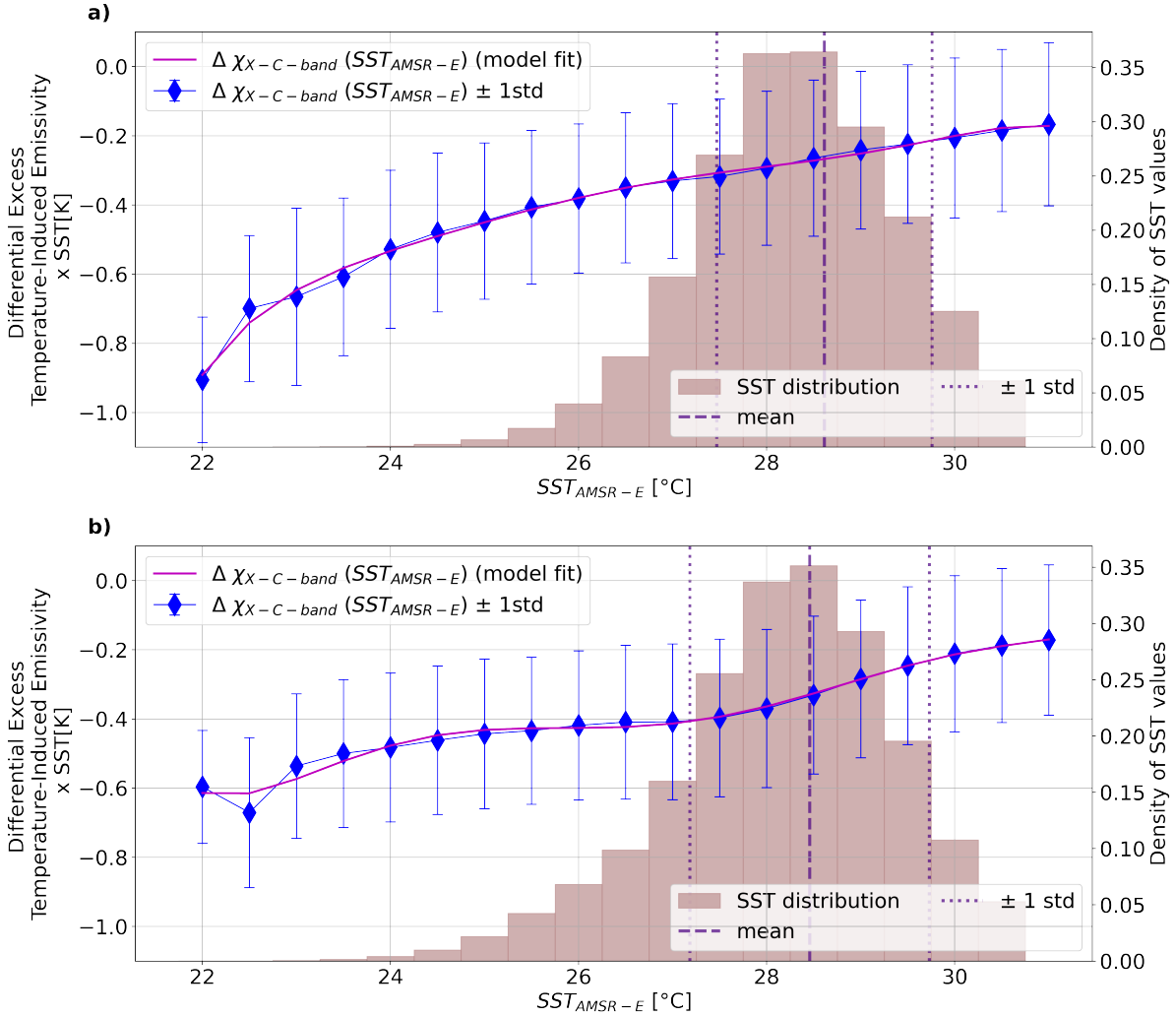


Figure 3.6 – Differences in the  $SST_{AMSR-E}$  induced empirical residuals  $\chi_f(SST_{AMSR-E})$ , between X- and C- bands, multiplied by the corresponding bin SST (blue filled diamonds) for a) ascending and b) descending satellite passes. The pink curve represents the difference between C- and X-band polynomial fits. The SST distribution is plotted in red in the background, with the dashed line represents the median and the dotted line  $\pm 1$  standard deviation.

$E_{v,f}^{AMSR-E}$  is therefore corrected for the excess wind-induced emission  $\xi_f(U_{10})$ , determined for each passes and each frequency, using fifth order polynomial fits to the AMSR-E

median residuals  $\xi_f = e_{rough,f,v}(U_{10})$  as function of wind speed (pink curve in Figure 3.6):

$$\xi_f(U_{10}) = e_{rough,f,v}(U_{10}) = \sum_{i=1}^5 a_{0,i,f} \cdot U_{10}^i \quad (3.7)$$

where the  $a_{0,i,v}$  coefficients are provided in **Appendix A.I** for the ascending and descending satellite passes, respectively. The perfectly flat sea surface emission  $e_{v,f}^{flat,AMSR-E}$  can then be estimated for the C- and X- bands using (Eq. 3.7) and subtracted it to the total sea surface emissivity.

Note that the MW12's model predicts that the differences between the X- and C-band for the 1<sup>st</sup>, and, 2<sup>nd</sup> azimuthal harmonic terms of the roughness-induced emissivity (which contain the wind-direction dependence of the surface emissivity) are smaller than 0.05 K in amplitude for the low to moderate wind speed conditions. Although wind direction impacts could clearly affect the SSS retrieval quality (0.05 K  $\sim$  1 pss), as a first step, we chose to neglect the wind/wave directional effects on emissivity.

#### 3.2.4.4.2 Empirical SST-dependent correction

After correcting for the wind-induced emissivity, the remaining residual difference with the expected flat surface emissivity at each frequency  $\chi_f = e_{v,f}^{flat,AMSR-E} - e_{v,f}^{flat,CCI}(SSS_{CCI}, SST_{AMSR-E})$  were further bin-averaged as a function of  $SST_{AMSR-E}$ . We found significant residual thermal biases as function of SST for both frequencies. As illustrated in Figure 3.6, the bin-averaged residual  $\chi_f$  varies as a function of SST, with an amplitude ranging from -0.2 to -0.4 K (equivalent of 4 to 8 pss) for the usual range of BoB SST (26-30 °C). For the coldest water within the BoB (< 26°C, usually found north of 18 °N in winter) the amplitude of  $\chi_f$  increase even more to reach  $\sim$ -0.9 K for the ascending satellite passes. For the warmer waters with SST > 30°C, the amplitude of  $\chi_f$  is practically similar for descending passes than for ascending passes. To correct for these remaining apparent 'thermal' effects, we estimated the mean of  $\chi_f(SST_{AMSR-E})$  in each SST bins (width of 0.25 °C) for each type of pass, and for each frequency and approximate them using 6<sup>th</sup> order polynomial corrections, following:

$$\chi_f(SST_{AMSR-E}) = \sum_{i=1}^6 t_{i,f} \cdot SST_{AMSR-E}^i \quad (3.8)$$

where the  $t_i^f$  coefficients are provided in Appendix A.II.

The flat surface emission is then estimated at each frequency after successive corrections for the wind and residual temperature impacts:

$$e_{v,f}^{flat,AMSR-E'} = E_{v,f} - e_{rough,f,v}(U_{10}) - \chi_f(SST_{AMSR-E}). \quad (3.9)$$

### 3.2.4.4.3 Empirical water vapor and liquid water dependent correction

The third and final empirical adjustment aims at correcting for residual atmospheric impacts. To this end, we averaged the remaining biases  $\epsilon_f = e_{v,f}^{flat,AMSR-E'} - e_{v,f}^{flat,CCI}(SSS_{CCI}, SST_{AMSR-E})$  as a function of the AMSR-E Level2B atmospheric columnar cloud liquid Water  $L$  (bin width 0.0025 mm) and atmospheric columnar water vapor  $V$  (bin width 1 mm). As illustrated by Figure 3.7 and Figure 3.8, we found residual biases  $\epsilon_f$  as function of both atmospheric columnar water vapor  $V$  and atmospheric columnar cloud liquid Water  $L$ .  $\epsilon_f$  is particularly large for high water vapor values ( $>50$  mm) and small cloud liquid water content ( $|L| < 0.05$  mm), particularly for descending passes (Figure 3.8a, c). Median estimates of  $\epsilon_f(V, L)$  in each  $V$  and  $L$  bins and for each frequency was approximated by 5<sup>th</sup> order bivariate polynomial corrections (Figure 3.7b, Figure 3.8b), following:

$$\epsilon_f(V, L) = \sum_{i=0}^5 \sum_{j=0}^{5-i} d_{i,j,f} V^i L^j \quad (3.10)$$

where  $V$  and  $L$  are the atmospheric columnar water vapor (in [mm]) and the atmospheric columnar cloud liquid water content (in mm), respectively. The 28 polynomial coefficients  $d_{i,j,f}$  are given in Appendix A.III for each frequency.

Overall, prior to evaluating the frequency contrast between the C- and X- band perfectly flat sea surface emission  $\Delta e_v^{AMSR-E}$  (Eq. 3.3), the specular sea surface emissivity is therefore determined at each frequency using the following suite of corrections:

$$e_{surf,f}^{flat,AMSR-E''} = E_{v,f} - e_{rough,f,v}(U_{10}) - \chi_f(SST_{AMSR-E}) - \epsilon_f(V, L) \quad (3.11)$$

where  $E_{v,f}$ ,  $e_{rough,f,v}(U_{10})$ ,  $\chi_f(SST_{AMSR-E})$  and  $\epsilon_f(V, L)$ , are determined from (Eq. 3.2), (3.7), (3.8), and (3.10), respectively.

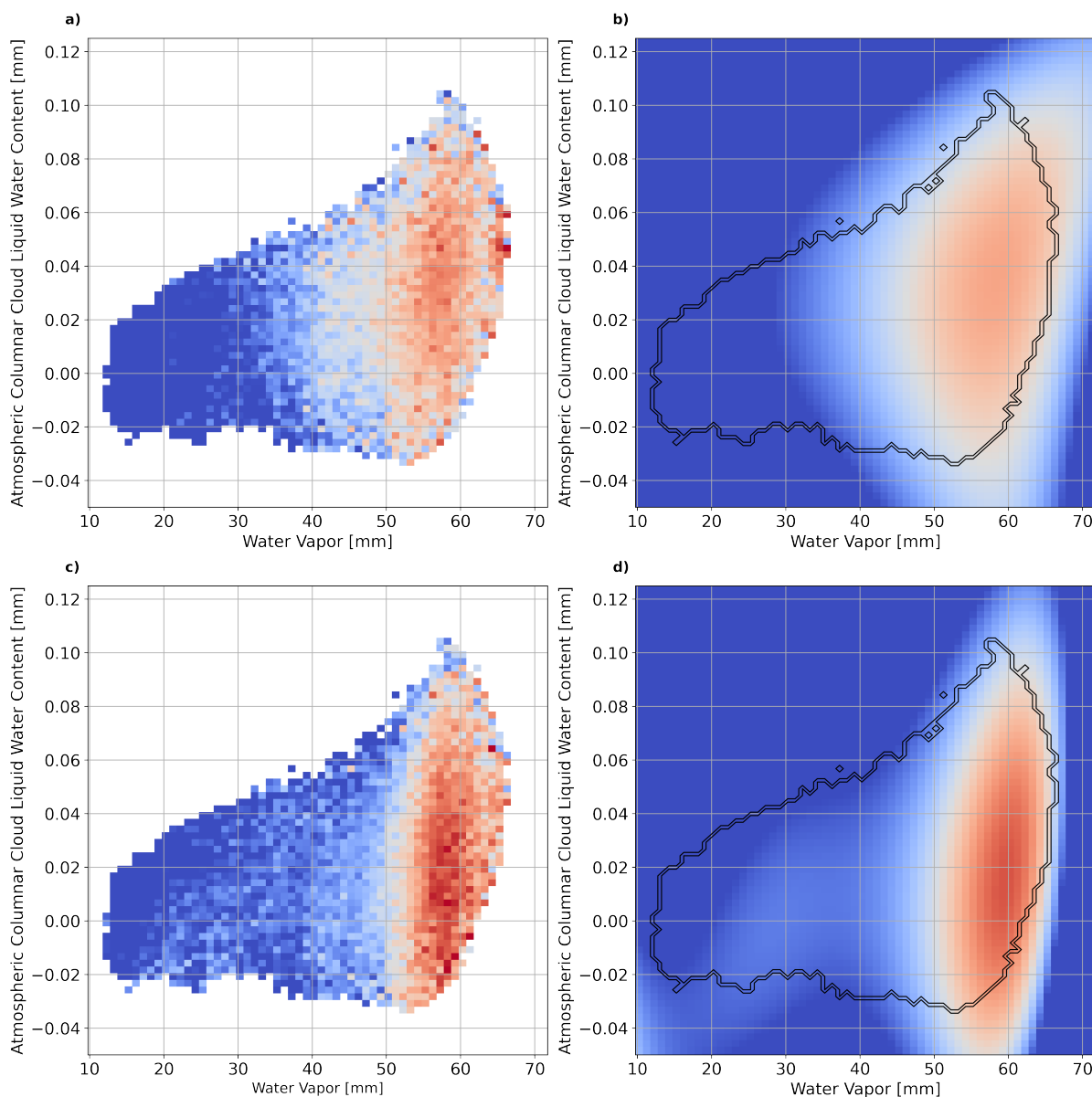


Figure 3.7 – Residual biases  $\epsilon_f$  for ascending passes, between the estimated AMSR-E flat surface emissivity data and the flat surface emissivity model prediction (using CCI SSS and SST data) as a function of both atmospheric columnar water vapor ( $V$ ) and atmospheric columnar cloud liquid Water ( $L$ ), for a) C-band and b) X-band. The right column displays the polynomial fit to these residual biases.

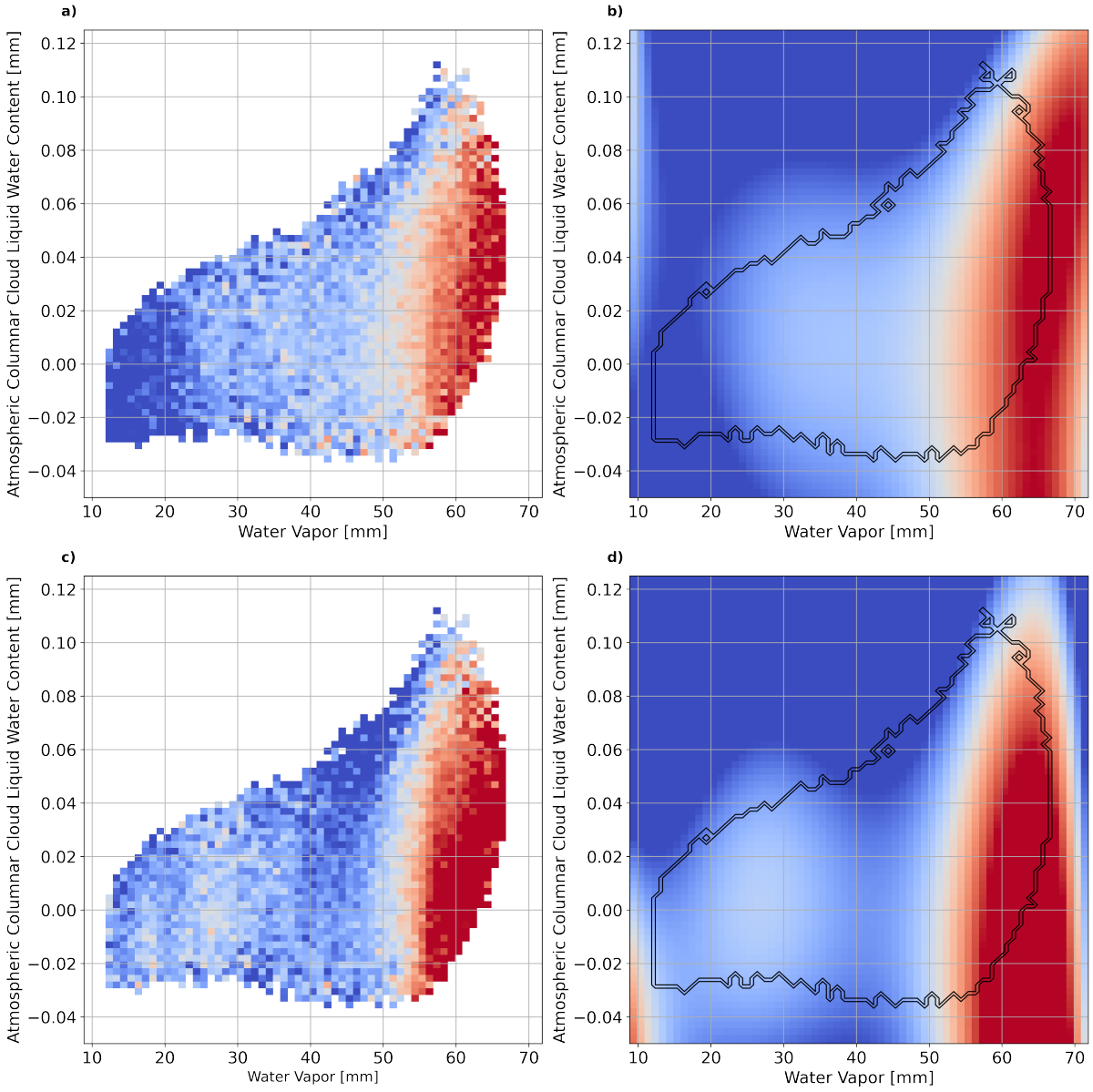


Figure 3.8 – Residual biases  $\epsilon_f$  for descending passes, between the estimated AMSR-E flat surface emissivity data and the flat surface emissivity model prediction (using CCI SSS and SST data) as a function of both atmospheric columnar water vapor ( $V$ ) and atmospheric columnar cloud liquid Water ( $L$ ), for a) C-band and b) X-band. The right column displays the polynomial fit to these residual biases.

### 3.2.4.5 Additional spatial and temporal filtering

Once these empirical corrections have been applied, we use (Eq. 3.5) to calculate the X-minus C- bands flat surface emissivity difference  $\Delta e_{surf,f}^{flat,AMSR-E''}$  on a daily basis for both

the A and D passes. We then apply a second screening of the data, by removing values which are further away than 3 MAD from the median at each location, independently for the A and D passes. The MAD is evaluated over the full archive period from May 2002 - September 2011 period. An additional spatial smoothing is performed, based on the median over a sliding  $0.75^\circ \times 0.75^\circ$  window. Hereafter we note the resulting emissivity  $\Delta e_{surf,f}^{flat,AMSR-E}$ .

### 3.2.4.6 Specific SSS inversion algorithm for the BoB

Using the collocated  $SSS_{CCI}$ ,  $SST_{AMSR-E}$  and  $\Delta e_{surf,f}^{flat,AMSR-E}$  the common period (2010-2011) we finally determined a geophysical model function used to retrieve SSS in the previous period. We computed the theoretical flat surface emissivity as a function of the AMSR-E SST and CCI SST  $\Delta e_{v,f}^{flat,CCI}(SSS_{CCI}, SST_{AMSR-E})$  using equation (Eq. 3.4). The median of the co-located  $SSS_{CCI}$  was then computed as a function of  $\Delta e_{v,f}^{flat,CCI}(SSS_{CCI}, SST_{AMSR-E})$  ( $1 \times 10^{-4}$  wide bins) and  $SST_{AMSR-E}$  ( $0.25^\circ \text{C}$  wide bins), to empirically determine a bivariate GMF relating the three variables, namely:

$$SSS = GMF(SST_{AMSR-E}, \Delta e_v^{CCI}). \quad (3.12)$$

This empirical relation between SSS and the flat surface emissivity contrasts between the C and X bands, and SST and SSS for the Bay of Bengal can be approximated using a  $2^{nd}$ -order polynomial fit (Figure 3.9):

$$SSS = \sum_{i=0}^2 \sum_{j=0}^2 s_{i,j} (\Delta e_v^{CCI})^i SST_{AMSR-E}^j \quad (3.13)$$

where the  $s_{i,j}$  coefficients are provided in Appendix A.IV. SSS over the May 2002 to October 2011 period can then be obtained by plugging the corrected, quality-controlled and spatio-temporally filtered daily emissivity contrast  $\Delta e_{surf,f}^{flat,AMSR-E}$  and co-located  $SST_{AMSR-E}$  into (Eq. 3.13).

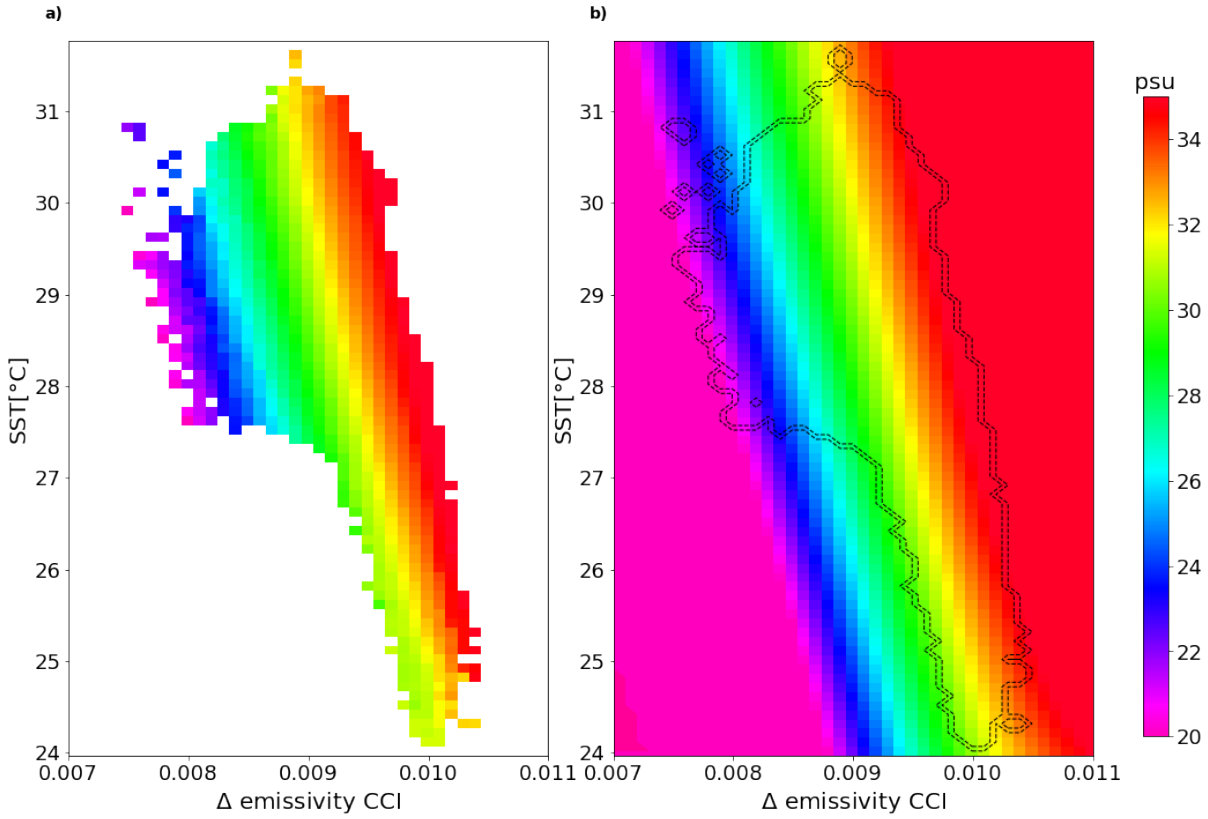


Figure 3.9 – a) Bin-averaged observation of  $SSS_{CCI}$  (color) as a function of the frequency differential emissivity contrasts  $\Delta e_B^{CCI}$  (x-axis) and the co-located  $SST_{CCI}$  (y-axis) in the BoB. b) Third order polynomial fit to the data shown in a) with in dotted lines the contour of the existing data.

### 3.2.5 AMSR-E SSS retrieval and validation

#### 3.2.5.1 Consistency check: comparison with CCI data

Prior to the validation of the new  $SSS_{AMSR-E}$  dataset, we first check the consistency between the seasonal cycles of the CCI and AMSR-E SSS data, derived for the full period of each product (CCI: 2010-2019; AMSR-E: 2002-2011). As can be seen from Figure 3.10,  $SSS_{AMSR-E}$  generally captures the broad spatial patterns and seasonal cycle of  $SSS_{CCI}$ . Both datasets indeed display saltiest water (SSS around 33 or above) to the southwest, in regions which are closest to the Arabian Sea, while the northeast of the basin is generally fresher. This gradient is strongest during and after the southwest monsoon, i.e. in June-July-August (JJA) and September-October-November (SON)

(Figure 3.10 c, g and Figure 3.10 d, h), where SSS drops below 28 pss in the vicinity of the Ganges-Brahmaputra (north of 20°N) and Irrawaddy (around 15°N, 95°E) estuaries.

Despite this broad agreement, the  $SSS_{AMSR-E}$  dataset displays several clear biases relative to  $SSS_{CCI}$ . It displays a clear fresh bias, of 2 pss or more, all along the coastal rim of the Bay, from boreal spring (March-April-May (MAM)) to fall (SON), while the Central BoB tends to display a weaker salty bias (Figure 3.10 jkl). During December-January-February (DJF), the  $SSS_{AMSR-E}$  dataset displays a salty bias of 1 pss or more throughout the interior Bay of Bengal, while the east coast of India and Andaman sea tend to remain slightly too fresh. Overall, this comparison with CCI (which was used as a training dataset over the common period) indicates that it is possible to reconstruct the broad features of the basin-scale SSS seasonal cycle from AMSR-E data, but that significant biases remain, the clearest one being a fresh bias along the east coast of India and in the coastal Andaman Sea.

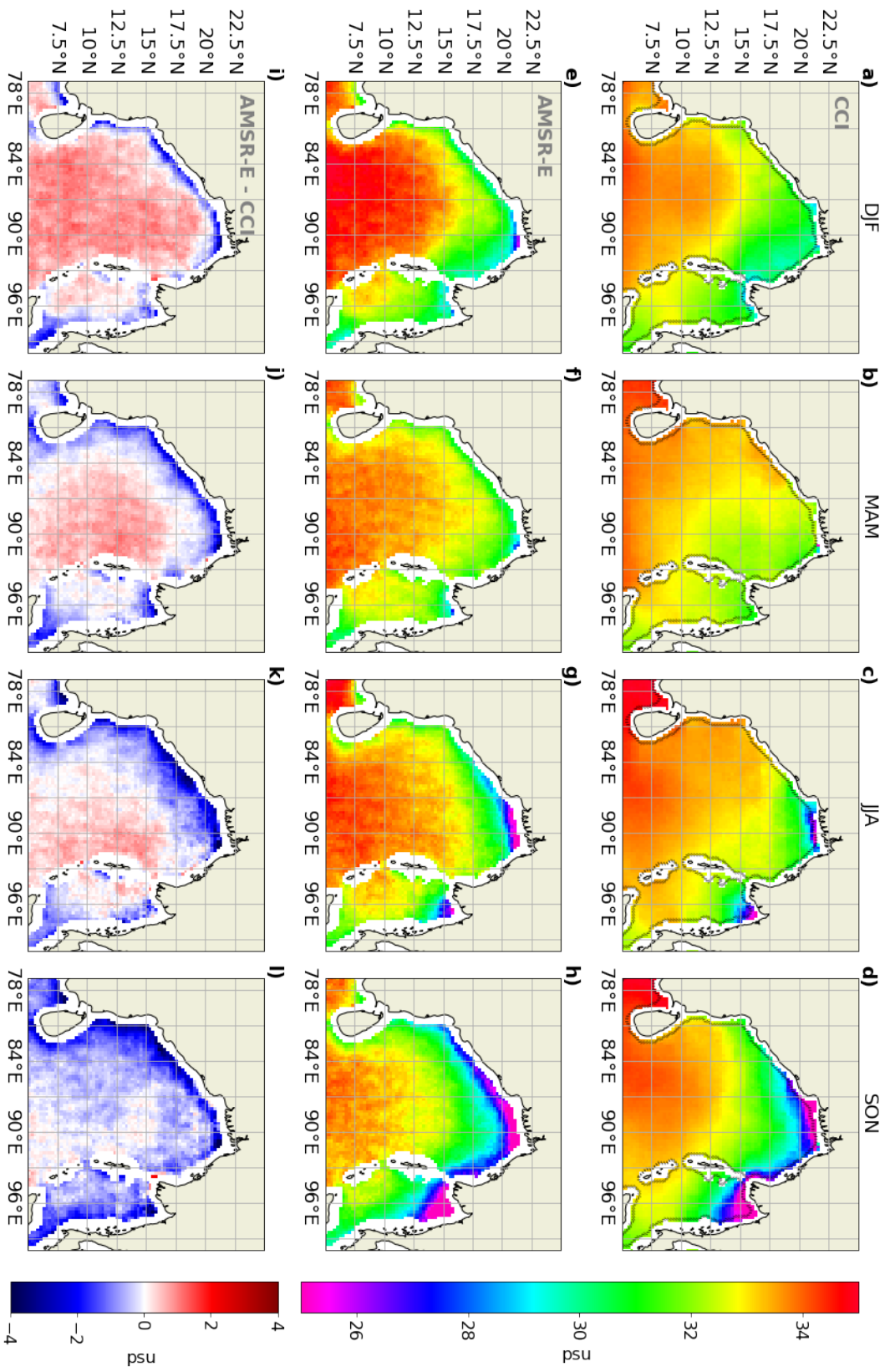


Figure 3.10 – Seasonal (first column: December-February; second column: March-May; third column: June-August; last column: September-November) averaged SSS from: CCI data (top; 2010-2019) and AMSR-E data (middle; 2002-2011) and their difference (bottom).

### 3.2.5.2 Validation with in-situ data

The previous figure was not a validation to independent data, since CCI data has been used as a training dataset to build our  $SSS_{AMSR-E}$  dataset. To validate the retrieved  $SSS_{AMSR-E}$  we now use the co-located in situ salinity from the Array for Real-time Geostrophic Oceanography (ARGO) dataset at its shallowest depth (see section 3.2.3.3). We remind that this dataset was reduced to a  $1/4^\circ \times 1/4^\circ$  x monthly grid, by taking the averages of grid cells with at least 2 observations (Figure 3.11b). Figure 3.11a displays a histogram of the amount of in situ data per salinity bin, and of the AMSR-E versus in situ SSS. As seen on the histogram, there are very few data at low SSS (below 31 pss) in the in situ dataset, while such fresh water span large areas of the Northeast BoB in JJA, SON and DJF (Figure 3.10a,c,d), indicating that it will be difficult to validate satellite products for low SSS. The red curve displays the median of the AMSR-E SSS per in situ salinity bin. This curve indicates that, despite a relatively large random error around the median estimate, the retrieved  $SSS_{AMSR-E}$  is unbiased at  $SSS \leq 34$  pss but has an up to 1 pss fresh bias at  $SSS \geq 34.5$  (associated with the Southwest BoB in JJA to SON, see Figure 3.10). Overall, the correlation between  $SSS_{AMSR-E}$  and the collocated ARGO data is 0.66. and the rms-difference between both datasets is 1.09 pss, against, respectively, around 0.85 and 0.6 pss for the CCI SSS in this region Akhil et al. (2016b). The better performance of the CCI SSS was to be expected, given the much higher sensitivity of brightness temperature to SSS in the L- than in the X- minus C-band. But the overall picture is that the AMSR-E method is able to capture the broad SSS variations in the Bay of Bengal.

### 3.2.5.3 Comparing AMSR-E and ocean re-analyses SSS interannual variability

As discussed in the introduction, our main objective in this study is to be able to reconstruct SSS interannual variations prior to the L-Band SSS retrievals era: that are insufficiently constrained by in situ satellite data. In this section, we hence aim at evaluating the capacity of  $SSS_{AMSR-E}$  to reproduce SSS interannual variations in the BoB. Given that in situ data coverage is not sufficient to describe BoB interannual SSS variations before 2010, we use 5 oceanic reanalyses to estimate the consensus SSS interannual variability (the ensemble mean) and uncertainties (spread around that mean). We focus on two regions in which strong interannual variability has been underlined in

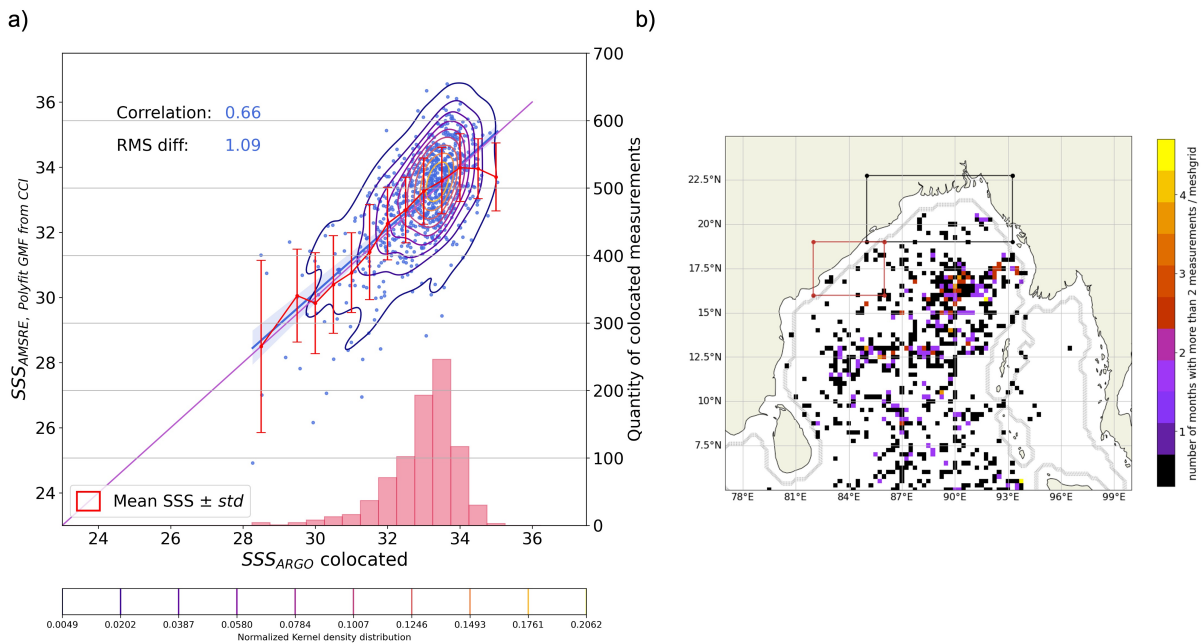


Figure 3.11 – a) Scatterplot of SSS from AMSR-E versus co-located SSS from ARGO floats with their kernel density distribution in color contours (see bottom legend). The blue line represents the linear regression with the 95% confidence interval in translucent blue. The red curve is the mean value with its standard deviation for each bin (0.5 pss) with more than 3 observations. The barplot in red is the distribution of the number of collocated measurements in each bin. b) Spatial distribution of ARGO measurements used in the scatter plot (a). The black box shows the northern BoB zone [19°N-22.75°N; 85°E-93.25°E] and the East Coastal Indian (EIC) [16°N-19°N; 82°E-86°E] is displayed in red: both are used in Figure 3.12.

the past (e.g. Akhil et al., 2014; Chaitanya et al., 2014b): the northern BoB around the Ganga-Brahmaputra (GB) estuary, and the East Coast of India (ECI) (see Figure ??b). As can be seen on Figure 3.12, the oceanic re-analyses compare reasonably well with the CCI interannual SSS variability over both regions (correlation of 0.79 with a rms difference of 0.52 pss for the GB area, and 0.74 / 0.51 pss over the ECI). This relatively good agreement of the re-analyses with the CCI dataset over the 2010-2020 period suggests that the re-analyses can be used as a reference over the anterior 2002-2010 period (we note however, that there are less direct in situ salinity measurements over this period, and that the re-analyzed SSS is only constrained through the model forcing, physics and the assimilation of other data such as altimetry and sea surface temperature).

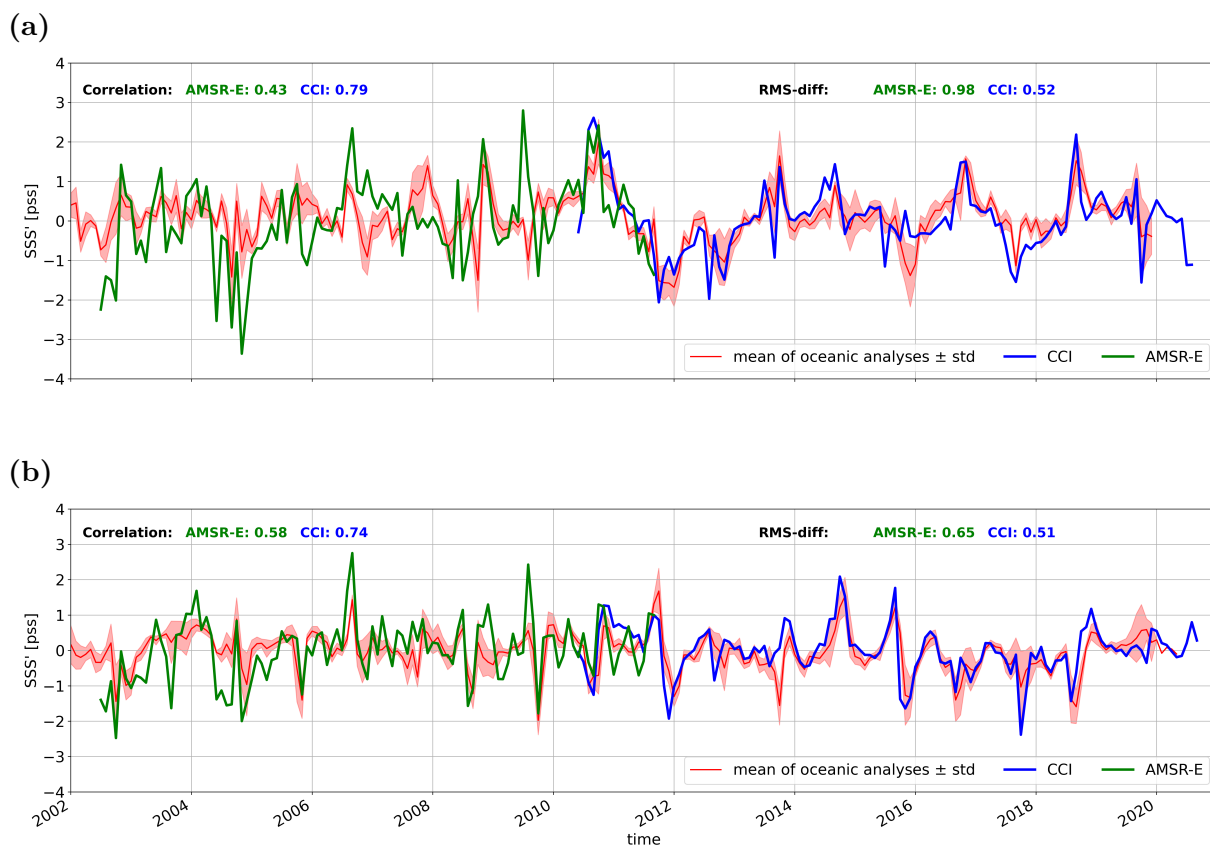


Figure 3.12 – a) SSS anomalies from AMSR-E (green) and CCI (blue), and the averaged SSS anomalies from the models Glorys 1/12, ORAS, Glorys2v4, UKMO, and CMMC (red) with the shading indicating the inter-model spread ( $\pm 1$  std, averaged for a) the northern BoB and b) the East Coast of India (see those geographical boxes in Figure 3.11). On the top of each figure is the correlation between the reanalysis and AMSR-E (blue) and CCI (green) on the left and on the right their Root-mean-square difference.

Near the GB estuary, the re-analyses & AMSR-E SSS do not match well (Figure 3.12a), with correlation of 0.43 and a rms-difference of 0.98 psu. These are worse scores than those of the CCI vs re-analyzed SSS comparison over the more recent period. More specifically, the AMSR-E SSS has little in common with the year-to-year variations from the re-analysis, except maybe during the common CCI & AMSR-E period. Although the re-analyses are weakly constrained by salinity observations over this period, this is an indication that our current SSS reconstruction has little skill for SSS interannual variations in the Northern BoB. The picture is more favorable along ECI (Figure 3.12b).

Although the correlation with re-analysis data remains low (0.58), the rms-difference

is lower (0.65 pss) and there is a relatively long period where the low frequency SSS variations in the AMSR-E and re-analyzed datasets match qualitatively well (2005 to the end of the record). The relatively low correlation and high rms are due to a couple of strong “spikes” in the reconstructed  $SSS_{AMSR-E}$  interannual anomalies, for instance in 2003, 2004, late 2008 and 2009. More generally, the stronger prevalence of “spikes” in the reconstructed  $SSS'_{AMSR-E}$  than in  $SSS'_{CCI}$  suggests that the AMSR-E reconstructions contain intermittent spurious signals, that could either be related to radio frequency interferences, or improperly filtered land contamination and remaining uncorrected effects caused by the wind or low SST (not shown). Overall, the comparison with SSS anomalies from ocean re-analyses suggests little skill in the Northern BoB, but limited skill along the east coast of India, giving some hope than an improved reprocessing will allow to reconstruct pre-2010 SSS interannual variations from AMSR-E in the Bay of Bengal. We will come back to this in the discussion.

## 3.2.6 Summary and Discussion

### 3.2.6.1 Summary

SSS has a very strong spatial and temporal variability in the Bay of Bengal (up to 10 pss range). The very strong haline stratification in the BoB is thought to influence air-sea interactions below tropical cyclones, primary productivity, and possibly climatological rainfall. However, the basin-scale interannual SSS variations are only measured since 2010 in this basin, with the advent of L-band satellite SSS remote sensing. Before that date, the in situ data coverage in the BoB was not really sufficient to describe basin-scale SSS variations. In the present study, we therefore aim at reconstructing pre-2010 BoB SSS based on AMSR-E data. The AMSR-E radiometer indeed comprises a channel in the C-band. Although this channel is much less sensitive to SSS than in the L-band, previous studies have illustrated that a careful data processing can allow to capture SSS signals in regions with strong SSS contrasts, and high SST such as the Bay of Bengal. The similar sensitivity of the X- and C- bands to wind and SST signals allows to reduce the impact of those parameters, by considering X- minus C- brightness temperature contrasts. The X- minus C- sensitivity to SSS is still low (0.05 K/pss), implying that a very careful elimination of other residual signals is necessary. We find strong brightness temperatures differences between ascending and descending passes, especially close to land masses.

(i) Separate land-sea masks are hence applied to ascending and descending passes to

eliminate contamination of ocean points downstream of passages over land. (ii) The ascending and descending passes are processed independently, with distinct empirical corrections. We indeed further obtain (iii) empirical corrections of surface wind, SST, and atmospheric water contents (performed in that order) based on CCI SSS and AMSR-E collocated wind, SST, and atmospheric water data over the SMOS/Aquarius-AMSR-E common period. An additional screening of the data, to eliminate outliers ( $> 3$  MAD from the median) over the entire time-series and  $0.75^\circ \times 0.75^\circ$  median smoothing is also found to strongly influence the final data performance.

Comparing the retrieved SSS climatology with that of CCI indicates that our product broadly reproduces the observed climatology, despite fresh biases near coasts.  $SSS_{AMSR-E}$  has a 0.66 correlation, 1.09 pss rms-difference to co-located in situ surface salinity from ARGO floats, which is not as good as L-band radiometers but indicates some skill. Since the main interest of such product is to reconstruct interannual SSS variations prior 2010, we did compare the SSS interannual variations with those from ocean re-analyses in two hotspots for SSS interannual variability: the northern BoB and east coast of India. Oceanic re-analyses compare reasonably well with L-band radiometry over the recent period, suggesting that they also have some skill for SSS variations before 2010. The comparisons with those re-analyses suggest that our current product has little skill over the Northern Bay of Bengal. The comparison along the east coast of India is however more favorable. While our product sometimes displays some spurious SSS spikes, it is also able to reproduce the broad SSS interannual variations in re-analyses over quite long periods (3-5 years). This confirms that AMSR-E contains some useful information about BoB SSS interannual variability, but that an improved data processing may be required. We discuss this in the following section.

### 3.2.6.2 Discussion

Following a first demonstration of SSS retrieval capability from AMSR-E low frequency channel data in the highly contrasted region of the Amazon river plume (Reul et al., 2009), the current paper establishes the basis for an SSS reconstruction algorithm from AMSR-E data in the Bay of Bengal. As could be expected from the relatively low C-band sensitivity to SSS, and the risk of land contamination and radio-frequency interferences in the land-encircled BoB, this is a tricky task, and our current dataset still has issues. We however think that the skill for reproducing some observed interannual

signals along the west coast of India is promising and suggest some possible avenues for improving this algorithm in the future.

We found a large impact of the data screening to exclude land-sea contaminated points (not shown). The fact that there is a residual fresh bias along all the coasts (Figure 3.10 i-j-k-l) or that there are spurious “spikes” in the reconstructed SSS interannual time series (Figure 3.12) suggest that land contamination has not entirely been eliminated. The elimination of points contaminated by land signals is currently very simple and based on two separate static masks that eliminate points downstream of land on ascending and descending passes, respectively. Applying a more stringent mask or applying a more dynamical screening (based on differences between successive A and D passes for instance) are probably the main avenues that will allow to improve the SSS retrieval.

Wind, SST, and water vapor empirical corrections are currently applied in three consecutive steps. Although we did investigate the effect of the order of these corrections, and found little sensitivity (not shown), methods based on neural networks would allow to perform all these corrections in a single step and more optimal fashion. The advantage of a neural-network-based method is that additional parameters can also be introduced, such as the distance to the coast or the direction of the wind (we currently take only the norm of the wind into account in our empirical correction, while WM12’s model indicate the wind direction-dependent component of the correction can be non-negligible).

The fact that the AMSR-E derived SSS interannual anomalies better match the ensemble model re-analyses along the East Coast of India than in the Northern part of the BoB (Figure 3.12), where the SSS contrasts and variability are higher, is a bit counterintuitive. It can be nevertheless partially understood given the differing Sea Surface Temperature conditions in the two regions. Climatological SST is colder in winter (DJF) near the Ganga and Brahmaputra estuaries ( 25.5 °C) than along the East Coast of India (27°C or more). As shown in Figure 3.1, the sensitivity of the X-minus C-band emissivity contrasts to SSS drops significantly with decreasing SST (from 0.05 K/pss at 29°C to 0.03 K/pss at SST=25°C). In addition, the sensitivity to SST increases with decreasing SSS (from -0.05 K/°C at SSS=35 pss to -0.075 K/°C at SSS=20 pss). These two effects probably act together to decrease the signal to noise ratio and therefore to increase the uncertainty in the AMSR-E SSS retrievals for the Northern part of the

BoB. The better results obtained by Reul et al. (2009) for the case of the Amazon river plume waters are probably also associated with the warmer SST in that region.

Furthermore, the common period between AMSR-E and CCI, from which the empirical corrections are estimated, is short and known for a suboptimal SMOS data. Further constraining the correction estimate by also using in situ data over a longer period should be explored. Since our objective is to reconstruct SSS interannual variations (the SSS climatology is otherwise well constrained by in situ and L-band altimetry data), a methodology that works with brightness temperature interannual anomalies (and hence eliminates the mean state error) may also need to be tested.

The first release of the SMOS SSS retrievals were hardly usable for the Bay of Bengal, displaying a worse performance than that described here for  $SSS_{AMSR-E}$  (Akhil et al., 2016b). Later, an improved reprocessing with an improved bias correction and data screening near land allowed to strongly reduce those errors, turning the SMOS dataset into a useful one for the BoB (Akhil et al., 2020; Boutin et al., 2018). While we recognize that the current SSS retrieval still has significant issues and may not be usable for oceanographic studies in its current state, we think that the promising interannual SSS signals it captures in some regions of the BoB are sufficiently encouraging for pushing more work on an improved data processing to obtain 8 more years of interannual SSS estimates over that region.

## Acknowledgment

The authors would like to thank the ESA Sea Surface Salinity Climate Change Initiative (CCI) for providing the Sea Surface Salinity (SSS) v03.21. M.M acknowledges funding for her PhD work, provided by the French Brittany region and Centre National d'Études Spatiales (CNES). The Argo data were collected and made freely available by the International Argo Program and the national programs that contribute to it. (<https://argo.ucsd.edu>, <https://www.ocean-ops.org>). The Argo Program is part of the Global Ocean Observing System.

### 3.3 Corrective Measures for Developing Accurate Algorithms

In this section, I provide additional elaboration of the corrections implemented to derive the final algorithm described in Section 3.2.4.2.

Note that all the early versions used the auxiliary SST issued from the Operational Sea Surface Temperature and Ice Analysis (OSTIA) (a infrared based daily composite from the CCI). The CCI SST is a "night-time" foundation SST, representative of the diurnal cycle free SST. AMSR-E SST retrieval, on the other hand, uses a monthly climatology of SSS to correct its impact on the brightness temperature. Because of this, we preferred to rely on the SST first. However, after comparing the ascending and descending pass AMSR-E SST, we discovered that the diurnal warming impact on the SSS retrieval was significant. This finding will be detailed further in a subsequent section. Note that all versions include a basic outlier filtering (removing  $(\Delta e - Median) \geq 3 * MAD$ ).

As mentioned in Section 3.2.4.4, the empirical corrections have been applied in the following order: surface wind, SST, and atmospheric water contents. The choice to remove first the wind impacts comes directly as the surface winds have the strongest impacts on the brightness temperature (Reul et al., 2009). The relative impacts of SST and atmospheric water content are quite similar, thus thanks to their non-correlated behavior their order should not matter. In practice, it has been verified that their relative order does not influence the out-coming algorithm.

#### 3.3.1 The Impact of the Empirical GMF

Initially, the empirical GMF was supposed to be customized with the AMSR-E dataset by calculating which SSS was obtained for a given SST and a given  $\Delta e_B$ . As can be seen in Figure 3.13a the reconstruction creates a strong overestimation for  $SSS < 33$  psu and an underestimation for a  $SSS > 32$  psu. By using the empirical GMF, calculated with the theoretical flat surface  $\delta T_B$  using  $SSS_{CCI}$  based on MW12's dielectric constant model, as explained in Section 3.2.4.6, I can obtain a more accurate reconstruction (see Figure 3.13b). There is still an over- and under-estimation for SSS below and above 33 psu respectively, but the regression line aligns much better with the  $x=y$  line. However, the distribution around the regression line spread, the correlation slightly decreases (from 0.61 to 0.52) and the rms-difference strongly increases (from 0.89 pss to 1.37 pss).

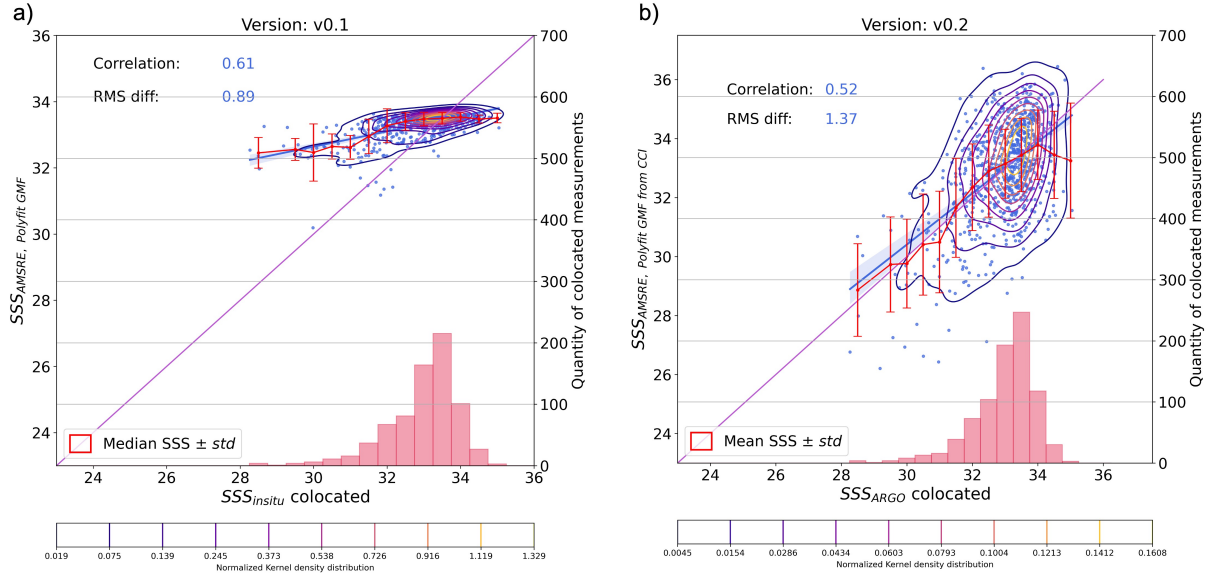


Figure 3.13 – Scatterplot of SSS from AMSR-E versus co-located ARGO data with their kernel distribution in color contours. The blue line represents the linear regression with the 95% confidence interval in translucent blue. The red curve is the mean value with its standard deviation for each bin (0.5 pss) with more than three observations. The barplot in red is the distribution of the number of collocated measurements in each bin. To calculate the  $SSS_{AMSR-E}$  I use in a) the GMF created by AMSR-E  $\Delta e_B^{CCI}$  and in b) the theoretical GMF  $\Delta e_B^{CCI}$ .

Note also that the use of the empirical GMF based on MW12 increases the quantity of correlated measurements between in situ and AMSR-E SSS (see the barplot distributions in Figure 3.13). This is caused by the lack of similar  $\Delta e_B^{AMSR-E}$ , that has been sorted out during the creation of the GMF (a minimum amount of 10 values is required in order to be counted). Thus not accounted  $\Delta e_B^{AMSR-E}$  will leave a gap. As the GMF is based on MW12's model over the full range, no gaps occurs, increasing the co-located spots. However, using MW12 for the GMF is also the source for data scattering. Aberrant values occurring less than ten times will not be removed and thus will affect the monthly results.

### 3.3.2 The Impact of the Learning Period

In order to increase the correlation and decrease the rms-difference between AMSR-E and in situ SSS, I try to find improvements which will lead to less dispersion around the regressions line. In the early versions, I used a refinement period which was divided in

two. One period was to be used for the algorithm development, the second one for the validation. As the common period is already really short, the lack of data can induce an error. Using in situ data for validation, I was thus able to increase the learning period to the common integral period (June 2010 - September 2011).

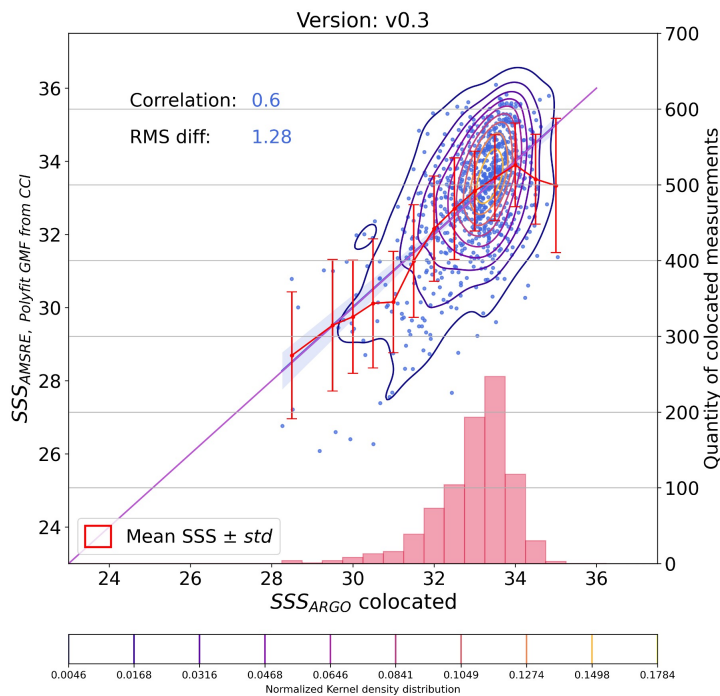


Figure 3.14 – Same as Figure 3.13 for the GMF based on MW12 and the full period were used to calculate the empirical corrections on surface wind, SST, and atmospheric water components.

As shown in Figure 3.14, the correlation has indeed slightly increased (0.6). But there was still outliers (rms-difference: 1.28 ps) that I try to further remove.

### 3.3.3 The Impact of the AMSR-E Swath Directionality

By analyzing the results as a function of the satellite flight direction, i.e., separating ascending and descending passes, I discovered the existence of strong differences, principally along the coast (see Figure 3.15). This is mainly caused by the relative direction of the viewing angle of the instrument during its orbital motion. As the BoB is a region surrounded by land masses, their effect on instrument passes varies depending on the direction of the pass - whether it is pointed towards the region (ascending) or away

from it (descending)(see Figure 3.15). This impact the brightness temperature (and thus emissivity). I have thus proceeded separately ascending and descending data, calculating the empirical corrections, filtering and SSS inversion independently. Only when the  $SSS_{AMSR-E}$  has been determined, I merged the data and calculated the monthly mean.

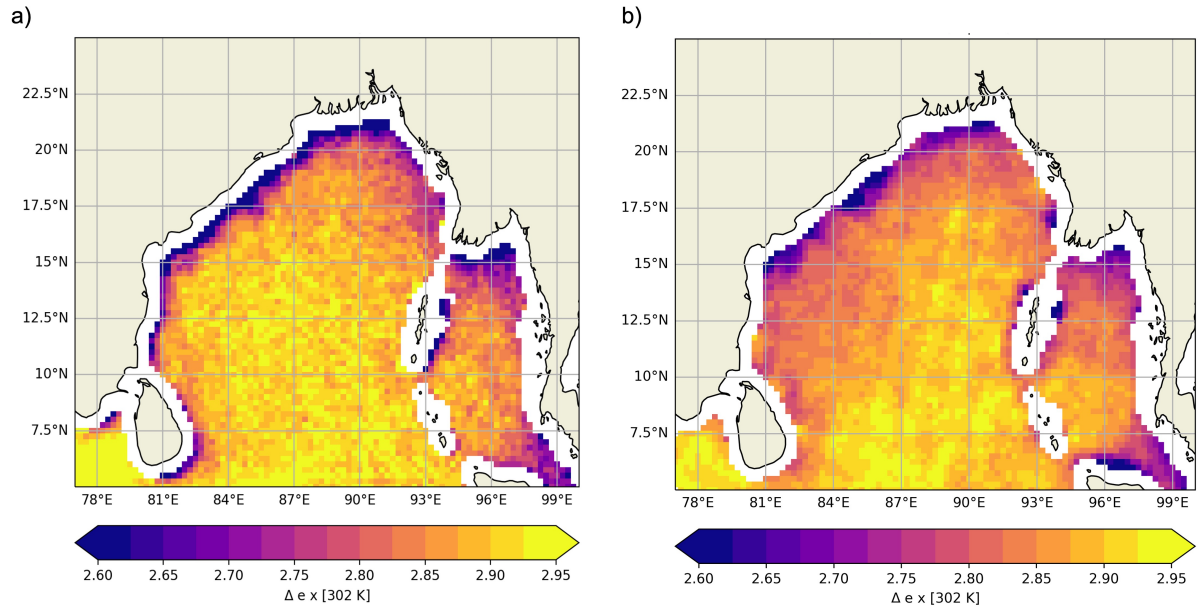


Figure 3.15 – Temporal median of the raw emissivity difference  $\Delta e$  in the Bay of Bengal (before empirical refinement are applied) for a) ascending and b) descending satellite passes.

As shown in Figure 3.16, the specific processing for each type of pass indeed increases the accuracy of the SSS retrieval: the correlation slightly increases (0.63) and the rms-difference decreases (1.18 pss). However, separating the data per satellite pass-type seems also to increase slightly the overestimation for the lower SSS ( $SSS < 30$  pss).

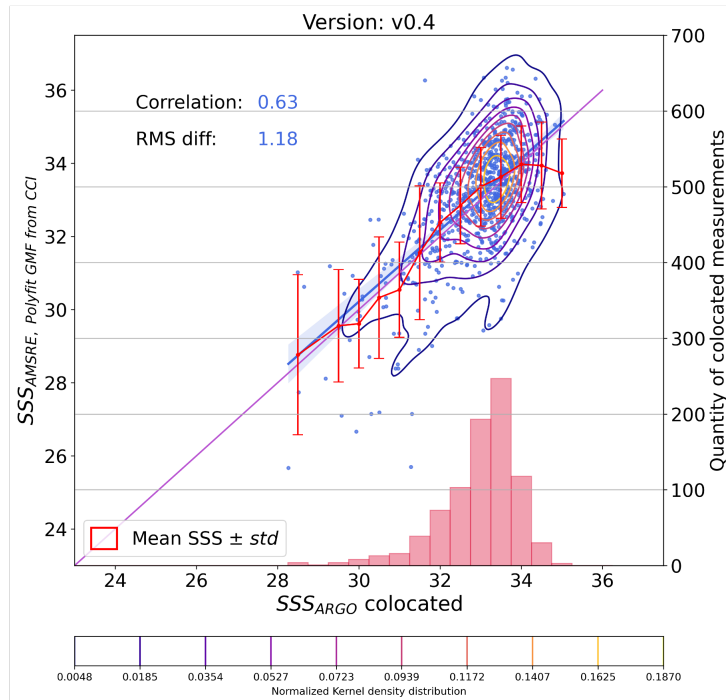


Figure 3.16 – Same as Figure 3.14, applied separately on ascending and descending data.

### 3.3.4 The Impact of Additional Filtering

In order to increase the accuracy of the retrieved SSS, I attempted to improve the filtering as there were still large differences between the temporal median of ascending and descending data (shown in Figure 3.4c). This is particularly true in the offshore region, where large spreads of land-sea contaminated signals can be found and they should not be used in the algorithm. The detailed filtering was explained Section 3.2.4.3. The spatial impact of the filtering can be seen in Figure 3.20b, that shows in blue the boundary used before the filtering and in black the boundary used once the land-contamination filter applied.

This filtering indeed increases the correlation (0.68), and the dispersal around the regression line seems to lessen as the rms-difference drops to 1.06 pss. But the overestimation of lower SSS does not seem to improve. As can be seen in Figure 3.17 outliers exist for low SSS ( $SSS \approx 24$  pss).

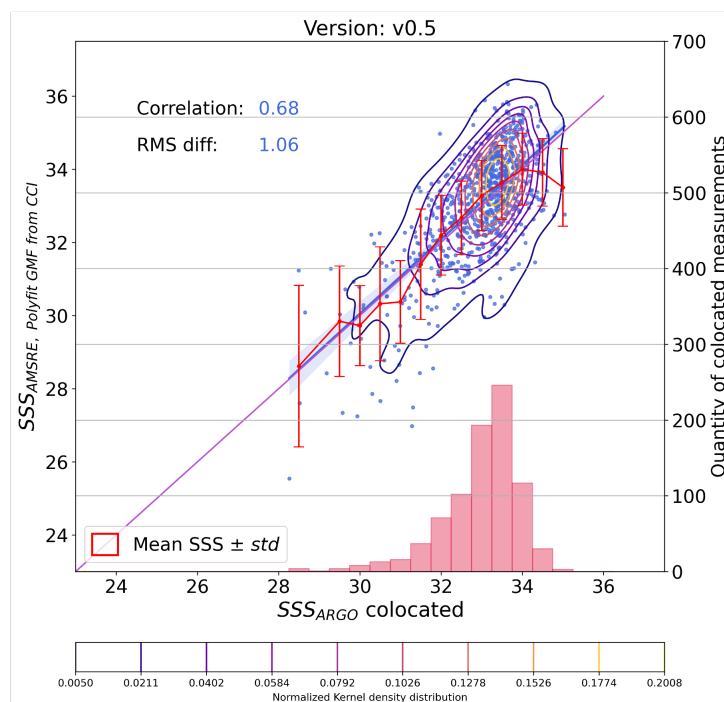


Figure 3.17 – Same as Figure 3.14 with additional filtering.

### 3.3.5 The Impact of the Diurnal Cycle

As discussed in Section 3.2.4.2.1, we initially planned to use the auxiliary SST product from CCI for the retrieval algorithm. However, as we conducted our study, we recognized the significance of the diurnal cycle, which prompted us to switch to AMSR-E data.

This change resulted in the final algorithm, given the scatterplot in Figure 3.11a. While the correlation slightly decreased from 0.68 to 0.66, we observed a minor increase in the rms-difference by 0.05 pss.

### 3.3.6 Influences of IOD

As a reminder, the Indian Ocean Dipole (IOD) is an irregular oscillation of sea surface temperatures in the Indian Ocean. It is characterized by anomalous cooling or warming of sea surface temperatures in the eastern and western parts of the Indian Ocean, respectively.

In their study, Akhil et al. (2016a) conducted a modeling study to examine the relationship between the IOD and the interannual variability in the BoB. To do this,

the authors calculated the Empirical Orthogonal Function (EOF) of the seasonal (SON) anomaly of the SSS in an attempt to identify the dominant modes of variability in the BoB. With a correlation of 0.88, between the first Principal Components (PC) of the EOF and the Dipole Mode Index (DMI) (measure of the strength and polarity of the IOD) of 0.88 they found a strong link between the River in the sea and the IOD. The second PC in its turn shows a strong (0.76) correlation with interannual variability of the river runoff in the north of the bay.

However, during recent studies Akhil et al. (2020) shows a far less obvious impact (correlation of 0.66) between the first PC and the DMI when using Soil Moisture and Ocean Salinity (SMOS) data. Moreover, the first EOF shows both signals linked to the river in the sea and the runoff.

In order to better understand this variation of the patterns, I use the reconstructed AMSR-E data to calculate its EOF. Even if the EOF done in Akhil et al. (2020) is only based on 9 years, which is statistically not accurate, I decided to redo the analysis with the  $SSS_{AMSR-E}$  for comparison. Note also that I decided to replace the DMI with the Sea level Dipole Index (SDI) to represent the variation of the IOD. The SDI is a Sea level anomaly based Dipole Mode Index.

Unlike previous studies (Akhil et al., 2016a; Akhil et al., 2020), the first two modes of the reconstructed AMSR-E EOF data exhibit distinct characteristics. The first mode (Figures 3.18a and b) appears to be mainly negative and only weakly correlated with the IOD (correlation of 0.15). However, the signal in the Andaman Sea is moderately correlated with the Irrawaddy discharges (correlation of 0.44), while the strong negative anomaly does not correspond to the Ganga-Brahmaputra runoff.

The second mode exhibits similarities with the second mode of the EOF of model SSS (Akhil et al., 2016a), with a negative signal in the northern part of the bay and a positive anomaly along the East Indian Coast extending to Sri Lanka. The correlation with the IOD has also improved to 0.59.

These results may be due to the underestimation of SSS for low SST, which is particularly pronounced near the northern coast. As a result, accurate reconstruction is challenging, and the dominant negative SSS anomaly will always be detected first by the EOF analysis. However, the second mode suggests an impact of the IOD on the EICC, as previously hypothesized (Akhil et al., 2016a; Akhil et al., 2020). Further analysis is

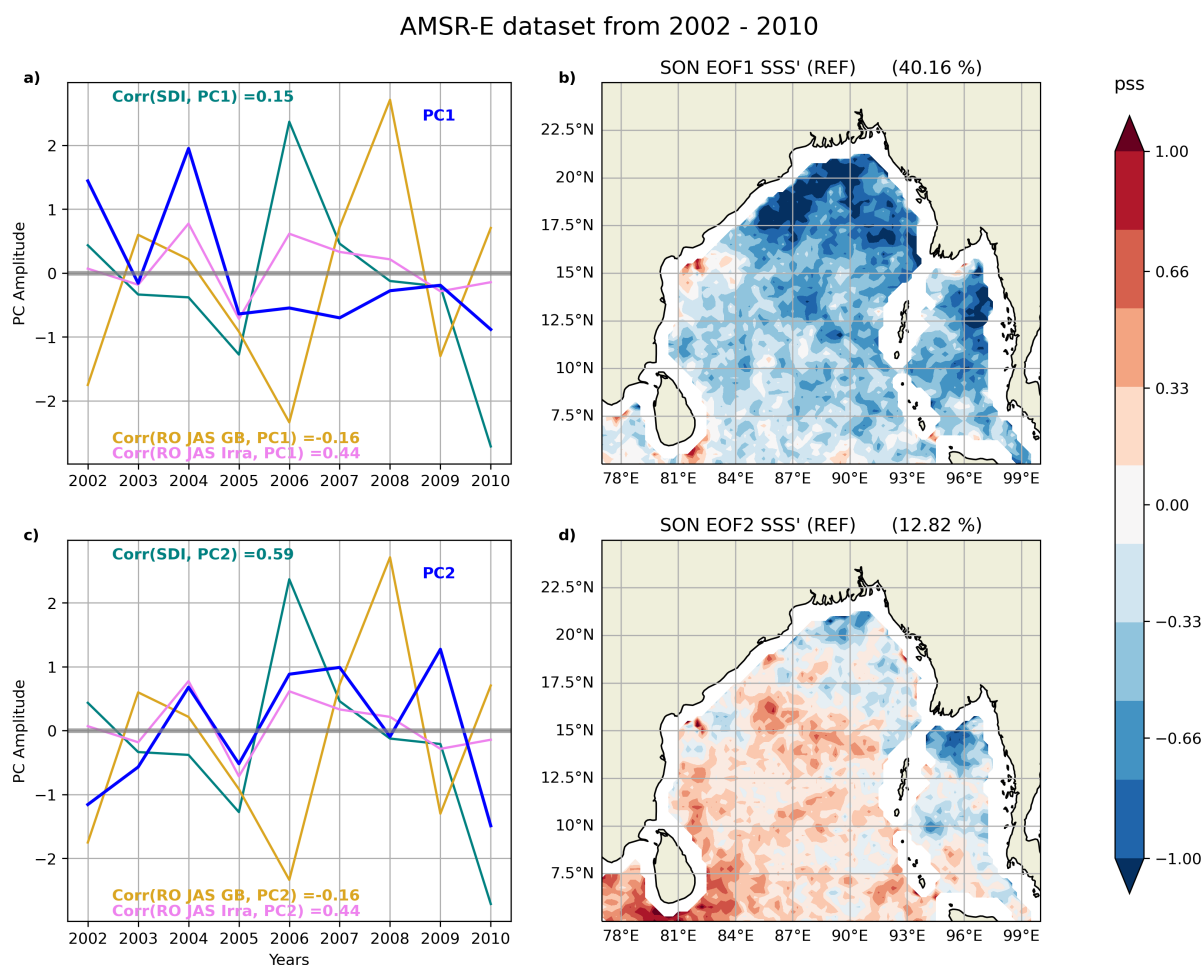


Figure 3.18 – a) and c) Time series of the normalized principal component of the first and second modes (PC1 and PC2) from an empirical orthogonal function (EOF) analysis of SON AMSR-E SSS interannual anomalies (blue), normalized SON Sea Level Anomaly-based Dipole Mode Index (SDI) (green), normalized JJA River Runoff from Ganges-Brahmaputra (yellow) and Irrawaddy (pink) from Jason-2 altimetry (Papa et al., 2012). The correlation of PC1 with the three different indices are indicated at the top and bottom of the panel. b) and d) Regression of SON AMSR-E SSS interannual anomalies (SSS', colour) to PC1 and PC2 over the 2002–2010 period. Top figures corresponds to first and the bottom figures to the second mode.

needed to investigate the potential influence of the IOD on the extension of the "river in the sea".

Figure 3.19 depicts the extension of the freshwater tongue averaged within 200 km from the East Indian coast and the average anomaly of the SON. It is observed that in 2006, when the IOD had a strong positive anomaly, the extension of the freshwater

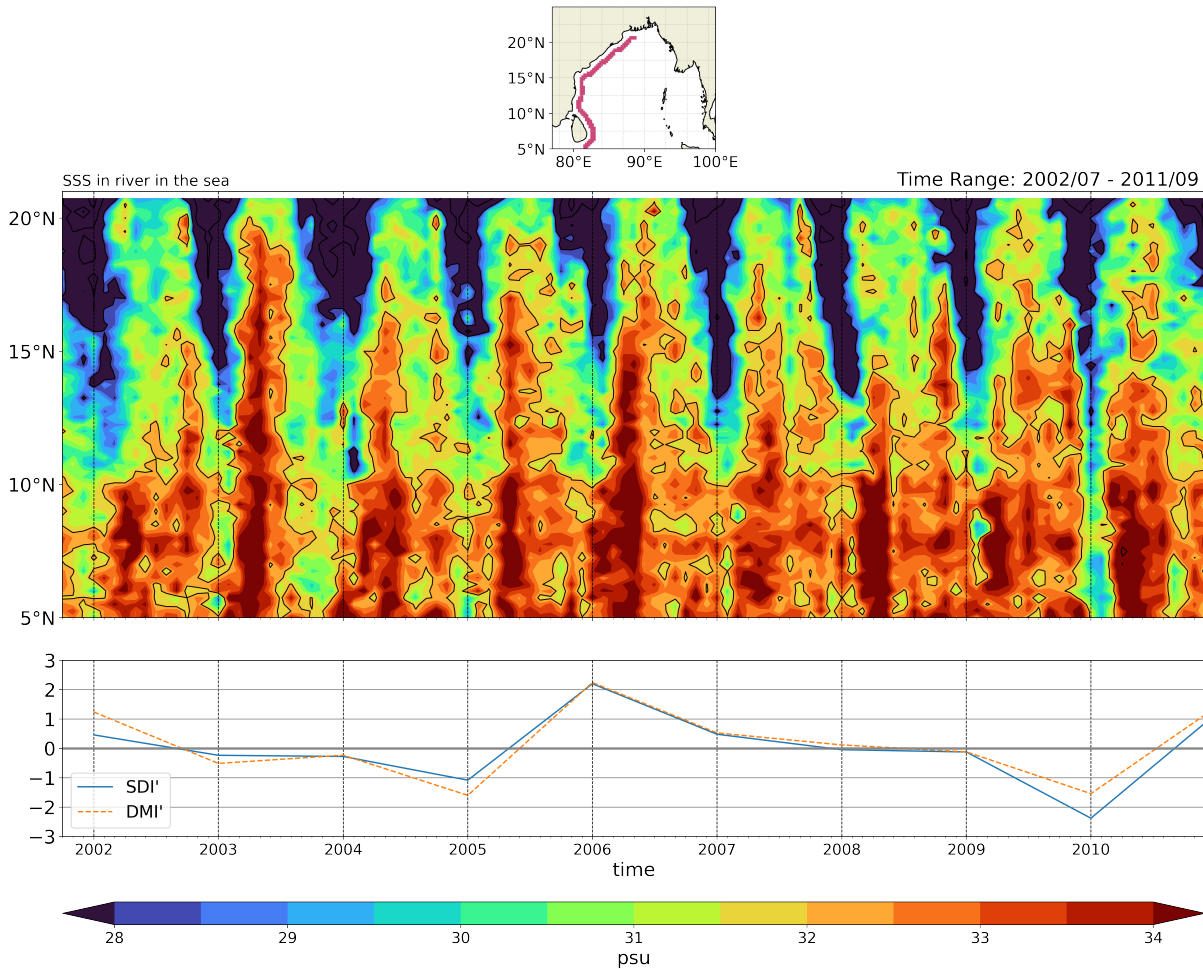


Figure 3.19 – Hovmöller diagram for the "River in the sea" for the entire AMSR-E period. Top panel is the geographical situation of the studies area (distance to the coast less than 200 km). Middle panel represents the longitude SSS mean of the highlighted section from the top panel. Bottom panel is the SDI anomaly mean for SON which is closely linked to the IOD. Note that the x-axis of the middle and bottom panel represents the time between 2002 and 2011 and that the ticks are set on the October Period, when the IOD is reaching its peak, for each year.

seemed to be shorter than usual, whereas in 2010, which had a strong negative anomaly, there was a significant extension of the tongue. These findings are consistent with those of Akhil et al. (2020), who found that positive IOD events tend to lead to a negative SSS anomaly and negative IOD to a positive anomaly along the west coast of the BoB.

However this relation is not systematically verified with AMSR-E SSS. For instance, in 2005, the SDI negative anomaly was stronger than in 2004, but the freshwater tongue

seemed to be stronger and longer in 2004. The same holds for 2002, where the freshwater was strongly present despite a positive SDI anomaly.

### 3.4 Additional results since submission

In Figure 3.11, I showed the validation of the AMSR-E SSS using ARGO data only. Since the submission of the paper, I was able to use a combined (Argo profilers and measurements from ships of opportunity, described in Section 2.2) in situ dataset to carry out a more advanced validation.

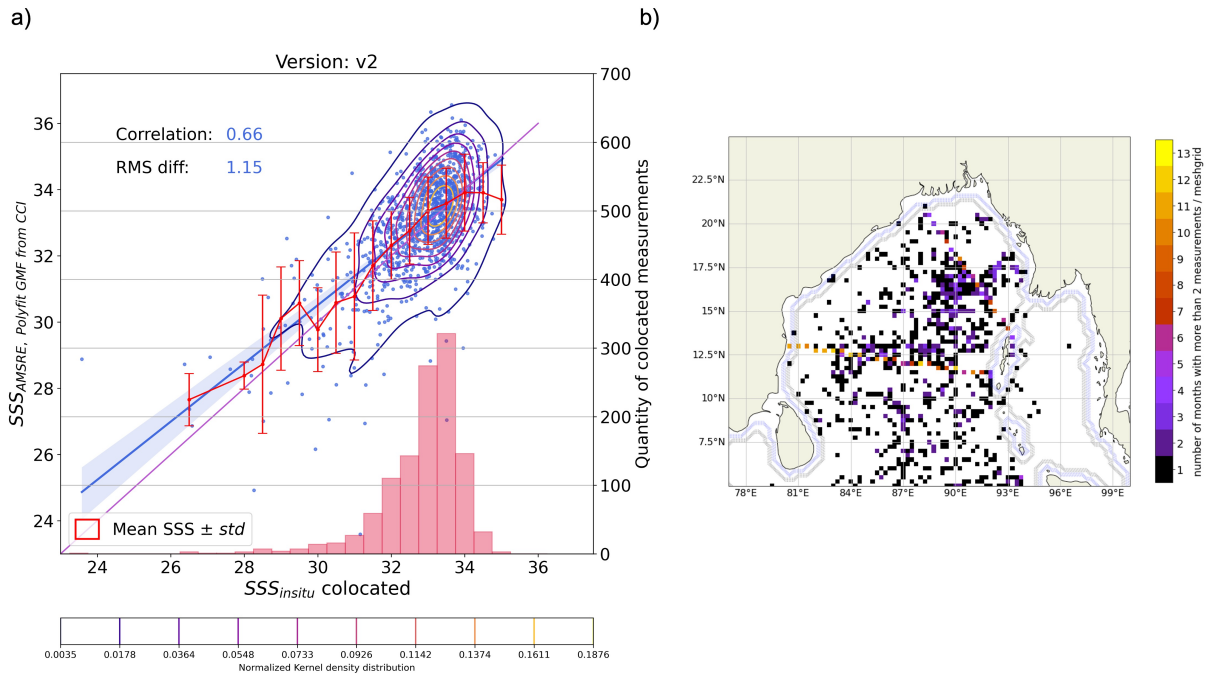


Figure 3.20 – a) Scatterplot of SSS from AMSR-E versus co-located SSS from in situ data with their kernel density distribution in color contours (see bottom legend). The blue line represents the linear regression with the 95% confidence interval in translucent blue. The red curve is the mean value with its standard deviation for each bin (0.5 pss) with more than 3 observations. The barplot in red is the distribution of the number of collocated measurements in each bin. b) Spatial distribution of ARGO and ship measurements used in the scatter plot (a). The dotted contour line in blue shows the coastal boundary before applying additional filtering, the black one is the coastal boundary once the filter applied (used in Section 3.3.4).

Comparing Figure 3.20 to Figure 3.11, it is possible to see the impact of the added data.

Data in the low SSS regions (SSS < 27 pss) can be identified and validated. Indeed, the regression line does moves away from the x=y line, and the rms-difference does increase (from 1.09 pss to 1.15 pss), but this is mostly due to local points in the really low SSS zones. As explained in Section 3.2.4.1, the sensitivity of  $\Delta T_v$  to SST in the BoB is  $\sim 0.04$  K/°C. For low SSS (see Figure 3.1b),  $\delta\Delta T_v/\delta SST$  increases, reaching -0.065 K/°C at SSS = 20 pss. Thus due to SST larger errors are expected in the SSS retrieval from AMSR-E for low SSS. Thus distancing from the x=y line is expected for these SSS values. However, for the SSS values between 28 pss and 31 pss the accuracy seems to increase as error bars decrease. The correlation however is not impacted and remains at 0.66.

# INTRINSIC AND EXTERNALLY-DRIVEN SSS VARIABILITY IN THE BOB

---

As previously mentioned in Section 1.3.3, several phenomena can influence the salinity non-seasonal variability in the BoB. In this chapter, the influence of these phenomena (in particular the IOD and oceanic eddies) on SSS will be briefly introduced, prior to validating numerical experiments from the IMpacts of freshwater discHarge interannual variability on Ocean heaT-salt contents and rEgional sea level change over the altimetry Period (IMHOTEP) dataset, and using them to assess BoB salinity variability.

## 4.1 Influences ...

### 4.1.1 ... of the IOD

In Section 3.3.6, it was shown that - despite some encouraging results - the AMSR-E data does not always resolve the BoB SSS interannual variability well, and hence cannot be used to describe the IOD SSS signature in the BoB. Acknowledging this limitation, I use the reference data from the CCI dataset and follow the EOF approach outlined in (Akhil et al., 2016a) to describe the IOD SSS signature in the BoB, but adding one more year (2019) to the dataset used in this study (2010 to 2018 period).

Figure 4.1b displays a pattern similar to the EOF based on the Sea Surface Salinity Anomaly ( $SSS'$ ) of SMOS presented by Akhil et al. (2020). The first modes exhibits a strong negative signal in the northern and eastern parts of the BoB. There is also a positive anomaly in the southwestern part of the BoB, which is strongest along the east Indian coast.

This mode was earlier attributed to the effect of the IOD, through changes in the basin-scale circulation (Akhil et al., 2016a). The correlation between the first PC and the runoffs of the GB and Irrawaddy are indeed low (0.17) excluding them as a possible

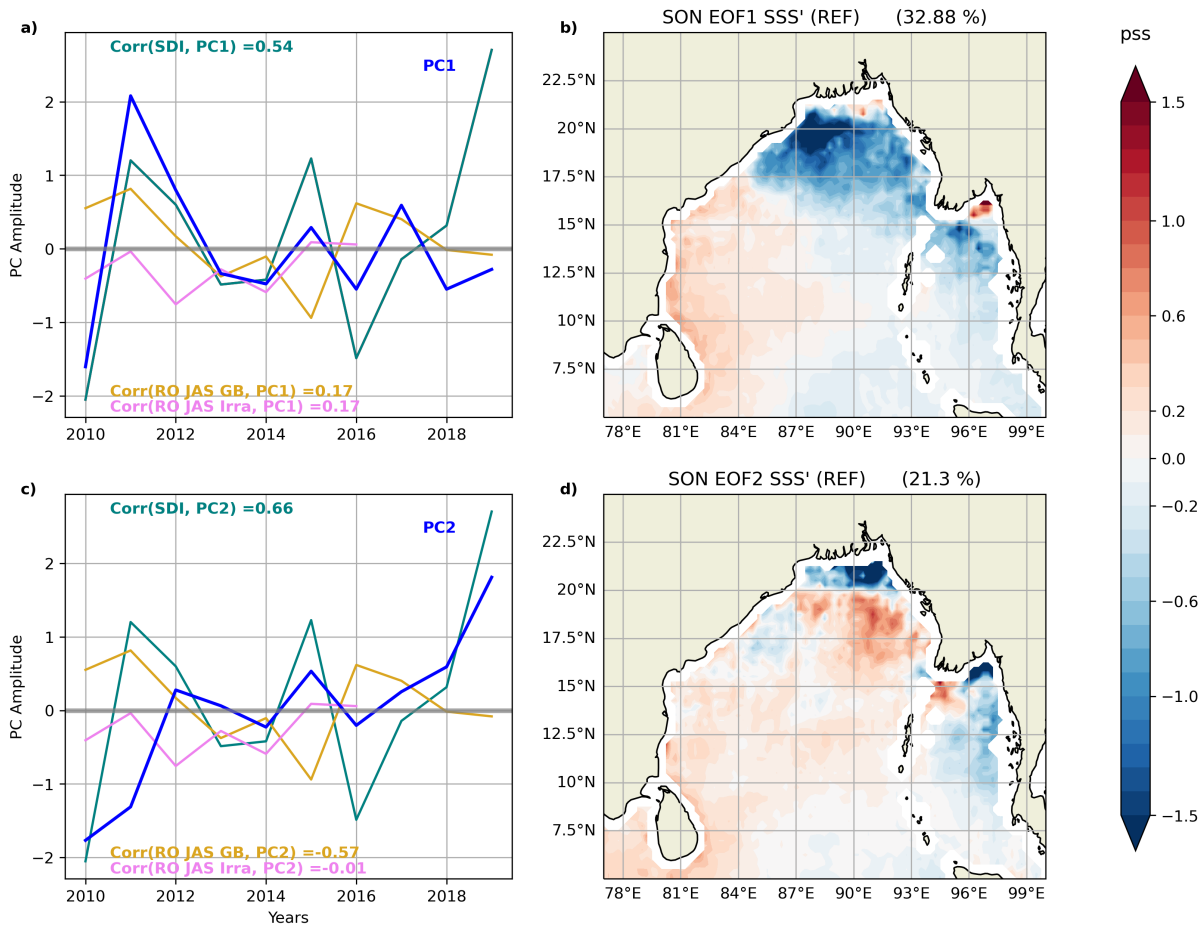


Figure 4.1 – a) and c) Time series of the normalized principal component of the first and second modes (PC1 and PC2) from an empirical orthogonal function (EOF) analysis of SON CCI SSS interannual anomalies (blue), normalized SON Sea Level Anomaly-based Dipole Mode Index (SDI) (green), normalized JJA River Runoff from Ganges-Brahmaputra (yellow) and Irrawaddy (pink) from Jason-2 altimetry (Papa et al., 2012). The correlation of PC1 with the three different indices are indicated at the top and bottom of the panel. b) and d) Regression of SON AMSR-E SSS interannual anomalies (SSS', colour) to PC1 and PC2 over the 2002–2010 period. Top figures corresponds to first and the bottom figures to the second mode.

source. The correlation with the dipole mode index, that we use (the SDI) is higher but only 0.54. This is lower than the correlation obtained in the longer (1993 to 2012) modeling study of (Akhil et al., 2016a) (who found a correlation of 0.76), indicating that the relation with the IOD is either weaker other that period, or intermittent, as already pointed out by (Akhil et al., 2020).

The second mode displays a negative pattern along the river estuaries, much more

localized than for the first mode, suggesting that it corresponds to the effect of rivers. The associated PC is both correlated with the SDI (0.66) and anti-correlated with the GB river runoff (-0.57), suggesting that this mode does not separate clearly those two contributions, as was the case in (Akhil et al., 2016a)

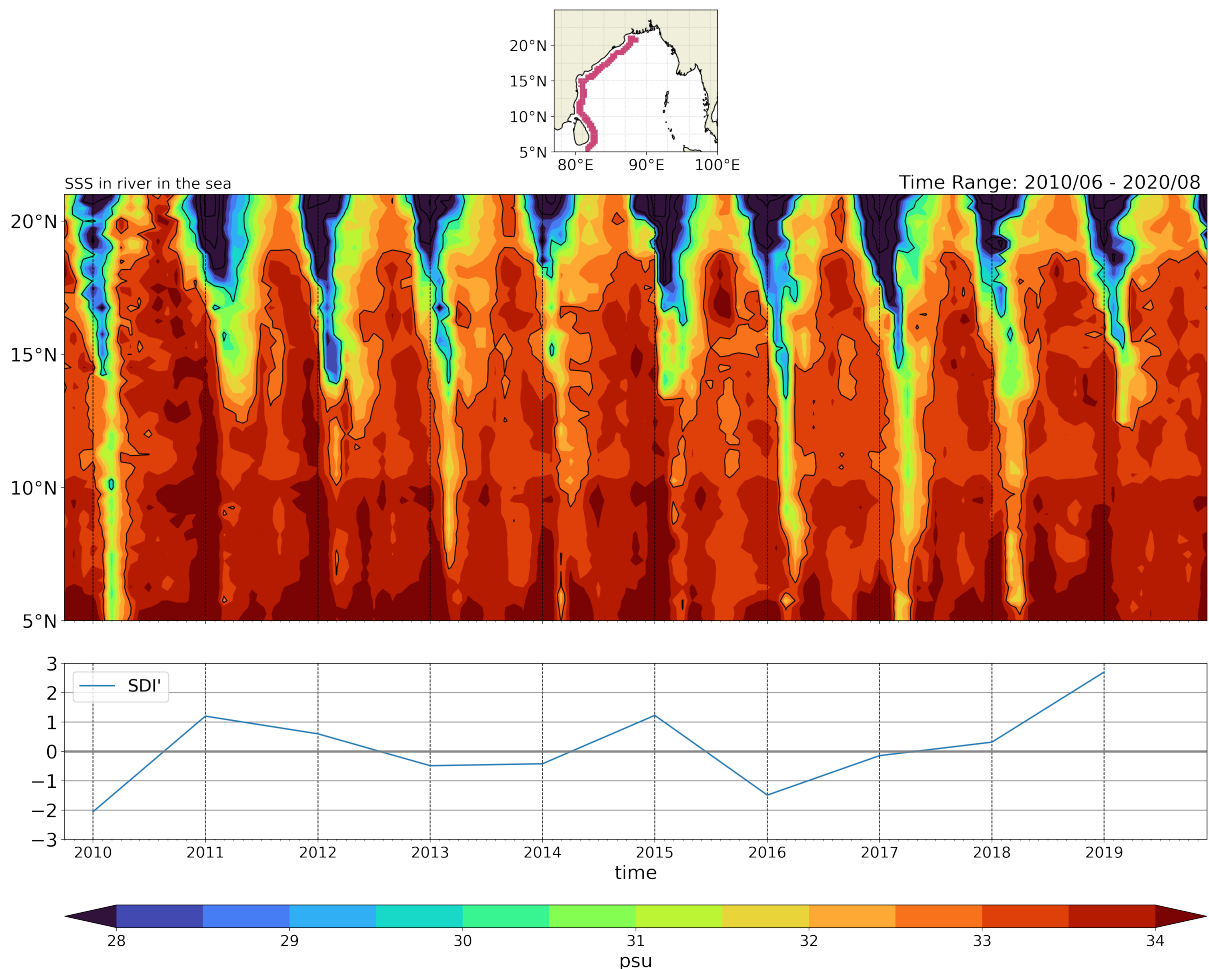


Figure 4.2 – Hovmöller diagram for the "River in the sea" for the entire CCI period. Top panel is the geographical situation of the studies area (distance to the coast less than 200 km). Middle panel represents the longitude SSS mean of the highlighted section from the top panel. Bottom panel is the SDI anomaly mean for SON which is closely linked to the IOD. Note that the x-axis of the middle and bottom panel represents the time between 2002 and 2011 and that the ticks are set on the October, when the IOD is reaching its peak, for each year.

The Hovmöller diagram shown in Figure 4.1 suggests some anti-correlation between

the river in the sea and the SDI, as noted by Akhil et al. (2020), with for instance low salinity all the way to 5°N in 2010 and 2016 (both negative IOD years), and a river in the sea that does not expand southward of 12°N in 2019, 2015 or 2011 (positive IOD years). However, similar to the Hovmöller diagram for AMSR-E (Figure 3.19), the intensity of the IOD and the extension of the river in the sea do not always match. For example, the IOD has a similar negative intensities in 2013 and 2014, but the river extends more southward in 2013. Similarly, the river extends quite far south in 2017 and 2018, while those are not strong negative IOD years. This indicates that other mechanisms than the IOD probably drive the river in the sea extension or interfere with it.

### 4.1.2 ... of Eddies

Mesoscale eddies are numerous and energetic in the BoB (Chelton et al., 2011; G Chen et al., 2012; Cui et al., 2016; Lin et al., 2019). They have a horizontal scale of the order of 100 km to 150 km in the Bay of Bengal (Chelton et al., 2011), a characteristic size which is similar to the width of the EICC, and previous studies have shown their ability to modulate and even divert the course of the river in the sea (Benshila et al., 2014; Fournier et al., 2017; Hareesh Kumar et al., 2013) (see Figure 4.3) and to transport freshwater horizontally (Chaitanya et al., 2021; Cui et al., 2022).

The EOF and the Hovmöller diagram raise several questions. The modeling study of (Akhil et al., 2016a) identified two clear modes of interannual variability in the BoB, one clearly associated with changes in circulation driven by the IOD wind anomalies, and a second one associated with the GB runoff interannual anomalies. The modeling study of Nyadjro (2021) also highlighted a strong positive anomaly caused by the IOD that creates anomalies in SON resembling the 1st EOF from (Akhil et al., 2016a) (see their Figure 4). The observational analysis above yields different results. First, it does not successfully disentangle the IOD and GB-induced SSS variations, and the link between the IOD and the river in the sea extension does not seem as robust as in the modeling studies.

There are several possible explanations for these findings. The remote sensing dataset covers a shorter period than the modeling study of (Akhil et al., 2016a) (2010 to 2019 against, 1993 to 2012, i.e., 10 vs 20 years, as AMSR-E oceans brightness temperature data has not shown enough sensitivity), that may not allow to properly disentangle the effects of the IOD from those of river runoffs. Another possible explanation for the differences between the model and the observed data is the failure to consider the localization and intensity of eddies. The Figure 4 of Nyadjro (2021) for instance displays a strong

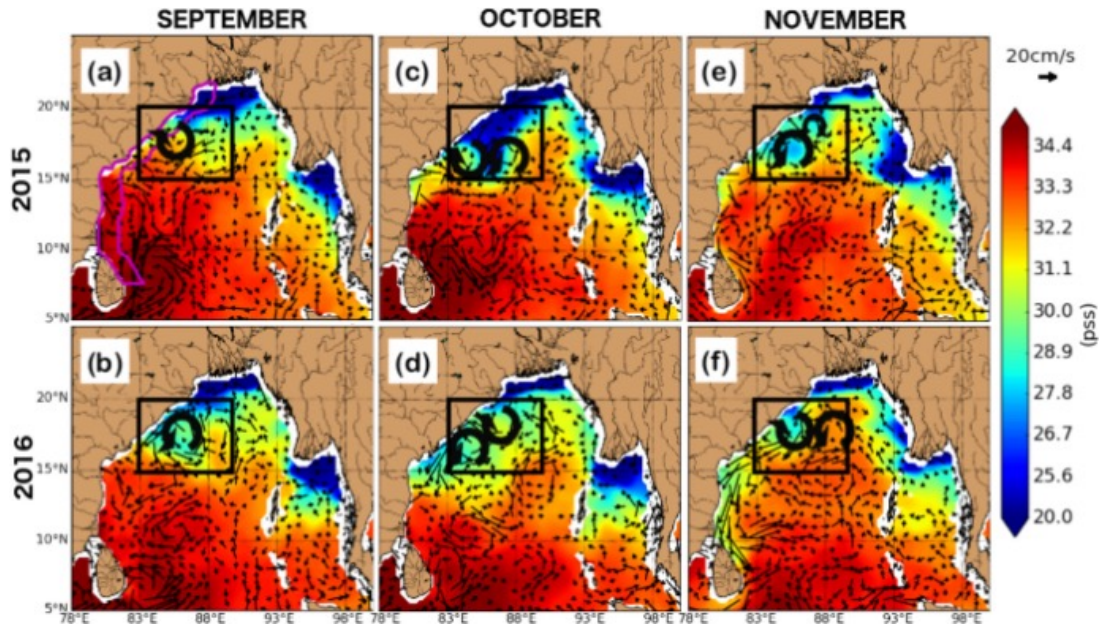


Figure 4.3 – (a), (c), and (e) SMAP SSS for September, October, and November in 2015 and (b), (d), and (f) 2016. Monthly AVISO currents are represented on top, only one vector in three is represented and currents below  $10 \text{ cm s}^{-1}$  are not displayed (after Fournier et al. (2017)). The good agreement between the SSS and current structures associated with both the EICC and eddies indicate that advection plays a strong role in controlling the SSS structure along the west coast of India, with a strong stirring of the SSS field by meso-scale eddies.

modulation of the SSS spatial patterns by mesoscale eddies (Akhil et al., 2016a).

Contrary to the IOD, for which the BoB SSS anomalies are largely due to the wind-driven BoB circulation anomalies (Akhil et al., 2016a), eddies are not directly driven by surface fluxes. Instead, they grow by extracting energy from the background flow through the barotropic and/or baroclinic instability mechanisms (e.g., G Chen et al., 2012). They are generated *internally* through oceanic instabilities, rather than *forced* by an external momentum or buoyancy forcing. This has important consequences. For instance, an oceanic simulation that is not constrained by ocean data will be able to reproduce the signals that are externally forced, such as the response to the IOD. While a general circulation model experiment will spontaneously produce eddies through the aforementioned instability processes, it will only reproduce the statistics of these eddies, but not the location of individual eddies, due to strong sensitivity of the eddy field to initial conditions, e.g., its chaotic nature. This means a forced ocean model can reproduce the observed SSS signals associated with the IOD, but not that associated with individual

eddies, which has strong consequences for how to validate it to observations.

Some of the studies mentioned above (Benshila et al., 2014; Fournier et al., 2017; Hareesh Kumar et al., 2013) suggest that the signals associated with eddies are not negligible, and that they can for instance modulate the river in the sea (see Figure 4.3). The main question that is explored in the current chapter is thus to work out the relative contributions of externally forced and internally-generated oceanic signals to SSS non-seasonal variations in the BoB. More specifically, can the eddy-induced transport divert the "river in the sea" some years or blur it significantly?

## 4.2 Methodology of the variability determination

In order to answer the scientific question regarding the intrinsic variability of SSS in the Bay of Bengal, I use the ensemble simulation outputs described in Section 2.4.

This ensemble approach has been used since the 1990's for the atmosphere (e.g., Rowell, 1998). In the latter, turbulence instabilities give rise to anticyclones and depressions (sizes of about 1000/2000 km) that could already be resolved by the numerical capacity of atmospheric models (typical resolutions of about 200 km). In ocean sciences however, ensemble simulations are a quite recent and innovative approach, as turbulent mesoscale eddies have typical sizes of 100/200 km. Following a workshop of the CLIVAR Ocean Model Development Panel in 2014, one can quote the Treguier et al. (2014) CLIVAR exchanges publication : "Eddying ocean simulations pose a new challenge because of the emergence of intrinsic variability caused by oceanic instabilities (Penduff et al., 2014; Penduff et al., 2011). Together with the increased synoptic variability in high resolution atmospheric models, these extra modes of variability in the ocean make ensemble simulations necessary to study cause and effect relationships in the Earth's climate."

As presented in Section 2.4, the IMHOTEP project adopts such an ensemble approach, which gives a good framework to quantify the contribution of ocean intrinsic variability (i.e., eddies) to the total non-seasonal variability of SSS in the BoB. The method to compute each component of the variability from ensemble simulations is well established (e.g., Bessières et al., 2017; Carret et al., 2021; Leroux et al., 2018) and is recalled hereunder.

**Definition of the forced and intrinsic components** In the present work, the main signal I consider is the SSS anomaly relative to the seasonal cycle (i.e., non seasonal SSS

anomaly), which is first computed for each member of the dataset. Hereunder this original signal at time index  $t$ , and for member index  $j$  will be noted  $x_j(t)$ .

The forced component of the signal,  $X(t)$ , is estimated as the mean of all ensemble members at every time step :

$$X(t) = \langle x_j(t) \rangle = \frac{1}{M} \sum_{j=1}^M x_j(t)$$

where  $\langle . \rangle$  is the ensemble mean operator, and  $M$  is the total number of ensemble members. This yields a single time series at each spatial point, which is called the "ensemble mean" signal.

The intrinsic components of the signal is then defined as the difference between the original signal of each member and the ensemble mean:

$$x'_j(t) = x_j(t) - X(t)$$

In our case, this yields 10 time series at each spatial point for each of the 10 members of the ensemble. By construction, the average of the intrinsic signal is thus zero both at each time step and also over the total population.

**Forced Variability** Forced Variability refers to changes in a system or phenomenon that result from external factors or forces. In the case of climate simulations, these external factors can include natural factors such as changes in solar radiation or volcanic eruptions, as well as human-caused factors such as greenhouse gas emissions and land-use changes. For the case of this study (oceanic simulations), those external factors are atmospheric forcings (i.e., winds, heat fluxes, precipitations or runoffs).

The amplitude of the forced variability  $\sigma_{forced}$  is given by the temporal standard deviation of the ensemble mean at each grid point:

$$\sigma_{forced} = \sqrt{Var_{time}[X(t)]} = \sqrt{\frac{1}{T-1} \sum_{t=1}^T (X(t) - \overline{X(t)})^2}$$

where  $Var_{time}[\cdot]$  is the time variance operator,  $\overline{\cdot}$  is the time mean operator, and  $T$  is the total number of time-steps (in days, months, years...).

**Intrinsic Variability** Intrinsic Variability refers to variations in a system or phenomenon that arise from within the system itself, without the influence of external forces or factors. The dynamical response of the nonlinear ocean to the atmospheric variability is complex: dynamical system approaches and diagnostics of potential vorticity balances have demonstrated that in presence of stochastic, seasonal, or constant atmospheric forcing, oceanic non-linearity can intrinsically generate and sustain variability of the horizontal circulation at interannual time scales (Penduff et al., 2011). Global ocean simulations indeed show that resolving mesoscale turbulence (i.e., eddies, even partly) promotes the emergence of low-frequency chaotic intrinsic variability which causes substantial random fluctuations of the ocean state variables (e.g., sea level) up to multiple decades in eddy-active regions of the world ocean. This random low-frequency chaotic intrinsic variability is superimposed on the atmospherically forced (or simply “forced”) fluctuations, which are directly controlled by the atmospheric variability (Penduff et al., 2019). It is important to note that intrinsic variability is much weaker in non-turbulent ocean models, and that for the case of the BoB study, the latter is generated by the numerous eddies present in that basin.

The estimation of the amplitude of intrinsic variability involves the computation of the "ensemble spread",  $\epsilon^2(t)$ . This spread is the unbiased ensemble variance (represented as  $Var_{\text{ens}}[\cdot]$ ) of the intrinsic components of all members:

$$\epsilon^2(t) = Var_{\text{ens}}[x'_j(t)] = \frac{1}{M-1} \sum_{j=1}^M \left( x'_j(t) - \underbrace{\langle x'_j(t) \rangle}_{=0} \right)^2 = \frac{1}{M-1} \sum_{j=1}^M x'_j(t)^2$$

That ensemble spread indicates how dispersed or concentrated the data is around the ensemble mean at each time-step. The amplitude of the intrinsic variability is then obtained by the square root of the time average of the spread :

$$\sigma_{\text{intrinsic}} = \sqrt{\overline{\epsilon^2(t)}}$$

**Total Variability** Total variability refers to the sum of all sources of variability in the system. The amplitude of the total variability in each member  $j$  and at each grid point is:

$$\sigma_{\text{tot},j}^2 = Var_{\text{time}}[x_j(t)] = \frac{1}{T-1} \sum_{t=1}^T \left( x_j(t) - \overline{x_j(t)} \right)^2$$

The amplitude of the total variability can be obtained by calculating the ensemble

mean of the above expression:

$$\sigma_{tot} = \sqrt{\langle \sigma_{tot,j}^2 \rangle}$$

As shown in Leroux et al. (2018), the amplitudes of the three variabilities defined above are linked by the sum of their squared values:

$$\sigma_{tot}^2 = \sigma_{forced}^2 + \sigma_{intrinsic}^2$$

### 4.3 Validation of the IMHOTEP dataset

In this section, my objective is to investigate whether the intrinsic variability of the oceans, including the role of eddies, contributes to the SSS interannual variability in the BoB. More specifically, I will investigate the potential role of eddies in modulating the influence of the IOD on the "river in the Sea" length. To achieve this goal, ensemble simulations produced with the NEMO Ocean General Circulation model (Madec et al., 2022), referred to as IMHOTEP hereafter (see Section 2.4). The study employs the reference experiment from the IMOTHEP dataset, specifically the "EGAI" experiment. This experiment consists of 10 ensemble members and spans a period of 39 years (1980-2018). Interannual surface boundary conditions include a careful prescription of interannually-varying runoffs. Since this dataset is new, its reliability is first assessed in the next subsection, in particular the representation of the SSS, IOD and eddies.

#### 4.3.1 Removal of a spurious SSS signal in the IMHOTEP dataset

To begin with, the time series of the bay-averaged SSS in IMHOTEP is compared with CCI validation dataset, and the Glorys  $\frac{1}{12}^\circ$  (hereafter Glorys) reanalysis. Figure 4.4a shows that the temporal behavior of the Glorys dataset is similar to that of the CCI dataset during their common period (correlation of 0.73), which suggests that Glorys can be considered a reliable extension of the CCI dataset (note that the CCI data was not assimilated into Glorys).

The IMHOTEP time-series of the SSS anomaly has a positive bias of  $\sim 0.3$  pss before 2000,  $\sim -0.2$  pss bias from 2000 to 2010, and  $\sim -0.5$  bias after 2013, with significant "steps" between those periods, as shown in Figure 4.4a. These steps are also visible in Appendix B.I, where the difference maps between these periods are displayed. The origin

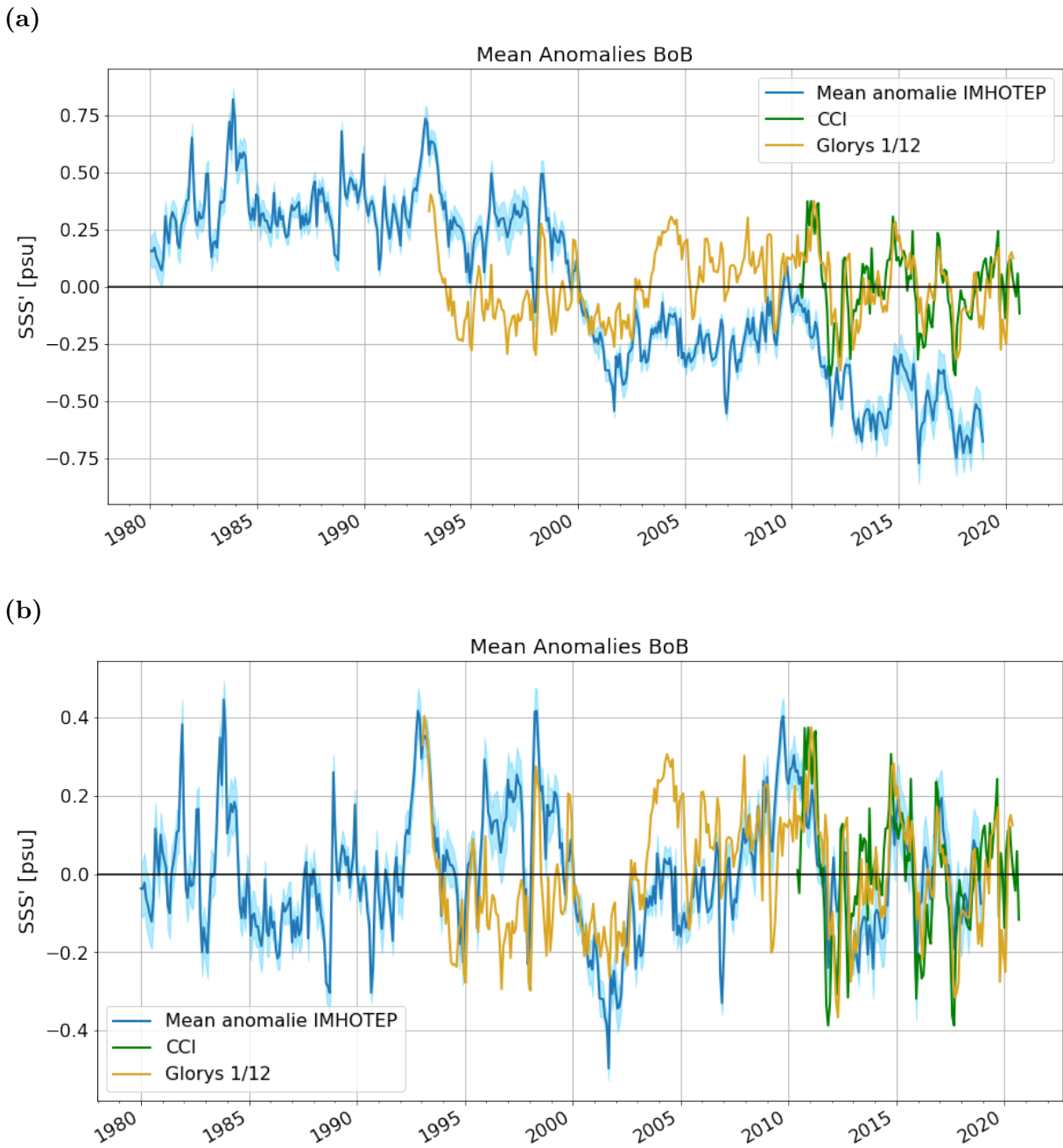


Figure 4.4 – Time series of monthly averaged SSS anomalies in the BoB between 1980 and 2020 for a) raw IMHOTEP data and b) detrended IMHOTEP data. In blue is the average anomaly of IMHOTEP, the light-blue shade behind is the standard deviation between the different members. Yellow represents the Ocean reanalysis Glorys  $1/12^\circ$  and green represents the CCI dataset.

of this behavior will have to be clarified, but it may be due to a drift in either the runoff or precipitation forcing. Thus, it was decided to remove this artificial trend, through a nonlinear detrending.

The detrending is calculated at each IMHOTEP gridpoint, by fitting a fourth-order polynomial to the annual mean ensemble mean SSS. Figure 4.4b shows that this detrending successfully removes the "steps" in the anomalies (see Appendix B.I). While this strongly reduce the offset with the CCI reference dataset over the common period, there are still some important offsets with Glorys SSS during several years, such as 1997 or 2004. This suggest that, while our detrending strategy was successful in removing most of the spurious basin-average drift, there are probably some spurious SSS signals remaining for the basin-average SSS.

To investigate the behavior in specific regions of interest in the bay, the analysis is further carried out in two boxes as shown in Figure B.1 and B.2: those regions are selected because they encompass the GB river mouth, and the east coast of India, hence regions where SSS signals associated with river runoff and the IOD, respectively, can be large. While the spurious SSS drifts was very visible on the BoB average SSS, its is much less visible for the northern BoB (see Figure 4.5a). The correlation between IMHOTEP and Glorys has for instance not changed with the detrend (0.73 before and after, and the rms-difference between drops only by 0.02 pss, from 0.79 to 0.77 pss.

The second region of interest is situated in the western boundary zone of the BoB. In this region, the effect of the spurious drift is more pronounced and appears as a negative drift in the IMHOTEP time-series (see Figure 4.6a). Applying the detrending largely removed this spurious signal, although some notable differences sometimes appear between the Glorys reanalysis and IMHOTEP such as in 1995 and 2005. But overall, the detrending has removed most of the spurious signals in the two regions of interest, and there is in general a good phase relation between the IMHOTEP ensemble mean and Glorys reanalysis. The strong decrease of the rms-difference between IMHOTEP and Glorys from 0.70 pss to 0.58 pss and the bias from IMHOTEP from 0.44 to 0.31 and the improvement of the correlation from 0.41 to 0.51 suggest that this corrected dataset can be used to estimate the internally generated and externally forced SSS variability in the BoB. Thus, the detrended IMHOTEP dataset is always used in the rest of the chapter.

### 4.3.2 Seasonal Cycle Validation

The seasonal SSS cycle in the IMHOTEP run is now to be validated against those in the CCI and Glorys datasets. Figure 4.7 shows that both IMHOTEP and Glorys display similar patterns of SSS climatology, with low SSS close to the Ganga-Brahmaputra and Irrawaddy estuaries during and after the monsoon, and a southward expansion of this fresh water along the west coast of India in SON. Although the coastal values are not available in the CCI dataset, values a bit more offshore suggest that IMHOTEP and Glorys tend to have too low SSS close to the estuaries, especially in SON and DJF. The southward expansion of the river in the sea in the two modelling datasets in DJF is not very clear in the CCI dataset. IMHOTEP exhibits overestimated of SSS relative to CCI around and east of Sri Lanka. Overall, the climatological SSS is hence reasonable in IMHOTEP, despite too low SSS near estuaries.

### 4.3.3 Validation of non-seasonal signals

To validate IMHOTEP, a detailed comparison of Sea Surface Salinity (SSS) and Sea Level Anomaly (SLA) is performed, between an IMHOTEP member and the Glorys (for Sea Level Anomaly (SLA)) and CCI (for SSS) datasets for the SON season (see Figure 4.9 and Figure 4.8, respectively). For each variable, I compute the standard deviation of IMHOTEP and the reference dataset, their correlation and rms-difference. I focus my comparisons on the SON season because it is the season where the "river in the sea" is most developed (Figure 4.7, Akhil et al., 2014 ) and where the IOD-induced variability is strongest (Akhil et al., 2016a; Akhil et al., 2020). I will also show later that it is the season when the intrinsic SSS variability is strongest.

I start by SLA, because it is both a proxy for the coastal circulation anomalies associated with the IOD and for eddies. Glorys (which assimilates altimetry data) has a strong variability in the western half of the BoB, with maxima of up to 10-12 cm west of Sri Lanka and the west coast of India between 13 and 19°N. Those correspond to regions of strong eddy activity (Cui et al., 2016), which are severely underestimated in IMHOTEP (the sea level std is rather 6-8 cm in those regions). This underestimated variability, and the fact that the eddies in a free simulation can not be in phase with those in observations, as demonstrated by the weak correlations in the western half of the BoB, result in a root mean square error of over 12 cm. The correlations between IMHOTEP and Glorys are on the other hand high at the BoB periphery, i.e., along the coastal waveguide. This sug-

gests that wind-forced wave signals that travel around the BoB as coastal Kelvin waves are well reproduced by IMHOTEP. Overall, IMHOTEP strongly underestimates the eddy variability in the BoB (which may be an issue for our study, as will be discussed later). This may be due to the fact that its horizontal resolution of  $1/4^\circ$  is only eddy-permitting but not eddy-resolving (Lellouche et al., 2021)

In summary, the IMHOTEP correctly reproduces the SLA variations along the coast where the forced variability is strongest, but its accuracy decreases in areas where intrinsic variability becomes stronger. Similar results were obtained for the remaining seasons, which are presented in Appendix B.III.

Let us now discuss the SSS non-seasonal variations validation. The SSS variability is strong near the GB and Irrawaddy estuaries in CCI, and along the west coast of India. IMHOTEP displays a similar pattern, but with a much larger variability. Therefore, it can be concluded that the IMHOTEP overestimates the SSS non-seasonal variability. The correlation with CCI SSS anomalies tends to be lower than that for sea level, and much more patchy. There are areas in the BoB periphery where this correlation reaches 0.8, but the correlation in most of the BoB central part is quite low, between 0 and 0.4. This can either suggest that the forced SSS salinity signals are not well reproduced by the model, for instance because of a deficient rain or wind forcing. But it may also as well indicate a strong contribution for intrinsic SSS variations in the BoB central part.

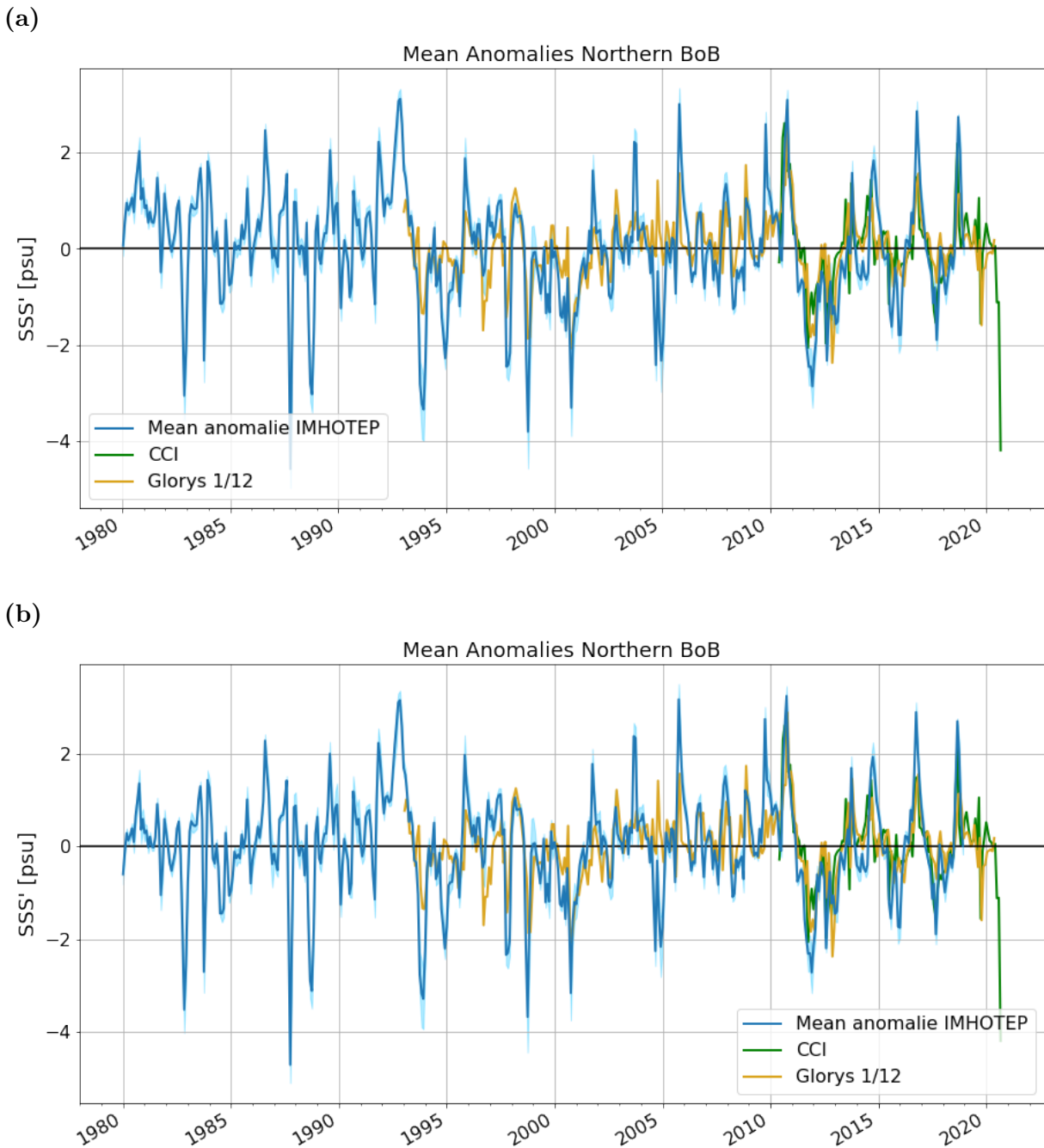


Figure 4.5 – Time series of monthly averaged  $SSS'$  in the Northern BoB ( $[19^{\circ}\text{N}-22.75^{\circ}\text{N}; 85^{\circ}\text{E}-93.25^{\circ}\text{E}]$ , black box in Figure B.2) between 1980 and 2020 for a) raw IMHOTEP data and b) detrended IMHOTEP data. In blue is the average anomaly of IMHOTEP, the light-blue shade behind is the standard deviation between the different members. Yellow represents the Ocean reanalysis Glorys  $1/12^{\circ}$  and green represents the CCI dataset.

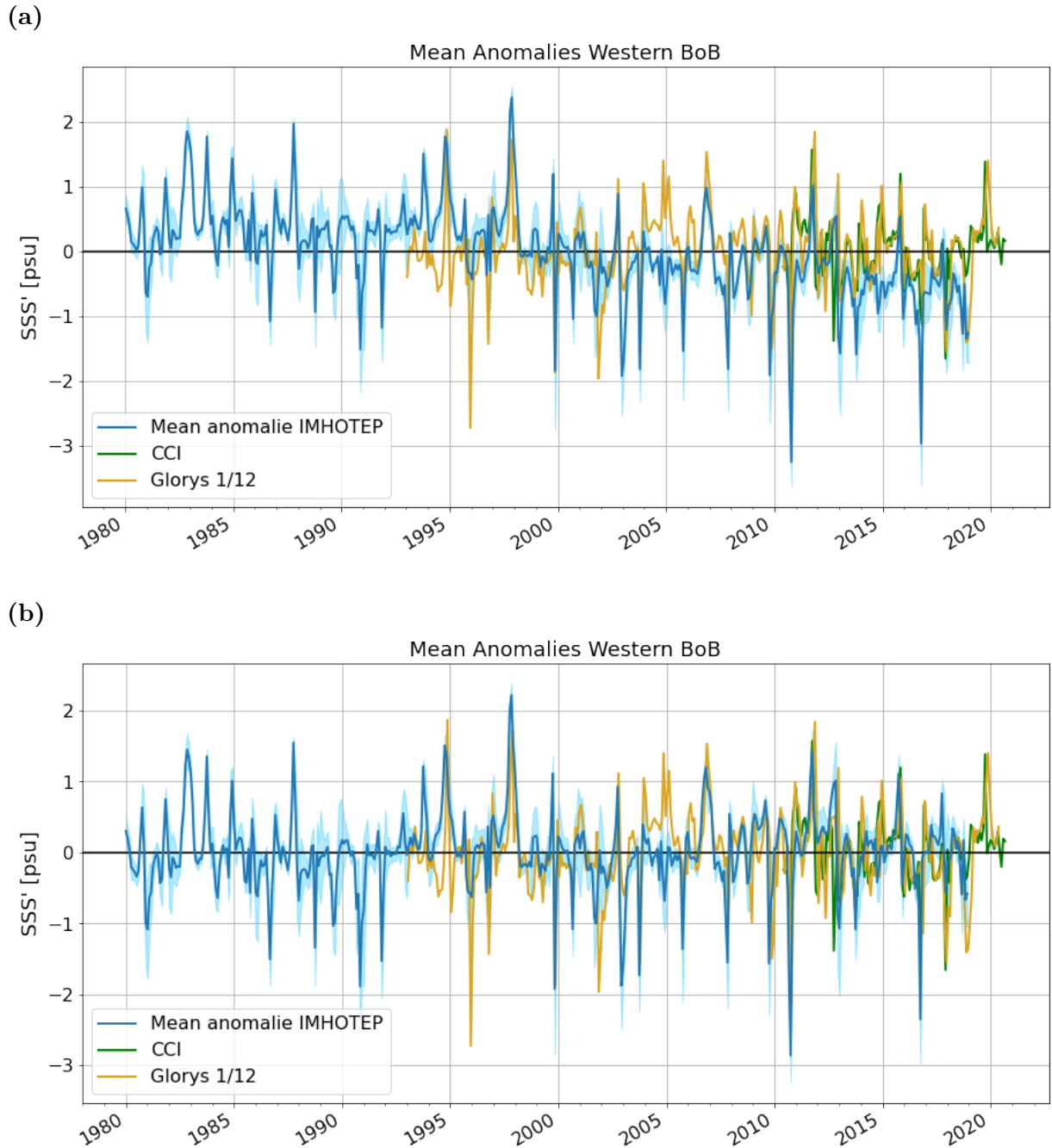


Figure 4.6 – Time series of monthly averaged  $SSS'$  in the Western BoB ( $[12.5^{\circ}\text{N}-16^{\circ}\text{N}; 79^{\circ}\text{E}-82^{\circ}\text{E}]$ , red box in Figure B.2) between 1980 and 2020 for a) raw IMHOTEP data and b) detrended IMHOTEP data. In blue is the average anomaly of IMHOTEP, the light-blue shade behind is the standard deviation between the different members. Yellow represents the Ocean reanalysis Glorys  $\frac{1}{12}^{\circ}$  and green represents the CCI dataset.

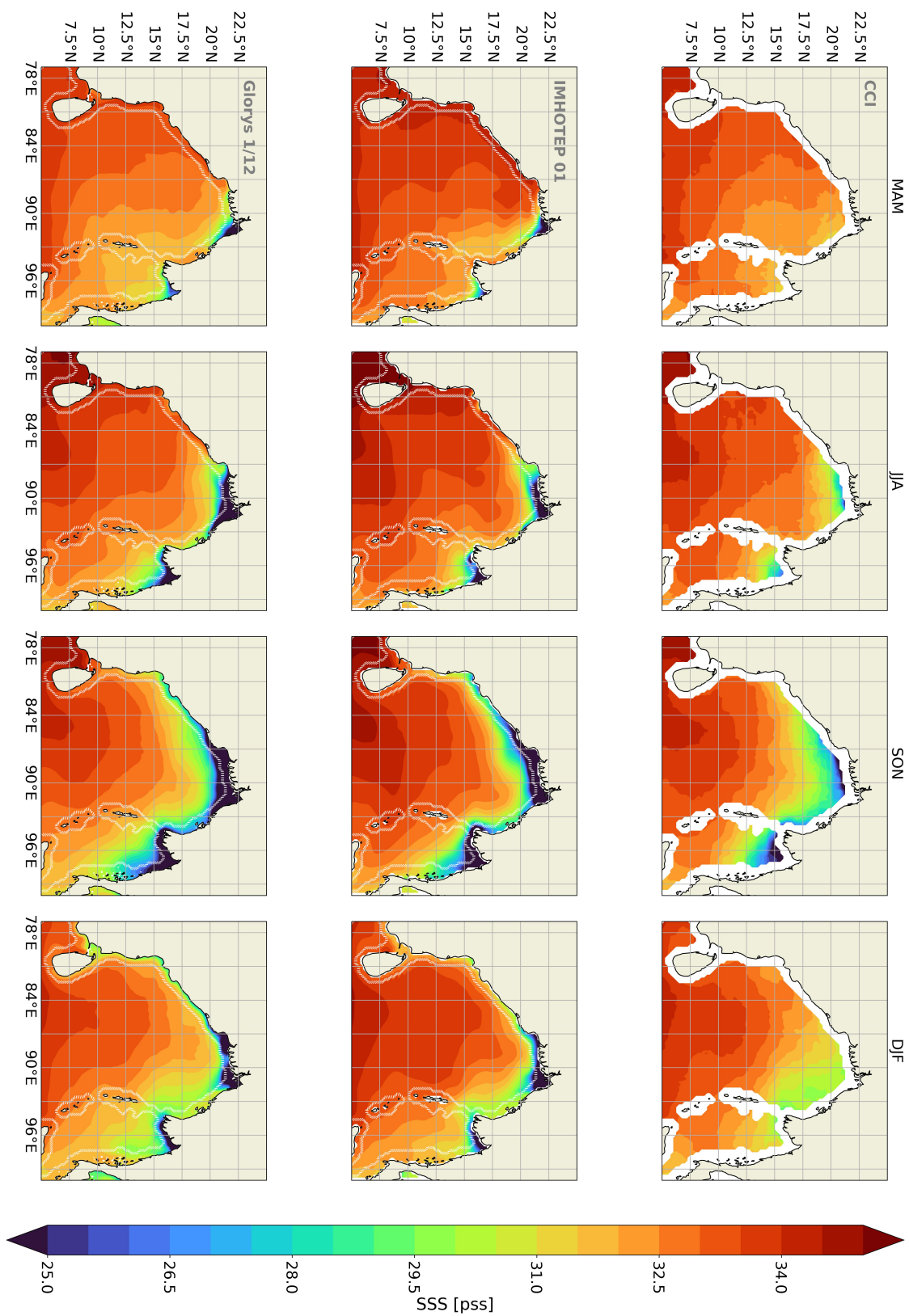


Figure 4.7 – Seasonal averaged SSS in the BoB for the datasets (the season in grey apply for each line) for the entire period of each dataset. The dotted white line represents the limit of the remote data.

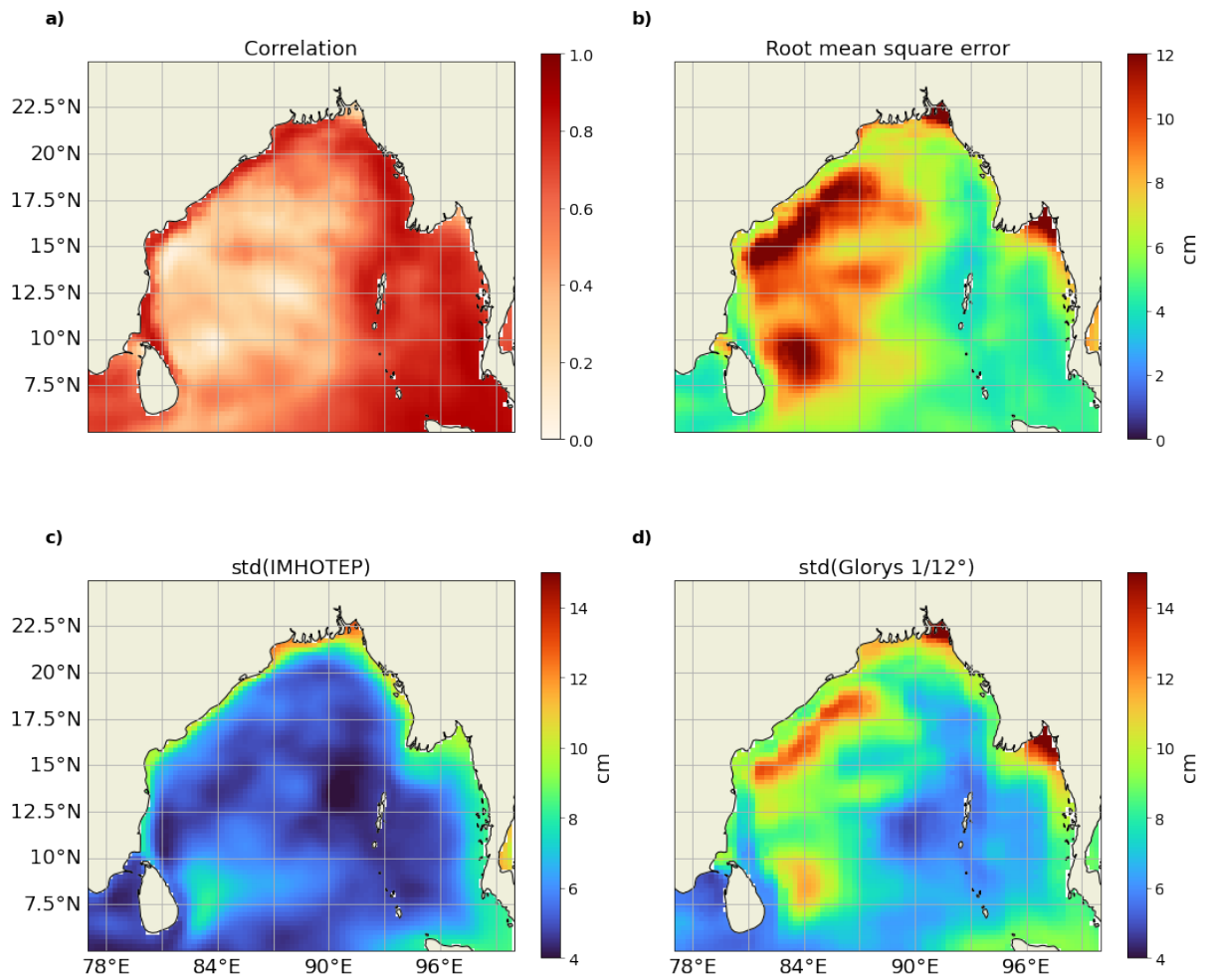


Figure 4.8 – SON averaged SLA anomaly from one member of IMHOTEP and CCI data using the common period between the two datasets (1993-01 to 2018-12): a) is their correlation, and b) their root mean square difference. The bottom panels are the standard deviation for each dataset.

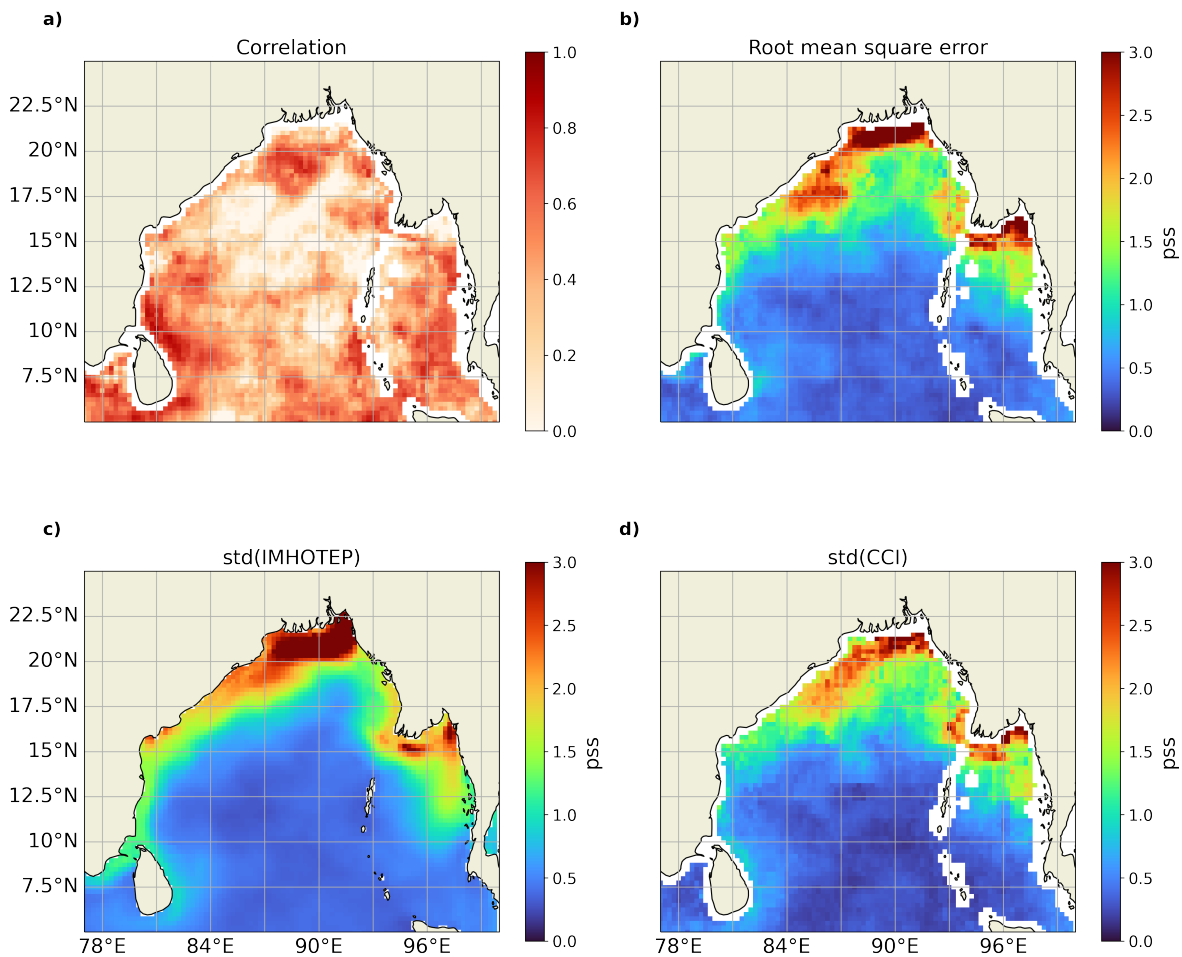


Figure 4.9 – SON averaged  $SSS'$  from one member of IMHOTEP and GLORYS data, using the common period between the two datasets (2010-06 to 2018-12): a) is their correlation, b) their root mean square difference. The bottom panels are the standard deviation for each dataset.

After this generic validation of the IMHOTEP non-seasonal variability, a more specific comparison of the SSS signals associated with the IOD to those in observations is made. The structure associated with the IOD are obtained by regressing the SON average sea-level, currents and SSS anomalies to the SON average IOD index.

The sea level anomaly (Figure 4.10 d, e) indicates negative sea level anomalies in the periphery of the BoB. As already described by Akhil et al. (2016a), Akhil et al. (2020), the signature of positive IOD events is associated with a weakening of the EICC, and more generally an anticyclonic circulation in the BoB, due to upwelling Kelvin waves generated by the equatorial easterlies, that travel along the equatorial and coastal waveguide. Akhil et al. (2016a) attributed the resulting SSS anomalies largely to the effect of advection, with fresh anomalies in the northeast BoB (and more specifically close to the GB and Irrawaddy estuaries), and salty anomalies along the est coast of India. The large-scale SLA pattern in IMHOTEP is qualitatively similar to that in Glorys, consistent with downwelling coastal Kelvin waves radiated from the equatorial region. The coastal sea level anomalies are however weaker in IMHOTEP as in Glorys, as well as the alongshore current anomalies.

Figure 4.10b is similar to the analysis in Akhil et al. (2020), with one additional year and the CCI dataset instead of SMOS. The resulting pattern is thus very close to that obtained in that study, and also similar to the modeling study of Akhil et al. (2016a). There are negative SSS anomalies in the Northeast BoB, and positive anomalies along the east coast of India. Those can be explained as follow: the weaker than usual EICC exports less freshwater southward along the east Indian coast, resulting in fresher water to the northeast, and saltier water along the coast of India (Akhil et al., 2016a). The IMHOTEP simulation completely misses the freshening of the northeast BoB in response to the IOD, and underestimates the salty signal along the East Coast of India during positive IOD events. I come back to the consequences of these biases in the discussion.

To further investigate the impact of the IOD, a Hovmöller diagram was created along the East Indian Coast for the IMHOTEP dataset. Figure 4.11 shows a varying extension of the river in the sea. Large positive IOD events (1994, 1997, 2006, 2011, 2015) are always associated with a river in the sea that does not extend southward of 14°N. Negative IOD events (1996, 1998, 2005, 2010, 2016) are on the other hand associated with a river in the sea that extends quite far south. However, the extension does not seem to be solely related to the IOD, with for instance a "short" river in the sea for the 2002 and 2004 neutral years, and a long one for the 2007 and 2001 near-neutral years. The Hovmöller

diagram confirms the findings from the CCI dataset and the interference of additional forces that impact the river in the sea.

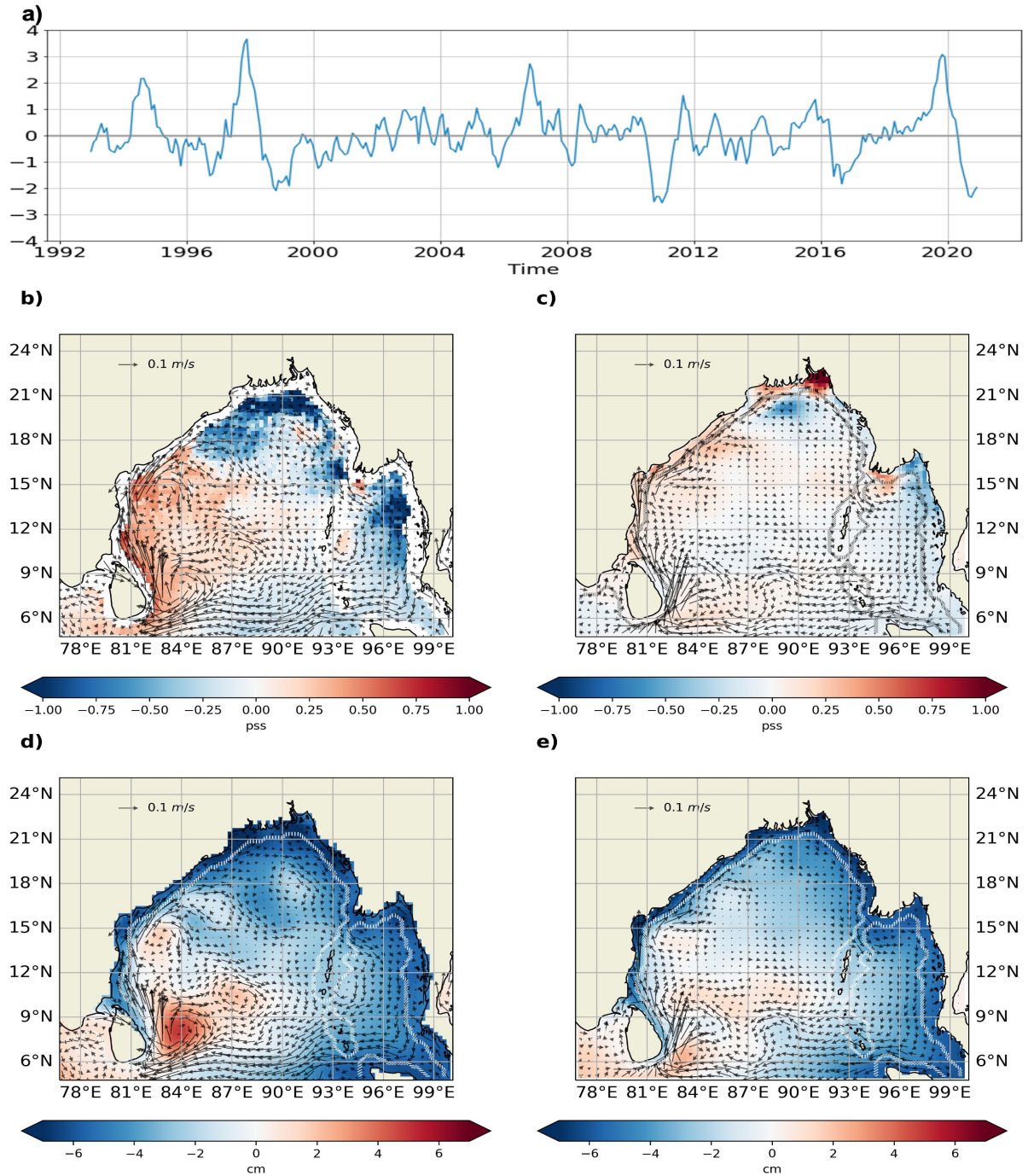


Figure 4.10 – a) Normalized IOD SDI index between 1993 and 2020. The bottom panels show regressions of the anomalies to that index for the entire common period SON, for: b) the CCI  $SSS'$  (2010-2019), c) IMHOTEP  $SSS'$  (member 07, 1993-2018), and d) Glorys SLA anomaly (1993-2018), and e) IMHOTEP SLA anomaly (member 07, 1993-2018) with the IOD in each point. Above is the regressed current anomaly from GlobeCurrent dataset (b and d) and IMHOTEP model (c and e). The dotted line in b, c, d) represents coastal limit of the CCI data.

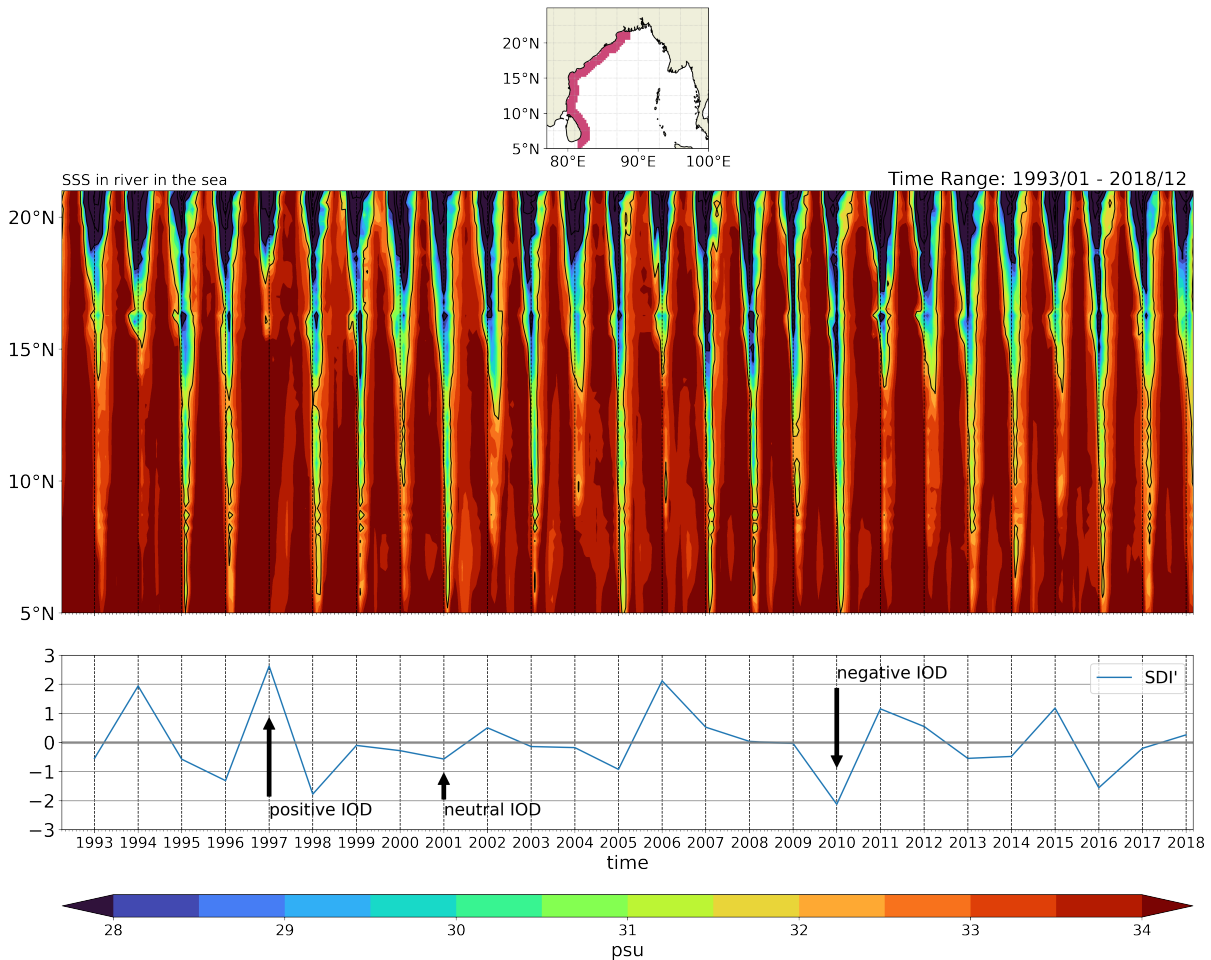


Figure 4.11 – Hovmöller diagram for the "River in the sea" for the entire IMHOTEP period. Top panel is the geographical situation of the studies area (distance to the coast less than 200 km). Middle panel represents the longitude SSS mean of the highlighted section from the top panel. Bottom panel is the SDI anomaly mean for SON which is closely linked to the IOD. Note that the x-axis of the middle and bottom panel represents the time between 1993 and 2018 and that the ticks are set on the October, when the IOD is reaching its peak, for each year. The arrows represents the years used for the snapshots.

In summary, in the sections above, it has been shown that the corrected IMHOTEP experiments tend to reasonably represent the SSS seasonal climatology, to underestimate the eddy variability. The circulation anomalies associated with the IOD are reasonably reproduced. The IMHOTEP dataset does not reproduce the right sign of the response to the IOD in the Northeastern BoB. On the other hand, the SSS response along the east coast of India is reasonably reproduced, albeit underestimated.

## 4.4 Intrinsic Variability: qualitative analysis

Despite the shortcomings mentioned above, the big advantage of the IMHOTEP simulations is that they provide an ensemble, from which the forced and intrinsic variability can be estimated. Below, the impact of the intrinsic variability is illustrated first by showing snapshot of the SSS and surface current fields in different members, before working out the amplitude of the intrinsic sea level (proxy for eddies) and resulting SSS variability, and its contribution to the total variability using the method described just in Section 4.2.

Illustrations of the impacts of the intrinsic (eddies) signals on the SSS and currents fields can be seen through example snapshots (Figure 4.12, 4.13, 4.14).

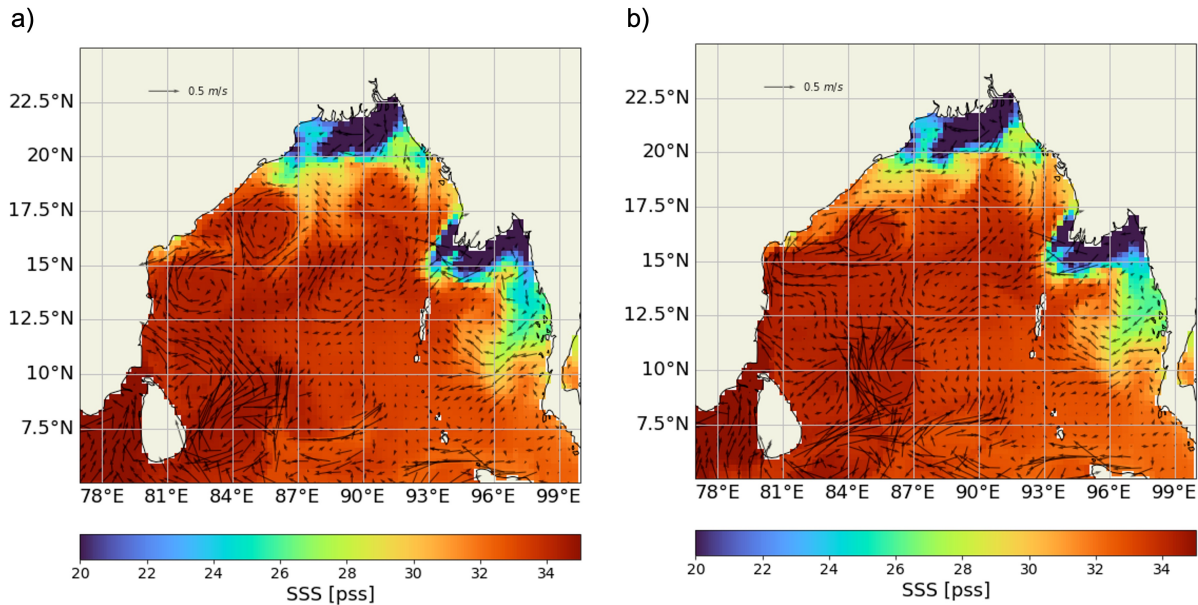


Figure 4.12 – Snapshots of SSS (in the background) and current, averaged over October 1997. a) is the snapshot of IMHOTEP run 05 and b) run 09.

The first snapshot corresponds to 1997, a positive IOD year. Figure 4.12a illustrates the role of the surface currents in shaping the SSS field, as fronts in SSS and major current structures clearly coincide. While the major features of the SSS field are similar in those two experiments (which for instance display freshwater pattern near the estuaries), differences in the location of individual eddies result in strong localized differences in SSS. For instance, the presence of an eddy around  $16^{\circ}\text{N}$  clearly induces a freshwater ( $\text{SSS} \leq 28$  pss) circulation toward the Bay interior in panel a), while the eddy is smaller in panel b), which leads to the creation of a freshwater tongue, albeit short.

The second snapshot corresponds to 2010, a negative, IOD year. Figure 4.13 also illustrates the role of the surface currents in shaping the SSS field, as fronts in SSS and major current structures clearly coincide. Compared to the positive IOD (Figure 4.12), the currents along the coast are much stronger, creating a pronounced "river in the Sea", which expands all the way southward to Sri Lanka. However, the two experiments display differences in the location of individual eddies, which results in strong localized differences in SSS. For instance, the presence of an eddy around  $17.5^{\circ}\text{N}$  clearly induces a freshwater ( $\text{SSS} \leq 26$  pss) circulation toward the Bay interior in panel b). Also the presence of many eddies in the center of the bay around  $5^{\circ}\text{N}$  and  $7.5^{\circ}\text{N}$  in panel a) prevent strong currents

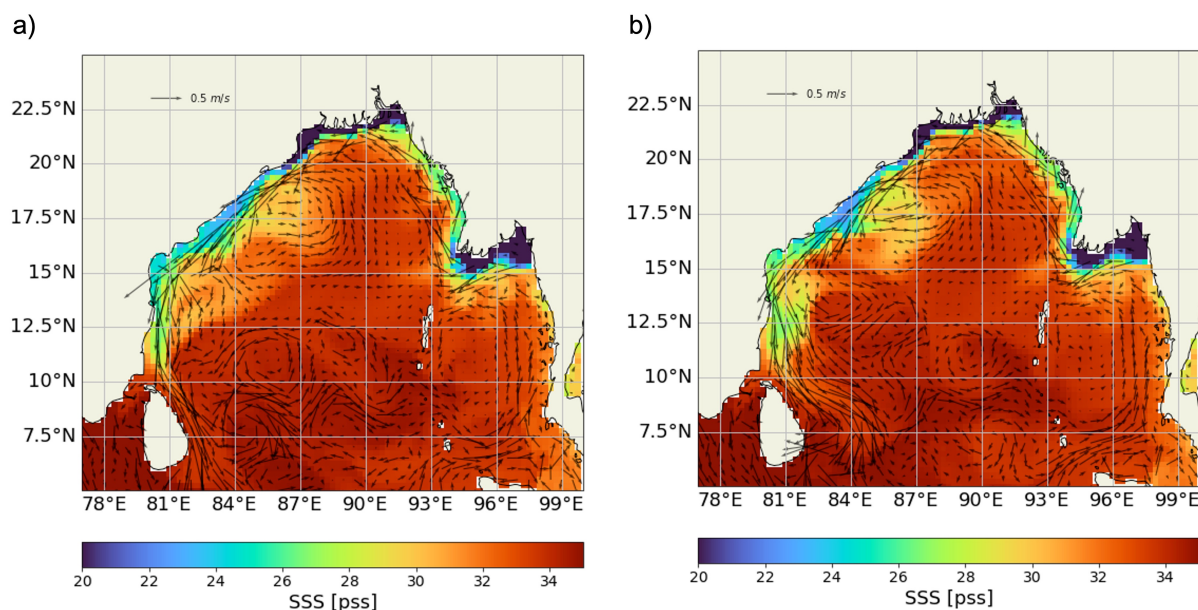


Figure 4.13 – Snapshots of SSS (in the background) and current, averaged over October 2010. a) is the snapshot of IMHOTEP run 04 and b) run 10.

like in panel b) to develop, stopping the extension of waters around 28 psu around 10°N. However, the width of the tongue is bigger for run 04. These eddies do not exist for the run 10, permitting a strong current along the coast of Sri Lanka, providing fresher water (30 psu) down to 7°N.

The last snapshot (Figure 4.14) corresponds to a IOD neutral year (2001), but which has a quite developed river in the sea on Figure 4.11. Again, the mesoscale distribution of SSS is strongly influenced by the eddy field. In this snapshot it becomes clear that the influence of the eddies in neutral years is significant. In panel a), the presence of the eddy around 20°N completely obstructs the extension of the freshwater southwards. Whereas in panel b) the eddy is not present, letting the river in the sea extend itself until 15°N. However, water with an SSS of 31 psu has been transported until Sri Lanka for both runs. This again seems to indicate that the effect of eddies is mostly local, and does not really influence the overall extension of the river in the Sea.

It thus seems that "atypical" years in terms of the SSS response to the IOD compared to the pattern obtained by Akhil et al. (2016a), Akhil et al. (2020) cannot really be explained by intrinsic SSS variability, which seems to influence more the offshore extent of freshwater rather than its expansion along the coast. I come back to this point later in the conclusion section.

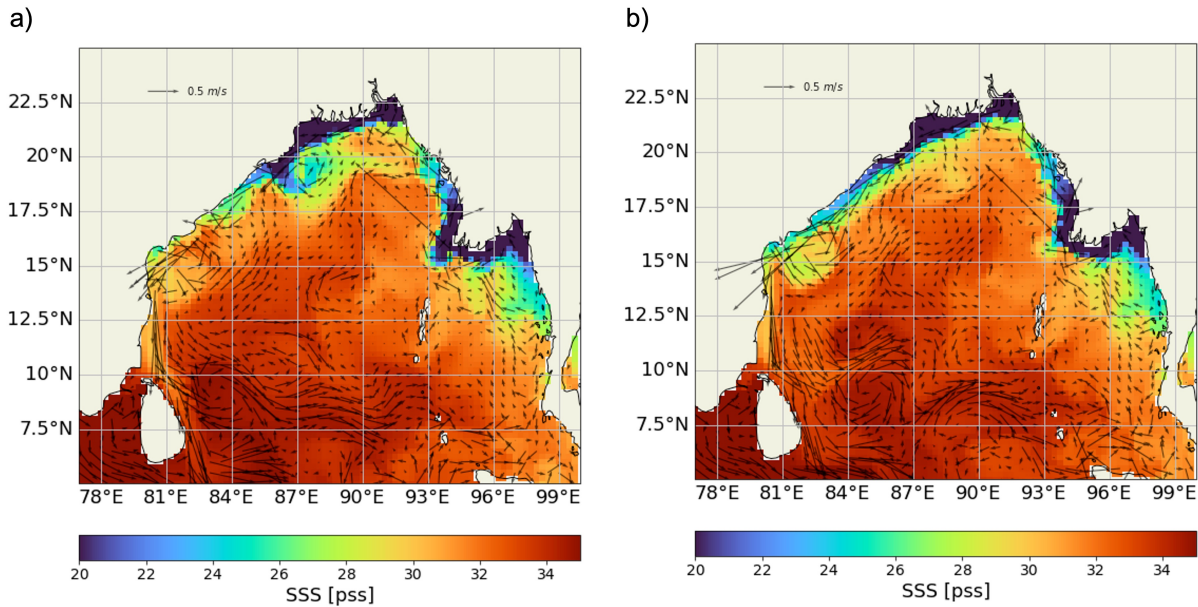


Figure 4.14 – Snapshots of SSS (in the background) and current, averaged over October 2001. a) is the snapshot of IMHOTEP run 04 and b) run 06.

## 4.5 Intrinsic Variability: quantitative analysis

The impact of eddies on intrinsic variability has been examined qualitatively in the previous section, and in order to further explore this relationship, the connection between intrinsic variability of SSS and SLA is shown in Figure 4.15.

The intrinsic variability of the SLA is highest during spring (MAM), which is consistent with the eddy seasonality of Figure 4.11 in Cui et al. (2016). The patterns reveal an increase of the intrinsic variability when moving westwards, with the strongest signal in the offshore region East of India. During summer, the variability decreases, reaching its minimum in autumn (SON). However, it is likely that IMHOTEP underestimates the intrinsic SLA signal during fall, since Cui et al. (2016) only find a 30% weaker value in fall than in summer in observations against a > 50% reduction in this case.

In contrast, the intrinsic variability of the SSS exhibits a different seasonality pattern, peaking mostly during fall (SON) and winter (DJF) along the river in the sea. This is consistent with the regions of strong SSS gradients and large (eddy) internal variability, which are probably caused by the horizontal stirring of SSS gradients by the mesoscale eddy velocity field.

The seasonally varying intrinsic and forced variability of SLA and SSS in the BoB can

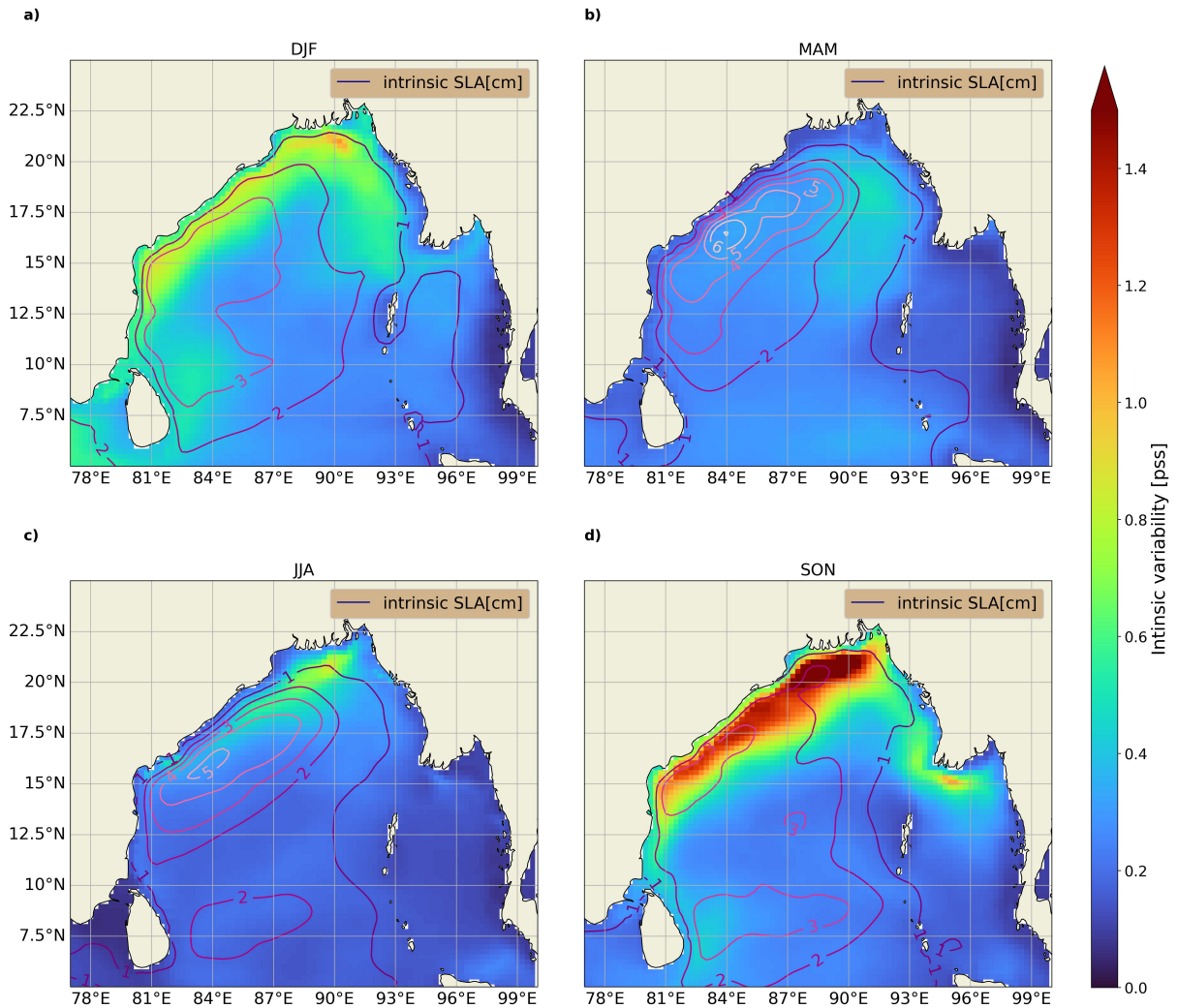


Figure 4.15 – Amplitude of SSS (shading) and SLA (contours) intrinsic variability estimated from the IMHOTEP ensemble.

be observed in Figure 4.16 and 4.17. These figures show the ratio between the intrinsic variability and the total variability, which is averaged for each season.

Figure 4.16 illustrates the dominance of forced SLA variability along the entire coast due to forced wave signals in the coastal waveguide. This dominance of forced variability expands westward in the eastern half of the BoB, mostly due to the westward radiation of Rossby waves from the coastal waveguide. However, the influence of eddies becomes progressively larger in the western half of the BoB (see Figure 4.15), resulting in a decrease of the forced variability contribution.

To summarize, while the forced SLA variability dominates near the east Indian coast

due to the coastal trapping of signals, the sea level and ocean circulation signals are strongly influenced by intrinsic variability further offshore in the western half of the Bay of Bengal.

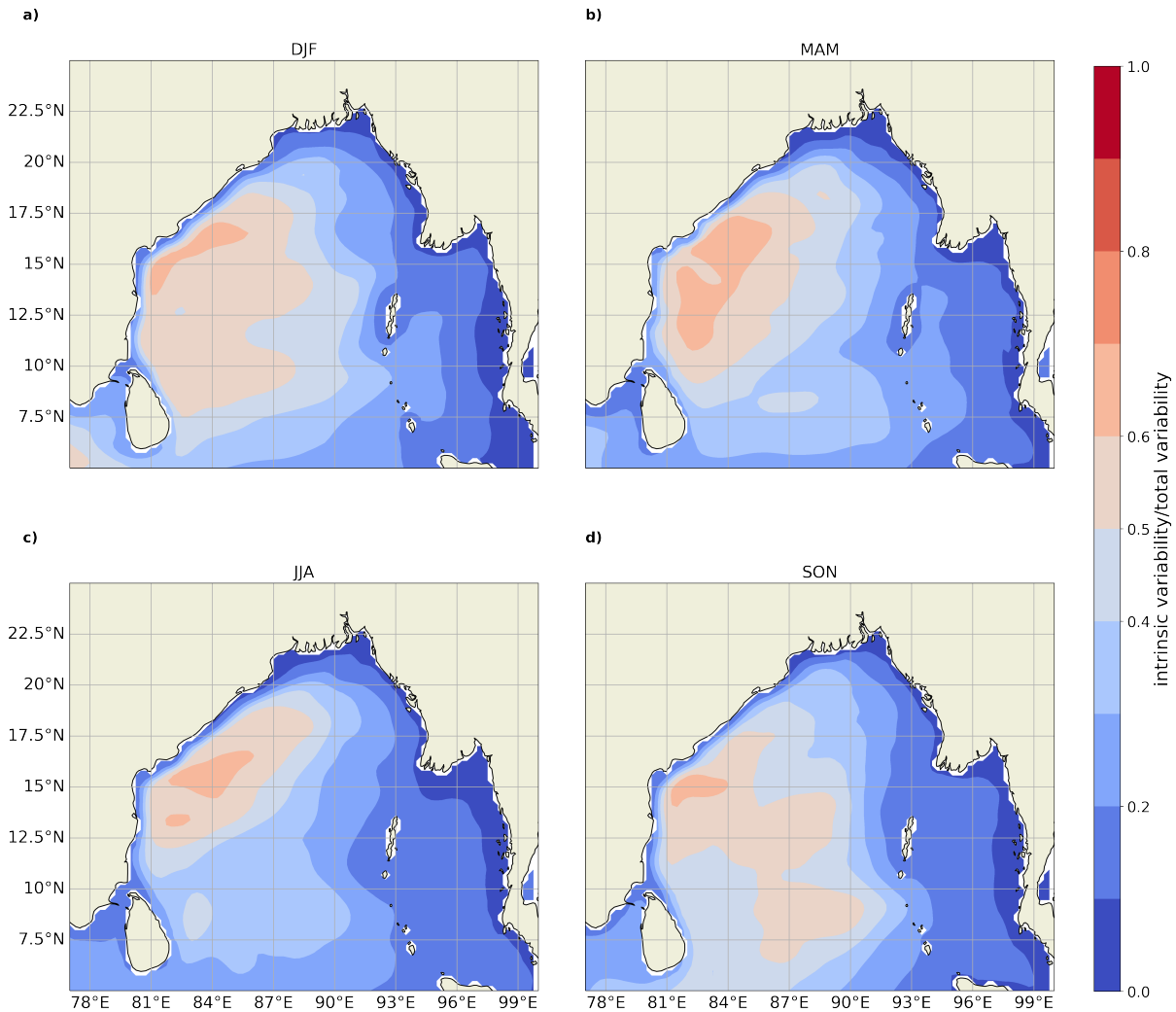


Figure 4.16 – Seasonal averaged intrinsic to total standard deviation ratio for SLA in the BoB using IMHOTEP data.

Figure 4.17 reveals similar patterns for the SSS internal variability contribution as for that of the SLA, suggesting a strong control of the SSS gradient by circulation features in the BoB. This finding is consistent with the snapshots presented in the previous section and is supported by the sensitivity experiments conducted by Akhil et al. (2016b), which showed that wind-driven SSS anomalies are the main driver of forced variability in the BoB (rather than rain or freshwater fluxes). Specifically, in response to the current

anomalies, wind-forced signals travel as coastal and Rossby waves, and the forced variability dominates near coasts or offshore of the BoB eastern boundary. However, most of the SSS variability in the Bay interior, especially in the western half of the BoB, is due to stirring by mesoscale eddies and is thus intrinsic.

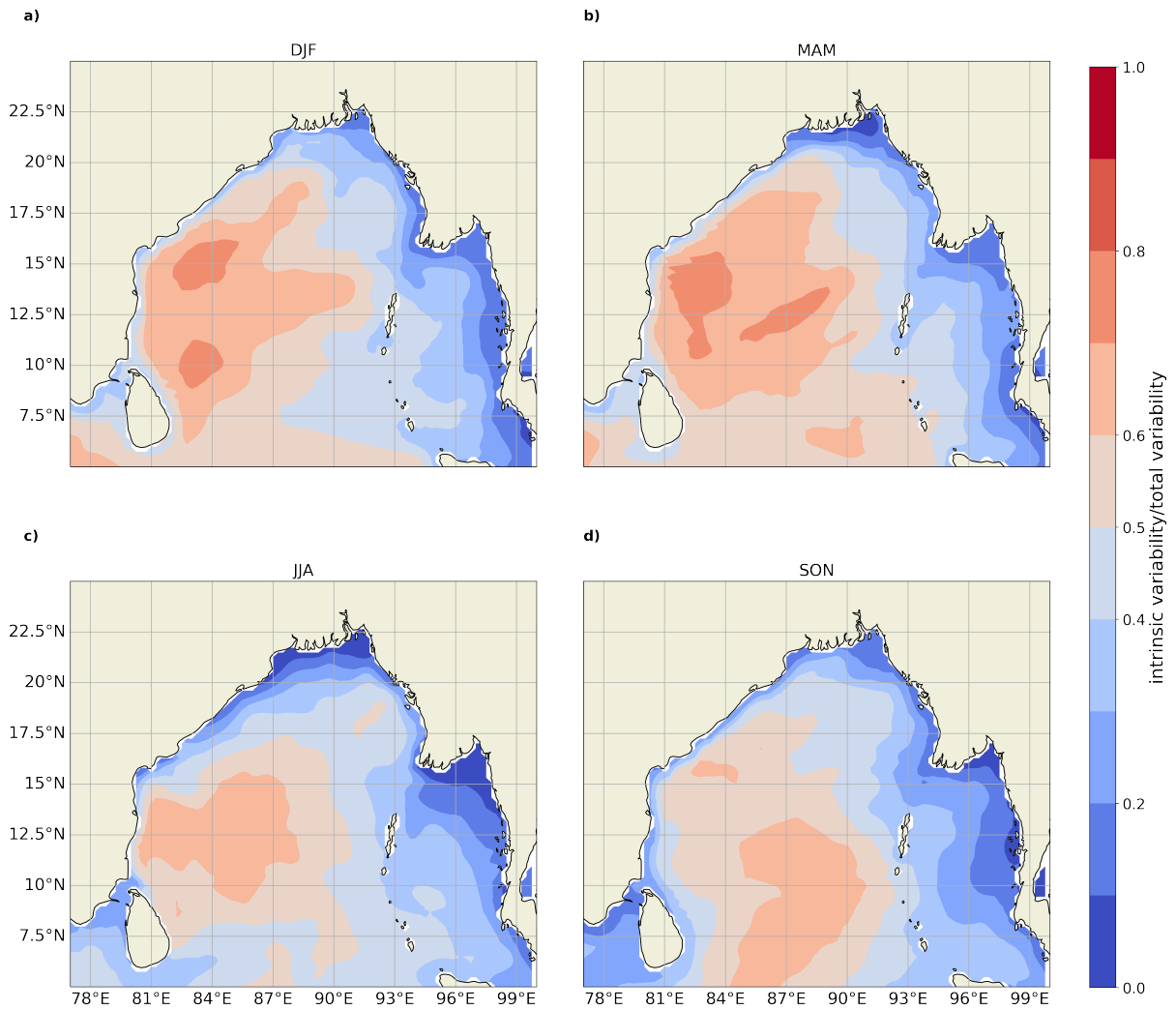


Figure 4.17 – Seasonal averaged intrinsic to total standard deviation ratio for SSS in the BoB using IMHOTEP data.

However, Figures 4.16 and 4.17 only display the ratio of intrinsic variability to total variability. Therefore, it is possible that regions highlighted by the dominance of intrinsic or forced variability possess only weak variability and are of no concern. To contextualize intrinsic variability, Figure 4.18 also shows the total SSS variability in the bay, highlighting when the intrinsic variability is responsible for over 50% (dots) and 70% (stars) of the total

standard deviation. This enables the identification of regions where the total variability is not only large but also controlled by eddies.

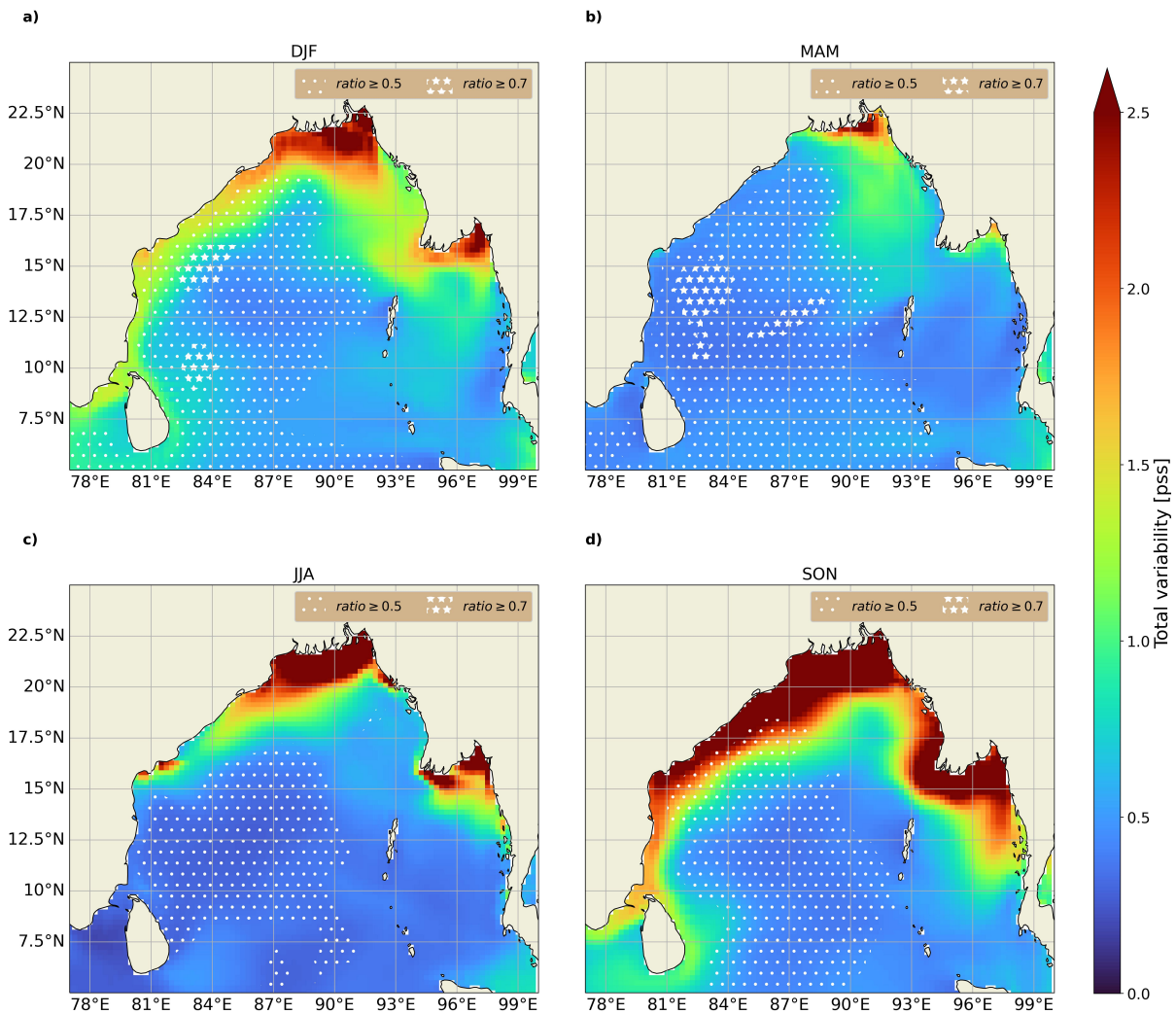


Figure 4.18 – Background represents the total non-seasonal standard deviation of SSS for each season. The dots (stars) represents the zones where the ratio of intrinsic variability to total variability exceeds 50% (70%) respectively.

Figure 4.18 demonstrates that regions where intrinsic variability dominates the total variability, such as in the middle of the basin, tend to have relatively weak non-seasonal SSS variability. This is because the climatological SSS gradients in these regions are relatively weak, making mesoscale eddy stirring less efficient in generating strong SSS variability.

On the other hand, the offshore flank of the river in the sea is an exception. This region is characterized by not only large total SSS variability, but also a significant contribution from eddies, accounting for more than 50% (and more than 70% in DJF) of its variability. This is due to the strong climatological SSS gradient and the presence of eddies, particularly in SON and DJF. Therefore, in this region alone, the strong SSS variability is a result of a strong contribution from intrinsic variability.

Along the coast, however, the eddy amplitude strongly diminishes (see Figure 4.15) while there is a dominant forced circulation response within one Rossby radius of the coast. This can be, associated with coastal Kelvin waves traveling in the coastal waveguide. As a result, forced SSS variability dominates very close to the coast and eddies mostly control the offshore extension of the river in the sea rather than its southward expansion.



# CONCLUSION AND PERSPECTIVES

---

## Conclusion

The general aim of this dissertation was to study the seasonal to interannual variability of the sea surface salinity in the Bay of Bengal (BoB). This study in the BoB is all the more necessary as SSS there is believed to influence regional rainfall through air-sea interactions (Shenoi et al., 1999), tropical cyclones (Neetu et al., 2019; Neetu et al., 2012), and the biogeochemical productivity in the BoB (e.g., Prasanna Kumar et al., 2002). Prior to 2010, the only available source of SSS data in the BoB were in situ observations, albeit sparse and not sufficient to describe basin-scale variations. Only with the beginning of the L-band radiometer era in 2009, a better SSS monitoring was possible, enabling the long-term study of the bay. However, the processes that control SSS variability in the BoB, especially at interannual timescales remain poorly understood. While the merged CCI dataset has a good quality in the BoB, it only spans 13 years, which is not really sufficient to really constrain interannual SSS variability.

Reul et al. (2009) and Song and Wang (2017) have demonstrated the possibility of using C- and X-band radiometers, launched before SMOS, to reconstruct SSS for the Amazon plume and in the South China Sea. This opens potential for reconstructing BoB SSS for 9 additional years over the 2002-2011 period. Although the C-band channel is much less sensitive to SSS than the L-band, a careful data processing can allow capturing SSS signals in regions with strong SSS contrasts and high SST, such as in the BoB. Considering the similar sensitivity of the X- and C-bands to wind and SST signals (while differing for SSS), it is possible to reduce the impact of those parameters by utilizing X-minus-C brightness temperature contrasts. However, it should be noted that the X-minus-C sensitivity to SSS is still low (0.05 K/pss, to compare with 0.6 K/pss for L-band), which highlights the importance of eliminating other residual signals with great care. Through my research, I used this method to reconstruct the SSS in the BoB, where its unique geographical structure makes an accurate reconstruction very challenging.

---

Thus, the first main hypothesis I tested in this research was: Can the Reul et al. (2009) method be used to reconstruct SSS in the BoB, by applying specific empirical corrections for this basin? And can the new SSS become accurate enough to study its variability at seasonal to interannual timescales?

During this dissertation, I have shown the impacts of different types of corrections on the C/X band emissivity contrast signal, that I discovered during my research. A pertinent finding was the significant differences in brightness temperatures between ascending and descending passes, particularly in the vicinity of land masses. To address this issue, I applied separate land-sea masks for ascending and descending passes to eliminate contamination of ocean points downstream of passages over land. Furthermore, I processed the ascending and descending passes independently, utilizing distinct empirical corrections. Additionally, I developed BoB-specific empirical corrections for surface wind, SST, and atmospheric water content, in that order, based on CCI SSS and AMSR-E collocated wind, SST, and atmospheric water data over the SMOS/Aquarius-AMSR-E common period. I also implemented an additional data screening step, which involved eliminating outliers ( $>3$  median absolute deviations from the median) over the entire time series and applying a  $0.75^\circ \times 0.75^\circ$  median smoothing filter. All these steps greatly enhanced the final data performance.

The comparison between the retrieved SSS climatology of the  $SSS_{AMSR-E}$  product and that of CCI indicates similarities, although the former generally underestimates SSS values less than 30 pss and exhibits strong fresh biases near the coasts. However, climatologies largely extrapolate off-shore data in these regions due to the very poor in situ data density within 100 km of the coasts (Chaitanya et al., 2014b), and the ocean simulations and re-analyses described in this PhD suggest lower SSS values than those measured by L-band radiometers (Akhil et al., 2020). So, despite its limitations, the  $SSS_{AMSR-E}$  product may capture some aspects of the seasonal climatology near coasts.

It is worth noting that the study of the impact of the IOD on SSS shows an important gap in the accuracy of the  $SSS_{AMSR-E}$  product, as no coherent pattern can be detected on the EOF. Also, the extension of the river in the sea can only be suspected, as a persistent underestimation is falsifying the signal. Thus it is impossible to analyze if the positive/negative IOD impacts the river in the sea by shortening/extending it.

While the focus of this study was on reconstructing interannual SSS variations prior to 2010, the comparison with ocean reanalyses in two hotspots for SSS interannual vari-

---

ability, the northern Bay of Bengal and the east coast of India, reveals some limitations of our current product. The product shows little skill in reproducing the SSS interannual variations over the northern Bay of Bengal. However, along the east coast of India, the product is able to reproduce the broad SSS interannual variations in reanalyses over quite long periods (3-5 years), despite some spurious SSS spikes during some other periods.

Overall, despite the limitations of the AMSR-E product, there are indications that it is sometimes able to capture interannual signals observed by the models along the Indian coast. This suggests that better filtering of the data could potentially extract more signal. Possible improvements of the filtering process are discussed in the Perspective section below.

The initial objective of the PhD study was to use the consolidated AMSR-E and CCI datasets to study the different controls of the SSS variability in the BoB. But given the relatively low performance of the  $SSS_{AMSR-E}$  product for the interannual variability, we decided to use a modeling strategy (project IMHOTEP) in the second part of the PhD.

Previous studies, such as Akhil et al. (2014), have identified basin-scale SSS variations associated with the IOD in the BoB, as well as localized variations near the Ganga-Brahmaputra estuary associated with river runoffs. However, recent analyses of the SMOS dataset by Akhil et al. (2020) (and similar analyses using CCI and including one more year of data in this thesis) suggest that the IOD influence on SSS in the BoB, particularly on the "river in the sea" along the east coast of India, is not systematic. Furthermore, it is difficult to clearly identify the impact of river runoffs from existing datasets. Given the significant role of eddies in influencing the SSS distribution of the BoB (Fournier et al., 2017), this study aimed to estimate the intrinsic (eddies) versus the forced (e.g., IOD and runoffs) SSS variability in the BoB to investigate whether eddy modulation could explain the not-so-systematic relation between the IOD and river in the sea.

As IMHOTEP has never been validated for the BoB region, it was unavoidable to first proceed with the validation. It permitted to see the necessity to remove a long-term spurious drift in the dataset. This drift removal seems to work relatively well when comparing with other datasets (CCI, Glorys re-analysis). Nevertheless, IMHOTEP underestimates the BoB eddy variability (probably due to its eddy-permitting horizontal resolution), slightly under-estimates the circulation response to the IOD, and only reproduces the SSS IOD response along the east coast of India (although it is underestimated). The consequences of those features are discussed in the perspectives section.

The analysis suggests that internal variability associated with meso-scale eddies dom-

---

inates both the SLA and SSS variability offshore of the east coast of India. However, forced signals are dominant near the coast and in the eastern half of the BoB due to the coastal waveguide influence and westward radiation of Rossby waves from the eastern rim of the BoB. The only region where both internal and total variability are strong (internal variability >50% of the total one) is on the seaward edge of the "river in the sea, where eddies modulate the offshore extension of the river" low SSS water, not its length, as supported by case studies conducted over several years.

## Perspectives

As I embarked on my PhD dissertation research, I became aware of the challenges posed by the low sensitivity of C-band to sea surface salinity (SSS) and the risks of land contamination and radio-frequency interference in the BoB. Despite these hurdles, my current dataset is the first attempt of SSS retrieval from AMSR-E data in the BoB and it shows promise in capturing non-seasonal SSS signals, as evidenced by the successful reproduction of certain observed interannual signals along the west coast of India. However, further improvements are necessary to enhance the algorithm's accuracy and reliability. It is worth noting that the SMOS SSS retrieval, when initially analyzed, was almost unusable for the BoB, and its performance was inferior to that of  $SSS_{AMSR-E}$  (Akhil et al., 2016b). Substantial improvements in pre-processing methods, including better, seasonally- and latitudinally-dependent bias correction and stricter data screening near land to remove remaining RFI's, were required to significantly reduce errors and transform the SMOS dataset into the valuable resource it is today for the BoB.

As I continue my research, I believe there is room for improvement in the AMSR-E SSS products for the BoB. While my current method includes two stationary masks to exclude data points downstream of land on both ascending and descending passes, there are more advanced masking techniques and dynamic screening methods that could enhance the precision of the  $SSS_{AMSR-E}$  measurements. For instance, a dynamic mask could compare neighboring pixels to remove local and temporal outliers that influence the spatial filtering, resulting in fewer spurious signals in the time-series.

Therefore, I plan to investigate these approaches to further enhance the accuracy and reliability of the  $SSS_{AMSR-E}$  retrieval. By implementing these more rigorous techniques, we can make significant progress in understanding this vital oceanographic parameter and contribute to a more precise and detailed understanding of the BoB's oceanography.

---

Furthermore, exploring alternative approaches to the current empirical corrections used in my study could be beneficial in improving the accuracy of SSS retrievals. While I applied wind, SST, and water vapor corrections in three sequential steps, utilizing neural networks could enable us to perform all corrections in a single step and account for nonlinear coupling between variables more effectively. This approach would also allow for the inclusion of additional parameters such as the distance to the coast or wind direction, which could be weighted accordingly to improve the final SSS retrieval. By exploring these alternative approaches, we may be able to further improve the accuracy and reliability of SSS retrievals from AMSR-E data in the BoB.

Finally, as the purpose of this study principally uses the SSS anomalies, a possible procedure could be the creation of a Sea Surface Salinity Anomaly retrieval algorithm. This approach would involve analyzing the differences between the observed SSS and the climatology values, and then deriving the Sea Surface Salinity Anomaly from those differences. This technique could reduce the impact of the errors and biases in the absolute SSS values and enable to focus more precisely on the oceanic variability. Therefore, implementing a Sea Surface Salinity Anomaly retrieval algorithm could be a promising avenue for further enhancing my research and increasing the understanding of the SSS variability in the BoB.

Looking far ahead, the planned launch of the Copernicus Imaging Microwave Radiometer (CIMR) satellite is expected to make significant contributions to the study of SSS. CIMR is a top-priority satellite mission within the European Commission's Copernicus Expansion program and will feature a radiometer imager operating across five spectral bands, corresponding to frequencies of 1.4, 6.9, 10.65, 18.7, and 36.5 GHz. As a result, analyzing radiometric data obtained from the same instrument in L-, C-, and X-channels could help to further refine the present algorithm in the future.

IMHOTEP appears to have several limitations in accurately capturing key features of SSS variability in the region. It underestimates eddies, which are an important driving force of internal SSS variability, by a significant amount (50%). Additionally, it does not reproduce well the IOD-induced SSS signals that have been observed in other studies (Akhil et al., 2016a; Akhil et al., 2020) using different data sources, such as SMOS and CCI. Furthermore, IMHOTEP appears to have overly strong SSS gradients near coasts, which may impact its ability to accurately capture SSS variability in these regions.

Given these limitations, it is difficult to determine if the estimate of the intrinsic variability contribution to the total SSS variability is too low or high. However, the

---

finding of a strong contribution of eddies to the offshore extension of the river of the sea confirms previous studies that have highlighted the importance of eddy stirring or offshore transport in this region (Benshila et al., 2014; Chaitanya et al., 2021; Fournier & Lee, 2021; Hareesh Kumar et al., 2013).

While a higher resolution ensemble simulation in the BoB would be ideal, it is currently unavailable. Therefore, a more thorough drift correction and validation process is necessary to ensure the robustness of our results. Presently, I use a rudimentary technique to correct for steps by calculating a basic temporal tendency and subtracting it from each data point. Nonetheless, a more sophisticated correction that addresses both the steps and any residual biases could be explored and employed to improve the precision of the findings. Additionally, further quantification of the impact of eddy field amplitude and climatological SSS gradients on internal variability is needed. This can be achieved by estimating observationally-derived values for eddy-induced SSS variability, which can then be compared with values from the model. Such analyses would enable us to better understand and model the complex dynamics of the Bay of Bengal, ultimately leading to improved predictions of future changes in the region.

Analyzing the simulations with a climatological river runoff in the BoB (IMHOTEP experiment ES) in addition to the existing simulations could be beneficial. These simulations could provide further insights into the potential sources of bias and the role of river runoff in driving variability in the BoB. By comparing these simulations with the ones used in this study (IMHOTEP experiment EGAI), a better understanding of the contribution of the river runoff to the forced BoB variability can be obtained.

Finally, my study suggests that while positive IOD years tends to be associated with a short "river in the sea" and negative IOD years with a long one, there are IOD-neutral years that also seem to have an unusually short or long river. The results of this study indicate that the eddies do not fully explain this "river in the sea" length modulation. Actually, they even suggest that the forced circulation signals dominate close to the east coast of India. While the IOD does induce an oceanic response in the BoB (Akhil et al., 2016a; Suresh et al., 2018), it is not the only phenomenon that can induce a circulation response in the BoB coastal waveguide. Several studies indicate that intraseasonal equatorial wind variations associated with the Madden Julian Oscillation in boreal winter (Zhang, 2005) and monsoon active-break phases in boreal summer (Goswami & Xavier, 2005) can induce strong circulation responses in the Northern Indian Ocean coastal waveguide (Suresh et al., 2013; Vialard et al., 2009). The resulting sea level variations typically have a period

---

of around 90 days, which is sufficient to generate significant variations in the EICC, and consequently, the river's flow into the sea, provided the phasing is appropriate. Moving forward, I plan to investigate whether these wind-driven variations could play a role in the non-seasonal variability of sea surface salinity (SSS) along the east coast of India, in conjunction with the Indian Ocean Dipole (IOD).

# APPENDIX FROM ARTICLE

---

## A.I

$a_{0i,f}$	Ascending		Descending	
	f = 6.8 GHz	f = 10.7 GHz	f = 6.8 GHz	f = 10.7 GHz
i=0	4.55354515e-05	6.60023653e-05	-1.16515076e-05	-1.16515076e-05
i=1	2.09064870e-04	7.96206640e-05	-1.42885312e-04	-9.32922404e-05
i=2	-4.28674303e-04	-4.53987148e-04	-3.33529218e-04	-4.04319115e-04
i=3	9.49419176e-05	1.02998222e-04	7.66957067e-05	9.29831895e-05
i=4	-6.87032960e-06	-7.52672386e-06	-5.29721074e-06	-6.61128385e-06
i=5	1.67845991e-07	1.85598494e-07	6.60023653e-05	6.60023653e-05

5<sup>th</sup> order polynomial ascending and descending wind induced emissivity coefficients  $a_{oi,f}$  for the C- and X-band frequencies as given in Eq.3.7 and determined in the BoB

## A.II

$t_{i,f}$	Ascending		Descending	
	f = 6.8 GHz	f = 10.7 GHz	f = 6.8 GHz	f = 10.7 GHz
i=0	2.63499185e+02	2.20884312e+02	-1.04280657e+02	-4.86684706e+01
i=1	-6.00288418e+01	-5.03863321e+01	2.33347011e+01	1.08065068e+01
i=2	5.68558781e+00	4.77798176e+00	-2.16724658e+00	-9.96113782e-01
i=3	-2.86559315e-01	-2.41081816e-01	1.06959414e-01	4.88054091e-02
i=4	8.10563336e-03	6.82638595e-03	-2.95887723e-03	-1.34092631e-03
i=5	-1.21999626e-04	-1.02847830e-04	4.35085315e-05	1.95933863e-05
i=6	7.63328013e-07	6.44114917e-07	-2.65716251e-07	-1.18981906e-07

6<sup>th</sup> order polynomial coefficients  $t_i^f$  of the thermal emissivity bias correction for the C- and X-band frequencies as given in Eq.3.8 and determined in the BoB for ascending and descending satellite passes

## A.III

$d_{i,j,f}$	Ascending		Descending	
	f = 6.8 GHz	f = 10.7 GHz	f = 6.8 GHz	f = 10.7 GHz
i=0, j=0	-3.50264332e-03	2.22884916e-03	2.32527351e-03	3.67007082e-03
i=0, j=1	-4.08847382e-03	-1.23501804e-02	2.15382596e-02	-4.45494257e-02
i=0, j=2	-3.31131723e-04	-4.49887910e-04	-1.26859538e-03	1.05529239e-03
i=0, j=3	-8.61949711e-06	-2.94679127e-05	1.05162124e-04	-1.70509590e-04
i=0, j=4	1.50643143e-06	2.74424721e-06	-6.21307755e-07	7.06122643e-06
i=0, j=5	2.52343397e-07	5.07044737e-07	-1.45497626e-07	1.08493874e-06
i=1, j=0	2.88007765e-04	-6.55557349e-04	-6.07893904e-04	-8.25076456e-04
i=1, j=1	3.24433230e-04	-9.56023842e-04	-2.06188487e-03	4.07079170e-03
i=1, j=2	-5.95877049e-03	-1.02646391e-02	-4.96649561e-03	-1.14132321e-02
i=1, j=3	-3.04249620e-05	-3.99784940e-04	2.18522673e-03	-2.83815099e-03

Table of the coefficients  $d_{i,j,f}$  for the bivariate empirical adjustment  $\Delta e_{atm,f}^{adj}(V, L)$  as given in Eq.3.10 for ascending and descending satellite passes.

---

## A.IV

$S_{i,j}$	
i=0, j=0	-3.73785349e+02
i=0, j=1	1.30285040e+01
i=0, j=2	-1.16547677e-01
i=1, j=0	3.68732658e+04
i=1, j=1	-5.52420318e+02
i=2, j=0	-7.79784479e+05

Table of coefficients  $S_{i,j}$  for the bivariate GMF as given in Eq. 3.13

# COMPLEMENTARY FIGURES

## B.I Temporal differences of SSS in the BoB

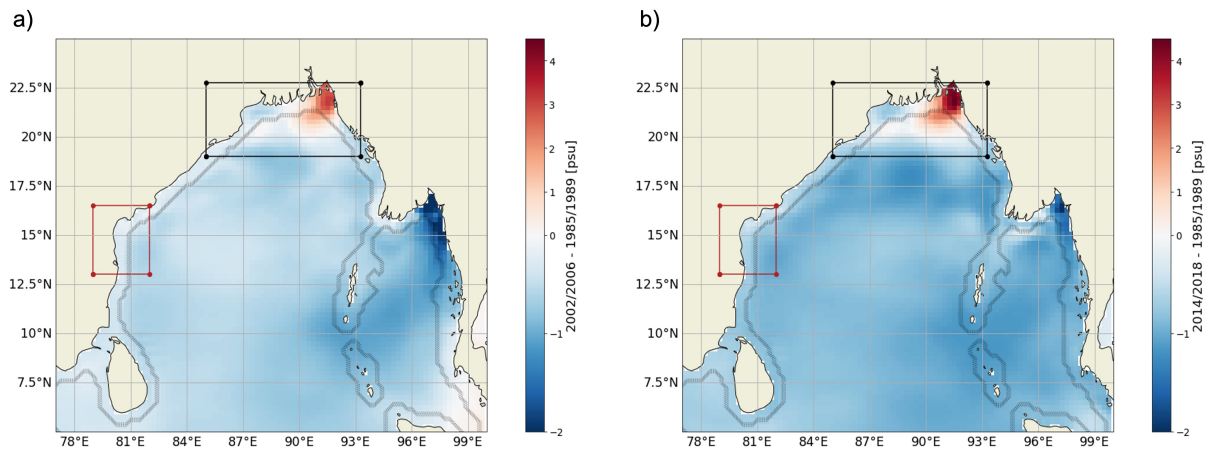


Figure B.1 – Difference between five years averaged SSS from the mean IMHOTEP dataset in the BoB. a) the difference between the 2002/2006 and 1985/1989 periods and b) for the difference between 2014/2018 and 1985/1989. The black and red boxes represents the regions of the Northern BoB and the western BoB used in Section 4.3.1.

---

## B.II Temporal differences of detrended SSS in the BoB

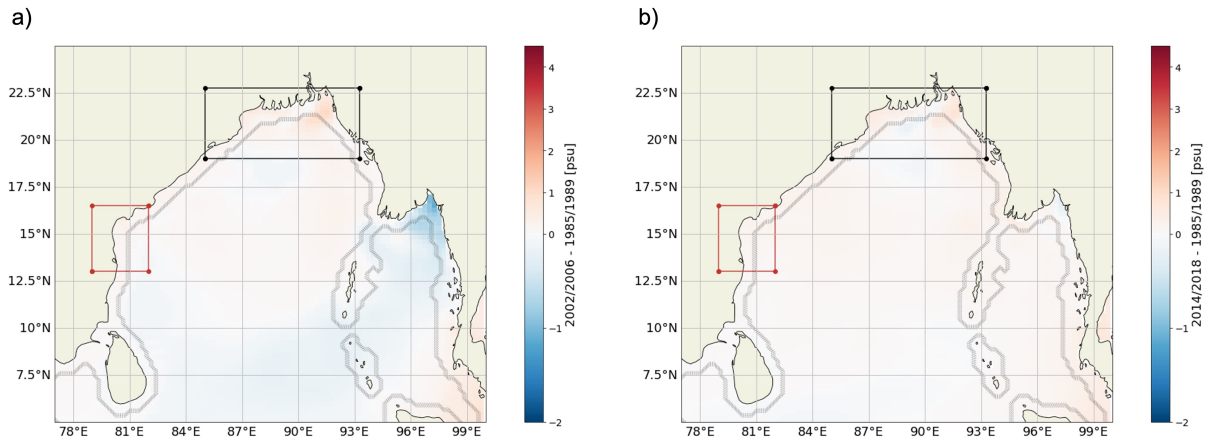


Figure B.2 – Difference between periodical averaged and detrended SSS in the BoB. a) the difference between the periods 2002/2006 and 1985/1989 and b) for the difference between 2014/2018 and 1985/1989. The black and red boxes represents the regions of the Northern BoB and the western BoB used in Section 4.3.1.

### B.III Seasonal Comparison between SLA from IMHOTEP and Glorys

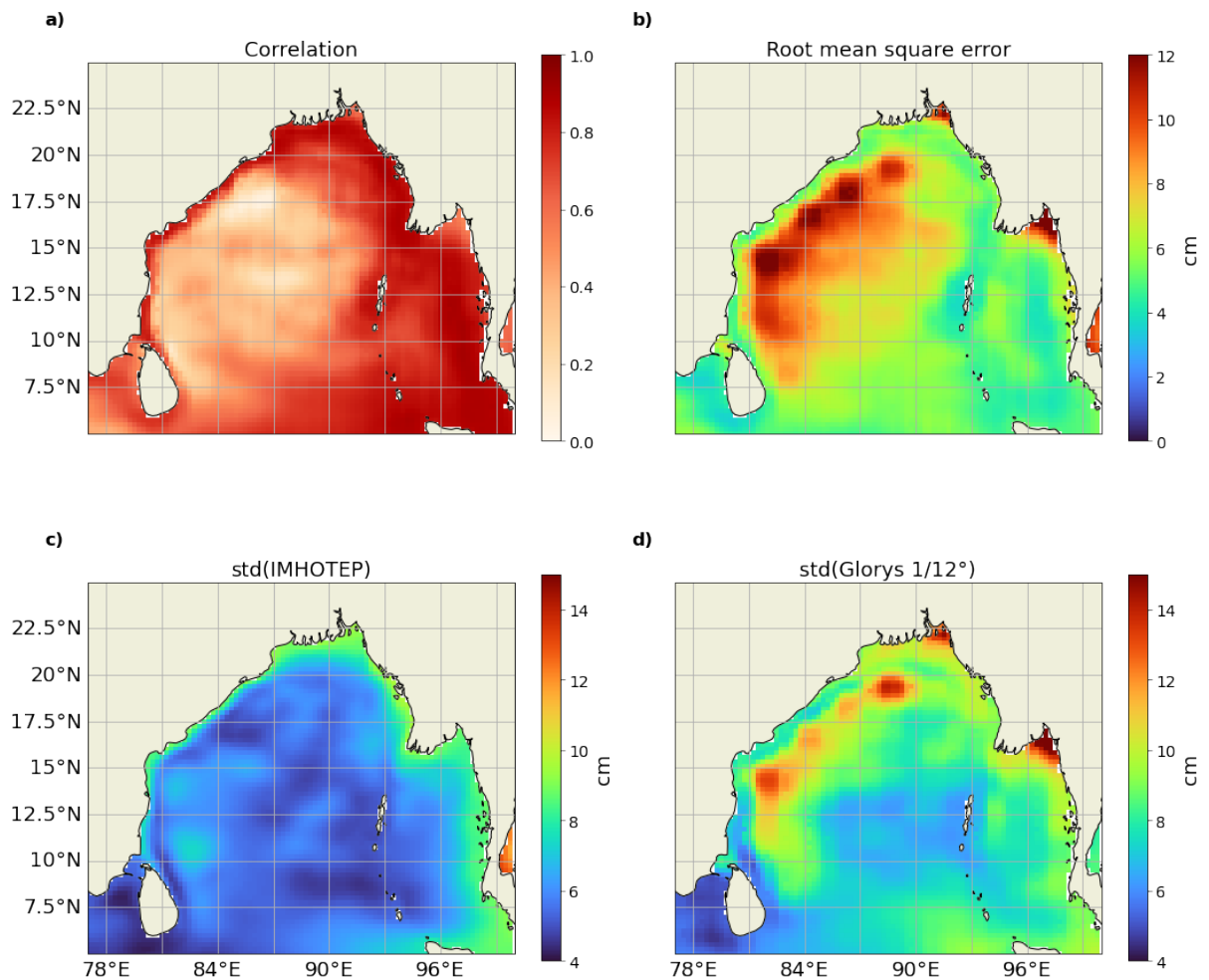


Figure B.3 – DJF averaged SLA anomaly from one member of IMHOTEP and CCI data using the common period between the two datasets (1993-01 to 2018-12): a) is their correlation, and b) their root mean square difference. The bottom panels are the standard deviation for each dataset.

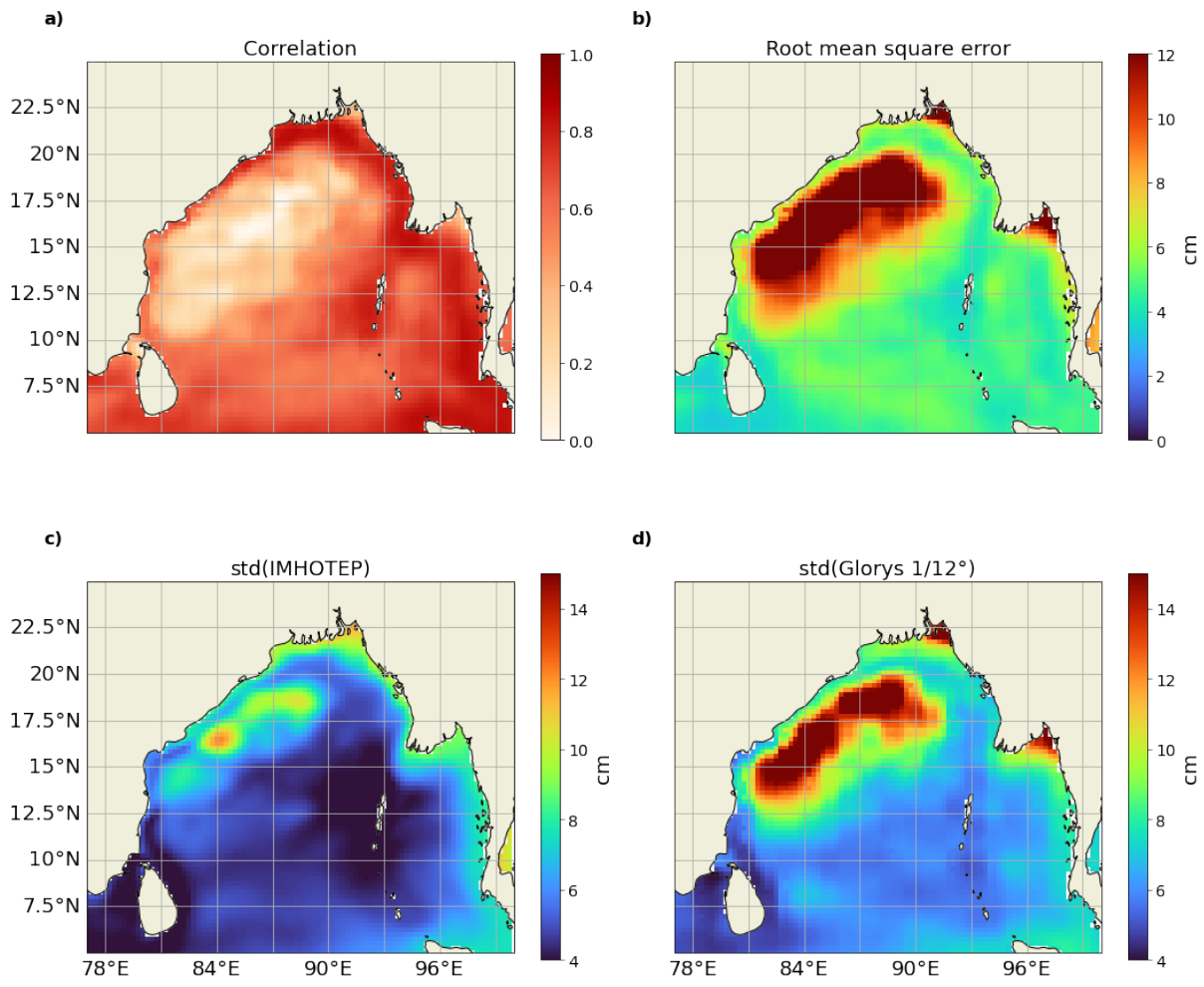


Figure B.4 – Same legend as B.3 for MAM.

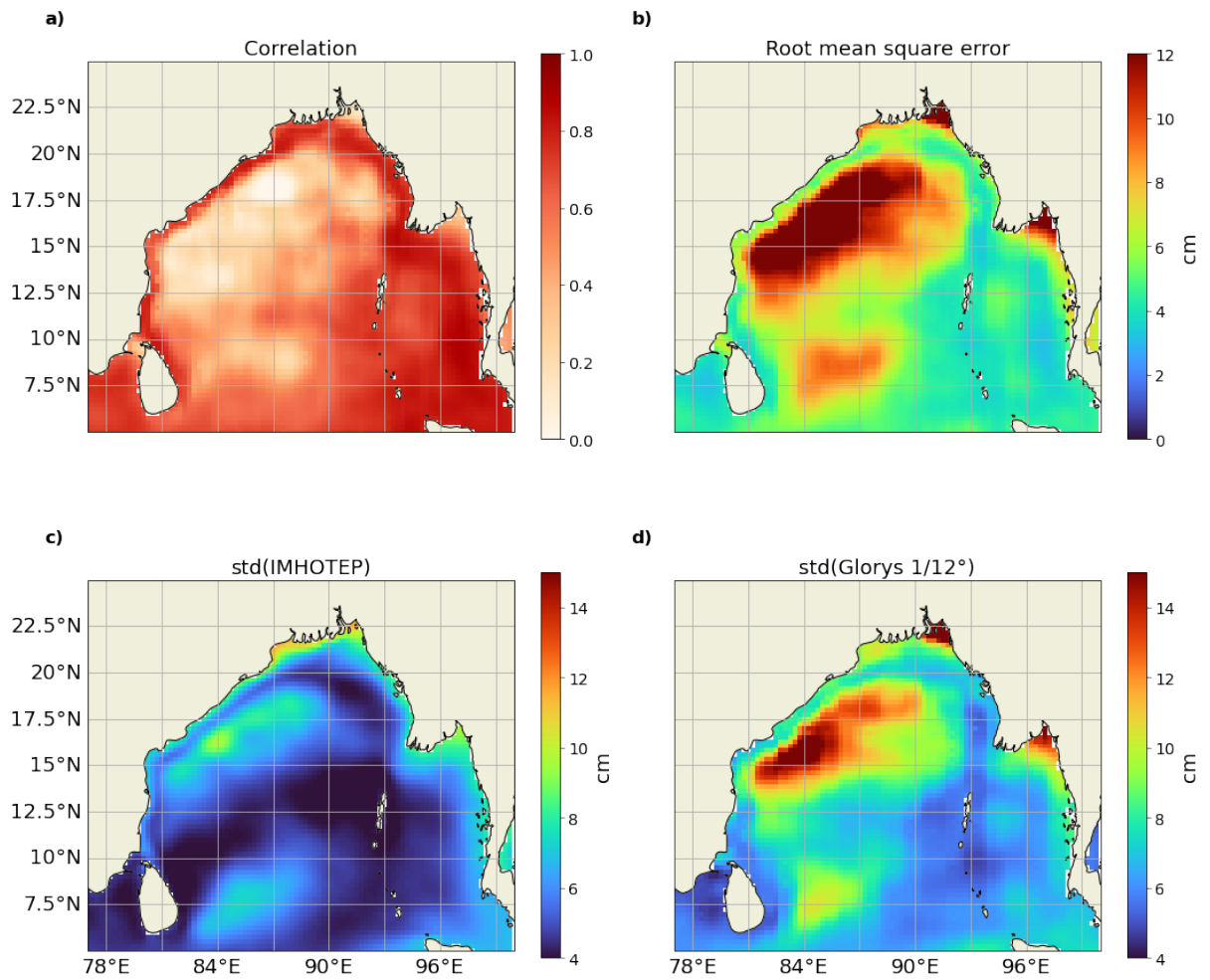


Figure B.5 – Same legend as B.3 for JJA.

---

## B.IV Seasonal Comparison between SSS from IMHOTEP and CCI

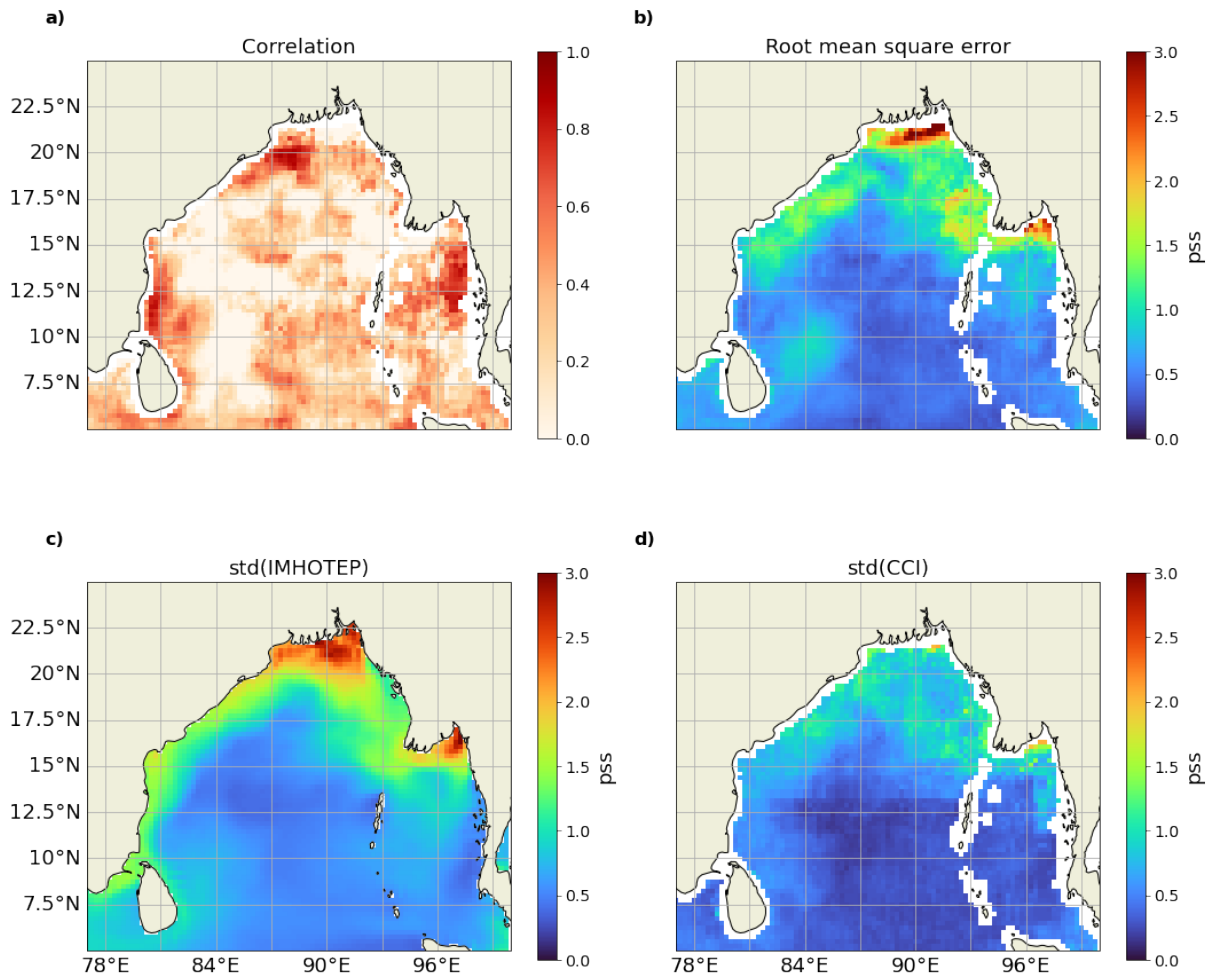


Figure B.6 – DJF averaged  $SSS'$  from one member of IMHOTEP and GLORYS data, using the common period between the two datasets (2010-06 to 2018-12): a) is their correlation, b) their root mean square difference. The bottom panels are the standard deviation for each dataset.

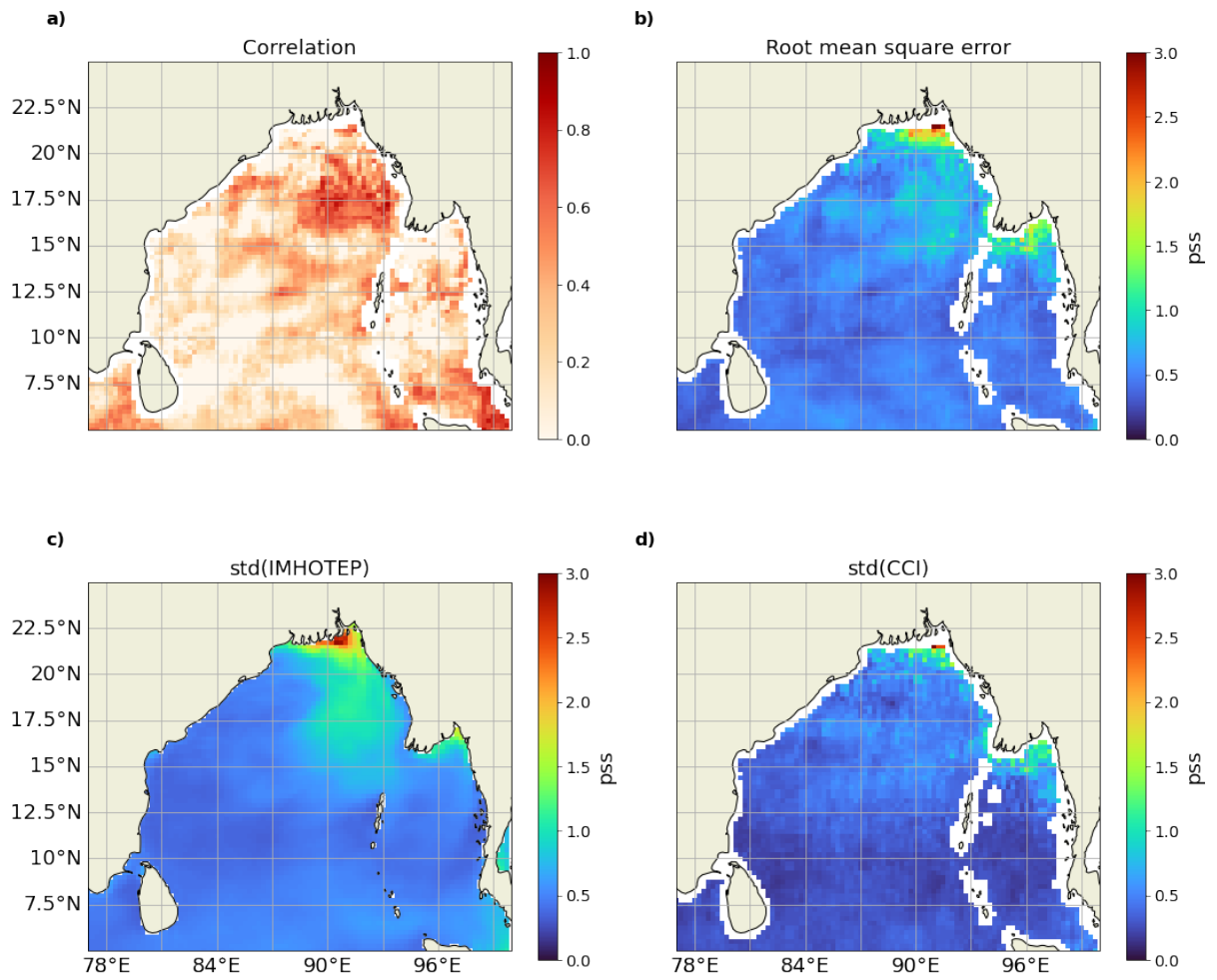


Figure B.7 – Same legend as B.6 for MAM.

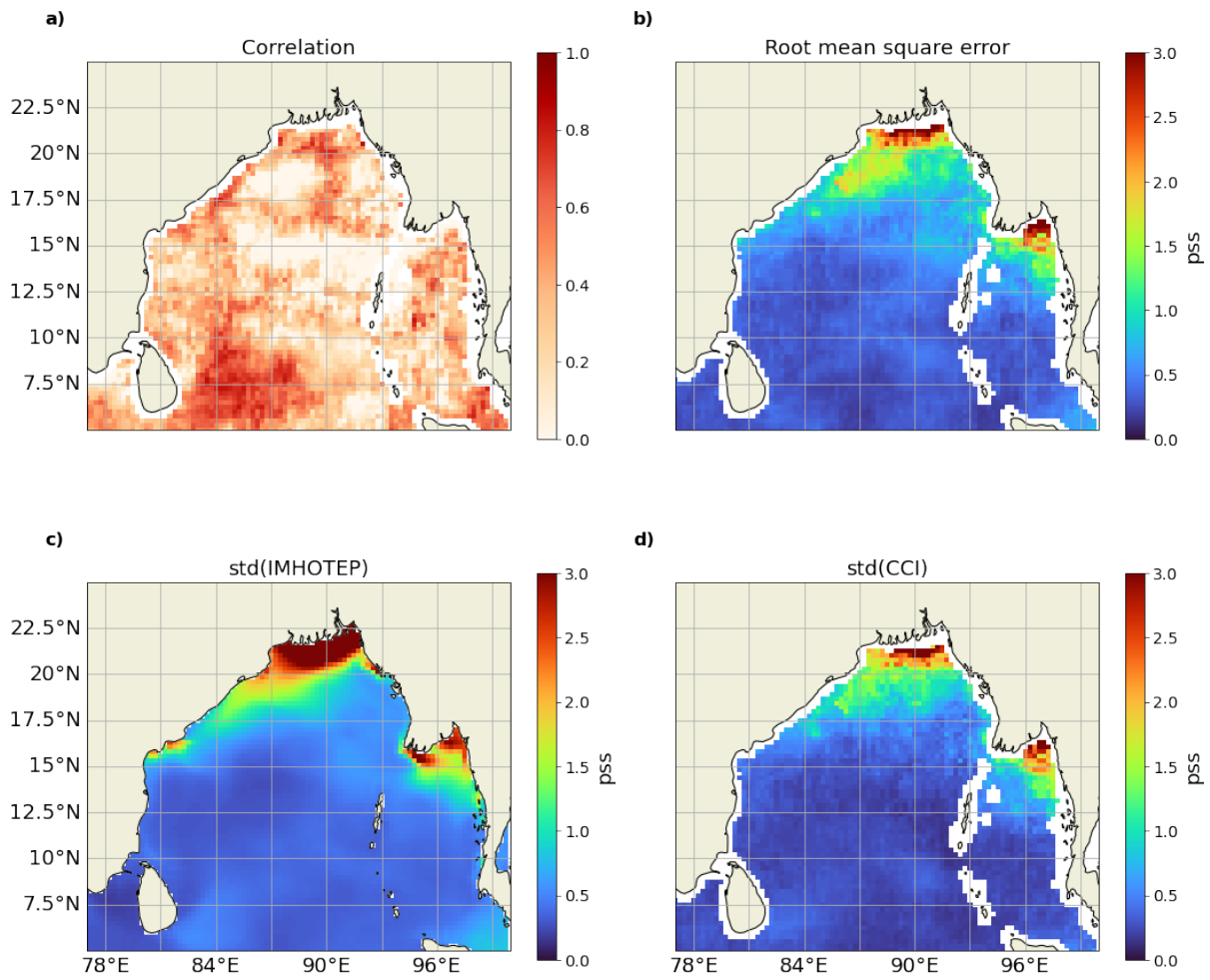


Figure B.8 – Same legend as B.6 for JJA.

## B.V Regression with the IOD for different datasets

Season DJF

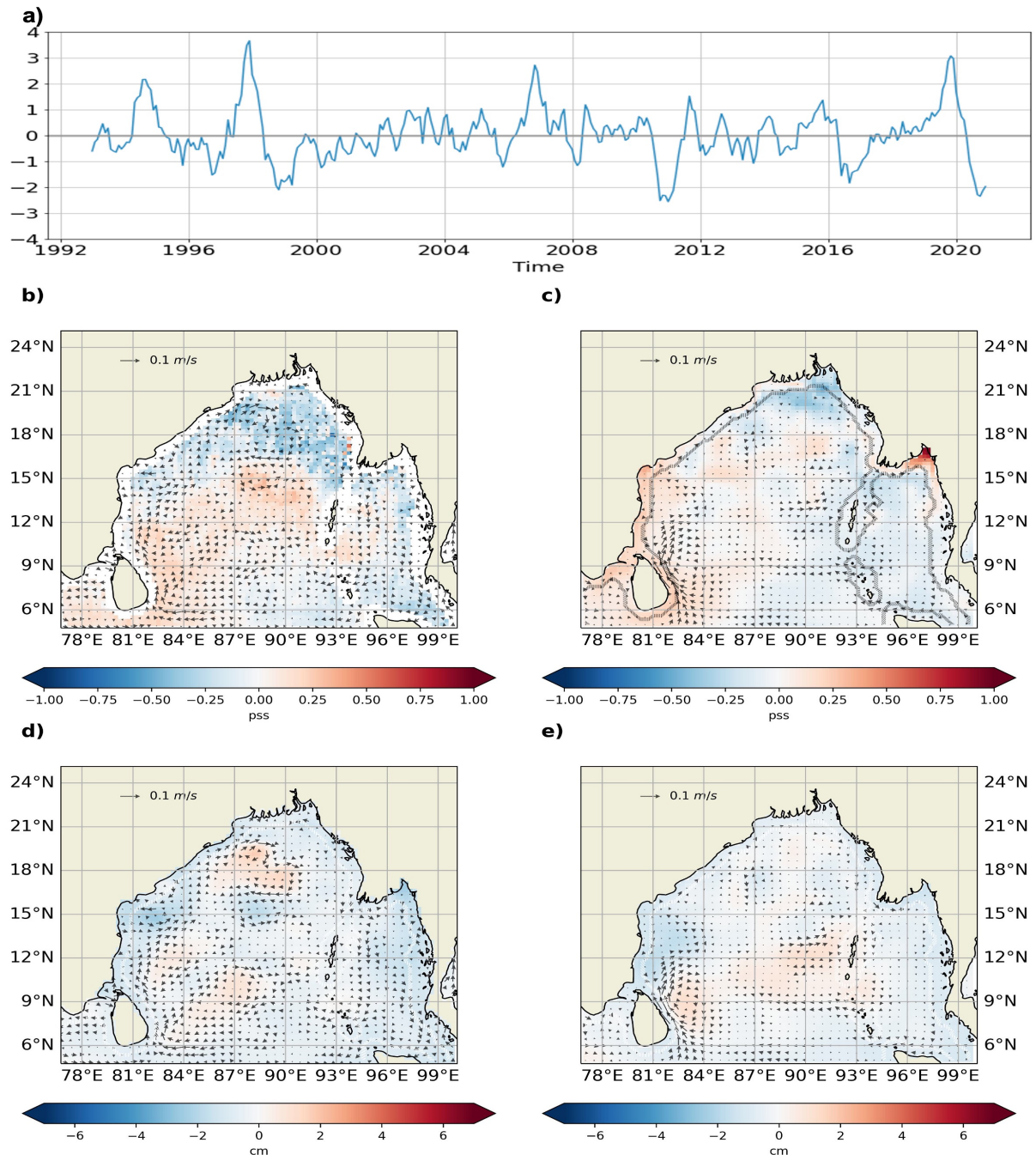


Figure B.9 – Same legend as 4.10 for DJF.

# Season MAM

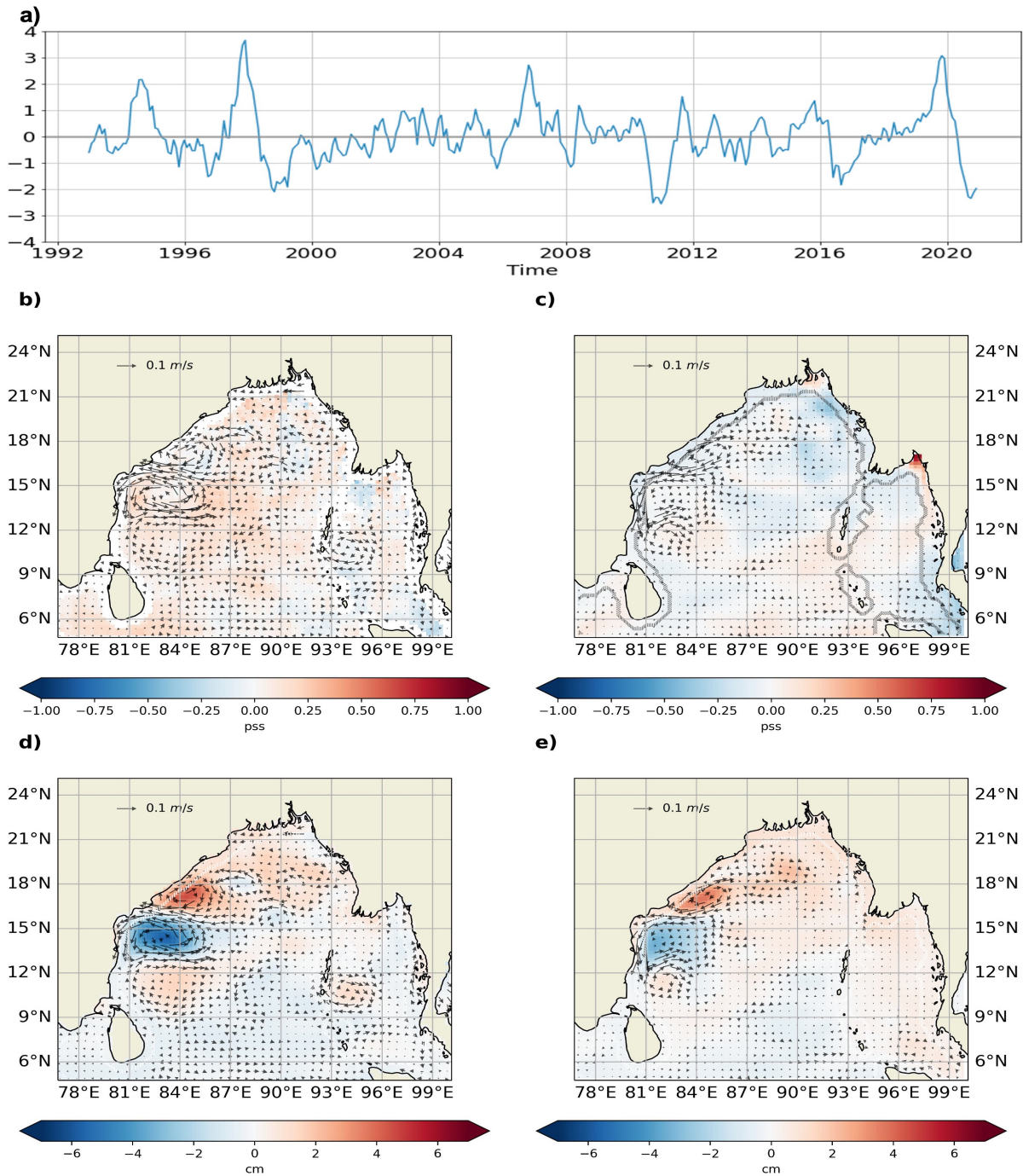


Figure B.10 – Same legend as 4.10 for MAM

## Season JJA

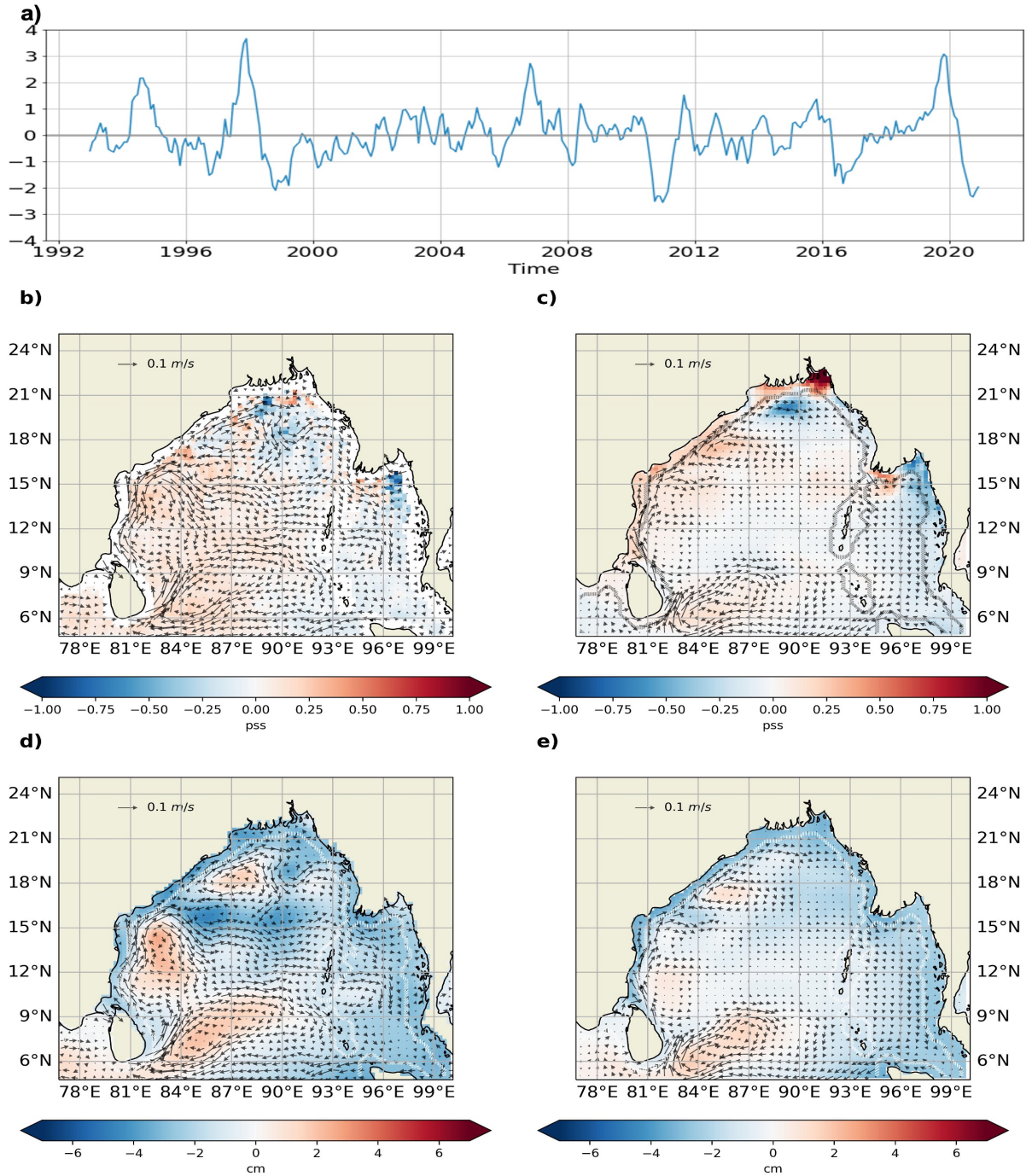


Figure B.11 – Same caption as in Figure 4.10 for JJA



## BIBLIOGRAPHY

---

- Akhil, VP, Durand, F, Lengaigne, M, Vialard, J, Keerthi, MG, Gopalakrishna, VV, Deltel, C, Papa, F, & de Boyer Montégut, C, (2014), A modeling study of the processes of surface salinity seasonal cycle in the Bay of Bengal, *Journal of Geophysical Research: Oceans*, 1196, 3926–3947, <https://doi.org/10.1002/2013JC009632>
- Akhil, VP, Lengaigne, M, Vialard, J, Durand, F, Keerthi, MG, Chaitanya, AVS, Papa, F, Gopalakrishna, VV, & de Boyer Montégut, C, (2016a), A modeling study of processes controlling the Bay of Bengal sea surface salinity interannual variability, *Journal of Geophysical Research: Oceans*, 121 12, 8471–8495, <https://doi.org/10.1002/2016JC011662>
- Akhil, VP, Lengaigne, M, Durand, F, Vialard, J, Chaitanya, AVS, Keerthi, MG, Gopalakrishna, VV, Boutin, J, & de Boyer Montégut, C, (2016b), Assessment of seasonal and year-to-year surface salinity signals retrieved from SMOS and Aquarius missions in the Bay of Bengal, *International Journal of Remote Sensing*, 37 5, 1089–1114, <https://doi.org/10.1080/01431161.2016.1145362>
- Akhil, V, Vialard, J, Lengaigne, M, Keerthi, M, Boutin, J, Vergely, J, & Papa, F, (2020), Bay of Bengal Sea surface salinity variability using a decade of improved SMOS re-processing, *Remote Sensing of Environment*, 248, 111964, <https://doi.org/10.1016/j.rse.2020.111964>
- Alam, MM, Hossain, MA, & Shafee, S, (2003), Frequency of Bay of Bengal cyclonic storms and depressions crossing different coastal zones, *International Journal of Climatology*, 23 9, 1119–1125, <https://doi.org/10.1002/joc.927>
- Allan, RP, Barlow, M, Byrne, MP, Cherchi, A, Douville, H, Fowler, HJ, Gan, TY, Pendergrass, AG, Rosenfeld, D, Swann, ALS, Wilcox, LJ, & Zolina, O, (2020), Advances in understanding large-scale responses of the water cycle to climate change [eprint: <https://onlinelibrary.wiley.com/doi/pdf/10.1111/nyas.14337>], *Annals of the New York Academy of Sciences*, 1472 1, 49–75, <https://doi.org/10.1111/nyas.14337>
- Alory, G, Delcroix, T, Téchiné, P, Diverrès, D, Varillon, D, Cravatte, S, Gouriou, Y, Grelet, J, Jacquin, S, Kestenare, E, Maes, C, Morrow, R, Perrier, J, Reverdin, G, & Roubaud, F, (2015), The French contribution to the voluntary observing ships

- 
- network of sea surface salinity, *Deep Sea Research Part I: Oceanographic Research Papers*, 105, 1–18, <https://doi.org/10.1016/j.dsr.2015.08.005>
- Argans, (2016), *SMOS Level 2 Ocean Salinity (L2OS) Algorithm Theoretical Basis Document (ATBD) (Version 3.13)* (tech. rep.), [https://smos.argans.co.uk/docs/deliverables/delivered/ATBD/SO-TN-ARG-GS-0007\\_L2OS-ATBD\\_v3.13\\_160429.pdf](https://smos.argans.co.uk/docs/deliverables/delivered/ATBD/SO-TN-ARG-GS-0007_L2OS-ATBD_v3.13_160429.pdf)
- Argo, (2022), Argo float data and metadata from Global Data Assembly Centre (Argo GDAC), <https://doi.org/10.17882/42182>
- Ashcroft, P, & Wentz, FJ, (2018), AMSR-E/Aqua L2A Global Swath Spatially-Resampled Brightness Temperatures (Tb), Version 4, <https://doi.org/10.5067/YL62FUZLAJUT>
- Balaguru, K, Chang, P, Saravanan, R, Leung, LR, Xu, Z, Li, M, & Hsieh, JS, (2012), Ocean barrier layers' effect on tropical cyclone intensification, *Proceedings of the National Academy of Sciences*, 109 36, 14343–14347, <https://doi.org/10.1073/pnas.1201364109>
- Balaguru, K, Foltz, GR, Leung, LR, Kaplan, J, Xu, W, Reul, N, & Chapron, B, (2020), Pronounced Impact of Salinity on Rapidly Intensifying Tropical Cyclones, *Bulletin of the American Meteorological Society*, 101 9, E1497–E1511, <https://doi.org/10.1175/BAMS-D-19-0303.1>
- Beal, L, Vialard, J, Roxy, MK, Li, J, Andres, M, Annamalai, H, Feng, M, Han, W, Hood, R, Lee, T, Lengaigne, M, Lumpkin, R, Masumoto, Y, McPhaden, MJ, Ravichandran, M, Shinoda, T, Sloyan, BM, Strutton, PG, Subramanian, AC, . . . Parvathi, V, (2020), A Road Map to IndOOS-2: Better Observations of the Rapidly Warming Indian Ocean, *Bulletin of the American Meteorological Society*, 101 11, E1891–E1913, <https://doi.org/10.1175/BAMS-D-19-0209.1>
- Beer, T, (2017), *Environmental Oceanography* (2nd ed.), CRC Press, <https://doi.org/10.1201/9780203756980>
- Bengtsson, L, (2010), The global atmospheric water cycle, *Environmental Research Letters*, 5 2, 025202, <https://doi.org/10.1088/1748-9326/5/2/025202>
- Benshila, R, Durand, F, Masson, S, Bourdallé-Badie, R, de Boyer Montégut, C, Papa, F, & Madec, G, (2014), The upper Bay of Bengal salinity structure in a high-resolution model, *Ocean Modelling*, 74, 36–52, <https://doi.org/10.1016/j.ocemod.2013.12.001>
- Bessières, L, Leroux, S, Brankart, JM, Molines, JM, Moine, MP, Bouttier, PA, Penduff, T, Terray, L, Barnier, B, & Sérazin, G, (2017), Development of a probabilistic

- 
- ocean modelling system based on NEMO 3.5: application at eddying resolution [Publisher: Copernicus GmbH], *Geoscientific Model Development*, 103, 1091–1106, <https://doi.org/10.5194/gmd-10-1091-2017>
- Bindlish, R, Jackson, T, Cosh, M, Tianjie Zhao, & O'Neill, P, (2015), Global Soil Moisture From the Aquarius/SAC-D Satellite: Description and Initial Assessment, *IEEE Geoscience and Remote Sensing Letters*, 125, 923–927, <https://doi.org/10.1109/LGRS.2014.2364151>
- Blanch, S, & Aguiasca, A, (2004), Seawater dielectric permittivity model from measurements at L band, *IEEE International IEEE International IEEE International Geoscience and Remote Sensing Symposium, 2004. IGARSS '04. Proceedings. 2004, 2*, 1362–1365, <https://doi.org/10.1109/IGARSS.2004.1368671>
- Boussidi, B, Cornillon, P, Puggioni, G, & Gentemann, C, (2019), Determining the AMSR-E SST Footprint from Co-Located MODIS SSTs, *Remote Sensing*, 116, 715, <https://doi.org/10.3390/rs11060715>
- Boutin, J, Reul, N, Koehler, J, Martin, A, Catany, R, Guimbard, S, Rouffi, F, Vergely, JL, Arias, M, Chakroun, M, Corato, G, Estella-Perez, V, Hasson, A, Josey, S, Khvorostyanov, D, Kolodziejczyk, N, Mignot, J, Olivier, L, Reverdin, G, . . . Mecklenburg, S, (2021a), Satellite-Based Sea Surface Salinity Designed for Ocean and Climate Studies, *Journal of Geophysical Research: Oceans*, 12611, e2021JC017676, <https://doi.org/10.1029/2021JC017676>
- Boutin, J, Vergely, J, Marchand, S, D'Amico, F, Hasson, A, Kolodziejczyk, N, Reul, N, Reverdin, G, & Vialard, J, (2018), New SMOS Sea Surface Salinity with reduced systematic errors and improved variability, *Remote Sensing of Environment*, 214, 115–134, <https://doi.org/10.1016/j.rse.2018.05.022>
- Boutin, J, Vergely, JL, Dinnat, EP, Waldteufel, P, D'Amico, F, Reul, N, Supply, A, & Thouvenin-Masson, C, (2021b), Correcting Sea Surface Temperature Spurious Effects in Salinity Retrieved From Spaceborne L-Band Radiometer Measurements, *IEEE Transactions on Geoscience and Remote Sensing*, 599, 7256–7269, <https://doi.org/10.1109/TGRS.2020.3030488>
- Boyer, TP, Garcia, HE, Locarnini, RA, Zweng, MM, Mishonov, AV, Reagan, JR, Weathers, KA, Baranova, OK, Seidov, D, & Smolyar, IV, (2018), World Ocean Atlas 2018, <https://www.ncei.noaa.gov/archive/accession/NCEI-WOA18>

- 
- Brainerd, KE, & Gregg, MC, (1995), Surface mixed and mixing layer depths, *Deep Sea Research Part I: Oceanographic Research Papers*, 429, 1521–1543, [https://doi.org/10.1016/0967-0637\(95\)00068-H](https://doi.org/10.1016/0967-0637(95)00068-H)
- Broecker, WS, (1997), Thermohaline Circulation, the Achilles Heel of Our Climate System: Will Man-Made CO<sub>2</sub> Upset the Current Balance?, *Science*, 278 5343, 1582–1588, <https://doi.org/10.1126/science.278.5343.1582>
- Camps, A, Font, J, Vall-llossera, M, Gabarro, C, Corbella, I, Duffo, N, Torres, F, Blanch, S, Aguasca, A, Villarino, R, Enrique, L, Miranda, J, Arenas, J, Julia, A, Etcheto, J, Caselles, V, Weill, A, Boutin, J, Contardo, S, ... Martin-Neira, M, (2004), The WISE 2000 and 2001 field experiments in support of the SMOS mission: sea surface L-band brightness temperature observations and their application to sea surface salinity retrieval, *IEEE Transactions on Geoscience and Remote Sensing*, 424, 804–823, <https://doi.org/10.1109/TGRS.2003.819444>
- Carret, A, Llovel, W, Penduff, T, & Molines, JM, (2021), Atmospherically Forced and Chaotic Interannual Variability of Regional Sea Level and Its Components Over 1993–2015 [eprint: <https://onlinelibrary.wiley.com/doi/pdf/10.1029/2020JC017123>], *Journal of Geophysical Research: Oceans*, 1264, e2020JC017123, <https://doi.org/10.1029/2020JC017123>
- Chahine, MT, (1992), The hydrological cycle and its influence on climate, *Nature*, 359 6394, 373–380, <https://doi.org/10.1038/359373a0>
- Chaitanya, AVS, Lengaigne, M, Vialard, J, Gopalakrishna, VV, Durand, F, Kranthikumar, C, Amritash, S, Suneel, V, Papa, F, & Ravichandran, M, (2014a), Supplement: Salinity Measurements Collected by Fishermen Reveal a “River in the Sea” Flowing Along the Eastern Coast of India [Publisher: American Meteorological Society], *Bulletin of the American Meteorological Society*, 95 12, ES241–ES245, retrieved February 8, 2023, from <https://www.jstor.org/stable/26219455>
- Chaitanya, AVS, Lengaigne, M, Vialard, J, Gopalakrishna, VV, Durand, F, Kranthikumar, C, Amritash, S, Suneel, V, Papa, F, & Ravichandran, M, (2014b), Salinity Measurements Collected by Fishermen Reveal a “River in the Sea” Flowing Along the Eastern Coast of India, *Bulletin of the American Meteorological Society*, 95 12, 1897–1908, <https://doi.org/10.1175/BAMS-D-12-00243.1>
- Chaitanya, AVS, Durand, F, Mathew, S, Gopalakrishna, VV, Papa, F, Lengaigne, M, Vialard, J, Kranthikumar, C, & Venkatesan, R, (2015), Observed year-to-year sea

- 
- surface salinity variability in the Bay of Bengal during the 2009–2014 period, *Ocean Dynamics*, *65* 2, 173–186, <https://doi.org/10.1007/s10236-014-0802-x>
- Chaitanya, AVS, Vialard, J, Lengaigne, M, d'Ovidio, F, Riotte, J, Papa, F, & James, RA, (2021), Redistribution of riverine and rainfall freshwater by the Bay of Bengal circulation, *Ocean Dynamics*, *71* 11-12, 1113–1139, <https://doi.org/10.1007/s10236-021-01486-5>
- Chelton, DB, Schlax, MG, & Samelson, RM, (2011), Global observations of nonlinear mesoscale eddies, *Progress in Oceanography*, *91* 2, 167–216, <https://doi.org/10.1016/j.pocean.2011.01.002>
- Chen, G, Wang, D, & Hou, Y, (2012), The features and interannual variability mechanism of mesoscale eddies in the Bay of Bengal, *Continental Shelf Research*, *47*, 178–185, <https://doi.org/10.1016/j.csr.2012.07.011>
- Chen, S, & Hu, C, (2017), Estimating sea surface salinity in the northern Gulf of Mexico from satellite ocean color measurements, *Remote Sensing of Environment*, *201*, 115–132, <https://doi.org/10.1016/j.rse.2017.09.004>
- Craig, PM, Ferreira, D, & Methven, J, (2017), The contrast between Atlantic and Pacific surface water fluxes [Publisher: Taylor & Francis \_eprint: <https://doi.org/10.1080/16000870.2017.1330454>], *Tellus A: Dynamic Meteorology and Oceanography*, *69* 1, 1330454, <https://doi.org/10.1080/16000870.2017.1330454>
- Cui, W, Yang, J, & Ma, Y, (2016), A statistical analysis of mesoscale eddies in the Bay of Bengal from 22-year altimetry data, *Acta Oceanologica Sinica*, *35* 11, 16–27, <https://doi.org/10.1007/s13131-016-0945-3>
- Cui, W, Zhang, J, & Yang, J, (2022), Seasonal variation in eddy activity and associated heat/salt transport in the Bay of Bengal based on satellite, Argo, and 3D reprocessed data, *Ocean Science*, *18* 6, 1645–1663, <https://doi.org/10.5194/os-18-1645-2022>
- Currie, JC, Lengaigne, M, Vialard, J, Kaplan, DM, Aumont, O, Naqvi, SWA, & Maury, O, (2013), Indian Ocean Dipole and El Niño/Southern Oscillation impacts on regional chlorophyll anomalies in the Indian Ocean, *Biogeosciences*, *10* 10, 6677–6698, <https://doi.org/10.5194/bg-10-6677-2013>
- D'Addezio, JM, Subrahmanyam, B, Nyadjro, ES, & Murty, VSN, (2015), Seasonal Variability of Salinity and Salt Transport in the Northern Indian Ocean, *Journal of Physical Oceanography*, *45* 7, 1947–1966, <https://doi.org/10.1175/JPO-D-14-0210.1>

- 
- Dandapat, S, & Chakraborty, A, (2016), Mesoscale Eddies in the Western Bay of Bengal as Observed From Satellite Altimetry in 1993–2014: Statistical Characteristics, Variability and Three-Dimensional Properties, *IEEE Journal of Selected Topics in Applied Earth Observations and Remote Sensing*, 911, 5044–5054, <https://doi.org/10.1109/JSTARS.2016.2585179>
- de Boyer Montégut, C, (2005), *Couche melangee oceanique et bilan thermohalin de surface dans l’Ocean Indien Nord* (Doctoral dissertation), Université Pierre et Marie Curie - Paris VI,
- de Boyer Montégut, C, Madec, G, Fischer, AS, Lazar, A, & Iudicone, D, (2004), Mixed layer depth over the global ocean: An examination of profile data and a profile-based climatology [eprint: <https://onlinelibrary.wiley.com/doi/pdf/10.1029/2004JC002378>], *Journal of Geophysical Research: Oceans*, 109 C12, <https://doi.org/10.1029/2004JC002378>
- de Boyer Montégut, C, Mignot, J, Lazar, A, & Cravatte, S, (2007), Control of salinity on the mixed layer depth in the world ocean, *Journal of Geophysical Research*, 112 C6, C06011, <https://doi.org/10.1029/2006JC003953>
- Debye, P, (1929), Polar molecules, *Chemical Catalog Company, Incorporation*, 4843, 1036–1037, <https://doi.org/10.1002/jctb.5000484320>
- Decharme, B, Delire, C, Minvielle, M, Colin, J, Vergnes, JP, Alias, A, Saint-Martin, D, Séférian, R, Sénési, S, & Voltaire, A, (2019), Recent Changes in the ISBA-CTRIP Land Surface System for Use in the CNRM-CM6 Climate Model and in Global Off-Line Hydrological Applications, *Journal of Advances in Modeling Earth Systems*, 115, 1207–1252, <https://doi.org/10.1029/2018MS001545>
- Dessier, A, & Donguy, JR, (1994), The sea surface salinity in the tropical Atlantic between 10°S and 30°N—seasonal and interannual variations (1977–1989), *Deep Sea Research Part I: Oceanographic Research Papers*, 41 1, 81–100, [https://doi.org/10.1016/0967-0637\(94\)90027-2](https://doi.org/10.1016/0967-0637(94)90027-2)
- Dijkstra, HA, (2008), *Dynamical oceanography*, Springer Verlag.
- Dinnat, EP, (2003), *De la détermination de la salinité de surface des océans à partir de mesures radiométriques hyperfréquences en bande L* (Doctoral dissertation).
- Dorigo, W, Dietrich, S, Aires, F, Brocca, L, Carter, S, Cretaux, JF, Dunkerley, D, Enomoto, H, Forsberg, R, Güntner, A, Hegglin, MI, Hollmann, R, Hurst, DF, Johannessen, JA, Kummerow, C, Lee, T, Luoju, K, Looser, U, Miralles, DG, . . . Aich, V, (2021), Closing the Water Cycle from Observations across Scales: Where

- 
- Do We Stand? [Publisher: American Meteorological Society Section: Bulletin of the American Meteorological Society], *Bulletin of the American Meteorological Society*, 102 10, E1897–E1935, <https://doi.org/10.1175/BAMS-D-19-0316.1>
- Drushka, K, Gille, ST, & Sprintall, J, (2014), The diurnal salinity cycle in the tropics, *Journal of Geophysical Research: Oceans*, 119 9, 5874–5890, <https://doi.org/10.1002/2014JC009924>
- Durack, PJ, & Wijffels, SE, (2010), Fifty-Year Trends in Global Ocean Salinities and Their Relationship to Broad-Scale Warming [Publisher: American Meteorological Society Section: Journal of Climate], *Journal of Climate*, 23 16, 4342–4362, <https://doi.org/10.1175/2010JCLI3377.1>
- Durack, PJ, Wijffels, SE, & Matear, RJ, (2012), Ocean Salinities Reveal Strong Global Water Cycle Intensification During 1950 to 2000, *Science*, 336 6080, 455–458, <https://doi.org/10.1126/science.1212222>
- Durand, F, Shankar, D, Birol, F, & Shenoi, SSC, (2009), Spatiotemporal structure of the East India Coastal Current from satellite altimetry, *Journal of Geophysical Research*, 114 C2, C02013, <https://doi.org/10.1029/2008JC004807>
- Durand, F, Alory, G, Dussin, R, & Reul, N, (2013), SMOS reveals the signature of Indian Ocean Dipole events, *Ocean Dynamics*, 63 11-12, 1203–1212, <https://doi.org/10.1007/s10236-013-0660-y>
- Ellison, W, Balana, A, Delbos, G, Lamkaouchi, K, Eymard, L, Guillou, C, & Prigent, C, (1998), New permittivity measurements of seawater, *Radio Science*, 33 3, 639–648, <https://doi.org/10.1029/97RS02223>
- Emery, W, (2001), Water Types And Water Masses. In *Encyclopedia of Ocean Sciences* (pp. 3179–3187), Elsevier, <https://doi.org/10.1006/rwos.2001.0108>
- Foltz, GR, & McPhaden, MJ, (2009), Impact of Barrier Layer Thickness on SST in the Central Tropical North Atlantic\*, *Journal of Climate*, 22 2, 285–299, <https://doi.org/10.1175/2008JCLI2308.1>
- Fournier, S, Vialard, J, Lengaigne, M, Lee, T, Gierach, MM, & Chaitanya, AVS, (2017), Modulation of the Ganges-Brahmaputra River Plume by the Indian Ocean Dipole and Eddies Inferred From Satellite Observations, *Journal of Geophysical Research: Oceans*, 122 12, 9591–9604, <https://doi.org/10.1002/2017JC013333>
- Fournier, S, & Lee, T, (2021), Seasonal and Interannual Variability of Sea Surface Salinity Near Major River Mouths of the World Ocean Inferred from Gridded Satellite and

- 
- In-Situ Salinity Products [Number: 4 Publisher: Multidisciplinary Digital Publishing Institute], *Remote Sensing*, 134, 728, <https://doi.org/10.3390/rs13040728>
- Gadgil, S, Joseph, PV, & Joshi, NV, (1984), Ocean–atmosphere coupling over monsoon regions [Number: 5990 Publisher: Nature Publishing Group], *Nature*, 3125990, 141–143, <https://doi.org/10.1038/312141a0>
- Gaillard, F, Diverres, D, Gouriou, Y, & Jacquin, S, (2015), SSS from French Research Vessels: Inventory of thermo-salinometer delayed mode data - 2014, retrieved February 7, 2023, from <https://archimer.ifremer.fr/doc/00251/36231/>
- Gaiser, P, St Germain, K, Twarog, E, Poe, G, Purdy, W, Richardson, D, Grossman, W, Jones, W, Spencer, D, Golba, G, Cleveland, J, Choy, L, Bevilacqua, R, & Chang, P, (2004), The WindSat spaceborne polarimetric microwave radiometer: sensor description and early orbit performance, *IEEE Transactions on Geoscience and Remote Sensing*, 4211, 2347–2361, <https://doi.org/10.1109/TGRS.2004.836867>
- Garcia-Eidell, C, Comiso, JC, Dinnat, E, & Brucker, L, (2017), Satellite observed salinity distributions at high latitudes in the Northern Hemisphere: A comparison of four products [eprint: <https://onlinelibrary.wiley.com/doi/pdf/10.1002/2017JC013184>], *Journal of Geophysical Research: Oceans*, 1229, 7717–7736, <https://doi.org/10.1002/2017JC013184>
- Gordon, A, Shroyer, E, Mahadevan, A, Sengupta, D, & Freilich, M, (2016), Bay of Bengal: 2013 Northeast Monsoon Upper-Ocean Circulation, *Oceanography*, 292, 82–91, <https://doi.org/10.5670/oceanog.2016.41>
- Gordon, AL, (1986), Interocean exchange of thermocline water [eprint: <https://onlinelibrary.wiley.com/doi/pdf/10.1029/JC091iC04p05037>], *Journal of Geophysical Research: Oceans*, 91C4, 5037–5046, <https://doi.org/10.1029/JC091iC04p05037>
- Goswami, BN, & Xavier, PK, (2005), Dynamics of “internal” interannual variability of the Indian summer monsoon in a GCM [eprint: <https://onlinelibrary.wiley.com/doi/pdf/10.1029/2005JD006042>], *Journal of Geophysical Research: Atmospheres*, 110D24, <https://doi.org/10.1029/2005JD006042>
- Hareesh Kumar, PV, Mathew, B, Ramesh Kumar, MR, Raghunadha Rao, A, Jagadeesh, PSV, Radhakrishnan, KG, & Shyni, TN, (2013), ‘Thermohaline front’ off the east coast of India and its generating mechanism, *Ocean Dynamics*, 6311, 1175–1180, <https://doi.org/10.1007/s10236-013-0652-y>

- 
- Held, IM, & Soden, BJ, (2006), Robust Responses of the Hydrological Cycle to Global Warming [Publisher: American Meteorological Society Section: Journal of Climate], *Journal of Climate*, 1921, 5686–5699, <https://doi.org/10.1175/JCLI3990.1>
- Hood, RR, Beckley, LE, & Wiggert, JD, (2017), Biogeochemical and ecological impacts of boundary currents in the Indian Ocean, *Progress in Oceanography*, 156, 290–325, <https://doi.org/10.1016/j.pocean.2017.04.011>
- IOC, SCOR, & IAPSO, (2010), *The international thermodynamic equation of seawater – 2010: Calculation and use of thermodynamic properties*. (tech. rep. No. 56), UNESCO, retrieved February 10, 2023, from [https://www.teos-10.org/pubs/gsw/pdf/TEOS-10\\_Manual.pdf](https://www.teos-10.org/pubs/gsw/pdf/TEOS-10_Manual.pdf)
- Kantha, L, & Clayson, C, (2003), Ocean Mixed Layer. In *Encyclopedia of Atmospheric Sciences* (pp. 291–298), Elsevier, <https://doi.org/10.1016/B0-12-227090-8/00093-2>
- Kawanishi, T, Sezai, T, Ito, Y, Imaoka, K, Takeshima, T, Ishido, Y, Shibata, A, Miura, M, Inahata, H, & Spencer, R, (2003), The advanced microwave scanning radiometer for the earth observing system (AMSR-E), NASDA’s contribution to the EOS for global energy and water cycle studies, *IEEE Transactions on Geoscience and Remote Sensing*, 412, 184–194, <https://doi.org/10.1109/TGRS.2002.808331>
- Kerr, YH, Waldteufel, P, Wigneron, JP, Delwart, S, Cabot, F, Boutin, J, Escorihuela, MJ, Font, J, Reul, N, Gruhier, C, Juglea, SE, Drinkwater, MR, Hahne, A, Martín-Neira, M, & Mecklenburg, S, (2010), The SMOS Mission: New Tool for Monitoring Key Elements of the Global Water Cycle, *Proceedings of the IEEE*, 985, 666–687, <https://doi.org/10.1109/JPROC.2010.2043032>
- Kilic, L, Prigent, C, & Jimenez, C, (2020), Sensitivities to ocean and sea ice parameters as a function of CIMR channels for arctic, mid-latitude, and tropical conditions. [Pages: 58240 Bytes Publisher: figshare], <https://doi.org/10.6084/M9.FIGSHARE.11709765.V1>
- Klein, L, & Swift, C, (1977), An improved model for the dielectric constant of sea water at microwave frequencies, *IEEE Journal of Oceanic Engineering*, 21, 104–111, <https://doi.org/10.1109/JOE.1977.1145319>
- Knauss, J, (1997), *Introduction to Physical Oceanography*, Prentice Hall, <https://books.google.fr/books?id=p58PAQAIAAJ>
- Kobayashi, S, Ota, Y, Harada, Y, Ebata, A, Moriya, M, Onoda, H, Onogi, K, Kamahori, H, Kobayashi, C, Endo, H, Miyaoka, K, & Takahashi, K, (2015), The JRA-55 Reanal-

- 
- ysis: General Specifications and Basic Characteristics, *Journal of the Meteorological Society of Japan. Ser. II*, 931, 5–48, <https://doi.org/10.2151/jmsj.2015-001>
- Krishnamohan, K, Vialard, J, Lengaigne, M, Masson, S, Samson, G, Pous, S, Neetu, S, Durand, F, Shenoi, S, & Madec, G, (2019), Is there an effect of Bay of Bengal salinity on the northern Indian Ocean climatological rainfall?, *Deep Sea Research Part II: Topical Studies in Oceanography*, 166, 19–33, <https://doi.org/10.1016/j.dsr2.2019.04.003>
- Kumari, A, Kumar, SP, & Chakraborty, A, (2018), Seasonal and Interannual Variability in the Barrier Layer of the Bay of Bengal, *Journal of Geophysical Research: Oceans*, 1232, 1001–1015, <https://doi.org/10.1002/2017JC013213>
- Lagerloef, G, Colomb, FR, Le Vine, D, Wentz, F, Yueh, S, Ruf, C, Lilly, J, Gunn, J, Chao, Y, Decharon, A, Feldman, G, & Swift, C, (2008), THE AQUARIUS/SAC-D MISSION [Publisher: Oceanography Society], *Oceanography*, 21 1, 68–81, retrieved February 3, 2023, from <https://www.jstor.org/stable/24860158>
- Lagerloef, G, & Font, J, (2010), SMOS and Aquarius/SAC-D Missions: The Era of Spaceborne Salinity Measurements is About to Begin, In V Barale, J Gower, & L Alberotanza (Eds.), *Oceanography from Space: Revisited* (pp. 35–58), Springer Netherlands, [https://doi.org/10.1007/978-90-481-8681-5\\_3](https://doi.org/10.1007/978-90-481-8681-5_3)
- Lang, R, Zhou, Y, Utku, C, & Le Vine, D, (2016), Accurate measurements of the dielectric constant of seawater at L band, *Radio Science*, 51 1, 2–24, <https://doi.org/10.1002/2015RS005776>
- Lascaratos, A, Roether, W, Nittis, K, & Klein, B, (1999), Recent changes in deep water formation and spreading in the eastern Mediterranean Sea: a review, *Progress in Oceanography*, 44 1, 5–36, [https://doi.org/10.1016/S0079-6611\(99\)00019-1](https://doi.org/10.1016/S0079-6611(99)00019-1)
- Le Vine, DM, Lagerloef, GSE, & Torrusio, SE, (2010), Aquarius and Remote Sensing of Sea Surface Salinity from Space [Conference Name: Proceedings of the IEEE], *Proceedings of the IEEE*, 98 5, 688–703, <https://doi.org/10.1109/JPROC.2010.2040550>
- Lee, K, Tong, LT, Millero, FJ, Sabine, CL, Dickson, AG, Goyet, C, Park, GH, Wanninkhof, R, Feely, RA, & Key, RM, (2006), Global relationships of total alkalinity with salinity and temperature in surface waters of the world’s oceans, *Geophysical Research Letters*, 33 19, L19605, <https://doi.org/10.1029/2006GL027207>
- Lellouche, JM, Greiner, E, Bourdallé-Badie, R, Garric, G, Melet, A, Drévilon, M, Bricaud, C, Hamon, M, Le Galloudec, O, Regnier, C, Candela, T, Testut, CE, Gasparin,

- 
- F, Ruggiero, G, Benkiran, M, Drillet, Y, & Le Traon, PY, (2021), The Copernicus Global 1/12° Oceanic and Sea Ice GLORYS12 Reanalysis, *Frontiers in Earth Science*, 9, 698876, <https://doi.org/10.3389/feart.2021.698876>
- Leroux, S, Penduff, T, Bessières, L, Molines, JM, Brankart, JM, Sérazin, G, Barnier, B, & Terray, L, (2018), Intrinsic and Atmospherically Forced Variability of the AMOC: Insights from a Large-Ensemble Ocean Hindcast [Publisher: American Meteorological Society Section: Journal of Climate], *Journal of Climate*, 31 3, 1183–1203, <https://doi.org/10.1175/JCLI-D-17-0168.1>
- Lewis, E, (1980), The practical salinity scale 1978 and its antecedents [Conference Name: IEEE Journal of Oceanic Engineering], *IEEE Journal of Oceanic Engineering*, 5 1, 3–8, <https://doi.org/10.1109/JOE.1980.1145448>
- Leys, C, Ley, C, Klein, O, Bernard, P, & Licata, L, (2013), Detecting outliers: Do not use standard deviation around the mean, use absolute deviation around the median, *Journal of Experimental Social Psychology*, 49 4, 764–766, <https://doi.org/10.1016/j.jesp.2013.03.013>
- Lin, X, Qiu, Y, & Sun, D, (2019), Thermohaline Structures and Heat/Freshwater Transports of Mesoscale Eddies in the Bay of Bengal Observed by Argo and Satellite Data, *Remote Sensing*, 11 24, 2989, <https://doi.org/10.3390/rs11242989>
- Llovel, W, Penduff, T, Meyssignac, B, Molines, JM, Terray, L, Bessières, L, & Barnier, B, (2018), Contributions of Atmospheric Forcing and Chaotic Ocean Variability to Regional Sea Level Trends Over 1993–2015 [eprint: <https://onlinelibrary.wiley.com/doi/pdf/10.1029/2018GL080838>], *Geophysical Research Letters*, 45 24, 13, 405–13, 413, <https://doi.org/10.1029/2018GL080838>
- Madec, G, Bourdallé-Badie, R, Chanut, J, Clementi, E, Coward, A, Ethé, C, Iovino, D, Lea, D, Lévy, C, Lovato, T, Martin, N, Masson, S, Mocavero, S, Rousset, C, Storkey, D, Müeller, S, Nurser, G, Bell, M, Samson, G, . . . Moulin, A, (2022), NEMO ocean engine [Publisher: Zenodo], <https://doi.org/10.5281/zenodo.6334656>
- Mahadevan, A, Spiro Jaeger, G, Freilich, M, Omand, M, Shroyer, E, & Sengupta, D, (2016), Freshwater in the Bay of Bengal: Its Fate and Role in Air-Sea Heat Exchange, *Oceanography*, 29 2, 72–81, <https://doi.org/10.5670/oceanog.2016.40>
- Martin, S, (2014), *An introduction to ocean remote sensing* (Second edition), Cambridge University Press.

- 
- McCreary, JP, Han, W, Shankar, D, & Shetye, SR, (1996), Dynamics of the East India Coastal Current: 2. Numerical solutions, *Journal of Geophysical Research: Oceans*, 101 C6, 13993–14010, <https://doi.org/10.1029/96JC00560>
- McDougall, TJ, Jackett, DR, Millero, FJ, Pawlowicz, R, & Barker, PM, (2012), A global algorithm for estimating Absolute Salinity [Publisher: Copernicus GmbH], *Ocean Science*, 8 6, 1123–1134, <https://doi.org/10.5194/os-8-1123-2012>
- McPhaden, M, Busalacchi, A, & Anderson, D, (2010), A TOGA Retrospective, *Oceanography*, 23 3, 86–103, <https://doi.org/10.5670/oceanog.2010.26>
- Mecklenburg, S, Drusch, M, Kerr, Y, martin-neira, M, Steven, D, Buenadicha, G, Reul, N, Daganzo, E, Oliva, R, & Crapolicchio, R, (2012), ESA’s Soil Moisture and Ocean Salinity Mission: Mission Performance and Operations, *IEEE Transactions on Geoscience and Remote Sensing - IEEE TRANS GEOSCI REMOT SEN*, 50, 1354–1366, <https://doi.org/10.1109/TGRS.2012.2187666>
- Meissner, T, & Wentz, F, (2002), An updated analysis of the ocean surface wind direction signal in passive microwave brightness temperatures, *IEEE Transactions on Geoscience and Remote Sensing*, 40 6, 1230–1240, <https://doi.org/10.1109/TGRS.2002.800231>
- Meissner, T, & Wentz, F, (2004), The complex dielectric constant of pure and sea water from microwave satellite observations, *IEEE Transactions on Geoscience and Remote Sensing*, 42 9, 1836–1849, <https://doi.org/10.1109/TGRS.2004.831888>
- Meissner, T, & Wentz, F, (2006), Polarization rotation and the third Stokes parameter: the effects of spacecraft attitude and Faraday rotation, *IEEE Transactions on Geoscience and Remote Sensing*, 44 3, 506–515, <https://doi.org/10.1109/TGRS.2005.858413>
- Meissner, T, & Wentz, FJ, (2012), The Emissivity of the Ocean Surface Between 6 and 90 GHz Over a Large Range of Wind Speeds and Earth Incidence Angles, *IEEE Transactions on Geoscience and Remote Sensing*, 50 8, 3004–3026, <https://doi.org/10.1109/TGRS.2011.2179662>
- Meissner, T, Wentz, FJ, & Ricciardulli, L, (2014), The emission and scattering of L-band microwave radiation from rough ocean surfaces and wind speed measurements from the Aquarius sensor [eprint: <https://onlinelibrary.wiley.com/doi/pdf/10.1002/2014JC009837>], *Journal of Geophysical Research: Oceans*, 119 9, 6499–6522, <https://doi.org/10.1002/2014JC009837>

- 
- Meissner, T, Wentz, FJ, & Vine, DML, (2018), The Salinity Retrieval Algorithms for the NASA Aquarius Version 5 and SMAP Version 3 Releases, *Remote Sensing*, 107, 1121, <https://doi.org/10.3390/rs10071121>
- Merchant, CJ, Embury, O, Roberts-Jones, J, Fiedler, E, Bulgin, CE, Corlett, GK, Good, S, McLaren, A, Rayner, N, Morak-Bozzo, S, & Donlon, C, (2014), Sea surface temperature datasets for climate applications from Phase 1 of the European Space Agency Climate Change Initiative ( SST CCI ), *Geoscience Data Journal*, 12, 179–191, <https://doi.org/10.1002/gdj3.20>
- Mignot, J, de Boyer Montégut, C, Lazar, A, & Cravatte, S, (2007), Control of salinity on the mixed layer depth in the world ocean: 2. Tropical areas [[\\_eprint: https://onlinelibrary.wiley.com/doi/pdf/10.1029/2006JC003954](https://onlinelibrary.wiley.com/doi/pdf/10.1029/2006JC003954)], *Journal of Geophysical Research: Oceans*, 112 C10, <https://doi.org/10.1029/2006JC003954>
- Mishra, AK, Dwivedi, S, & Shrivastava, A, (2015), High resolution simulation of the salinity variability in the Bay of Bengal and Arabian Sea during the years 1998–2014 using an ocean circulation model.
- Morisset, S, Reverdin, G, Boutin, J, Martin, N, Yin, X, Gaillard, F, Blouch, P, Rolland, J, & Salvador, J, (2012), SURFACE SALINITY DRIFTERS FOR SMOS VALIDATION, *Mercator Ocean – CORIOLIS Quarterly Newsletter*, 45, 33–37, <https://archimer.ifremer.fr/doc/00114/22552/>
- Myhre, G, Shindell, D, Bréon, FM, Collins, W, Fuglestvedt, J, Huang, J, Koch, D, Lamarque, JF, Lee, D, Mendoza, B, Nakajima, T, Robock, A, Stephens, G, Takemura, T, & Zhang, H, (2013), Anthropogenic and Natural Radiative Forcing. *In Climate Change 2013: The Physical Science Basis. Contribution of Working Group I to the Fifth Assessment Report of the Intergovernmental Panel on Climate Change* [Stocker, T.F., D. Qin, G.-K. Plattner, M. Tignor, S.K. Allen, J. Boschung, A. Nauels, Y. Xia, V. Bex and P.M. Midgley (eds.)] Cambridge University Press.
- Neetu, S, Lengaigne, M, Vialard, J, Samson, G, Masson, S, Krishnamohan, KS, & Suresh, I, (2019), Premonsoon/Postmonsoon Bay of Bengal Tropical Cyclones Intensity: Role of Air-Sea Coupling and Large-Scale Background State, *Geophysical Research Letters*, 464, 2149–2157, <https://doi.org/10.1029/2018GL081132>
- Neetu, S, Lengaigne, M, Vincent, EM, Vialard, J, Madec, G, Samson, G, Ramesh Kumar, MR, & Durand, F, (2012), Influence of upper-ocean stratification on tropical

- 
- cyclone-induced surface cooling in the Bay of Bengal, *Journal of Geophysical Research: Oceans*, 117C12, C12020, <https://doi.org/10.1029/2012JC008433>
- Nyadjro, ES, (2021), Impacts of the 2019 Strong IOD and Monsoon Events on Indian Ocean Sea Surface Salinity, *Remote Sensing in Earth Systems Sciences*, 43, 158–171, <https://doi.org/10.1007/s41976-021-00054-1>
- Nyadjro, ES, & Subrahmanyam, B, (2016), Spatial and temporal variability of central Indian Ocean salinity fronts observed by SMOS, *Remote Sensing of Environment*, 180, 146–153, <https://doi.org/10.1016/j.rse.2016.02.049>
- Nyadjro, ES, Subrahmanyam, B, & Shriver, JF, (2011), Seasonal variability of salt transport during the Indian Ocean monsoons, *Journal of Geophysical Research*, 116C8, C08036, <https://doi.org/10.1029/2011JC006993>
- Oreopoulos, L, Graham, S, & Przyborski, P, (2023), AMSR-E | Aqua Project Science, retrieved February 6, 2023, from <https://aqua.nasa.gov/amsr-e>
- Pant, V, Girishkumar, MS, Udaya Bhaskar, TVS, Ravichandran, M, Papa, F, & Thangaprakash, VP, (2015), Observed interannual variability of near-surface salinity in the Bay of Bengal: Salinity variability in the BoB, *Journal of Geophysical Research: Oceans*, 1205, 3315–3329, <https://doi.org/10.1002/2014JC010340>
- Papa, F, Bala, SK, Pandey, RK, Durand, F, Gopalakrishna, VV, Rahman, A, & Rossow, WB, (2012), Ganga-Brahmaputra river discharge from Jason-2 radar altimetry: An update to the long-term satellite-derived estimates of continental freshwater forcing flux into the Bay of Bengal, *Journal of Geophysical Research: Oceans*, 117C11, n/a–n/a, <https://doi.org/10.1029/2012JC008158>
- Peake, W, (1959), Interaction of electromagnetic waves with some natural surfaces, *IRE Transactions on Antennas and Propagation*, 75, 324–329, <https://doi.org/10.1109/TAP.1959.1144736>
- Penduff, T, Barnier, B, Terray, L, Bessières, L, Sérazin, G, Molines, M, & Brasseur, P, (2014), Ensembles of eddying ocean simulations for climate, *CLIVAR Exchanges, Special Issue on High Resolution Ocean Climate Modelling*, 19.
- Penduff, T, Juza, M, Barnier, B, Zika, J, Dewar, WK, Treguier, AM, Molines, JM, & Audiffren, N, (2011), Sea Level Expression of Intrinsic and Forced Ocean Variabilities at Interannual Time Scales [Publisher: American Meteorological Society Section: Journal of Climate], *Journal of Climate*, 24 21, 5652–5670, <https://doi.org/10.1175/JCLI-D-11-00077.1>

- 
- Penduff, T, Llovel, W, Close, S, Garcia-Gomez, I, & Leroux, S, (2019), Trends of Coastal Sea Level Between 1993 and 2015: Imprints of Atmospheric Forcing and Oceanic Chaos, *Surveys in Geophysics*, 406, 1543–1562, <https://doi.org/10.1007/s10712-019-09571-7>
- Penduff, T, Sérazin, G, Leroux, S, Close, S, Molines, JM, Barnier, B, Bessières, L, Terray, L, & Maze, G, (2018), Chaotic Variability of Ocean: Heat Content Climate-Relevant Features and Observational Implications, *Oceanography*, 312, <https://doi.org/10.5670/oceanog.2018.210>
- Peng, J, Misra, S, Piepmeier, JR, Dinnat, EP, Hudson, D, Le Vine, DM, De Amici, G, Mohammed, PN, Bindlish, R, Yueh, SH, Meissner, T, & Jackson, TJ, (2017), Soil Moisture Active/Passive L-Band Microwave Radiometer Postlaunch Calibration, *IEEE Transactions on Geoscience and Remote Sensing*, 559, 5339–5354, <https://doi.org/10.1109/TGRS.2017.2705342>
- Piepmeier, JR, Focardi, P, Horgan, KA, Knuble, J, Ehsan, N, Lucey, J, Brambora, C, Brown, PR, Hoffman, PJ, French, RT, Mikhaylov, RL, Kwack, EY, Slimko, EM, Dawson, DE, Hudson, D, Peng, J, Mohammed, PN, De Amici, G, Freedman, AP, ... Njoku, EG, (2017), SMAP L-Band Microwave Radiometer: Instrument Design and First Year on Orbit, *IEEE Transactions on Geoscience and Remote Sensing*, 554, 1954–1966, <https://doi.org/10.1109/TGRS.2016.2631978>
- Prasanna Kumar, S, Muraleedharan, PM, Prasad, TG, Gauns, M, Ramaiah, N, de Souza, SN, Sardesai, S, & Madhupratap, M, (2002), Why is the Bay of Bengal less productive during summer monsoon compared to the Arabian Sea?, *Geophysical Research Letters*, 2924, 88–1–88–4, <https://doi.org/10.1029/2002GL016013>
- Priyanka, K, Sarangi, R, Shanthi, R, Poornima, D, & Saravanakumar, A, (2022), Interannual and seasonal cycle of satellite derived sea surface salinity in the western Bay of Bengal, *Arabian Journal of Geosciences*, 1522, 1670, <https://doi.org/10.1007/s12517-022-10945-2>
- Rahmstorf, S, (2003), Thermohaline circulation: The current climate [Number: 6924 Publisher: Nature Publishing Group], *Nature*, 421 6924, 699–699, <https://doi.org/10.1038/421699a>
- Rahmstorf, S, (2006), Thermohaline Ocean Circulation, *Edited by S. A. Elias. Elsevier.*
- Rao, SA, & Behera, SK, (2005), Subsurface influence on SST in the tropical Indian Ocean: structure and interannual variability, *Dynamics of Atmospheres and Oceans*, 391, 103–135, <https://doi.org/10.1016/j.dynatmoce.2004.10.014>

- 
- Reul, N, Grodsky, SA, Arias, M, Boutin, J, Catany, R, Chapron, B, D'Amico, F, Dinnat, E, Donlon, C, Fore, A, Fournier, S, Guimbard, S, Hasson, A, Kolodziejczyk, N, Lagerloef, G, Lee, T, Le Vine, DM, Lindstrom, E, Maes, C, . . . Yueh, S, (2020), Sea surface salinity estimates from spaceborne L-band radiometers: An overview of the first decade of observation (2010–2019), *Remote Sensing of Environment*, 242, 111769, <https://doi.org/10.1016/j.rse.2020.111769>
- Reul, N, Saux-Picart, S, Chapron, B, Vandemark, D, Tournadre, J, & Salisbury, J, (2009), Demonstration of ocean surface salinity microwave measurements from space using AMSR-E data over the Amazon plume, *Geophysical Research Letters*, 36 13, L13607, <https://doi.org/10.1029/2009GL038860>
- Reul, N, Fournier, S, Boutin, J, Hernandez, O, Maes, C, Chapron, B, Alory, G, Quilfen, Y, Tenerelli, J, Morisset, S, Kerr, Y, Mecklenburg, S, & Delwart, S, (2014), Sea Surface Salinity Observations from Space with the SMOS Satellite: A New Means to Monitor the Marine Branch of the Water Cycle, *Surveys in Geophysics*, 35 3, 681–722, <https://doi.org/10.1007/s10712-013-9244-0>
- Reverdin, G, Cadet, DL, & Gutzler, D, (1986), Interannual displacements of convection and surface circulation over the equatorial Indian Ocean [eprint: <https://onlinelibrary.wiley.com/doi/pdf/10.1002/qj.49711247104>], *Quarterly Journal of the Royal Meteorological Society*, 112 471, 43–67, <https://doi.org/10.1002/qj.49711247104>
- Reyes, E, Aguiar, E, Bondoni, M, Berta, M, Brandini, C, Cáceres-Euse, A, Capodici, F, Cardin, V, Cianelli, D, Ciruolo, G, Corgnati, L, Dadić, V, Doronzo, B, Drago, A, Dumas, D, Falco, P, Fattorini, M, Fernandes, MJ, Gauci, A, . . . Orfila, A, (2022), Coastal high-frequency radars in the Mediterranean – Part 2: Applications in support of science priorities and societal needs [Publisher: Copernicus GmbH], *Ocean Science*, 18 3, 797–837, <https://doi.org/10.5194/os-18-797-2022>
- Reynaud, T, Kolodziejczyk, N, Maes, C, Gaillard, F, Reverdin, G, Desprez De Gesincourt, F, & Le Goff, H, (2022), Sea Surface Salinity from Sailing ships : Delayed mode dataset, annual release, <https://doi.org/10.17882/39476>
- Riser, SC, Freeland, HJ, Roemmich, D, Wijffels, S, Troisi, A, Belbéoch, M, Gilbert, D, Xu, J, Pouliquen, S, Thresher, A, Le Traon, PY, Maze, G, Klein, B, Ravichandran, M, Grant, F, Poulain, PM, Suga, T, Lim, B, Sterl, A, . . . Jayne, SR, (2016), Fifteen years of ocean observations with the global Argo array, *Nature Climate Change*, 6 2, 145–153, <https://doi.org/10.1038/nclimate2872>

- 
- Robinson, IS, (2004), *Measuring the oceans from space: the principles and methods of satellite oceanography* [OCLC: ocm53926711], Springer ; Praxis Pub.
- Rowell, DP, (1998), Assessing Potential Seasonal Predictability with an Ensemble of Multidecadal GCM Simulations, *Journal of Climate*, 11 2, 109–120, [https://doi.org/10.1175/1520-0442\(1998\)011<0109:APSPWA>2.0.CO;2](https://doi.org/10.1175/1520-0442(1998)011<0109:APSPWA>2.0.CO;2)
- Saji, NH, Goswami, BN, Vinayachandran, PN, & Yamagata, T, (1999), A dipole mode in the tropical Indian Ocean [Number: 6751 Publisher: Nature Publishing Group], *Nature*, 401 6751, 360–363, <https://doi.org/10.1038/43854>
- Saji, NH, Xie, SP, & Yamagata, T, (2006), Tropical Indian Ocean Variability in the IPCC Twentieth-Century Climate Simulations\*, *Journal of Climate*, 19 17, 4397–4417, <https://doi.org/10.1175/JCLI3847.1>
- Schmitt, RW, (2008), Salinity and the Global Water Cycle [Publisher: Oceanography Society], *Oceanography*, 21 1, 12–19, retrieved February 15, 2023, from <https://www.jstor.org/stable/24860148>
- Schott, FA, & McCreary, JP, (2001), The monsoon circulation of the Indian Ocean, *Progress in Oceanography*, 51 1, 1–123, [https://doi.org/10.1016/S0079-6611\(01\)00083-0](https://doi.org/10.1016/S0079-6611(01)00083-0)
- Schott, FA, Xie, SP, & McCreary, JP, (2009), Indian Ocean circulation and climate variability, *Reviews of Geophysics*, 47 1, RG1002, <https://doi.org/10.1029/2007RG000245>
- Sengupta, D, Bharath Raj, GN, Ravichandran, M, Sree Lekha, J, & Papa, F, (2016), Near-surface salinity and stratification in the north Bay of Bengal from moored observations: Salinity in the North Bay of Bengal, *Geophysical Research Letters*, 43 9, 4448–4456, <https://doi.org/10.1002/2016GL068339>
- Sengupta, D, Bharath Raj, GN, & Shenoi, SSC, (2006), Surface freshwater from Bay of Bengal runoff and Indonesian Throughflow in the tropical Indian Ocean, *Geophysical Research Letters*, 33 22, L22609, <https://doi.org/10.1029/2006GL027573>
- Sengupta, D, Goddalahundi, BR, & Anitha, DS, (2008), Cyclone-induced mixing does not cool SST in the post-monsoon north Bay of Bengal, *Atmospheric Science Letters*, 9 1, 1–6, <https://doi.org/10.1002/asl.162>
- Seo, H, Xie, SP, Murtugudde, R, Jochum, M, & Miller, AJ, (2009), Seasonal Effects of Indian Ocean Freshwater Forcing in a Regional Coupled Model\*, *Journal of Climate*, 22 24, 6577–6596, <https://doi.org/10.1175/2009JCLI2990.1>

- 
- Service, EUCM, (2019), Global Ocean Ensemble Physics Reanalysis, <https://doi.org/10.48670/MOI-00024>
- Sharma, R, Agarwal, N, Momin, IM, Basu, S, & Agarwal, VK, (2010), Simulated Sea Surface Salinity Variability in the Tropical Indian Ocean, *Journal of Climate*, *23*24, 6542–6554, <https://doi.org/10.1175/2010JCLI3721.1>
- Shen, CC, Liu, KK, Lee, MY, Lee, T, Wang, CH, & Lee, HJ, (2005), A novel method for tracing coastal water masses using Sr/Ca ratios and salinity in Nanwan Bay, southern Taiwan, *Estuarine, Coastal and Shelf Science*, *65* 1, 135–142, <https://doi.org/10.1016/j.ecss.2005.05.010>
- Shenoi, SSC, Saji, PK, & Almeida, AM, (1999), Near-surface circulation and kinetic energy in the tropical Indian Ocean derived from Lagrangian drifters, *Journal of Marine Research*, *57*6, 885–907, <https://doi.org/10.1357/002224099321514088>
- Shenoi, SSC, Shankar, D, & Shetye, SR, (2002), Differences in heat budgets of the near-surface Arabian Sea and Bay of Bengal: Implications for the summer monsoon, *Journal of Geophysical Research*, *107* C6, 3052, <https://doi.org/10.1029/2000JC000679>
- Singh, A, Gandhi, N, Ramesh, R, & Prakash, S, (2015), Role of cyclonic eddy in enhancing primary and new production in the Bay of Bengal, *Journal of Sea Research*, *97*, 5–13, <https://doi.org/10.1016/j.seares.2014.12.002>
- Somaraju, R, & Trumpf, J, (2006), Frequency, Temperature and Salinity Variation of the Permittivity of Seawater [Conference Name: IEEE Transactions on Antennas and Propagation], *IEEE Transactions on Antennas and Propagation*, *54* 11, 3441–3448, <https://doi.org/10.1109/TAP.2006.884290>
- Song, Q, & Wang, Z, (2017), Sea surface salinity observed from the HY-2A satellite, *Satellite Oceanography and Meteorology*, *21*, <https://doi.org/10.18063/SOM.2016.02.004>
- Sprintall, J, & Cronin, M, (2001), Upper Ocean Vertical Structure. In *Encyclopedia of Ocean Sciences* (pp. 3120–3128), Elsevier, <https://doi.org/10.1006/rwos.2001.0149>
- Stogryn, A, (1971), Equations for Calculating the Dielectric Constant of Saline Water (Correspondence), *IEEE Transactions on Microwave Theory and Techniques*, *19* 8, 733–736, <https://doi.org/10.1109/TMTT.1971.1127617>
- Stogryn, AP, Bull, HT, Rubayi, K, & Iravanchy, S, (1995), The microwave permittivity of sea and fresh water. GenCorp Aerojet, Azusa, CA., *The microwave permittivity of sea and fresh water. GenCorp Aerojet, Azusa, CA.*

- 
- Supply, A, (2020), *Étude des dessalures à la surface d'un océan stratifié à partir d'observations satellitaires et de mesures in-situ* (Doctoral dissertation).
- Supply, A, Boutin, J, Kolodziejczyk, N, Reverdin, G, Lique, C, Vergely, JL, & Perrot, X, (2022), Meltwater Lenses Over the Chukchi and the Beaufort Seas During Summer 2019: From In Situ to Synoptic View [eprint: <https://onlinelibrary.wiley.com/doi/pdf/10.1029/2021JC018388>], *Journal of Geophysical Research: Oceans*, *12712*, e2021JC018388, <https://doi.org/10.1029/2021JC018388>
- Suresh, I, Vialard, J, Lengaigne, M, Han, W, McCreary, J, Durand, F, & Muraleedharan, PM, (2013), Origins of wind-driven intraseasonal sea level variations in the North Indian Ocean coastal waveguide [eprint: <https://onlinelibrary.wiley.com/doi/pdf/10.1002/2013GL058312>], *Geophysical Research Letters*, *4021*, 5740–5744, <https://doi.org/10.1002/2013GL058312>
- Suresh, I, Vialard, J, Lengaigne, M, Izumo, T, Parvathi, V, & Muraleedharan, PM, (2018), Sea Level Interannual Variability Along the West Coast of India [eprint: <https://onlinelibrary.wiley.com/doi/pdf/10.1029/2018GL080972>], *Geophysical Research Letters*, *4522*, 12, 440–12, 448, <https://doi.org/10.1029/2018GL080972>
- Treasure, A, Roquet, F, Ansorge, I, Bester, M, Boehme, L, Bornemann, H, Charrassin, JB, Chevallier, D, Costa, D, Fedak, M, Guinet, C, Hammill, M, Harcourt, R, Hindell, M, Kovacs, K, Lea, MA, Lovell, P, Lowther, A, Lydersen, C, . . . de Bruyn, PN, (2017), Marine Mammals Exploring the Oceans Pole to Pole: A Review of the MEOP Consortium, *Oceanography*, *302*, 132–138, <https://doi.org/10.5670/oceanog.2017.234>
- Treguier, A, Böning, CW, Bryan, F, Danabasoglu, G, Drange, H, Taguchi, B, & Pirani, A, (2014), CLIVAR WGOMD Workshop on high resolution ocean climate modelling: outcomes and recommendations, *CLIVAR Exchanges No 65*, *19*, 3–6.
- Unesco, (1981a), *Background Papers and Supporting Data on the Practical Salinity Scale 1978-Unesco*.
- Unesco, (1981b), The practical salinity scale1978 and the international equation of state of seawater 1980, *Tenth Report of the Joint Panel on Oceanographic Tables and Standards (JPOTS)*, *25*.
- Unesco (Ed.), (1985), *The International System of Units (SI) in Oceanography*. (tech. rep.) [Medium: 131pp.], UNESCO, <https://doi.org/10.25607/OBP-666>

- 
- Vialard, J, Shenoi, SSC, McCreary, JP, Shankar, D, Durand, F, Fernando, V, & Shetye, SR, (2009), Intraseasonal response of the northern Indian Ocean coastal waveguide to the Madden-Julian Oscillation [\_eprint: <https://onlinelibrary.wiley.com/doi/pdf/10.1029/2009GL038450>], *Geophysical Research Letters*, 36 14, <https://doi.org/10.1029/2009GL038450>
- Vincent, EM, Emanuel, KA, Lengaigne, M, Vialard, J, & Madec, G, (2014), Influence of upper ocean stratification interannual variability on tropical cyclones, *Journal of Advances in Modeling Earth Systems*, 6 3, 680–699, <https://doi.org/10.1002/2014MS000327>
- Weaver, AJ, Bitz, CM, Fanning, AF, & Holland, MM, (1999), THERMOHALINE CIRCULATION: High-Latitude Phenomena and the Difference Between the Pacific and Atlantic, *Annual Review of Earth and Planetary Sciences*, 27 1, 231–285, <https://doi.org/10.1146/annurev.earth.27.1.231>
- Webster, PJ, Moore, AM, Loschnigg, JP, & Leben, RR, (1999), Coupled ocean–atmosphere dynamics in the Indian Ocean during 1997–98 [Number: 6751 Publisher: Nature Publishing Group], *Nature*, 401 6751, 356–360, <https://doi.org/10.1038/43848>
- Weller, R, Farrar, JT, Buckley, J, Matthew, S, Venkatesan, R, Lekha, JS, Chaudhuri, D, Kumar, NS, & Kuman, BP, (2016), Air-Sea Interaction in the Bay of Bengal, *Oceanography*, 29 2, 28–37, <https://doi.org/10.5670/oceanog.2016.36>
- Wentz, F, & Meissner, T, (2000), *Theoretical Basis Document AMSR Ocean Algorithm Version 2*.
- Wentz, F, & Meissner, T, (2004), AMSR-E/Aqua L2B Global Swath Ocean Products derived from Wentz Algorithm, Version 2, [https://doi.org/10.5067/AMSR-E/AE\\_OCEAN.002](https://doi.org/10.5067/AMSR-E/AE_OCEAN.002)
- Wilson, W, Yueh, S, Dinardo, S, & Li, F, (2004), High-stability L-band radiometer measurements of saltwater, *IEEE Transactions on Geoscience and Remote Sensing*, 42 9, 1829–1835, <https://doi.org/10.1109/TGRS.2004.833393>
- Wright, DG, Pawlowicz, R, McDougall, TJ, Feistel, R, & Marion, GM, (2011), Absolute Salinity, "Density Salinity" and the Reference-Composition Salinity Scale: present and future use in the seawater standard TEOS-10 [Publisher: Copernicus GmbH], *Ocean Science*, 7 1, 1–26, <https://doi.org/10.5194/os-7-1-2011>

- 
- Wunsch, C, (2002), What Is the Thermohaline Circulation? [Publisher: American Association for the Advancement of Science], *Science*, 298 5596, 1179–1181, <https://doi.org/10.1126/science.1079329>
- Yu, L, Josey, SA, Bingham, FM, & Lee, T, (2020), Intensification of the global water cycle and evidence from ocean salinity: a synthesis review, *Annals of the New York Academy of Sciences*, 1472 1, 76–94, <https://doi.org/10.1111/nyas.14354>
- Zhang, C, (2005), Madden-Julian Oscillation [eprint: <https://onlinelibrary.wiley.com/doi/pdf/10.1029/2004RG000158>], *Reviews of Geophysics*, 43 2, <https://doi.org/10.1029/2004RG000158>
- Zhou, Y, Lang, RH, Dinnat, EP, & Le Vine, DM, (2017), L-Band Model Function of the Dielectric Constant of Seawater [Conference Name: IEEE Transactions on Geoscience and Remote Sensing], *IEEE Transactions on Geoscience and Remote Sensing*, 55 12, 6964–6974, <https://doi.org/10.1109/TGRS.2017.2737419>
- Zhou, Y, Lang, RH, Dinnat, EP, & Le Vine, DM, (2021), Seawater Debye Model Function at L-Band and Its Impact on Salinity Retrieval From Aquarius Satellite Data [Conference Name: IEEE Transactions on Geoscience and Remote Sensing], *IEEE Transactions on Geoscience and Remote Sensing*, 59 10, 8103–8116, <https://doi.org/10.1109/TGRS.2020.3045771>





**Titre :** Étude de la variabilité de la salinité de surface dans le Golfe du Bengale à partir de données satellitaires radiométriques en bande C/X et d'un modèle d'océan

**Mot clés :** Salinité de Surface Océanique, Baie du Bengale, radiomètres, variabilité intrinsèque, modèle océanique

**Résumé :** La salinité de la surface de la mer (SSS) est considérée comme ayant une influence sur les précipitations régionales (interactions air-mer, cyclones tropicaux) et la productivité biogéochimique dans la baie du Bengale (BoB). Cependant, avant l'ère des radiomètres bande L, les données de SSS dans la BoB étaient rares et insuffisantes pour décrire les variations à l'échelle du bassin. Cette thèse vise à reconstruire les variations de SSS à l'échelle du bassin en utilisant de données satellitaires radiométriques en bande C & X. La comparaison de la climatologie de SSS obtenue par AMSR-E et celle de l'Initiative sur les changements climatiques indique des similitudes, mais la première sous-estime généralement les valeurs de SSS en dessous de 30 pss et présente de fortes erreurs de fraîcheur

près des côtes. Dans une seconde partie, cette étude examine l'impact des tourbillons sur le phénomène de la "rivière dans la mer" le long de la côte Est de l'Inde. Les résultats indiquent que la variabilité intrinsèque domine les anomalies du niveau de la mer et de la SSS le long de la côte Ouest, tandis que les signaux forcés prédominent près des côtes et dans la moitié Est de la BoB. Les tourbillons modulent fortement l'extension offshore de la "rivière dans la mer", mais moins son extension vers le Sud. La validation de la méthodologie met en évidence des limites de sous-estimation de la variabilité des tourbillons et fournit des informations sur les dynamiques complexes de la BoB et le rôle des tourbillons dans la modulation de la variabilité de la SSS.

**Title:** Study of the variability of surface salinity in the Bay of Bengal from C/X band radiometric satellite data and an ocean model

**Keywords:** Sea Surface Salinity, Bay of Bengal, radiometers, intrinsic variability, ocean model

**Abstract:** The Sea Surface Salinity (SSS) is believed to influence regional rainfall (air-sea interactions, tropical cyclones), and the biogeochemical productivity in the Bay of Bengal (BoB). However, prior to the L-band radiometer era, SSS data in the BoB were scarce and insufficient to describe basin-scale variations. This thesis aims to reconstruct the rare and inadequately described SSS variations at the basin scale in the BoB using C- & X-band radiometric satellite data. Comparing the retrieved SSS climatology of AMSR-E and that of Climate Change Initiative indicates similarities, but the former generally underestimates SSS values below 30 pss and exhibits strong fresh biases near the

coasts. In a second part, this study examines the impact of eddies on the "river in the sea" along the East Coast of India and reveals that intrinsic variability dominates sea level anomaly and SSS along the West Coast, while forced signals dominate near the coast and in the eastern half of the BoB. Eddies strongly modulate the offshore extension of the "river in the sea," but have a lesser influence on its southward extension. The validation of the methodology highlights limitations in underestimating eddy variability and provides insights into the complex dynamics of the BoB and the role of eddies in modulating SSS variability.